NONLINEAR OPTICAL MICROSCOPY AND SPECTROSCOPY BY PULSE SHAPING OF A COHERENT FIBER SUPERCONTINUUM

BY

YUAN LIU

DISSERTATION

Submitted in partial fulfillment of the requirements
for the degree of Doctor of Philosophy in Bioengineering
in the Graduate College of the
University of Illinois at Urbana-Champaign, 2015

Urbana, Illinois

Doctoral Committee:

Professor Stephen A. Boppart, Chair
Professor Martin Gruebele
Associate Professor Kimani C. Toussaint, Jr.
Assistant Professor Su-A Myong

ABSTRACT

Nonlinear optical microscopy and spectroscopy enable three-dimensional sub-μm-resolution imaging with deeper penetration and reduced photodamage, and have been established as powerful methods in biomedicine. The most appealing aspect of nonlinear optical imaging is the wealth of molecular contrast derived from various multiphoton processes. Two-photon and three-photon fluorescence microscopy visualizes endogenous fluorophores. Second and third harmonic generation microscopy maps optical non-centrosymmetry and heterogeneity. Coherent Raman scattering spectroscopic imaging probes intrinsic molecular vibrations. An integrated platform with combined modalities realizes label-free imaging of diverse biomolecules, and is highly desirable for biomedical fields. However, bringing these techniques together is not trivial due to the complexity of laser and imaging systems, and the requirements of modalities need to be met and often compromised. These limitations have hindered the biological application and clinical translation of the technology. In this thesis, multimodal nonlinear optical imaging by pulse shaping of a coherent fiber supercontinuum is demonstrated and applied to breast cancer research. The supercontinuum is generated in an all-normal-dispersion fiber, achieving a spectrum spanning the optical biological window with high coherence and high power. Efficient two-photon and three-photon fluorescence microscopy, second and third harmonic generation microscopy, as well as coherent anti-Stoke Raman scattering spectroscopic imaging are performed by adaptive pulse shaping of the supercontinuum pulses. Different molecules and structures in normal and cancerous human breast tissues are visualized, and the complimentary multiphoton signals and the vibrational spectrum form a complete molecular profile for analyzing the biochemical composition *in situ*. Using this approach, mammary tumor development in a carcinogen-induced rat model is investigated in a 9-week longitudinal study. Multiphoton molecular biomarkers and their transformation, such as regulated cellularity, collagen organization, elastin organization, angiogenesis, lipid degradation, and distribution of microvesicles are identified and correlated by multimodal imaging. The proposed technology presents simplicity and applicability, and may have a broader impact in biomedical research and fundamental science.

ACKNOWLEDGEMENTS

I would like to first thank my advisor, Professor Stephen A. Boppart for his advice and support during my years in the Biophotonics Imaging Laboratory. It is of great honor to conduct exciting research under his supervision. I learned a lot from him on how to pursue novel scientific ideas. The breadth of his knowledge and the way he resolves engineering impossibilities really affects my attitude toward scientific research. I also learned a great deal from him on how to interact with and influence people. His sincere care for people around him and his communication skills are things I wish I could have absorbed more during my time in Urbana-Champaign.

This thesis would not have been possible without several individuals. I sincerely appreciate Dr. Haohua Tu's contribution on the fiber continuum generation, which realized the pulse shaping microscopy and spectroscopy system. I am grateful for Eric Chaney's help on the animal experiments, ensuring that the challenging studies ran smoothly. I am thankful for Dr. Youbo Zhao's suggestions from the experimental details to daily life, which enabled me to overcome a lot of difficulties. I really appreciate Darold Spillman and Marina Marjanovic for their help and care of every little thing that makes our lives easier. I want to thank several graduate students in the Biophotonics Imaging Laboratory, Wladimir Benalcazar, Benedikt Graf, Adeel Ahmad, Sixian You, and Andrew Bower, for the valuable and happy time we spent together on research. I also want to express my gratefulness to all the members in the Biophotonics Imaging Laboratory. It was a great pleasure to be in this big family, to work with so many talented people from different fields, and to have fun outside the laboratory together.

I am very thankful for the support from my family, my father, my mother, my brother, his wife, and their lovely kids. At last, I want to thank my girlfriend, Manqian Qian. Their endless love and understanding were always fueling me during these years in Urbana-Champaign.

TABLE OF CONTENTS

1. INTRODUCTION 1
   1.1. Nonlinear optical imaging 1
   1.2. Ultrafast pulse shaping 2
   1.3. Fiber supercontinuum generation 3
   1.4. Breast cancer detection and diagnosis 4
   1.5. Scope of the thesis 4
2. BACKGROUND 7
   2.1. Nonlinear optical processes in microscopy and spectroscopy 7
      2.1.1. Two-photon fluorescence (2PF) 8
      2.1.2. Second harmonic generation (SHG) 9
      2.1.3. Three-photon fluorescence (3PF) 10
      2.1.4. Third harmonic generation (THG) 11
      2.1.5. Coherent anti-Stokes Raman scattering (CARS) 12
      2.1.6. Stimulated Raman scattering (SRS) 13
   2.2. Molecular imaging capabilities 14
   2.3. Ultrafast pulse shaping and coherent control 20
      2.3.1. Design of a pulse shaper 21
      2.3.2. Principles of pulse shaping 22
      2.3.3. Coherent control of optical processes 23
   2.4. Fiber supercontinuum generation 26
      2.4.1. Supercontinuum generation in photonic crystal fibers 26
      2.4.2. Mechanisms in fiber supercontinuum generation 27
      2.4.3. Applications in microscopy and spectroscopy 31
3. DEVELOPMENT OF THE COHERENT FIBER SUPERCONTINUUM 33
   3.1. Generation of the coherent fiber supercontinuum 33
   3.2. Compression and shaping of the supercontinuum pulses 39
   3.3. Wave-breaking extended coherent fiber supercontinuum 42
4. PULSE SHAPING FOR NONLINEAR OPTICAL MICROSCOPY AND SPECTROSCOPY 49
   4.1. Local pulse compression for 2PF, SHG, 3PF and THG microscopy 49
      4.1.1. Principles of local pulse compression 49
      4.1.2. Nonlinear optical microscopy by shaping supercontinuum pulses of 900-1160 nm 52
      4.1.3. Nonlinear optical microscopy by shaping supercontinuum pulses of 780-1300 nm 60
   4.2. Adaptive spectral focusing for hyperspectral CARS imaging 65

4.2.1. Optimal spectral focusing for CARS imaging in the CH stretching region 65
4.2.2. Adaptive spectral focusing for CARS imaging and capability of SRS imaging 67
4.3. Single-beam CARS spectroscopy in the fingerprint region 70
4.3.1. Single-beam interferometric CARS spectroscopy 70
4.3.2. Optimized amplitude shaping for single-beam CARS spectroscopy 77
5. LABEL-FREE MULTIMODAL MULTIPHOTON MOLECULAR IMAGING 84
5.1. Evolution of multimodal multiphoton imaging 84
5.2. Multimodal multiphoton molecular imaging by shaping supercontinuum pulses 87
5.2.1. Flexible excitation and detection for multimodal multiphoton imaging 87
5.2.2. Multimodal multiphoton imaging and molecular profiles of human breast cancer 89
5.3. Remarks on multimodal multiphoton molecular imaging 98
5.3.1. Validation of nonlinear optical imaging modalities 98
5.3.2. Three-dimensional imaging capability 99
5.3.3. Hyperspectral CARS imaging in the CH stretching region 102
5.3.4. Extended excitation map by tailored supercontinuum pulses 105
6. MULTIPHOTON MOLECULAR IMAGING OF BREAST CANCER DEVELOPMENT 107
6.1. Nonlinear optical imaging in breast cancer research 107
6.2. Animal procedures and imaging setup 109
6.2.1. Animal procedures 109
6.2.2. Imaging sites selection 110
6.2.3. Imaging setup 112
6.2.4. Pulse processing 114
6.2.5. Resolution of the imaging modalities 114
6.2.6. Multiphoton molecular profile analysis 115
6.3. Multimodal multiphoton imaging of breast cancer development 115
6.3.1. Multimodal imaging of early breast cancer development 116
6.3.2. Multimodal imaging of late breast cancer development 126
6.4. Remarks on the angiogenic states based on the 3PF-sensitive microvesicles 151
7. MULTIPHOTON MOLECULAR PROFILES AND BIOMARKERS IN BREAST CANCER DEVELOPMENT 156
7.1. Multiphoton molecular profiles of biomolecules in breast cancer development 156
7.1.1. Molecular profiles in early breast cancer development 157
7.1.2. Molecular profiles in late breast cancer development 163
7.2. Multiphoton molecular biomarkers in breast cancer development 167
7.2.1. Molecular biomarkers in early breast cancer development 167

7.2.2. Molecular biomarkers in late breast cancer development 174
8. CONCLUSIONS AND FUTURE DIRECTIONS 183
8.1. Conclusions 183
8.2. Future directions 185
REFERENCES 187

1. INTRODUCTION

This chapter presents an introduction to the key elements of the thesis, including nonlinear optical imaging, ultrafast pulse shaping, fiber supercontinuum generation, as well as breast cancer detection and diagnosis. The scope of the thesis is discussed at the end of the chapter.

1.1. Nonlinear optical imaging

With the development of ultrafast lasers, nonlinear optical microscopy and spectroscopy have emerged as power tools in biomedical fields since the emergence of two-photon fluorescence (2PF) microscopy in the early 1990s[1]. Three-photon fluorescence (3PF) microscopy extends the nonlinear excitation spectral range into ultra-violet wavelengths, where a large number of endogenous fluorophores can be excited by a near-infrared laser[2]. The synergy of second harmonic generation (SHG) microscopy enables visualization of non-centrosymmetric media, such as collagen and myosin, in biological tissues[3]. Third harmonic generation (THG) maps the optical heterogeneity, serving as an unique modality for structural imaging in transparent materials[4]. Coherent anti-Stokes Raman scattering (CARS) and stimulated Raman scattering (SRS) open up a new dimension of chemical imaging based on molecular vibrations[5,6]. The most appealing advantage of nonlinear optical imaging is the diverse molecular contrast from the various modalities, as illustrated in Fig. 1.1. Each modality is capable of visualizing a specific set of biomolecules without exogenous labeling. Combined together, these imaging methods establish a platform to image an enlarged pool of molecules in biological samples. The nonlinear optical responses create a profile of molecular signatures for understanding the biochemical composition of the microenvironment *in situ*. In addition, these technologies provide three-dimensional sub-μm-resolution imaging with deeper penetration and reduced photodamage, and have made a broad impact in oncology, neuroscience, embryology, and other research areas[7-10].

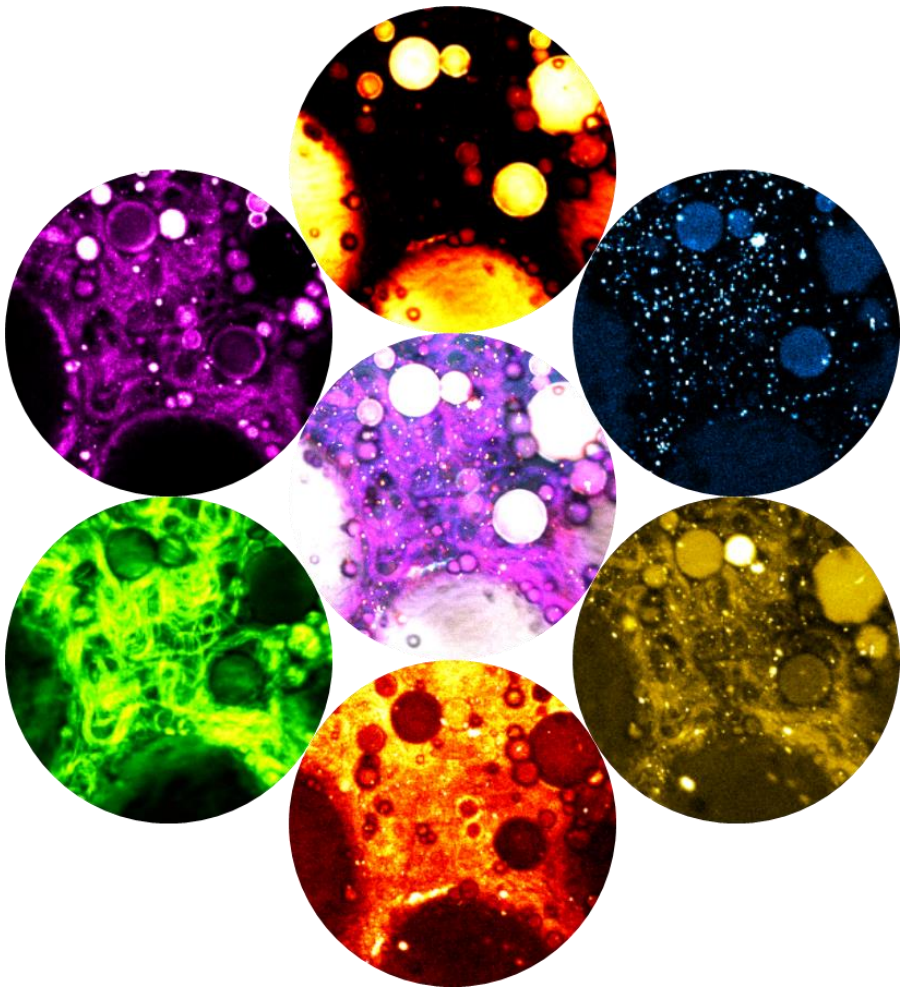

Fig. 1.1. Label-free multimodal nonlinear optical imaging of a cancerous human breast tissue. Clockwise (from top): CARS 2850 cm^{-1}, 3PF, 2PF, CARS 3050 cm^{-1}, SHG, THG images; centered: pseudo-histology generated from the multimodal images. Image diameter: 175 µm.

1.2. Ultrafast pulse shaping

As nonlinear optical processes involve higher-order interaction of the light pulses with matter, the "shape" of the optical pulses will affect the nonlinear response. This shape represents the temporal profile of the electric field, which can be depicted by the temporal amplitude and phase, or by the corresponding frequency domain representation through a Fourier transform. For nonlinear optical imaging, ultrafast pulses of temporal widths ranging from picoseconds down to femtoseconds are considered. Controlling the temporal shape of these pulses is not straightforward, however, because of the limited speed of electronic devices for modulation at picosecond or femtosecond time scales. Nevertheless, this issue can

be circumvented by tailoring the optical pulses in the frequency domain. This is achieved by employing chromatically dispersive optics, such as a grating or a prism pair, to disperse light in space, and by modulating individual frequency component of light with a spatial light modulator. The concept of ultrafast pulse shaping was first proposed by Weiner[11], and the technology has found wide applications in telecommunication, coherent control of complex systems, and nonlinear optical microscopy and spectroscopy[12]. In nonlinear optical microscopy and spectroscopy, the goal of ultrafast pulse shaping is to steer the nonlinear optical processes for contrast enhancement, selective detection, and information extraction. Various pulse shaping methods have been proposed for coherent control of nonlinear optical processes since the demonstration of controlling a two-photon transition[13]. However, applications of these methods to biomedical fields have been plagued by the complexity. Simple and practical approaches to customize the optical pulse shapes have been desired and would further benefit the translation of this technology from the bench-top to the bedside.

1.3. Fiber supercontinuum generation

Fiber supercontinuum (SC) generation was first discovered in 1999 by Ranka[14], as an attempt to investigate the extreme nonlinear optical processes in a microstructured fiber. The finding then initiated the supercontinuum revolution, and has had a profound impact in photonics field[15]. The progress of photonic crystal fiber technology further fostered the development of fiber SC, providing a flexible and cost-effective way to generate SC[16]. SC presents an unprecedented ultrabroad spectral bandwidth compared to conventional mode-locked solid-state lasers, and therefore is of great interest and value in biophotonic imaging. The fiber SC offers extracavity spectral broadening alleviating the cavity alignment of a broadband pulsed laser, as well as the intrinsic compatibility to fiber-based components for beam delivery in a clinical setting. However, SC sources have been notorious for their poor stability, low coherence, and low power. Limited applications in nonlinear optical microscopy and spectroscopy have been demonstrated, and the performance has not been comparable to that of the solid-state counterparts.

Particularly for ultrafast pulse shaping, highly-quality SC possessing excellent stability and coherence is desirable. Overcoming this engineering barrier to bring fiber SC into pulse shaping and multiphoton imaging is one of the goals of this thesis.

1.4. Breast cancer detection and diagnosis

As an unfortunately common life-threatening disease in females, breast cancer (BCa) is a major concern for human health and healthcare. In the United States, 1 of 8 women develop BCa during their lifetime, and BCa is ranked second among all cancer deaths[17]. Early detection and diagnosis of BCa are crucial to increase the patients' survival rate. Mammography is a typical screening tool for abnormal breast masses and calcifications, but the method presents limited sensitivity and specificity and is uncomfortable for the examinees[18]. Histopathology serves as the gold standard for diagnosis, but the tissue fixation, sectioning, and staining are labor-intensive and time-consuming. The sample preparation processes prevent the observation of the unperturbed biochemical microenvironment, and the diagnosis decision is subjective and may vary depending on the physician. Therefore, a high-speed label-free molecular imaging technology is demanded, and can be fulfilled by nonlinear optical techniques which enable visualization of the biochemical contents within a minute. Nonlinear optical imaging provides not only an alternative method for tissue biopsy but also the molecular information of a sample in its native state. The advancement with nonlinear optical imaging has the potential to improve BCa diagnosis and potentially facilitate tumor margin detection intraoperationally[19]. In addition, the method can be employed to identify molecular biomarkers in early BCa, and to understand their transformation during tumor progression. Addressing these questions is important for improving diagnosis and for establishing cancer therapy.

1.5. Scope of the thesis

The goal of this thesis is to develop a translational-friendly nonlinear optical imaging platform and to apply the technology to BCa research. The organization of the thesis is illustrated in Fig. 1.2. Chapter 2

provides an overview of the background knowledge, including nonlinear optical imaging, pulse shaping, and SC generation. Chapter 3 discusses the development of the fiber SC toward an ultrabroadband light source enabling pulse shaping and nonlinear optical imaging. Chapter 4 presents three pulse shaping strategies to customize the SC pulses for specific nonlinear optical microscopy and spectroscopy methods. Chapter 5 integrates the fiber SC and the pulse shaping methods to establish a multiphoton molecular imaging platform, and to image the biomolecular contents in cancerous and normal human breast tissues. Multiphoton molecular profiling was developed to analyze the biochemical composition *in situ* without any sample processing or exogenous labeling. With the imaging methods, Chapter 6 investigates the morphological features during mammary tumor progression in a carcinogen-induced murine model. Chapter 7 presents the multiphoton molecular analysis in order to identify the molecular biomarkers for BCa detection. Chapter 8 concludes the thesis and provides a future outlook.

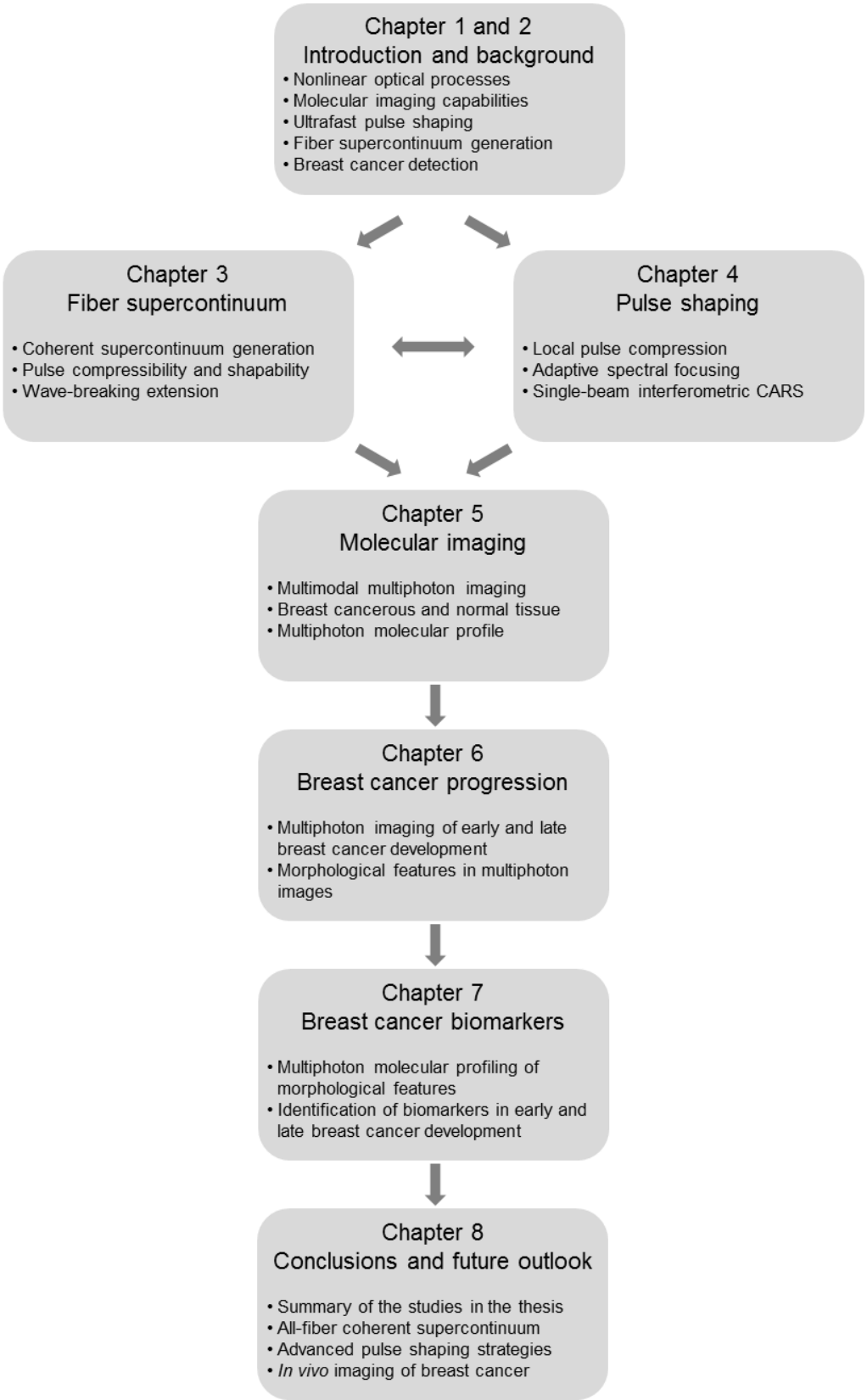

Fig. 1.2. Organization of the contents in the thesis.

2. BACKGROUND

In this chapter, the background knowledge of the thesis will be presented, including the physics of nonlinear optical processes, their molecular imaging capabilities, the principles of pulse shaping and coherent control, and the mechanisms in fiber supercontinuum generation.

2.1. Nonlinear optical processes in microscopy and spectroscopy

Nonlinear optical microscopy and spectroscopy are based on nonlinear processes that occur when high intensity optical pulses interact with matter. The nonlinear optical imaging techniques have been established and brought into biomedical studies since the early 1990s[1-3,5,6,20]. Compared to conventional optical microscopy and spectroscopy, there are several notable advantages of these nonlinear methods, such as intrinsic molecular contrast from different physical mechanisms, three-dimensional imaging capabilities due to localized nonlinear excitation, as well as deeper imaging penetration depth and reduced photodamage by the use of near-IR light sources[7-10]. In this section, some of the most commonly-used and important nonlinear modalities adopted in this thesis are introduced, including two-photon fluorescence (2PF), second harmonic generation (SHG), three-photon fluorescence (3PF), third harmonic generation (THG), coherent anti-Stokes Raman scattering (CARS), and stimulated Raman scattering (SRS). Their physical mechanisms, energy-level diagrams, and molecular contrast are discussed. The nonlinear processes are modeled in the frequency domain to facilitate later discussion on the effects of pulse shaping.

2.1.1. Two-photon fluorescence (2PF)

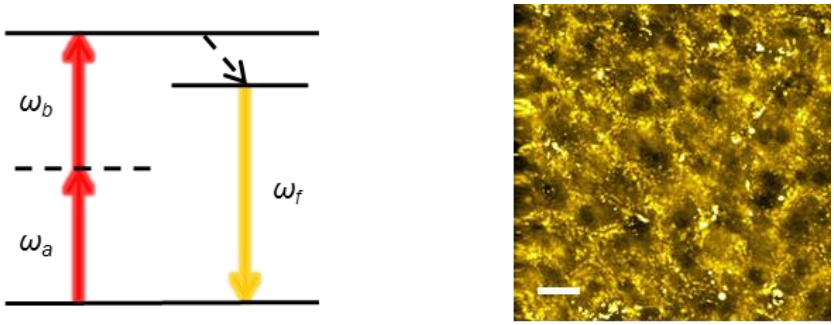

Fig. 2.1. (Left) The energy-level diagram of 2PF. ω_a, ω_b: frequencies of the incident photon pair; ω_f: frequency of the emitted fluorescence photon. (Right) A 2PF image of rat liver. Scale bar: 25 μm.

Compared to conventional one-photon absorption in fluorescence microscopy, two photons are simultaneously absorbed by a fluorophore in 2PF, followed by energy relaxation and fluorescence emission[1]. The energy-level diagram of a 2PF process and a 2PF image of rat liver showing retinol in hepatocytes are demonstrated in Fig. 2.1. The absorption of the two photons through a transient virtual state leads to the excitation of a real state of energy that is the sum of those of the two photons. The nonlinear excitation frequency is at twice the fundamental frequency, or the nonlinear excitation wavelength is peaked at one-half of the fundamental wavelength. By using a near-infrared laser, this nonlinear process enables excitation of fluorophores that are typically excited by a laser emitting in the visible wavelength range. 2PF allows imaging of a wide collection of intrinsic fluorescent biomolecules, such as NAD(P)H[21], FAD[22], elastin[21], and retionol[21]. The 2PF process can be modeled as

$$S_{2PF}(\Omega) = \sigma_{em}(\Omega)\int_0^{\infty} d\omega \phi_F \sigma_{ab}(\omega) \left| \int_0^{\omega_a+\omega_b=\omega} d\omega_a d\omega_b A(\omega,\delta) E(\omega_a) E(\omega_b) \right|^2 \quad (2.1)$$

where S_{2PF} is the emitted 2PF, σ_{em} and σ_{ab} are the emission and absorption cross-sections of the fluorophores, and ϕ_F is the fluorescence quantum yield[8]. $A(\omega,\delta)$ depicts any absorption and phase change induced by the intermediate energy levels, which is generally ignored by assuming a system with no intermediate level. The integration within the squared modulus incorporates all the frequency pairs leading to the two-photon absorption at frequency ω[12].

2.1.2. Second harmonic generation (SHG)

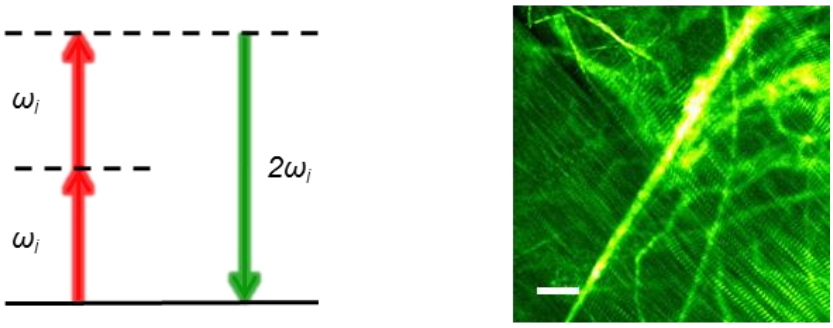

Fig. 2.2. (Left) The energy-level diagram of SHG. ω_i: frequency of the incident photon. (Right) An SHG image of rat muscle. Scale bar: 25 μm.

SHG is a second-order nonlinear process in which two photons of the same frequency interact with the material and are converted to one photon of doubled frequency[3]. The energy-level diagram of an SHG process and an SHG image of muscle tissue showing myofibrils are shown in Fig. 2.2. While two incident photons are participating in this process as in 2PF, SHG does not have the real absorption of the photons, and only virtual states are involved. The instantaneous electronic response is responsible for the frequency-doubled photon conversion. Because SHG is a parametric process, the phase of the incident photons is preserved. The molecular contrast of SHG is indirectly derived from the optical non-centrosymmetry[23]. The most important biological molecules and structures that can be visualized by SHG include collagen[21,24], myosin[24], tubulin[24], cellulose[25], and starch[25]. The SHG process can be described as

$$S_{SHG}(\Omega) = \left| \int_0^{\omega_a+\omega_b=\Omega} d\omega_a d\omega_b \chi^{(2)}(\Omega) E(\omega_a) E(\omega_b) \right|^2 \tag{2.2}$$

where $S_{SHG}(\Omega)$ is the generated SHG signal and $\chi^{(2)}(\Omega)$ is the second order nonlinear susceptibility. Note that here the sum frequency generation (SFG), induced by two incident photons of different frequencies, is also incorporated in the model.

2.1.3. Three-photon fluorescence (3PF)

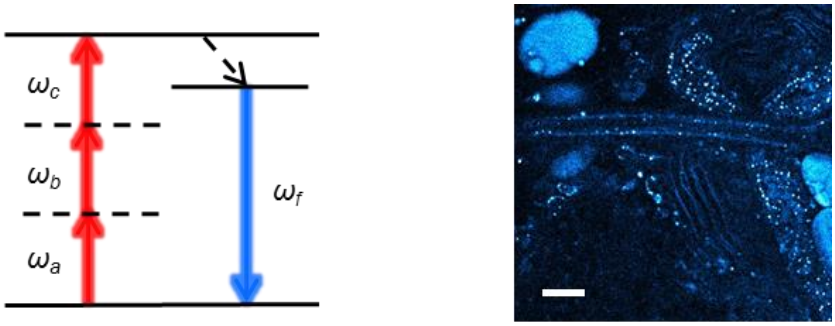

Fig. 2.3. (Left) The energy-level diagram of 3PF. ω_a, ω_b, ω_c: frequencies of three incident photons; ω_f: the frequency of the emitted fluorescence. (Right) A 3PF image of rat mammary tumor. Scale bar: 25 µm.

In 3PF, three photons are simultaneously absorbed to excite fluorescent molecules[2]. The effective excitation frequency is at three times the fundamental frequency. The energy-level diagram of 3PF and a 3PF image of rat mammary tumor showing lipid droplets and developing blood vessels are demonstrated in Fig. 2.3. The absorption of the three photons is through two transient virtual states, leading to the excitation of a real state of energy that is the sum of those of the three photons. In comparison to 2PF, this modality shares some common features of localized excitation, deeper imaging penetration, and reduced photodamage as a multiphoton fluorescence technique. Nevertheless, 3PF has a smaller excitation focal volume, and the 3PF excitation spectra of fluorophores resemble the 1PF excitation spectra due to the symmetry of transition selection rule[26,27]. The most valuable aspect of 3PF is perhaps that it extends multiphoton excitation deep into the ultra-violet wavelengths with a near-infrared excitation light source, allowing for imaging of important intrinsic fluorophores in this spectral range, such as tryptophan[21], serotonin[28], and melatonin[21]. As an example, for a conventional broadband Ti:saphhire laser with a 700-1000 nm emission spectra, 2PF and 3PF combined together offers a broad excitation spectral range of 233-500 nm. However, 3PF imaging requires higher laser power and longer integration time to compensate for its lower efficiency. The 3PF cross-section of tryptophan, serotonin, and melatonin are of the order of 10^{-84} cm^6s^2 as compared to the 2PF cross-section of common endogenous fluorophores of the order of 10^{-51} cm^4s. Therefore, 3PF has not been as widely applied as compared to 2PF imaging. The 3PF process can be modeled as

$$S_{3PF}(\Omega) = \sigma_{em}(\Omega)\int_0^{\infty} d\omega \phi_F \sigma_{ab}(\omega) \left| \int_0^{\omega_a+\omega_b+\omega_c=\omega} \mathrm{d}\omega_a d\omega_b d\omega_c A(\omega,\omega_a,\omega_b,\omega_c) E(\omega_a) E(\omega_b) E(\omega_c) \right|^2 \quad (2.3)$$

where S_{3PF} is emitted 3PF, σ_{em} and σ_{ab} are the emission and excitation cross-sections of the fluorophore, and ϕ_F is the fluorescence quantum yield[8]. $A(\omega,\omega_a,\omega_b,\omega_c)$ takes into account any absorption and phase change from the intermediate energy levels. The term within the squared modulus models all the frequency triplets leading to three-photon absorption at frequency ω.

2.1.4. Third harmonic generation (THG)

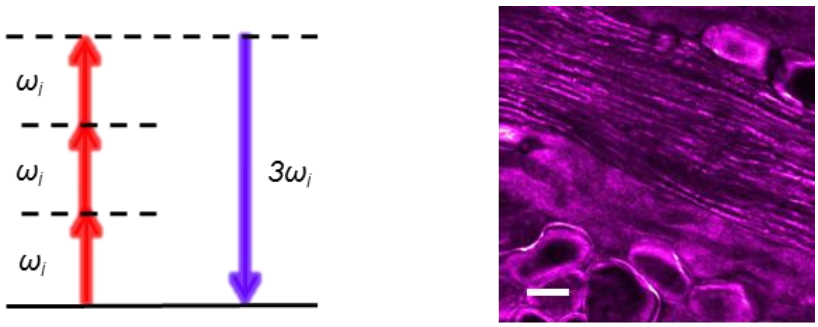

Fig. 2.4. (Left) The energy-level diagram of THG. ω_i: frequency of incident photon. (Right) A THG image of developing rat mammary tumor. Scale bar: 25 μm.

Like SHG, THG is also a parametric process in which the third harmonic of the incident light is generated[4]. The instantaneous electronic response converts three incident photons into one of tripled frequency, and no absorption is involved during this process. Fig. 2.4 demonstrates the energy-level diagram of the THG process and a THG image of a developing rat mammary tumor, showing lipid droplets, nerve fibers, and collagen fibers. THG originates from the optical heterogeneity and the interfaces of third-order nonlinear susceptibilities within the focal volume. No THG is observed in a homogeneous material because the Gouy phase shift results in destructive interference of the generated THG signal. Therefore, THG microscopy is more like a general-purpose imaging technique mapping heterogeneity and boundaries with an enhanced capability for detecting targets comparable to the focal volume of the beam. This modality is especially powerful in imaging transparent samples that are difficult

to probe with other optical imaging methods. THG has had significant applications in imaging lipid[22], embryonic development[29], and the nervous system[30]. The physical mechanism can be described as

$$S_{THG}(\Omega) = \left| \int_{0}^{\omega_a+\omega_b+\omega_c=\Omega} \mathrm{d}\omega_a d\omega_b d\omega_c \chi^{(3)}(\Omega) E(\omega_a) E(\omega_b) E(\omega_c) \right|^2 \quad (2.4)$$

where $S_{THG}(\Omega)$ is the THG signal. $\chi^{(3)}(\Omega)$ is the third order nonlinear susceptibility, and ω_a, ω_b, and ω_c are frequencies of three different photons, with their sum equal to the generated THG frequency at Ω.

2.1.5. Coherent anti-Stokes Raman scattering (CARS)

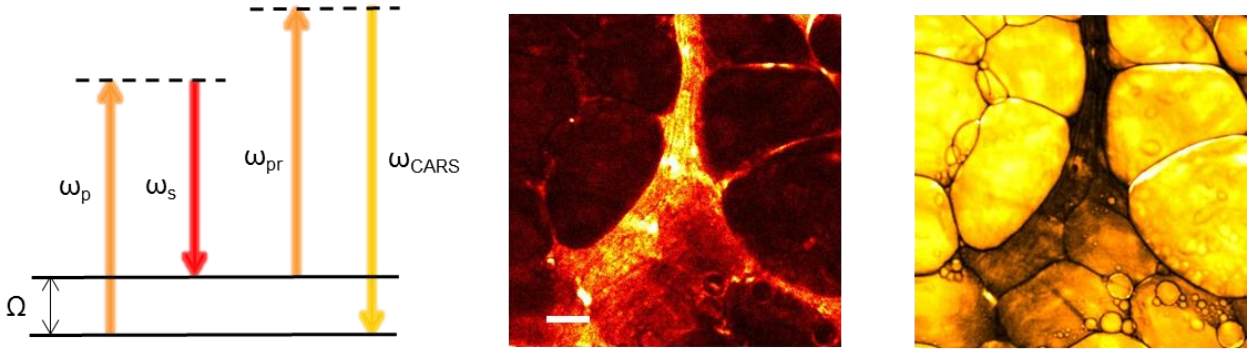

Fig. 2.5. (Left) The energy-level diagram of CARS. ω_p, ω_s, and ω_{pr}: frequencies of pump, Stokes, and probe photons; ω_{CARS}: frequency of the generated CARS photon; Ω: frequency of molecular vibration. (Middle) A CARS image at 3050 cm^{-1}, and (right) a CARS image at 2850 cm^{-1} of rat mammary tissue. Scale bar: 25 μm.

Coherent Raman scattering techniques, including CARS and SRS (described in next section), utilize molecular vibrations as the contrast mechanism[7,31]. The coherent enhancement offers orders-of-magnitude stronger signal and faster acquisition compared to spontaneous Raman scattering. CARS and SRS are therefore particularly desirable for chemical sensing and biomedical imaging. Fig. 2.5 displays the energy-level diagram of CARS and two vibrational images at 3050 cm^{-1} and 2850 cm^{-1} showing stroma and adipocytes, respectively, in rat mammary tissue. Interestingly, CARS was first discovered in 1965 in Ford Motor Company, a "car" company[32]. The technique became more popular after 1999 when three-dimensional CARS imaging was demonstrated under the tight-focusing condition, alleviating the cumbersome phase matching consideration for practical applications[5]. In CARS, the pump and Stokes fields first coherently drive the molecular vibration at their frequency difference through a virtual state.

The probe field is then scattered off the vibration to generate a blue-shifted CARS field. The most important applications of CARS include imaging a variety of lipid and protein biomolecules (see Table 2.1)[7]. The CARS process can be modeled in two steps,

$$A(\Omega) = \chi^{(3)}(\Omega)\int_0^\infty E_p(\omega')E_s^*(\omega'-\Omega)d\omega' \tag{2.5}$$

$$P(\omega) = \int_0^\infty A(\Omega)E_{pr}(\omega-\Omega)d\Omega \tag{2.6}$$

where E_p, E_s, and E_{pr} are the pump, Stokes, and probe fields, respectively. $A(\Omega)$ is amplitude of the molecular vibration, and $\chi^{(3)}(\Omega)$ is the third-order nonlinear susceptibility, including both the resonant $\chi_R^{(3)}(\Omega)$ and non-resonant $\chi_{NR}^{(3)}(\Omega)$ contributions. One of the greatest limitations in CARS is the non-resonant background, which oftentimes distorts the Raman line-shape. Various solutions to this problem have been developed, including maximum entropy[33,34], Kramers-Kronig transformation[35-38], interferometric detection[19,39,40], and ultrafast pulse shaping[41-44]. While different approaches possess their own advantages and disadvantages, minimizing artifacts and supervision, as well as improving experimental simplicity all need to be considered when adopting one for a specific application.

2.1.6. Stimulated Raman scattering (SRS)

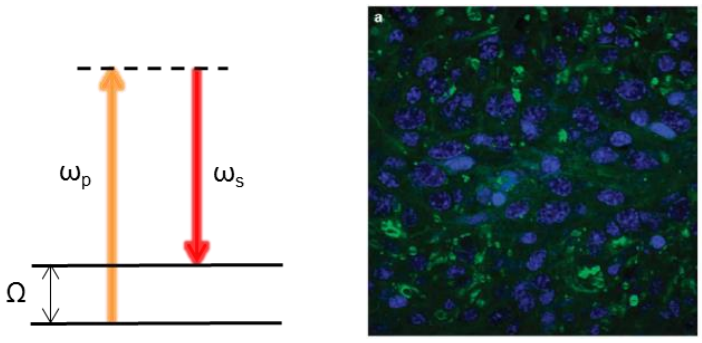

Fig. 2.6. The energy-level diagram of SRS. ω_p and ω_s: frequencies of pump and Stokes photon; Ω: frequency of molecular vibration. A SRS image of mouse mammary tumor (Green: 2845 cm^{-1}, blue: difference of 2940 cm^{-1} and 2845 cm^{-1}). Image dimension: 116 x 116 μm^2. (Reprinted by permission from Macmillan Publishers Ltd: Laboratory Investigation, Freudiger, C.W. et al. Multicolored stain-free histopathology with coherent Raman imaging[45], copyright 2012).

SRS is another coherent Raman scattering technique that utilizes molecular vibrations as the contrast mechanism. SRS and CARS typically occur simultaneously when the frequency difference of the pump and Stokes fields match a specific molecular vibrational. The energy-level diagram of the SRS process is illustrated in Fig. 2.6. Instead of detecting the blue-shifted CARS signal, the energy transfer from pump to Stokes fields through the transient virtual state is measured in SRS. This energy transfer can be detected with coherent Raman loss (CRL) when probing the loss of the pump beam, or coherent Raman gain (CRG) when probing the gain of the Stokes beam[6,46,47]. The SRS photon is coherent, co-propagating, and possessing the same frequency as the incident fields. Therefore, the SRS photon also experiences homodyne amplification from the incident fields. Nevertheless, the signal is still weak compared to the lasers, so high-speed modulation with lock-in detection is utilized to detect the SRS signal[6,46,47]. While SRS in theory has the same sensitivity as compared to CARS, what makes SRS attractive to the biomedical imaging field is its non-resonant background-free nature and linear proportionality of the signal to molecular concentration[48-53]. Following the expressions in CARS, the SRL in SRS can be modeled as[54]

$$A(\Omega) = \chi^{(3)}(\Omega)\int_0^\infty E_p(\omega')E_s^*(\omega'-\Omega)d\omega' \tag{2.7}$$

$$P(\omega) = \int_0^\infty A(\Omega)E_s(\omega-\Omega)d\Omega \ , \tag{2.8}$$

and the homodyne-amplified response can be written as

$$\Delta I_{SRL} = \int_0^\infty P(\omega)E_p(\omega)\mathrm{d}\omega \ . \tag{2.9}$$

2.2. Molecular imaging capabilities

As discussed in the previous section, the diverse physical mechanisms involved in nonlinear optical processes enable label-free molecular imaging of biological tissues. Table 2.1 summarizes the literature of the endogenous biomolecules and structures that can be visualized by 2PF, SHG, 3PF, THG, as well as

CARS and SRS. The most important applications in each modality are highlighted with different colors. The reported excitation or incident wavelengths for 2PF, SHG, 3PF, and THG, and the vibrational frequencies for CARS and SRS, are listed. The fluorophores in 2PF and 3PF are categorized based the spectral range of a conventional Ti:sapphire laser as the excitation source (fundamental: 700-1000 nm, 2P excitation: 350-500 nm, 3P excitation: 233-333 nm). While nonlinear optical imaging has found broad applications in various biological systems, this table is intended to serves as a starting point to incorporate the seemingly endless number of intrinsic biomolecules that can be imaged by these modalities. For more discussion on the molecular imaging capabilities of each modality, readers are referred to these publications and the references within[7,10,21,31,55-58].

Note that the table presents a comparison of molecules visualized by different modalities and will be utilized to identify the biomolecular composition in the multiphoton imaging studies in later chapters (see next page for Table 2.1).

Table 2.1. Intrinsic biomolecules and structures revealed by nonlinear optical imaging.

Modality	CARS and SRS	2PF	SHG	3PF	THG
Mechanism	Molecular vibration	2-photon excited fluorescence	Non-centrosymmetry	3-photon excited fluorescence	Optical heterogeneity
Molecules	Biological environments Vibration @ frequency (cm-1)		Excitation or incident wavelength (nm)		
Amino acid					
Phenylalanine	Cheese[59], HEK-293 cell[60], murine liver[61], yeast cell[62] C-H aromatic stretching @ 3060[59] Ring breathing @ 1002[62], 1004[59-61]				
Proline	Murine liver[61] C-C stretching @ 855[61], 938[61]				
Tryptophan	Cheese[59] C-H aromatic stretching @ 3060[59]			Mouse choroid plexus[21], mouse small intestine[21] 750[21]	
Carbohydrate					
Cellulose	Corn stover[63] C-C stretching @ 1100[63] C-O stretching @ 1100[63]		Acetobacter[64], celery petioles[25], lantana stem[25], maize stem[65], *Valonia*[64] 830~840[25], 900[64], 1230[65]		
Starch			*Commelina communis L*[65], Chara coralline[66], rice[25] 830~840[25], 1064[66], 1230[65]		
Lipid	3T3 cell[67], 3T3-L1 cell[68,69], Cheese[59], CHO cell[51], drosophila[60], guinea pig axonal myelin[70], HEK-293 cell[60], HeLa cell[71], human artery[72], human lung cancer cell[6], human perivascular tissue[73], liver cell[74], mayonnaise[59], MCF-7 cell[60], microalgae[51], mouse brain tissue & tumor[6,61], mouse ear skin[48,51], mouse skin[48], rat liver[50], soydrink[59]; yeast cell[62] C-C stretching @ 1080[59] CH_2 scissoring @ 1300, 1440-1445[59] CH bending @ 1456[62] CH_2 stretching @ 2840[69], 2843-2847[67], 2844[73], 2845[6,48,59,60,68,71,72], 2850[50,51,61,69,73,74] CH_3 stretching @ 2920[6], 2930[62, 72], 2935[69], 2940[51]				*A. thaliana*[22], *D. melanogaster*[22], hepatocyte[22], mouse brain[30], mouse lung[22], mouse skin[75], rat liver[22], soy bean[22], Zebrafish embryo[29] 1180[22], 1200[29,30]
Lipid-bilayer	3T3 cell[76], *Shewanella putrefaciens*[5] C-H aliphatic stretching @ 2870[76], 2878[5]				
Lipid-unsaturated	3T3-L1 cell[69], HL60 cell[47], human lung cancer cell[6], mayonnaise[59], MCF-7 cell[60], rat liver[50], yeast cell[62] =CH stretching @ 3005[59], 3015[6] C=C stretching @ 1650-1655[59], 1654[69], 1655[60,62], 1659[47], 1660[50]				

Table 2.1. Intrinsic biomolecules and structures revealed by nonlinear optical imaging (continued).

Cholesterol	Mouse aorta[77], pig artery[78] C=C stretching @ 1669[78] CH_2 stretching @ 2855[77], 2907[77], 2945[77] CH_3 stretching @ 2869[77], 2945[77], 2966[77]		Mouse aorta[77] 800~820[77]		
Retinol	Mouse ear skin[7,48], mouse skin[6] C=C stretching @ 1594[7] ,1595[6], 1596[48]	Mouse choroid plexus[21], mouse lung[22], mouse small intestine[21] 750[21], 860[22]			
Nucleic acid	3T3 cell[76], Drosophila[60], HEK-293 cell[60], MCF-7 cell[60], mouse brain tissue & tumor[61], murine liver[61], yeast cell[62] O-P-O stretching + pyrimidine ring breathing @ 785[60,61] PO_2^- stretching @ 1090[60,76], 1099[62]				
DNA			Herring sperm[79] 800[79]		
Polyphosphate	Yeast cell[62] PO_2^- stretching @ 1160[62]				
Porphyrin					
Chlorophyll		*Commelina communis L*[80], Moss leaf[25] 830[25], 1230[80]			
Hemozoin					Red blood cell[81] 1170[81]
Protein	Cheese[59], *Drosophila*[60], HeLa cell[71], human artery[72], human perivascular tissue[73], human skin[48], MCF-7 cell[60], microalgae[51], mouse ear skin[48, 51], mouse skin[48], rat liver[50], soydrink[59], yeast cell[62] CH_3 stretching @ 2924[73], 2930[59,62,72], 2940[51], 2942[73], 2950[48,50] Amide I @ 1650[59], 1655[60,71], 1656[62] CH bending @ 1452[62], 1456[62] CH deformation @ 1340[62] Amide III @ 1240[62] C-H aromatic stretching @ 3060[59]				
Collagen	Murine liver[61], murine pancreatic duct[61] C-C stretching @ 855[61], 938[61]	RAFT model[82] 730~750[82]	Black tetra fish scale[24], human skin[21], mouse arteriole[21], mouse articular cartilage-meniscus junction[21], mouse ear skin[24], mouse femur[21], mouse heart[21], mouse lung[22], mouse mammary gland & tumor[21], mouse ovary[21], mouse skin[75,] RAFT model[82], rat tail tendon[21] 750~920[21], 730~880[82], 850[24], 860[22], 1180[75]		Mouse skin[75] 1180[75]

Table 2.1. Intrinsic biomolecules and structures revealed by nonlinear optical imaging (continued).

Elastin		Human skin[21], mouse arteriole[21], mouse lung[22] 740~750[21], 860[22]			
Hemoglobin	Mouse brain tissue & tumor[61] C-C stretching @ 1548[61], 1565[61]				Human erythrocyte[83], mouse erythrocyte[75] 1180[75], 1260~1320[83]
Keratin	Human hair[84] Amide I @ 1601-1666[84] Amide III @ 1238-1246[84] Phenylalanine @ 1003[84] S-O stretching @ 1036[84]	Mouse hair shaft[24] 850[24]			
Myosin			*C. elegans* muscle[24], chicken embryonic cardiomyocyte[85], *Drosophila* myocyte[86], human muscle[87], mouse muscle[24,75,85,87,88], rat cardiomyocyte[89], scallop muscle[85] 830[86], 850[24], 880[90], 900[85], 920[87], 1042[86], 1064[89], 1180[75], 1230[88]		Mouse muscle[75,88], rat cardiomyocyte[89] 1064[89], 1180[75], 1230[88]
Tubulin			*C. elegans* embryo[24], rat brain[91], Zebrafish embryo[29] 760~880[91], 850[24]		
Others					
FAD		Dog cardiomyocyte[92], hamster cheek pouch[93], mouse lung[22], mouse muscle[87], RAFT model[82] 700-975[92],800~880[82], 860[22], 890[93], 920[87]			
Lignin	Alfalfa[94], corn stover[63] C=C aromatic stretching @ 1600[63,94]	Celery petioles[25], lantana stem[25] 830v840[25]			
Melatonin				Mouse pineal gland[21] 750[21]	

Table 2.1. Intrinsic biomolecules and structures revealed by nonlinear optical imaging (continued).

NAD(P)H		Dog cardiomyocyte[92] hamster cheek pouch[93], mouse heart[21], mouse lung[22], mouse mammary gland & tumor[21], mouse muscle[95], mouse pineal gland[21], mouse small intestine[21], RAFT model[82], rat cardiomyoctes[89] 700~750[92], 700[22], 710~720[95], 730~800[82], 740~750[21], 800[93], 837[89]			
Serotonin				Mouse pineal gland[21], RBL-2H3 cell[28] 700[28], 750[21]	
Ubisemiquinone	Yeast cell[62] C=C stretching @ 1602[62]				
Water	Mayonnaise[59], mouse skin[48], rat liver[50], soydrink[59] O-H stretching @ 3250-3500[48,50,59]				
Other micro and macro structures					
Dentin					Human tooth[96] 1050~1300[96]
Enamel			Human tooth[97] 1230[97]		Human tooth[96,97] 1050~1300[96], 1230[97]
Embryo system					*Drosophila* embryo[98], Zebrafish embryo[29] 1180[98], 1200[29]
Lipofuscin		Human neurofibrillary tangle[21] 740[21]			
Mitochondria	HeLa cell[5] C-H aliphatic stretching @ 2913[5]				
Nervous system					Mouse brain[30], mouse neuron[99], mouse skin[75] 1180[75], 1200[30], 1500[99]
Thylakoid membrane			Rice leaf[65] 1230[65]		
***Raman labeling**					
Alkyne label	*C. elegans*[71], HeLa cell[71], THP-1 macrophage[71], hippocampal neuron[71] C≡C stretching @ 2125[71]				
Deuterium label	Human skin[48], liver cell[74] C-D stretching @ 2105[74], 2120[48]				

"v": or; "~": tunable in between laser wavelengths; "*": External Raman labeling.

2.3. Ultrafast pulse shaping and coherent control

Ultrafast pulse shaping tailors the spectral-temporal profiles of picosecond to femtosecond pulses, and coherent control of nonlinear processes is enabled by engineering the amplitude, phase, and polarization of the spectral components of the pulses[11,100]. As the nonlinear optical processes are sensitive to high-intensity electric fields, the shape of optical pulses has a significant effect on the nonlinear response. The concept of pulse shaping was brought into nonlinear optical microscopy and spectroscopy in the late 1990s and is still an active research area today[12,13,101]. In the context of nonlinear optical microscopy and spectroscopy, the aims of pulse shaping include contrast enhancement, selective detection, and spectrum or information extraction. Coherent control of 2PF, SHG, CARS, and SRS has been demonstrated, with various pulse shaping strategies to steer the nonlinear processes. Table 2.2 lists the pulse shaping methods demonstrated for controlling different nonlinear optical processes, with the representative references chosen based on the biomedical relevance and the earliest reported time.

Table 2.2. Pulse shaping methods for controlling nonlinear optical processes.

Modality	Method	Ref
2PF	Sinusoidal phase	[102]
	Binary phase	[103]
	Anti-symmetric phase	[104]
	Adaptive phase	[105]
	Transform-limited compression	[106]
SHG	Sinusoidal phase	[107]
3PF	Sinusoidal phase	[108]
CARS	Sinusoidal phase	[101]
	Time-resolved pump-probe	[109]
	Spectral focusing	[110]
	Narrowband probe	[111]
SRS	Molecule-specific shape	[49]

It is worthwhile to note that not all of these pulse shaping methods are ready for biomedical translation. Some of these methods have only been demonstrated in artificial samples or in limited experimental conditions. The reasons include: (1) the need for multiple acquisitions with different pulse shapes to retrieve the desired information or to optimize the pulse shape, (2) the slow refresh rate (tens of milliseconds) of the liquid crystal array in the pulse shaper, and (3) the demand on the spectral phase stability of the phase-only shaping methods. For biomedical imaging applications, pulse shaping

strategies employing fewer phase masks or relying on less sophisticated spectral phases might be more practical.

2.3.1. Design of a pulse shaper

Before discussing more about coherent control of nonlinear optical processes, the fundamentals of pulse shaping are first presented in this section. For ultrafast pulses of picosecond to femtosecond temporal width, the optical field is too short to be modulated by available electronic devices[11]. Through a Fourier transform, a short temporal width is translated into a broad spectral bandwidth. Therefore, it is more feasible to shape ultrafast pulses in the frequency domain. To access individual spectral components, chromatically dispersive optics, such as a grating or prism pair, can be used to spread and recombine different wavelengths of light. A spatial light modulator (SLM) is employed to modulate the individual frequency components. The most common pulse shaper adopts a 4f geometry with an SLM at the Fourier plane, as illustrated in Fig. 2.7.

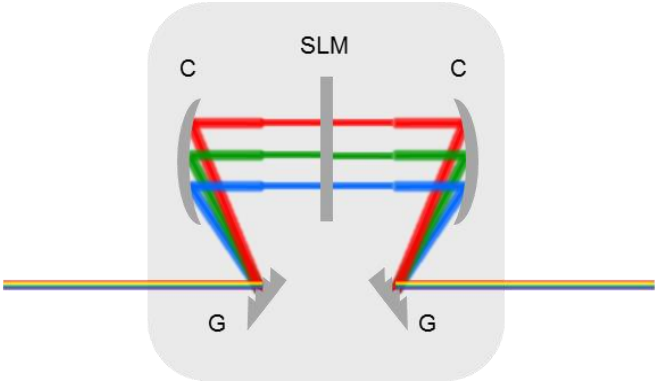

Fig. 2.7. Schematic of a 4f pulse shaper. C: curved mirror; G: grating; SLM: spatial light modulator.

The first half of the shaper resembles a spectrometer. A grating or a prism is used to spread out different frequency components of the incident pulses, then a curved mirror or a lens is employed to focus the beams onto the Fourier plane. A pixelated SLM is placed at the Fourier plane to modulate individual frequency components. Typically, the beam diameter at the SLM is designed to match the SLM pixel size for optimal spectral resolution of spectral amplitude, phase, or polarization modulation. The second half of the shaper is like a mirror image of the first half, consisting of a spectrograph that recombines the

frequency components to reconstitute the output pulses. The liquid crystal arrays inside the SLM act like a series of phase retardation or advance elements (in single-layer SLMs) or a tunable waveplate (in dual-layer SLMs) to control the spectral elements. Depending on the specifications of the SLM, different types of modulations can be performed. An SLM with a single-layer liquid crystal array allows for only phase shaping, while an SLM with dual-layer liquid crystal arrays supports either phase-and-polarization or phase-and-amplitude shaping in different configurations.

2.3.2. Principles of pulse shaping

By shaping the pulses in the frequency domain, one can equivalently tailor the ultrafast pulses in the time domain. This can be understood by the representations of the electric field in both the time domain and the frequency domain, which are related through a Fourier transform

$$E(\omega) = FT[e(t)] \tag{2.10}$$

where $E(\omega)$ and $e(t)$ are complex electric fields in the frequency and the time domains, respectively. Thus, by knowing the spectrum and the spectral phase, the temporal field can be constructed by computing an inverse Fourier transform. To formulate the physical interpretation of ultrafast pulse shaping, the electric field in the time domain can be expressed as

$$e(t) = a(t)e^{iw_0 t} = |a(t)|e^{i\varphi(t)}e^{iw_0 t} \tag{2.11}$$

for which $a(t)$ is the slowly-varying amplitude and ω_0 is the carrier frequency of the field. The term $a(t)$ can be decomposed into an amplitude term $|a(t)|$ and a phase term $\varphi(t)$. Performing a Fourier transform, the complex field in the frequency domain can then be written as

$$E(\omega) = A(\omega-\omega_0) = |A(\omega-\omega_0)|e^{i\psi(\omega-\omega_0)} = |E(\omega)|e^{i\psi(\omega)} \tag{2.12}$$

where $|E(\omega)|$ is the amplitude of the electric field in the frequency domain and $\psi(\omega)$ is the spectral phase. In the frequency domain representation, the carrier frequency is incorporated as a frequency shift, resulting in a formulation that works perfectly for developing pulse shaping theory. While the spectral

phase depicts the phase of each individual frequency component, phase pulse shaping basically superimposes an arbitrary spectral phase through the SLM and onto the original spectral phase of the input pulses,

$$E_{out}(\omega) = E_{in}(\omega)e^{i\psi_{app}(\omega)} = |E(\omega)|e^{i[\psi_{in}(\omega)+\psi_{app}(\omega)]} = |E(\omega)|e^{i\psi_{out}(\omega)} \tag{2.13}$$

where $\psi_{app}(\omega)$, $\psi_{in}(\omega)$, and $\psi_{out}(\omega)$ are the applied spectral phase, the spectral phase of the incident pulses, and that of the shaped pulses, respectively. For the amplitude-and-phase shaping configuration, one has more degrees of freedom to control the amplitude of each frequency component. This can be modeled by adding an amplitude transmission function $T_{app}(\omega)$ to the equation,

$$E_{out}(\omega) = E_{in}(\omega)T_{app}(\omega)e^{i\psi_{app}(\omega)} = |E(\omega)|T_{app}(\omega)e^{i[\psi_{in}(\omega)+\psi_{app}(\omega)]} = |E(\omega)|T_{app}(\omega)e^{i\psi_{out}(\omega)} \ . \tag{2.14}$$

The above scalar representation does not take into account the polarization of the pulses. To model polarization pulse shaping, one can simply add a frequency-dependent vector term to describe the polarization state of the pulses.

2.3.3. Coherent control of optical processes

To date, pulse shaping has been applied to different nonlinear optical microscopy and spectroscopy techniques[12]. Nevertheless, it was fascinating when tailored ultrafast pulses were first employed to control nonlinear optical processes[13]. The underlying mechanism in coherent control, termed as quantum interference, describes the nonlinear optical process under consideration as an event with multiple pathways leading to it, and where each pathway is a multiphoton transition. The outcome of the event is the summation of the contributions from all the pathways. Mathematically, the concept can be written as

$$Q = |Q|e^{i\psi} = \sum_{i\in N} Q_i = \sum_{i\in N} |Q_i|e^{i\psi_i} \tag{2.15}$$

where Q is the event vector and is the summation of individual pathway Q_i with an amplitude $|Q_i|$ and a phase ψ_i. The schematic of the concept is illustrated in Fig. 2.8. Like summation in a vector space, the phase of each quantum pathway (vector) determines whether the interference (addition) would be

constructive or destructive. The resulting Q is a physical quantity also possessing an amplitude and a phase.

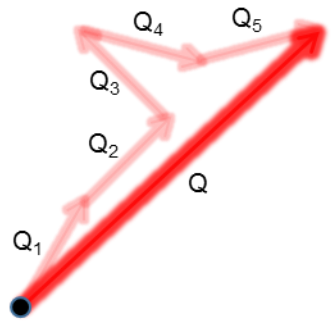

Fig. 2.8. The concept of quantum interference. Q_i: individual quantum pathway; Q: vector summation of all the pathways.

Thus far, this discussion has been limited to a single frequency. A more complete description of quantum interference, taking into account the frequency dependence, can be written as

$$Q(\omega) = |Q(\omega)|e^{i\psi(\omega)} = \sum_{i\in N} Q_i(\omega) = \sum_{i\in N} |Q_i(\omega)|e^{i\psi_i(\omega)} \quad . \tag{2.16}$$

The event at frequency ω includes all the individual pathways at frequency ω. The concept is illustrated in Fig. 2.9. The frequency-dependent representation possesses an amplitude and a phase, resembling what has been presented in the complex electric fields in the frequency domain. One can think of the frequency-resolved quantum interference as a spectrum with a spectral phase, which matches well with the formulation of the pulse shaping theory in the previous section.

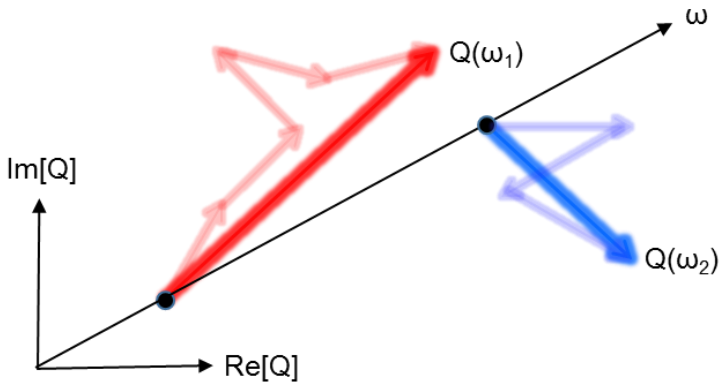

Fig. 2.9. The concept of frequency-resolved quantum interference. $Q(\omega_1)$ and $Q(\omega_2)$ are quantum pathways at frequencies ω_1 and ω_2, respectively.

Here, the optical processes are of interest, as well as the events that these pathways lead to. Intuitively, modulating the spectral phase does not afford control in a one-photon process. This is because only the amplitude of that single frequency component affects the transition[112], unless there is cross-talk between the process at different frequencies or the coherence of the pulses is passed onto the system and to the next controllable event. However, the question becomes more interesting in a nonlinear optical process in which multiple photons are involved. The phase relationship between the spectral components effectively modify the phase of the multiphoton transitions leading to the nonlinear process, effectively enabling coherent control of the targeted process. In different nonlinear optical processes, such as those introduced in the previous section, the spectral phase plays different roles in the coherent control. As an example, consider an SHG process,

$$S_{SHG}(\Omega) = \left| \int_0^{\omega_a+\omega_b=\Omega} d\omega_a d\omega_b \chi^{(2)}(\Omega) E(\omega_a) E(\omega_b) \right|^2 . \tag{2.17}$$

In this case, the measurable signal is the SHG spectrum $|S_{SHG}(\Omega)|^2$. The control of the SHG process is through the modulation of the two-photon transition $E^{(2)}(\Omega)$ given in

$$\begin{aligned} E^{(2)}(\Omega) &= \int_0^{\omega_a+\omega_b=\Omega} d\omega_a d\omega_b E(\omega_a) E(\omega_b) \\ &= \int_0^{\omega_a+\omega_b=\Omega} d\omega_a d\omega_b \, |E(\omega_a)||E(\omega_b)| \, e^{i[\psi_a(\omega_a)+\psi_b(\omega_b)]} . \end{aligned} \tag{2.18}$$

The individual pathway leading to SHG is the argument inside the integral, the product of a pair of frequency components with their frequency sum equal to the SHG frequency. The phases of the frequency pair are added together as the phase of the pathway. The integral takes into account all the frequency pairs leading to the same SHG frequency. Note that the SHG frequency conversion is described by $\chi^{(2)}(\omega)$, and would be the excitation cross-section in 2PF and 3PF. By engineering the spectral phase of the fields, one can cause constructive and destructive interference of the transitions at a specific SHG frequency, and therefore control the generated SHG field and spectrum. In this section, the principles of controlling

nonlinear optical processes are presented. More discussion of pulse shaping for nonlinear optical microscopy and spectroscopy will be included in Chapter 4.

2.4. Fiber supercontinuum generation

2.4.1. Supercontinuum generation in photonic crystal fibers

In optical fibers, light is transmitted within a small modal area. The tight confinement and therefore the elevated optical intensity make fiber waveguide a media in which nonlinear processes can occur more easily. The nonlinearity in optical fibers mainly originates from the intensity-dependent refractive index[16,113]. Various nonlinear processes, as will be discussed later, combined with linear dispersion influence the propagation of light, resulting in nonlinear frequency conversion[15,113]. The spectrum, power, and other properties of the newly generated spectral components depend on the pump laser and the fiber parameters. This characteristic of nonlinear frequency conversion is especially appealing to biophotonic imaging, because new spectral bands can be created for a desired application by coupling an available solid-state laser into a specific strand of fiber. In comparison to optical parametric oscillators or amplifiers, the technology provides a cost-effective and simple method based on extracavity frequency conversion. Particularly of interest is the ultrabroad spectral broadening that provides a continuum of frequency components – supercontinuum (SC) generation[15,114].

Today, SC of various characteristics can be generated easily in an optical laboratory because of the dispersion engineering that is possible with photonic crystal fiber (PCF)[15,114]. The development of PCF began in the 1990s with the concept of creating photonic crystal structures in optical fiber in order to employ the photonic band gap effect as a guiding mechanism[16]. However, the earliest PCF and a majority of the later PCFs used in SC generation are actually designed with a solid core and surrounding air-hole structures. The microstructures create a higher effective refractive index in the core and enable index-guiding similar to that found in conventional optical fibers. The high refractive index in the core area provides a natural environment for SC generation. Nevertheless, the most powerful aspect of the PCF

technology is perhaps the capability to manufacture different photonic crystal structures, which allows customization of fiber parameters for specific applications. The dispersion profile, the supporting wavelengths, and the propagating modes can be adjusted by varying the core and the air-hole geometry, such as the air-hole dimension (hole diameter) and the hole-to-hole distance (pitch). This dispersion engineering capability opens up new research and applications that cannot be achieved with conventional optical fibers.

The SC revolution was initiated with the demonstration of ultrabroadband continuum generation spanning 400-1500 nm in a PCF[14]. In this work, and most others involving SC generation, the PCFs were designed to possess a zero-dispersion wavelength (ZDW) close the pump laser wavelength[15,114]. Pumping in the proximity of the ZDW minimizes the dispersion experienced by the pulses and maximize the nonlinearity and instability to extend the SC spectral bandwidth. This type of fiber SC has been researched extensively and has been known to generate the broadest spectrum. However, the intrinsic instability has limited the applicability to biomedical imaging and especially to the target application in the thesis, ultrafast pulse shaping for nonlinear optical imaging. This is because the stability requirement for the spectrum, spectral phase, and the polarization of the light source is demanding for ultrafast pulse shaping to control the nonlinear optical processes. The instability of the SC in ZDW fiber can potentially cause fluctuations of the controlled nonlinear processes. Therefore, a highly coherent SC with long-term stability and sufficient power is desirable of high-precision pulse shaping applications.

2.4.2. Mechanisms in fiber supercontinuum generation

The spectral broadening in SC generation involves complex mechanisms resulting from the linear and nonlinear processes experienced by light propagating in the optical fibers. In this section, the role of each optical process is first introduced qualitatively, and the theory depicting the combined processes is then presented. The discussion is formulated from the viewpoint of generating a coherent SC for pulse shaping in nonlinear optical imaging. To begin, Fig. 2.10 summarizes the convoluted mechanisms in SC

generation. The fundamental linear process is dispersion, and the nonlinear processes include self-phase modulation (SPM), Raman scattering, and four-wave mixing (FWM) or modulation instability (MI)[15,114]. These processes might have different degrees of effects depending on the experimental conditions, and it is the continuous interplay between them that causes the complex evolution of the SC.

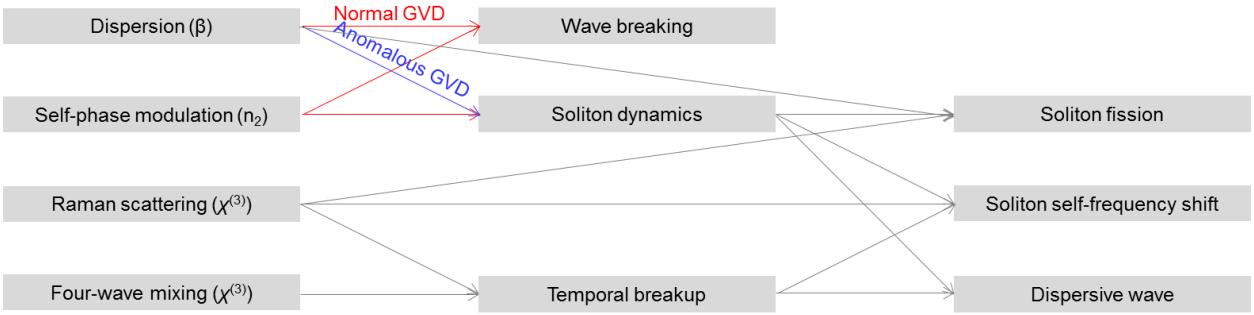

Fig. 2.10. Convoluted linear and nonlinear processes in SC generation. GVD: group velocity dispersion. Normal GVD and self-phase modulation leads to wave breaking, while anomalous GVD and self-phase modulation leads to soliton dynamics. Self-phase modulation also contributes to normal GVD.

In femtosecond laser pumped SC generation, the two most important mechanisms are dispersion and SPM. When pumping in the normal group velocity dispersion (GVD) regime, both the fiber dispersion and the SPM contribute to normal GVD. The spectral broadening in this case is limited by the reduced nonlinear broadening as a results of the large positive chirp. Therefore, this route of SC generation is typically avoided when intending to generate the broadest spectrum. As the pulses propagate along the fiber, the SPM-broadening in the normal GVD regime will lead to self-steepening, shock formation, and eventually optical wave breaking[113-117]. Despite the reduced bandwidth, one important advantage of this type of SC is that the spectral broadening maintains the coherence of the propagating pulses and is more immune to noise and fluctuations[113,114,118,119]. The SC is stable in amplitude and phase, presenting an attractive opportunity for pulse shaping and nonlinear optical imaging applications. The reduced nonlinear broadening can be remedied by pumping with higher power, increasing the fiber length to some extent, or fabricating a dispersion-flattened dispersion-decreased fiber.

When pumping in the anomalous GVD regime, the balance between normal GVD caused by SPM and anomalous GVD from the fiber supports soliton propagation[15,113,114]. The higher-order soliton dynamics

can be invoked when pumping in the proximity of the ZDW. However, the higher-order solitons typically do not follow periodic pulse evolution in practice. The pulse break-up, termed as soliton fission, is induced by perturbation from higher-order dispersion and stimulated Raman scattering, and divides one soliton pulse into N sub-pulses. These sub-pulses then undergo Raman soliton self-frequency shift (RSSS) and/or dispersive wave-generation (DWG). The RSSS can be easily understood as wavelength shifting toward longer wavelengths by a Raman shift, while the DWG involves linear and nonlinear phase matching conditions to generate a temporally broad wave in the normal GVD regime. This type of SC is noisy because the input fluctuations can be amplified through MI. To generate a coherent SC through this route, precise control of the incident pulses and the fiber length is necessary so that the coherent soliton dynamics broadening dominates the effect of MI. However, the method is susceptible to experimental conditions and might suffer from reproducibility[119]. Therefore, even though this type of SC can generate the broadest SC spectrum, it is not suitable for coherent control applications[119,120].

While our interest is in femtosecond laser pumped coherent SC for pulse shaping in nonlinear optical imaging applications, it is worthwhile to mention briefly the picosecond laser and the use of longer pulses for pumped SC. In this type of SC, the spectral broadening mainly originates from MI and Raman scattering regardless of whether one is pumping in the normal or anomalous GVD regime. The pulses experience temporal break up and propagate under the effects of RSSS and DWG. As mentioned earlier, the noise can be amplified through MI, and the SC is oftentimes unstable and suffers from noise and fluctuations.

Finally, the above-mentioned physical mechanisms can be considered together. The nonlinear pulse propagation in optical fiber can be modeled by the generalized nonlinear Schrödinger equation (GNLSE) as[15,113,114]

$$\frac{\partial A(z,T)}{\partial z}+\frac{\alpha}{2}A-\sum_{k\geq 2}\frac{i^{k+1}\beta_k}{k!}\frac{\partial A(z,T)}{\partial T^k}=i\gamma(1+i\tau_s\frac{\partial}{\partial T})(A(\mathrm{z,T})\int_{-\infty}^{+\infty}R(T')\,|\,A(\mathrm{z,T-T'})\,|^2\,dT') \tag{2.19}$$

where A is the pulse envelope, z is the coordinate of the propagation direction, T is the coordinate of the retarded time-frame co-moving with the pulse at its group velocity, α is the attenuation coefficient, β_k is the dispersion coefficient of order k, γ is the nonlinear coefficient, τ_s is a time scale depicting the dispersion of nonlinearity, and R is the Raman response function. The left-hand side of the equation depicts the linear effects (attenuation and dispersion) while the right-hand side describes the nonlinear effects (nonlinearity and the dispersion of nonlinearity). These coefficients can be represented as

$$\gamma = \frac{\omega_0 n_2(\omega_0)}{cA_{eff}(\omega_0)} \tag{2.20}$$

where n_2 is the nonlinear refractive index, and A_{eff} is the effective modal area,

$$\tau_s = \frac{1}{\omega_0} \tag{2.21}$$

and

$$\begin{aligned} R(T) &= (1-f_R)\delta(t) + f_R h_R(t) \\ &= (1-f_R)\delta(t) + f_R \frac{\tau_1^2+\tau_2^2}{\tau_1\tau_2^2}\exp(-t/\tau_2)\sin(t/\tau_1)\theta(t) \end{aligned} \tag{2.22}$$

which includes an instantaneous electrical response described by δ(t), a delta function, and a delayed Raman response $h_R(t)$. The term θ(t) is the heavyside step function. Different forms of the GNLSE can be presented or derived to account for different situations. A frequency domain representation can be adopted for simplicity in numerical simulations[113,114]. Here the most basic form is demonstrated as a mean to interpret the physical mechanisms. As an example, consider a loss-less situation so that α is ignored, and the equation can be rewritten as

$$\frac{\partial U(z,T)}{\partial z} - \sum_{k\geq 2}\frac{i^{k+1}\beta_k}{k!}\frac{\partial U(z,T)}{\partial T^k} = \frac{1}{L_{NL}}\left(i - \frac{1}{\omega_0}\frac{\partial}{\partial T}\right)\left(U(z,T)\int_{-\infty}^{+\infty} R(T')\,|U(z,T-T')|^2\,dT'\right) \tag{2.23}$$

where $U(z,T)$ is the normalized pulse amplitude

$$U(z,T) = \frac{A(z,T)}{\sqrt{P_0}}\ , \tag{2.24}$$

and P_0 is the peak power. The nonlinear length L_{NL} can be expressed as

$$L_{NL} = \frac{1}{\gamma P_0} \quad . \tag{2.25}$$

In this form of the GNLSE, the analysis can be focused on the interaction of dispersion and nonlinearity. The characteristic nonlinear length L_{NL} is not only a measure of the nonlinearity but is also important in understanding the soliton dynamics. The soliton order can be calculated as

$$N = \left(\frac{L_{NL}}{L_D} \right)^{1/2} \tag{2.26}$$

where L_D is the dispersion length given by

$$L_D = \frac{T_0^2}{\beta_2} \tag{2.27}$$

in which T_0 is a measure of pulse width, and β_2 is the second-order dispersive coefficient. This form of the GNLSE will be revisited when modeling the coherent SC generation in the all-normal-dispersion fiber in Chapter 3.

2.4.3. Applications in microscopy and spectroscopy

The ultrabroadband SC presents a unique type of light source that enables a wide variety of nonlinear optical imaging techniques after proper spectral selection and pulse processing. In addition, fiber SCs offer extracavity spectral broadening, fiber-based system compatibility, single-mode beam profile, and flexibility as an add-on to a solid-state laser. These advantages make SC especially appealing for biophotonic imaging applications.

2PF imaging using SC was first demonstrated by Jureller et al[121], in which a cavity-dumped laser was used to pump a tapered fiber. Spectral filtering of the SC and pulse compression by a prism pair produced narrowband compressed pulses for 2PF imaging of fluorescent beads. Another interesting study of 2PF imaging using SC generated in PCF was demonstrated by McConnell et al[122]. The pump laser was a

typical Ti:sapphire laser delivering pulses of 800-860 nm, 256 fs, and 76 MHz. The PCF that was used had a ZDW at 900 nm so that the SC was generated in the normal GVD regime, and therefore possessed high coherence. The SC was compressed by a grating compressor for efficient 2PF imaging of biological samples. These early studies demonstrated some of the key elements of multiphoton imaging using SC – spectral filtering, pulse compression, and coherent SC generation in the normal GVD regime.

CARS microscopy and spectroscopy also benefit from the nonlinear frequency conversion of SC to create another pump or Stokes beam alongside the pump laser (Note the difference between the CARS pump beam and the pump laser here). Paulsen et al. first demonstrated this feasibility by utilizing a short-wavelength peak in the SC spectrum as the CARS pump beam and the pump laser as the Stokes beam[123]. Kee et al. and Kano et al. demonstrated multiplex CARS spectroscopic imaging by employing the broadband SC as the Stokes beam[124,125]. In this configuration, broadband CARS spectra up to 2500 cm^{-1} were obtained. Later studies following this direction employed non-resonant background removal algorithms, such as maximum entropy and the Kramers-Kronig transform, to achieve background-free CARS spectroscopic imaging and have found great breakthroughs in recent years[36,61,62,126]. A spectral focusing technique, developed by chirping both the pump and Stokes pulses for CARS imaging, was first combined with a SC light source by Pegoraro et al.[127]. In the spectral focusing configuration, the SC was spectrally filtered to the desired spectral bands, and the pump and the Stokes pulses were chirped so that their frequency difference remained the same during the interaction time to generate coherent molecular vibrations. This approach provides high-speed and high-spectral-resolution CARS imaging from SC light sources, and can be integrated well with other nonlinear optical imaging modalities.

3. DEVELOPMENT OF THE COHERENT FIBER SUPERCONTINUUM

In this chapter, the development of the coherent fiber supercontinuum (SC) is presented. The generation of the coherent fiber SC is experimentally demonstrated. Shaping of the SC pulses is examined for coherent control applications. Wave-breaking extended SC is then discussed, and is further improved by utilizing a polarization maintaining fiber. These advancements bridge the SC generation to pulse shaping for the studies on nonlinear optical imaging in later chapters. Some of the results shown in this chapter are adapted from the recently published works[119,120,128], with permission.

3.1. Generation of the coherent fiber supercontinuum

As discussed in Section 2.4, the ultrabroad bandwidth of the SC is appealing for biophotonic imaging applications, along with other advantages like extracavity spectral broadening and the potential for fiber beam delivery[15]. However, some drawbacks intrinsic to this type of light source, such as low coherence, poor stability, and reduced power, have limited the use of SC in nonlinear optical imaging. Conventionally, the SC is generated using fibers with zero-dispersion wavelengths (ZDWs) within the SC spectral range[15,113,114]. By inducing soliton dynamics, ultrabroadband SC could be achieved. Even though studies have demonstrated successful pulse compression to some extent, the coherence properties of these SC sources are unclear[129-135]. In addition, the high pulse energy and short fiber length used in some of the experiments might hinder further biomedical imaging applications.

To generate high quality fiber SC for nonlinear optical imaging, it is worthwhile to reconsider the fiber and the pumping conditions. It has been documented that the SC generated in all-normal-dispersion (ANDi) fibers presents excellent coherence and preserves the propagating pulses[15]. The limitation here, however, is the reduced spectral bandwidth. This issue can be resolved by the dispersion engineering capability of photonic crystal fiber (PCF), to develop an ANDi fiber with a flat and a reduced dispersion profile within the desired spectral range. A higher pump laser power and a longer fiber length can also

improve the ANDi SC bandwidth to some extent. Using this approach, high quality fiber SC has been generated with high coherence, improved stability, and sufficient power[115,118,136-138]. Nevertheless, the applicability of the coherent fiber SC to nonlinear optical imaging has yet to be proven. The route to biological imaging and the existing limitations need to be addressed. In this section, the generation of the coherent SC for future nonlinear optical imaging is presented.

From the perspective of biomedical imaging, a SC spectrum spanning the optical biological window (650-1350 nm) is ideal for minimal absorption and scattering within the samples (Fig. 3.1)[139]. As SC can be generated at different wavelengths depending on the choice of the pump laser and the fiber[115,118,119,136-138], a pump laser with a spectrum centered within the optical biological window is preferable. The nonlinear spectral broadening of such SC will extend toward both the short- and the long-wavelength ends of the spectrum to fill the optical biological window spectral range. This leads to the adoption of Yb-based pump lasers with central wavelengths around 1040 nm, rather than the commonly-used Ti:sapphire lasers in biophotonic imaging with the spectral range of 650-1000 nm. The corresponding ANDi fiber should possess a minimal dispersion wavelength (MDW) close to this central wavelength of the pump laser, as well as a flat and reduced dispersion profile for generating broader SC spectrum[115,118,136-138].

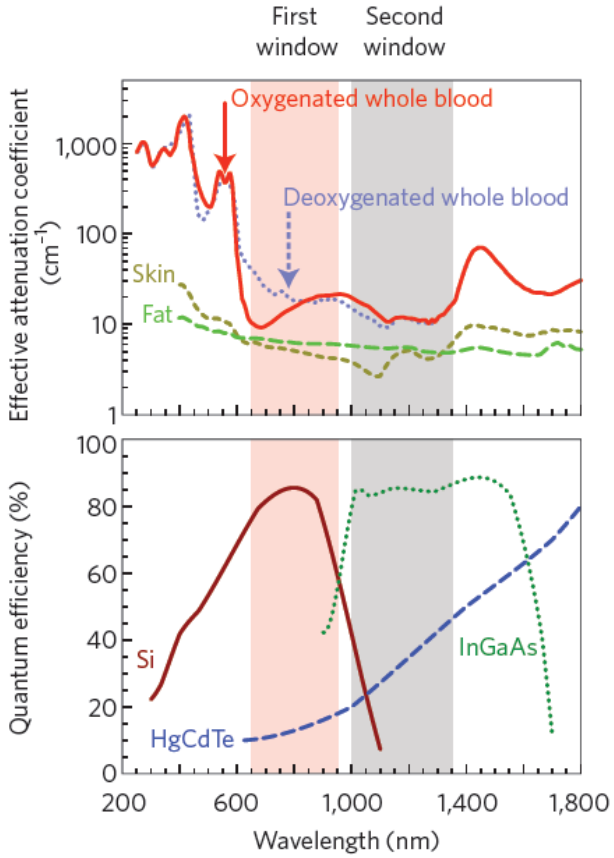

Fig. 3.1. Optical windows in biological tissue describe the optimal laser wavelength ranges for biomedical optical imaging which are determined by the attenuation coefficients of the major constituents in biological samples The first window is from 650 to 950 nm, and the second window is from 1000 to 1350 nm. HeCdTe: mercury cadmium telluride; InGaAs: indium gallium arsenide; Si: silicon. (Reprinted by permission from Macmillan Publishers Ltd: Nature Nanotechnology, Smith, A.M., Mancini, M.C. & Nie, S.M. Bioimaging second window for *in vivo* imaging[139], copyright 2009).

The experimental setup for coherent SC generation is illustrated in Fig. 3.2. An Yb:KYW laser delivering pulses of 1040 nm, 80 MHz, 200fs (FemtoTRAIN IC, High Q laser) was employed to pump a 90 mm length of ANDi PCF (NL-1050-NEG-1, NKT Photonics). A neutral density filter is employed to adjust the pump laser power, and a half-wave plate is used to align the polarization of the pump laser to the slow axis of the fiber. The pump laser was focused by an aspheric lens into the fiber core. Different incident powers were used to observe the effect of nonlinear spectral broadening, with the coupling efficiency maintained at 55%. The generated SC was collimated by another aspheric lens, and the spectra were recorded by an optical spectrum analyzer.

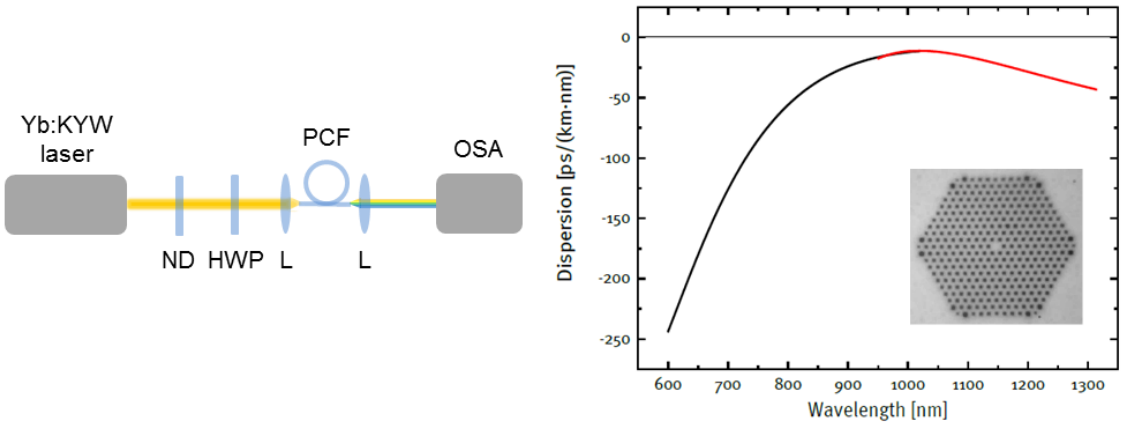

Fig. 3.2. (Left) Experimental setup for coherent fiber SC generation. HWP: half-wave plate; KYW: potassium yttrium tungstate; L: lens; ND: neutral density filter; OSA: optical spectrum analyzer; PCF: photonic crystal fiber; Yb: ytterbium. (Right) The dispersion profile and the microstructure of the PCF (data adapted from NKT Photonics[140]).

Theoretical modeling of the SC generation was carried out by using the scalar generalized nonlinear Schrödinger equation (GNLSE). For simplicity, the linear loss within the fiber was ignored for the short piece of fiber used here. The resulting scalar GNLSE can be written as mentioned in Section 2.4.2[15,113,114,119],

$$\frac{\partial U(z,T)}{\partial z}-\sum_{k\geq 2}\frac{i^{k+1}\beta_k}{k!}\frac{\partial U(z,T)}{\partial T^k}=\frac{1}{L_{NL}}\left(i-\frac{1}{\omega_0}\frac{\partial}{\partial T}\right)\left(U(z,T)\int_{-\infty}^{+\infty}R(T')\,|U(z,T-T')|^2\,dT'\right) \tag{3.1}$$

in which $U(z,T)$ is the normalized pulse envelope, z is the coordinate along the propagation direction, T is the retarded time frame co-moving with the pulses, β_k is the dispersion coefficient of order k, ω_0 is the carrier angular frequency of the pulses, L_{NL} is the nonlinear length of the fiber, and $R(T)$ is the Raman response function. In Equation (3.1), the left-hand side depicts the linear propagation of the pulses, with dispersion of all orders modeled by a series of β_k contributions. The right-hand side models the nonlinear processes. L_{NL} can be calculated from $1/(\gamma P_0)$, where γ is the nonlinear coefficient of the fiber and P_0 is the peak power. The term $R(T)$ accounts for the instantaneous electronic response and the delayed Raman response.

The measured and the simulated SC spectra are shown in Fig. 3.3. The spectra are observed to possess fringe-like features, which is characteristic of self-phase modulation (SPM), the main spectral broadening mechanism in ANDi fiber. The SC spectrum grows wider with elevated pump power, as can be expected

from the higher nonlinear response. The widest spectrum spans from 880 to 1180 nm, with a 300-nm bandwidth. While a broader spectrum can be obtained by a higher pumping power, nonlinear depolarization will be initialized in this weakly birefringent fiber (of order 10^{-5}), resulting in distortion of the spatio-temporal profile of the SC pulses and reduced stability. Nevertheless, this initial attempt to generate a coherent SC within the biological window demonstrated an alternate light source with a satisfactory bandwidth in a spectral range different from that of a Ti:sapphire laser.

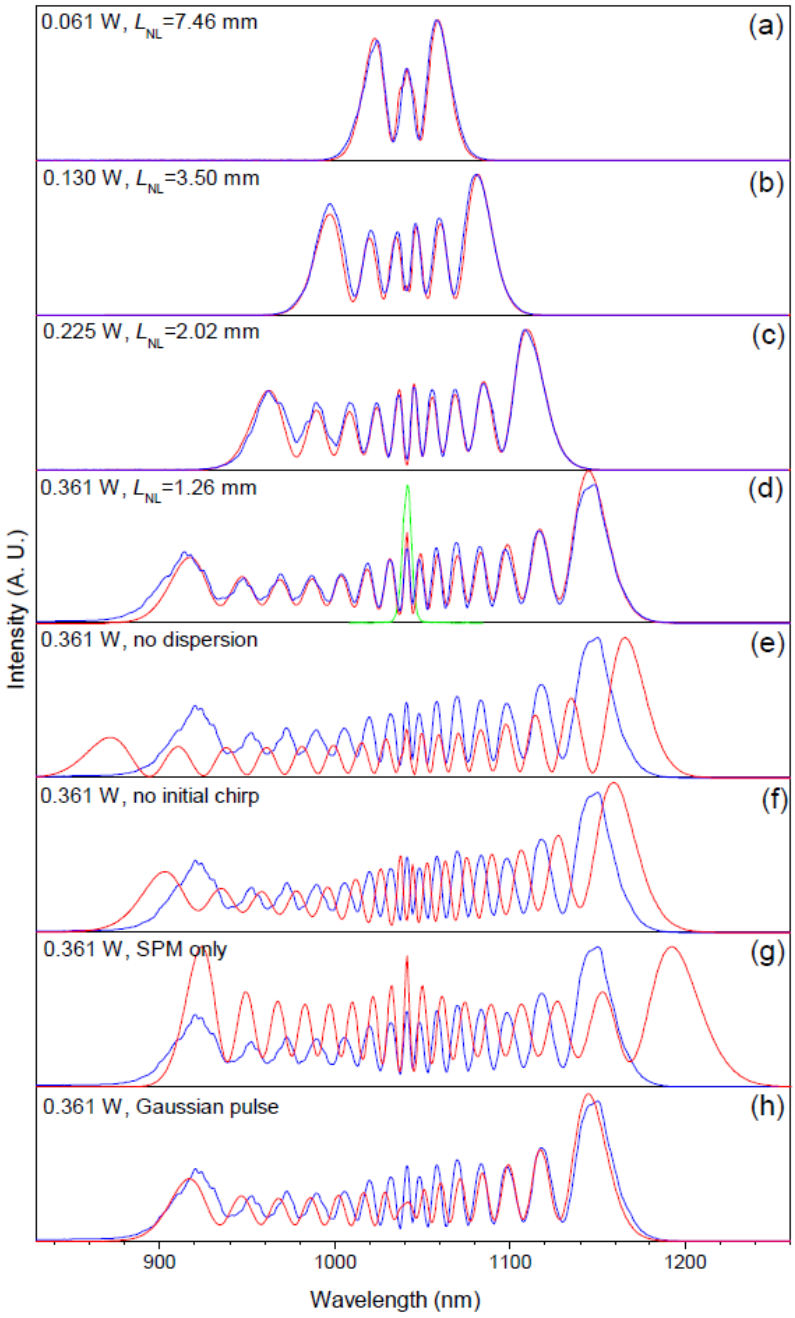

Fig. 3.3. The spectra of coherent SC generated in the ANDi fiber. (a-d) The measured (blue) and the simulated (red) SC spectra of several power levels (0.061, 0.130, 0.225, 0.361 W). The green curve in (d) shows the pump laser spectrum. (e-h) Comparison of simulated SC spectra under different conditions[119].

Taking into consideration the experimental parameters, the simulation agrees well with the experimental results [Fig. 3.3(a)-(d)][119]. Also, different dispersion and pulse characteristics were tested in the simulation to examine the effects of individual contributions [Fig. 3.3(e)-(h)]. With SPM only, the spectral broadening is symmetric toward both short- and long-wavelength ends. While the propagating

pulses are preserved in ANDi fiber, the pulses should have well-defined spectral-temporal profile, as compared to those generated in fibers with ZDW(s). The agreement between experiment and theory confirms the deterministic nature of the SC generation in the ANDi fiber. The results therefore point to the compressibility and shapability of the coherent fiber SC, which will be addressed in the following section.

3.2. Compression and shaping of the supercontinuum pulses

To demonstrate the feasibility of using the SC for pulse shaping in nonlinear optical imaging, a key step is to compress the SC pulses at the focal point of an objective[131,135,141]. In this section, compression and shaping of the SC pulses and are demonstrated. A pulse shaper allowing for higher-order dispersion compensation was employed to compress the SC pulses to the transform-limit (TL) at a high-NA objective focus, as compared to a grating or prism pair that can only remove linear chirp. The SHG spectra from a BBO crystal were shown to be responsive to different pulse shapes. The agreement between the experiments and the simulations proved the compressibility and shapability of the SC pulses[142].

The experimental setup is illustrated in Fig. 3.4. The SC generation portion is the same as that described in the previous section. Pulses from an Yb:KYW laser of 1040 nm, 229 fs, 80 MHz (FemtoTRAIN IC, High Q laser) were coupled into a 90-mm piece of ANDi fiber (NL-1050-NEG-1, NKT Photonics). The generated SC was collimated by an off-axis parabolic mirror and guided into a MIIPS-assisted pulse shaper (MIIPSBox 640, Biophotonics Solutions Inc.)[142,143]. The SC pulses were focused by a high-NA objective (LUMPlanFl/IR, 60xW, N.A. = 0.9, Olympus) into a BBO crystal, and the generated SHG spectra were detected by a spectrometer (USB4000, Ocean Optics) and used as feedback by the MIIPS algorithm.

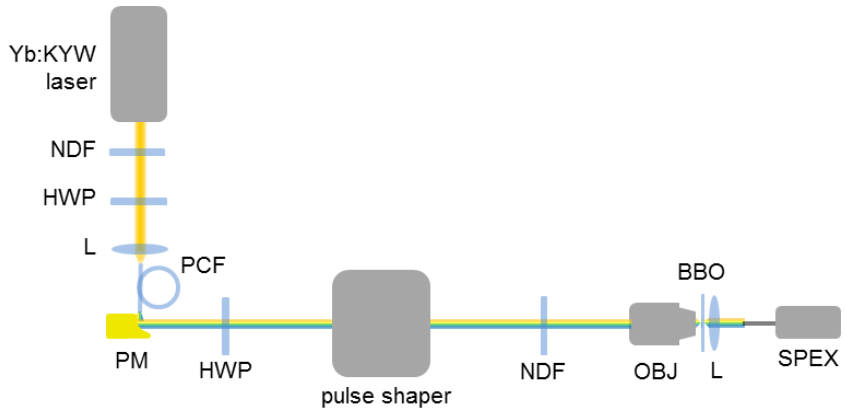

Fig. 3.4. Experimental setup for compression and pulse shaping of the coherent SC pulses under a high-NA objective. HWP: half-wave plate; KYW: potassium yttrium tungstate; L: lens; NDF: neutral density filter; OBJ: objective; PCF: photonic crystal fiber; PM: parabolic mirror; SPEX: spectrometer; Yb: ytterbium.

To assess the compressibility of the SC pulses at different degrees of spectral broadening, three different pump power levels were investigated. The output coupling powers tested were 90, 210, 350 mW, with a coupling efficiency maintained at 55%. The powers at the microscope objective focus were measured to be 18, 42, and 70 mW, respectively. All the powers at the objective focus were attenuated to 18 mW for comparison. The SC pulse measurement and compression at the objective focus were conducted using the MIIPS-assisted pulse shaper[142, 143]. The SHG spectra of the compressed and uncompressed SCs are shown in the left column in Fig. 3.5(a)-(c). The smooth SHG spectra after pulse compression show good agreement with the simulation results in the middle column in Fig. 3.5(a)-(c). On the other hand, the SHG spectra of the uncompressed pulses are highly structured. The difference between the experiments and the simulations is likely due to complex spatio-temporal fields at the tight focal volume[144]. The enhancement of the SHG signal was used to validate successful pulse compression, as shown in the insets in the left and the middle columns in Fig. 3.5(a)-(c). The experimental results agree well with the theoretically predicted values, confirming the TL pulse compression.

These SC spectra measured by an optical spectrum analyzer are shown in the right column in Fig. 3.5(a)-(c), along with the compressed and uncompressed spectral phases. The compressed spectral phase is observed to be flat across the SC spectrum, indicating near-TL pulse compression. From the SC spectra and the measured spectral phases, one can reconstruct the temporal profiles, as shown in the insets. The

temporal width (FWHM) of the intensities of the SC pulses are calculated to be 38.9, 16.5, and 10.8 fs, which are only slightly larger (<3%) than the theoretical values of the TL compressed pulses.

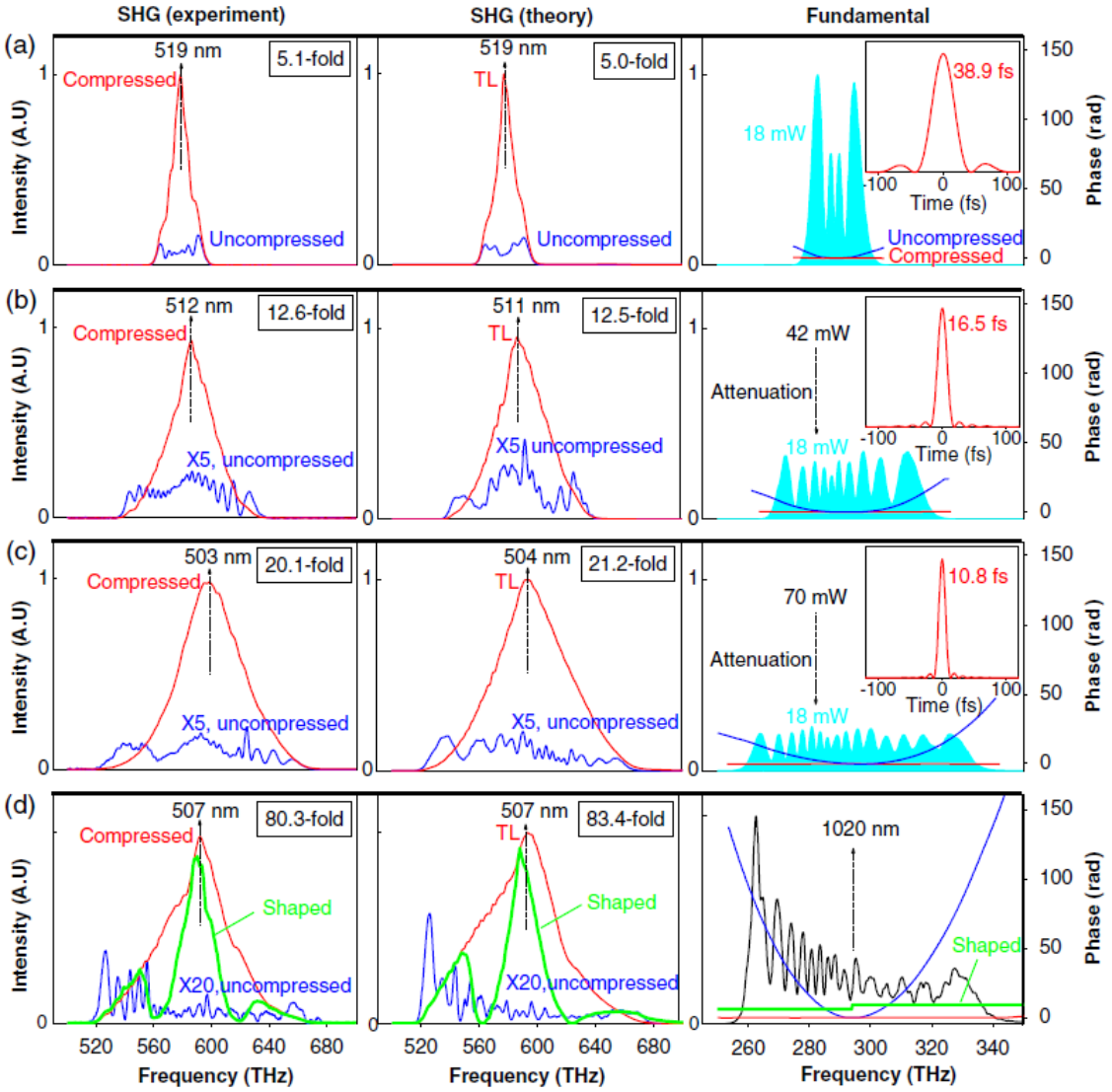

Fig. 3.5. TL compression and pulse shaping of the SC pulses. (a-c) Compression of the SC pulses at three different power levels. (Left column) experimental results. (Middle column) theoretical modeling. The insets show the SHG signal enhancement. (Right column) The spectra and the spectral phases of the compressed and uncompressed pulses. The insets shows the temporal profiles of the compressed pulses. (d) Experimental results obtained using a different pulse shaper, showing adaptive compression of the SC pulses with a different amount of dispersion. The SHG spectral response to a π-phase step demonstrates the shapability of the SC pulses[120].

The capability of arbitrary phase shaping to compress the SC pulses under a different experimental condition is demonstrated in Fig. 3.5(d). In this experiment, another pulse shaper with a larger intrinsic dispersion due to the optical components and alignment was employed. Nevertheless, the adaptive MIIPS pulse measurement and compression successfully compressed the pulses to the TL, and the simulations

agreed well with the experiments. The measured spectral phase and the enhancement of the SHG signal were observed to be higher, as expected from the larger dispersion in the system. The feasibility of shaping the SC pulses for controlling the nonlinear optical process is demonstrated as well. A π-phase step was introduced onto the flat-phase compressed SC pulses. The π-phase step would result in a two-photon excitation spectrum peaked at twice the step frequency[12]. This effect could be clearly observed in both the experiment and the simulation. This promising result shows the applicability of the coherent fiber SC for pulse shaping in nonlinear optical imaging applications.

To this point, the SC spectrum is limited to 880-1180 nm. For nonlinear optical microscopy and spectroscopy, a broader spectrum is desirable to support more modalities and to allow a broader spectral range of multiphoton transitions. The broader bandwidth can be attained by using higher input power, longer fibers, or shorter pump pulses. However, other nonlinear optical processes would take place and further complicate the SC generation in the attempt to push the limit of the bandwidth. In the next section, the effect of optical wave-breaking at elevated pump powers is discussed, leading to ultrabroadband high-quality fiber SC generation for nonlinear optical imaging applications.

3.3. Wave-breaking extended coherent fiber supercontinuum

Optical wave-breaking (WB) is a well-known effect that distorts the temporal and spectral properties of an optical pulse propagating along a normally dispersive optical fiber[116,117,145]. In the time domain, both the leading and trailing edges of the pulse break into interference-type oscillations, analogous to the breaking of water waves under shock formation. In the frequency domain, two sidelobes emerge from the short- and long-wavelength ends of the spectrum. WB degrades fiber SC pulse compressibility when using conventional prism or grating compressors[116,146]. Therefore, it has been considered as an undesirable factor and has not been utilized in SC pulse compression experiments[135,137,138,147-150]. However, recent studies have indicated the benefit of WB in generating spectrally smooth SC[136,151], which can potentially be compressed if an ideal compressor enabling arbitrary dispersion compensation is employed[149,150,152]. In

this section, generation and compression of the WB-extended fiber SC is presented. The additional bandwidth provided by WB along with its compressibility opens up more possibilities for nonlinear optical imaging applications.

As discussed in the previous sections, SC generated in the ANDi fiber demonstrates a broadband compressible light source, even though the pulse spectrum demonstrates the characteristic fringes of SPM[135,137,138,148-150]. SPM is the main spectral broadening mechanism in ANDi fiber and largely determines the spectral extent of the SC. If the SC is generated beyond the WB limit when using a higher input pulse energy, the spectral edges of the SC overlap temporally and interfere with the main SC to induce WB. Moreover, the spectral edges of the SC are further extended through four-wave mixing (FWM). The higher-order dispersion in the WB-extended SC can potentially be compensated by a pulse shaper, by which arbitrary phase shaping can remove both linear and nonlinear chirps of the SC pulses.

The experimental setup is similar to that described in the previous sections, as shown in Fig. 3.6. Here, a longer PCF (14 cm) of the same model (NL-1050-NEG-1, NKT Photonics) was used, and pulses of 1041 nm, 180 fs, and 80 MHz from a compact Yb:KYW laser (FemtoTRAIN IC model-Z, High Q laser) was employed as a pump source. A higher coupling efficiency of 60% was achieved, and a coupling power up to 270 mW was investigated. A half-wave plate was used to align the incident polarization along the slow-axis of the PCF to ensure that little polarization dynamics were induced during the SC generation, and that successful modeling of the fiber SC by the scalar GNLSE was possible. Higher pump powers would induce undesirable polarization issues and degrade the stability and reproducibility of the output pulses.

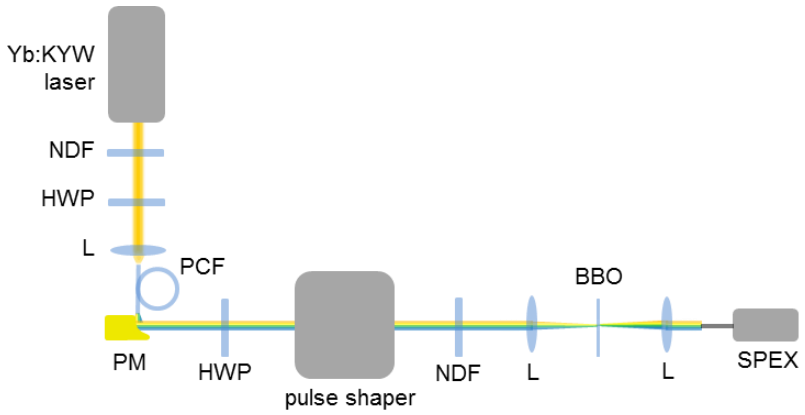

Fig. 3.6. Experimental setup for characterizing the wave-breaking extended SC pulses. HWP: half-wave plate; KYW: potassium yttrium tungstate; L: lens; NDF: neutral density filter; PCF: photonic crystal fiber; PM: parabolic mirror; SPEX: spectrometer; Yb: ytterbium.

The development of the WB-extended SC is shown in Fig. 3.7(a)–(c), in which the spectra of the fiber SC at three coupling powers (170 mW, 210 mW, and 270 mW) are demonstrated. At the lowest power [Fig. 3.7(a)], a long tail has emerged from the short-wavelength end of the SC spectrum. At the intermediate power [Fig. 3.7(b)], the tail develops into a well-defined sidelobe, which reveals the original near-infrared SC as a bright red beam in a dark optical laboratory. At the highest power (Fig. 3.7(c)), the sidelobe begins to merge with the SPM fringes, and at the same time a second tail emerges from the long-wavelength end of the SC. The spectral evolution observed at both edges of the SPM fringes strongly suggest the onset of optical WB[116]. The simulated spectra from the scalar GNLSE at the three coupling powers agree well with the observed spectra [Fig. 3.7(a)–(c)], confirming the WB extension.

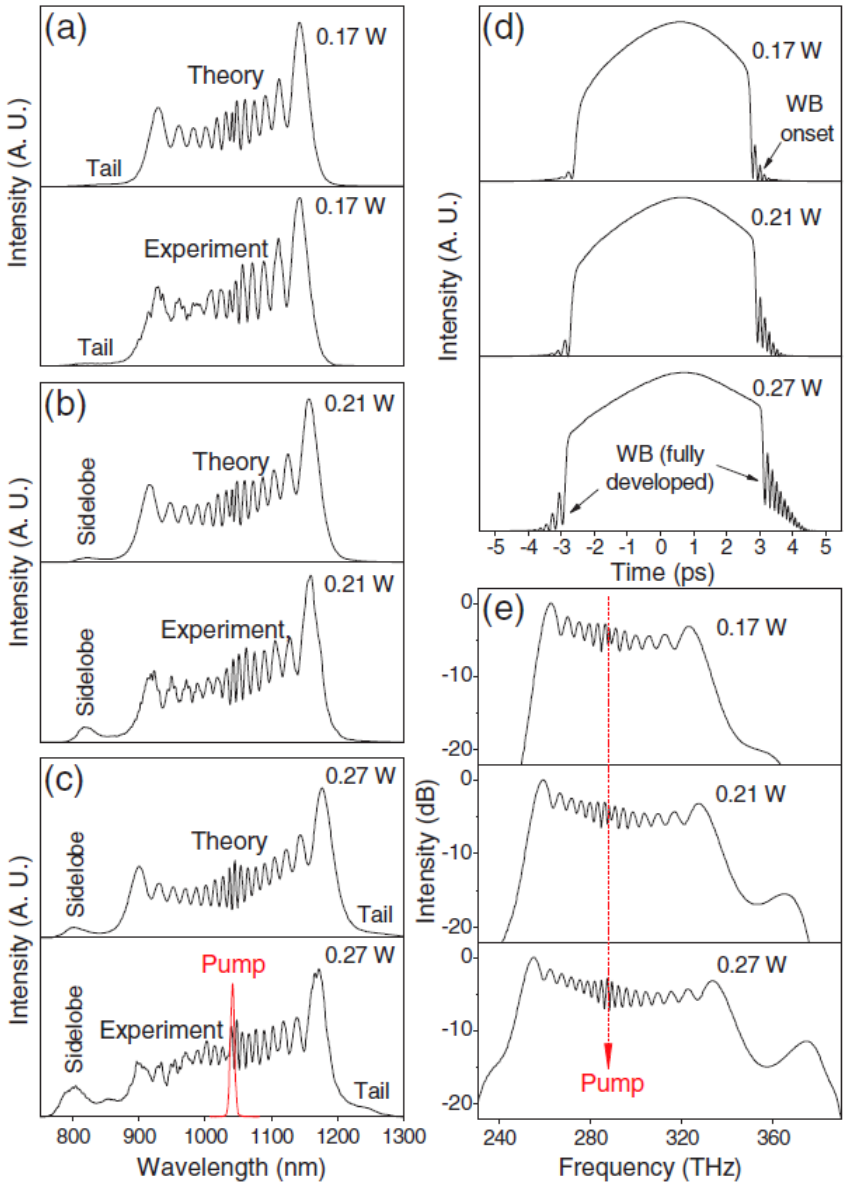

Fig. 3.7. Development of the WB bands in the coherent SC. (a)–(c) Experimental and theoretical spectra of the coherent SC at three coupling powers demonstrating the evolution of wave breaking. (d) The corresponding theoretical temporal profiles of the SC. (e) The theoretical spectra plotted in logarithmic scale with respect to optical frequency[128].

The origin of these spectral tails or sidelobes can be further clarified if the SC pulses are represented in the time domain [Fig. 3.7(d)] and in the optical frequency domain [Fig. 3.7(e)]. At the lowest coupling power of 170 mW, the trailing edge of the pulse experiences a more pronounced steepening effect than the leading edge, an effect known as self-steepening, as a results of SPM and normal dispersion[113]. In the frequency domain, this effect results in asymmetrical SPM spectral broadening of the spectrum. The

continuous interplay of the SPM spectral broadening and normal dispersion of the SC pulses creates an optical shock, evidenced by the temporal oscillations immediately following the trailing edge[115-117,136,137]. These oscillations reflect the interference between the short-wavelength components of the SC pulse, leading to the extended short-wavelength tail in the SC spectrum [Fig. 3.7(a)]. At higher coupling powers of 210 and 270 mW, these temporal oscillations strengthen, and the short-wavelength tail develops into an intense sidelobe [Fig. 3.7(b-c)]. By the same mechanism, WB occurs on the steepened leading edge of the pulse [Fig. 3.7(d)] to produce the long-wavelength tail in the SC spectrum [Fig. 3.7(c)][116,117,145]. The simultaneous appearance of the temporal oscillations and spectral tails at both the trailing and leading edges of the SC confirms the occurrence of WB[145].

In the pulse compression experiment, the fully WB-extended SC [Fig. 3.7(c)] was collimated by an off-axis parabolic mirror and guided into a 4f pulse shaper (MIIPSBox 640, Biophotonics Solutions, Inc.). The pulse compression and measurement was carried out in a free-space setup to minimize the system dispersion in this experiment. A typical MIIPS trace of parallel lines separated by π horizontally [Fig. 3.8(a)] indicates high-quality TL pulse compression[143,149]. The temporal profile of the compressed pulse calculated according to the residual phase [Fig. 3.8(b)] has a FWHM width of 6.4 fs with no strong temporal pedestal, and approximates the corresponding TL pulse of flat spectral phase [Fig. 3.8(c)].

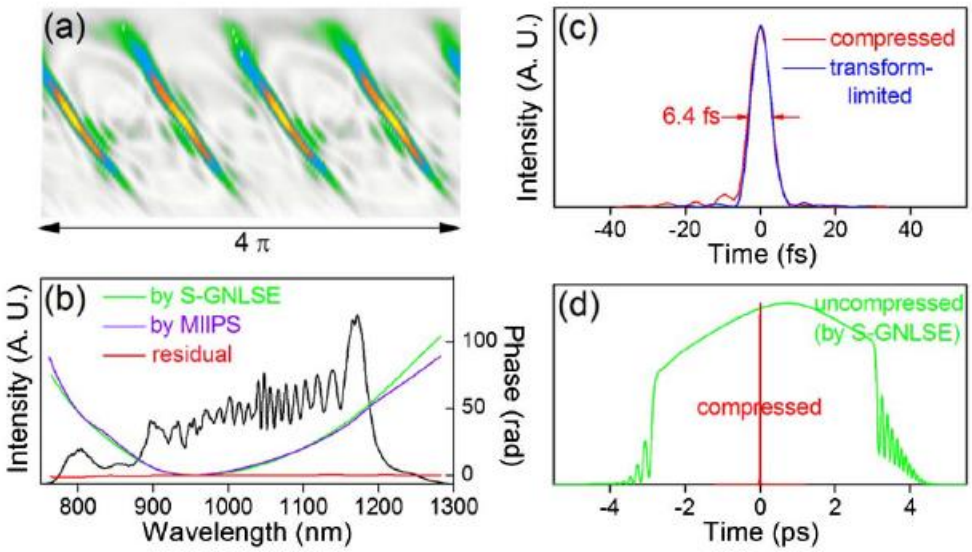

Fig. 3.8. Characterization of the spectral-temporal properties of the WB-extended SC. (a) MIIPS trace demonstrating successful pulse compression. (b) Comparison of measured (violet) and calculated (green) spectral phases, along with residual spectral phase (red); SC spectrum (black curve). (c) Temporal intensity profiles of compressed pulse (red) and that of the corresponding transform-limited pulse (blue). (d) Temporal intensity profiles of uncompressed (green) and compressed (red) pulses[128].

The measured spectral phase is compared with that predicted from the scalar GNLSE simulation[150]. The good agreement between the two [Fig. 3.8(b)] validates the MIIPS pulse measurement and compression. By using a pulse shaper, the higher-order dispersion is successfully compensated. The measured spectral phase shows a smooth feature, indicating that WB does not negatively affect the full phase compensation. The discrepancy at the edges of the spectral phase [Fig. 3.8(b)] is likely due to the slight difference in the experimental and simulated spectra, weaker SHG signal at the spectral edges, and the extended temporal width that is reaching the dynamic range of the pulse shaper[11].

The throughput of the pulse shaper allows for the generation of 0.1 W, 80 MHz, 6.4 fs (FWHM), near TL pulses at the objective focus. The spectrum, power, and temporal duration are comparable to a broadband Ti:sapphire laser and could be used for biophotonic imaging applications. A broader spectrum, higher power, and a shorter compressed pulse width above those of the current WB-extended SC may be attainable if the nonlinear polarization dynamics can be avoided[153]. In this section, it is demonstrated that WB is not an intrinsic barrier for high-quality pulse compression when a pulse shaper is employed to remove both linear and nonlinear chirps. The extended bandwidth and compressibility are crucial to incorporate the additional spectral bands for pulse shaping in nonlinear optical imaging applications.

To conclude this chapter, various aspects of the coherent fiber SC development, from generation, compression, pulse shaping, to spectral extension, are presented. The broad spectral bandwidth (880-1180 nm and 780-1130 nm), the compressibility, and the shapability are demonstrated and make this unique light source ideal for biophotonic imaging applications. In the next chapter, the coherent fiber SC of different spectra and powers will be incorporated into several nonlinear optical microscopy and spectroscopy techniques by specifically shaping the SC pulses.

4. PULSE SHAPING FOR NONLINEAR OPTICAL MICROSCOPY AND SPECTROSCOPY

In this chapter, several pulse shaping strategies for nonlinear optical microscopy and spectroscopy are discussed, including local pulse compression, adaptive spectral focusing, and optimized interferometric CARS. These pulse shaping methods are designed in order to fully utilize the spectral-temporal characteristics of the coherent fiber SC pulses. The principles and the applications to biomedical imaging of each method will be presented. Some of the results shown in this chapter are adapted from the recently published works[44,154], with permission.

4.1. Local pulse compression for 2PF, SHG, 3PF and THG microscopy

4.1.1. Principles of local pulse compression

Efficient multiphoton imaging relies on faithful delivery of ultrafast pulses to the biological samples. The ultrafast pulses, however, can be deteriorated by the dispersion introduced by the optics along the beam path. Pulse compressors such as a prism compressor, grating compressor, and pulse shaper have been used to recompress the pulses at the microscope objective focus for efficient multiphoton imaging[122,155-157]. High-quality pulse compression for signal enhancement is especially important when imaging endogenous biomolecular contrast, because the generated signal is typically much weaker than that of any external contrast agent. Additionally, improved imaging efficiency lowers the optical power needed and potentially reduces photodamage to the biological samples. Among different compressors, a pulse shaper provides higher-order dispersion compensation for transform-limited (TL) pulse compression and spectral phase tunability for ease of operation[157], and therefore presents as an ideal pulse processing device for multiphoton imaging.

The effects of the pulse width on the signal from two-photon (2P) and three-photon (3P) processes can be modeled concisely as,

$$S_{2p} \propto I(t)^2 \cdot \Delta\tau \propto (\frac{P}{\Delta\tau})^2 \cdot \Delta\tau \propto \Delta w \tag{4.1}$$

$$S_{3p} \propto I(t)^3 \cdot \Delta\tau \propto (\frac{P}{\Delta\tau})^3 \cdot \Delta\tau \propto (\Delta w)^2 \tag{4.2}$$

where P is the pulse energy and $\Delta\tau$ is the pulse width. Given the same pulse energy, the 2P (3P) signal is linearly (quadratically) proportional to the reciprocal of the pulse width. As the pulse width is inversely proportional to the bandwidth for TL pulses, the relation translates into a linear and quadratic dependence of the signal on the bandwidth. Therefore, using broadband compressed pulses can significantly enhance multiphoton imaging efficiency as compared to narrow-band excitation, particularly for higher-order processes such as 3PF and THG. Broadband compressed pulses can achieve high peak power with a high repetition rate (~80 MHz) laser commonly used in biomedical imaging applications. Nevertheless, one might not want to extend the bandwidth extensively, since an overly-broad bandwidth will lose the selectivity of multiphoton imaging in a complex biological microenvironment. A balance between signal efficiency and imaging selectivity should be met in practice.

The spectral resolution of a discretized pulse shaper defines the extent of the applicable spectral phase. To maintain the fidelity of the phase shaping, the introduced spectral phase is required to be smooth such that the phase difference between two adjacent pixels is much smaller than π[11,100]. This sets a limit to the amount of temporal delay or advance that a specific color of light can be tuned, given by

$$\tau(\omega) = -\frac{\delta\psi(\omega)}{\delta\omega} \tag{4.3}$$

$$\tau_{\max} = -\frac{\pi}{\delta\omega} \tag{4.4}$$

where τ is the frequency-dependent group delay, ψ is spectral phase, and ω is the angular frequency. In our system, the spectral resolution ($\delta\omega$) is 1.81 x 10^{12} rad/s (723-1300 nm, over 640 pixels in the pulse shaper SLM array), resulting in a $\tau_{\max}$ of 1.74 ps. For an ultrabroadband source, such as our fiber SC, the pulses experience a considerable amount of dispersion and can be significantly elongated in the optical

imaging system. Therefore, compressing the pulses at the full bandwidth "globally" using a pulse shaper is not feasible. Adding a grating or prism compressor can effectively remove the linear chirp but increase the system complexity, and also reduce the usable optical power for imaging. This situation can also pose an issue for clinical translation of the pulse shaping technology, particularly because fiber-based beam delivery could introduce a large amount of dispersion that lowers the multiphoton imaging efficiency.

The bandwidth for selective multiphoton imaging, and the extent of spectral phase shaping, coincidently lead to the concept of local compression – to compress a selective spectral range of the pulses using the pulse shaper. As illustrated in Fig. 4.1, the broadband and nonlinearly chirped SC pulses is first spectrally filtered to the desired spectrum by amplitude shaping for multiphoton imaging selectivity, and then the selected band is compressed by "locally" phase shaping for efficient signal generation.

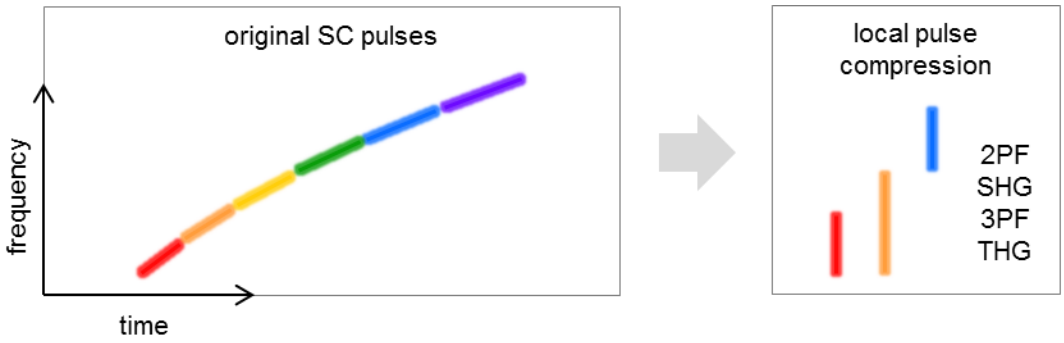

Fig. 4.1. Schematic of local pulse compression. The nonlinearly chirped SC pulses are spectrally filtered to the desired spectral bands and compressed to the transform-limit for selective and efficient multiphoton imaging.

The experimental demonstration of this concept is presented in Sections 4.1.2 and 4.1.3. In Section 4.1.2, local compression of the early SC generated in non-polarization-maintaining fiber, with a spectral bandwidth of 900-1160 nm, will be discussed. The locally compressed pulses are employed for efficient 2PF, SHG, and THG imaging of cell and tissue samples. In Section 4.1.3, local compression of the advanced SC generated in the polarization-maintaining fiber, with a spectral bandwidth of 780-1300 nm will be discussed. The SC pulses are highly chirped in this experiment for adaptive spectral focusing CARS (discussed in Section 4.2). However, local pulse compression still successfully compresses the selective pulses to the TL at the focus of the microscope objective for efficient 2PF, SHG, 3PF, and THG imaging of the murine mammary gland and mammary tumor samples.

4.1.2. Nonlinear optical microscopy by shaping supercontinuum pulses of 900-1160 nm

As discussed in Section 2.3, coherent control enables engineering of light-matter interactions for nonlinear optical microscopy and spectroscopy[12,158,159]. Control of two-photon (2P) excitation by shaping femtosecond pulses was first demonstrated by Meshulach et al[13,160]. Sinusoidal phase shaping[102], binary phase shaping[103], anti-symmetric phase shaping[104], and adaptive phase shaping[105] of ultrafast pulses have been demonstrated to selectively image fluorophores in biological samples. While phase-only shaping techniques have been studied extensively in 2PF imaging, the potential for amplitude shaping has not been fully utilized. Amplitude shaping to select the fundamental excitation spectra is practically robust and simple, and phase shaping, in addition, can compensate the dispersion to higher orders to enhance the excitation efficiency[106,161]. To date, pulse shaping techniques have not found wide applications in SHG and THG imaging[157,162]. This method can also be applied for SHG and THG imaging with arbitrary spectral ranges within the fundamental spectrum.

SC generation by pumping a photonic crystal fiber (PCF) with laser pulses offers an alternative broadband light source to mode-locked solid-state lasers[15]. The ultrabroad bandwidth and versatility of a PCF as an add-on to a solid-state laser makes it appealing for biophotonic imaging. Fiber SC has been utilized in 2PF microscopy, and improved 2PF efficiency using a compressed SC[122], short-wavelength 2PF imaging[163], simultaneous excitation of multiple fluorophores[164], and selective excitation by spectrally filtering a SC[165] have been reported. The combination of a SC source and pulse shaping can offer control of 2P excitation over an ultrabroad spectral range. Flexible pulse shaping of the SC light source to achieve selective excitation of fluorophores has been demonstrated[166]. However, shaping of SC for 2PF, SHG, and THG imaging of biological samples has not been shown.

In this section, multimodal nonlinear optical imaging by locally compressing fiber SC pulses of 900-1160 nm is demonstrated. The SC generated by pumping a PCF was spectrally filtered and compressed to near TL by a pulse shaper, as can be confirmed by the measured SHG spectra from a BBO crystal. The shaped pulses were employed to perform 2PF, SHG, and THG imaging of biological samples. Selective

and efficient 2PF imaging of fluorophores was achieved in GFP fibroblasts co-stained with Mitotracker Red CMXRos. 2PF, SHG, and THG imaging of a porcine skin cross-section enabled visualization of different intrinsic biomolecules. Improved efficiency of 2PF, SHG, and THG imaging was also demonstrated. The proposed approach shows potential to be developed as a powerful multimodal imaging method.

The experimental setup is shown in Fig. 4.2. Pulses from an Yb:KYW laser (FemtoTRAIN IC, High Q Laser) of 1040 nm and 80 MHz were coupled into a highly-nonlinear all-normal-dispersion (ANDi) PCF (NL-1050-NEG-1, NKT Photonics) for SC generation. The SC was collimated by a parabolic mirror and modulated by a MIIPS-assisted pulse shaper, which allows amplitude and phase shaping from 723 to 1300 nm over a 640-pixel liquid crystal (MIIPSBox 640, Biophotonics Solutions, Inc.). The SC was guided into an upright microscope (BX61WI, Olympus) modified for nonlinear optical imaging. A dichroic mirror (T700spxc-1500 Chroma Technology) reflected the SC into an objective (LUMPlanFl/IR, 60xW, N.A. = 0.9, Olympus) and transmitted the backward multiphoton signal from the samples. Imaging was performed by scanning a motorized stage (Bioprecision, Ludl Electronic Products). The multiphoton signal was detected by a photomultiplier tube (H7421-40, Hamamatsu) after passing through a bandpass filter wheel. SHG signal generated from a 10-μm-thick BBO crystal was acquired in the forward direction by a spectrometer (USB4000, Ocean Optics) to perform a MIIPS scan for pulse measurement and compression[142].

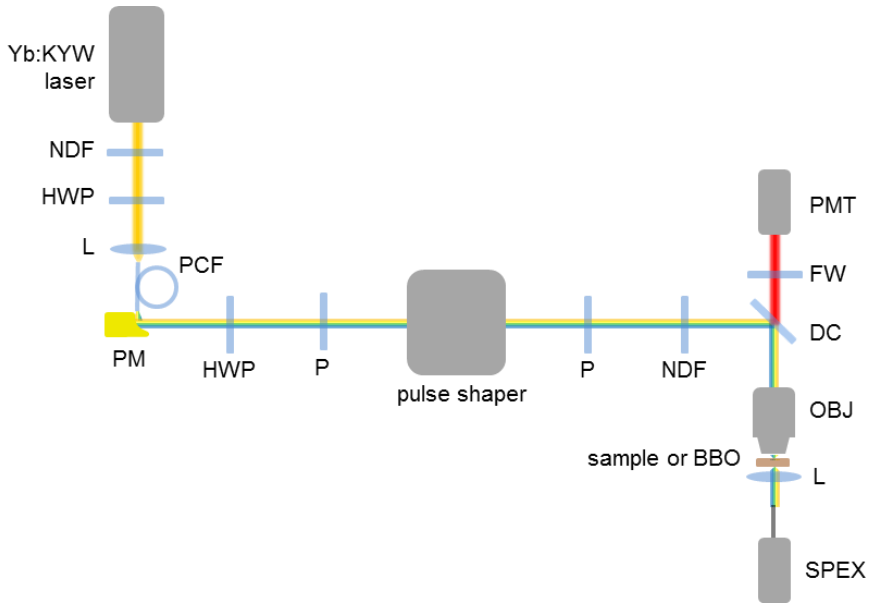

Fig. 4.2. The experimental setup for nonlinear optical microscopy by shaping supercontinuum pulses of 900-1160 nm. FW: filter wheel; HWP: half-wave plate; KYW: potassium yttrium tungstate; L: lens; NDF: neutral density filter; OBJ: objective; P: polarizer; PCF: photonic crystal fiber; PM: parabolic mirror; PMT: photomultiplier tube; SPEX: spectrometer; Yb: ytterbium.

For local pulse compression, amplitude shaping was first used to filter the fundamental spectra by blocking undesired wavelengths, as illustrated by the shaded areas in Fig. 4.3. The selected bands of 930-990 nm and 1100-1160 nm were designated as green and red pulses, respectively. Phase shaping was then used to compress the pulses by compensating the dispersion measured at the objective focus, as illustrated by the colored dashed lines in Fig. 4.3. The compressed and uncompressed pulses of two spectral ranges were used in the imaging sessions.

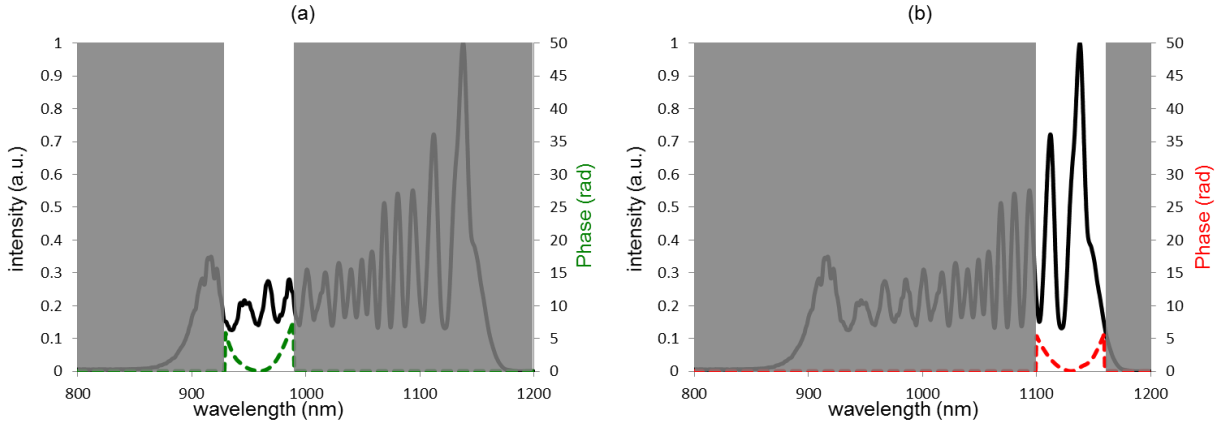

Fig. 4.3. Local pulse compression of the SC pulses of 900-1160 nm. The SC spectrum (black line), the amplitude shaping mask (shaded areas), and the measured spectral phase (colored dashed lines) are shown for (a) green (930-990 nm) and (b) red (1100-1160 nm) pulses. A spectral phase opposite to the one measured was introduced by the pulse shaper to compress each pulse[154]. (Copyright © 2012, IEEE)

For cell imaging, the mitochondria of mouse GFP-transfected 3T3 fibroblasts were labeled with Mitotracker Red CMXRos (M7512, Invitrogen) at a concentration of 100 nM for 15 minutes. Excess dye was washed off and replaced by fresh culture medium before 2PF imaging. The 2P excitation spectra of fluorophores were used to determine the pulses used for selective excitation. GFP, with an excitation peak around 480 nm, can be excited by green pulses from 930 to 990 nm[167], and Mitotracker Red CMXRos, with an excitation peak at 579 nm, can be excited by red pulses from 1100 to 1160 nm[168]. The SC power was controlled by a neutral density filter before entering the microscope. The imaging power under the objective in the GFP channel (520 ± 17 nm) was 3.1 mW for green pulses and 7.5 mW for red pulses. The power in the Red channel (620 ± 26 nm) was 0.6 mW for green pulses and 1.4 mW for red pulses. Different power levels were employed in the two channels due to the different sensitivity of targeted fluorophores and detection bandwidths. While only phase shaping was performed to compress the spectrally filtered pulses, the average power was the same when imaging with compressed and uncompressed pulses.

For tissue imaging, frozen porcine skin was cut to 100-μm-thick cross-sections and thawed before label-free multimodal nonlinear optical imaging. Green pulses (930-990 nm) were used in 2PF imaging in order to excite endogenous fluorescent biomolecules. For the spectral range selected, the possible fluorophores are FAD and elastin. Red pulses (1100-1160 nm) were used to avoid excitation crosstalk of 2PF in SHG imaging and to have higher detection quantum efficiency in THG imaging. Different bandpass filters were employed in front of the photomultiplier tube for acquiring different signals (2PF: 542 ± 25 nm, SHG: 562 ± 40 nm, THG: 376 ± 20 nm). The imaging power under the objective for 2PF, SHG, and THG were 3.3 mW, 1.7 mW, and 9 mW, respectively. These different power levels for each modality provided sufficient signal while preventing saturation of the photomultiplier tube.

The SHG spectra of green and red, compressed and uncompressed pulses are shown in Fig. 4.4 for evaluating their 2P excitation spectra. The SHG spectral ranges were confined by their fundamental spectra as controlled by amplitude shaping. The spectra are normalized to the maximal SHG intensity of

the compressed pulses in each color. By pulse compression, the SHG intensity within the desired spectral ranges was improved by 4.4 and 2.8 fold for green and red pulses, respectively.

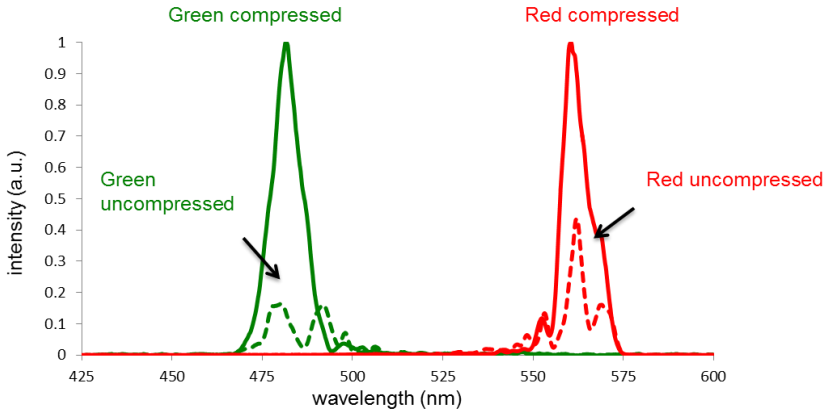

Fig. 4.4. SHG spectra of green compressed (solid green), green uncompressed (dashed green), red compressed (solid red), and red uncompressed (dashed red) pulses[154]. (Copyright © 2012, IEEE).

2PF images of cell samples from different detection channels (row) illuminated with different compressed pulses (columns) are shown in Fig. 4.5. In the GFP channel, the fluorescence signal from green compressed pulses is clearly seen while that from the red compressed pulses is not observable. In the Red channel, the fluorescence signal from red compressed pulses is clearly seen while that from green compressed pulses is relatively weak. This weak signal has similar features as that in the GFP channel and can be identified as emission crosstalk from the GFP fluorescence. These results demonstrate selective 2PF imaging of GFP and Mitotracker Red CMXRos by green and red compressed pulses, respectively.

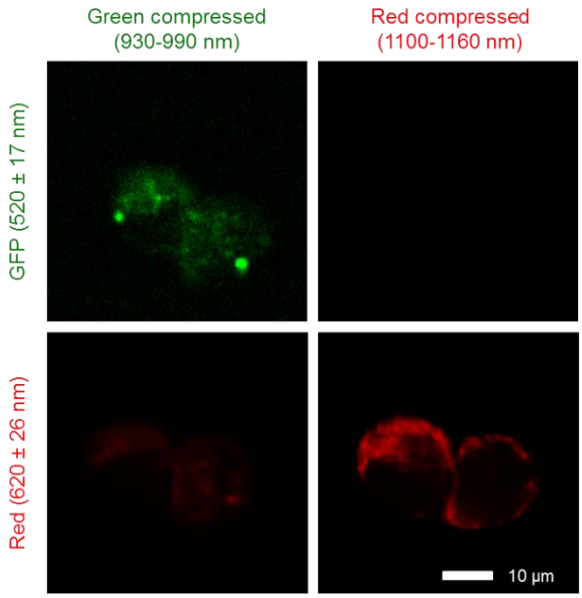

Fig. 4.5. Selective 2PF imaging of GFP-transfected fibroblasts co-stained with Mitotracker Red CMXRos acquired in different detection channels (rows) by illuminating with different compressed pulses (columns). The images in the same channels are represented with the same normalized contrast[154]. (Copyright © 2012, IEEE).

2PF images of the cell samples illuminated by compressed and uncompressed pulses are compared in Fig. 4.6. Images in which fluorophores were selectively excited are combined for illustration. Fig. 4.6(a) is merged from the image of green compressed pulses in the GFP channel and that from red compressed pulses in the Red channel. Fig. 4.6(b) is the uncompressed control. The fluorescence from compressed pulses is significantly improved compared to that from uncompressed pulses. The improvement of fluorescence intensity within the entire cellular area is calculated to be 3.6 and 3.2 fold for the green and red signals, respectively.

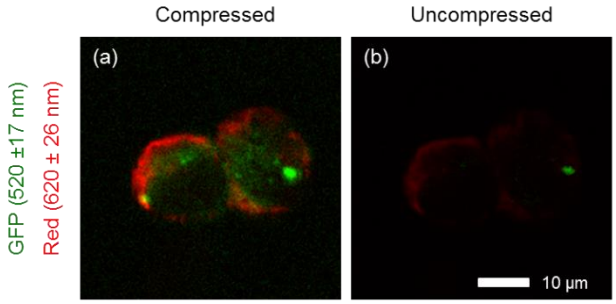

Fig. 4.6. 2PF images of GFP-transfected fibroblasts co-stained with Mitotracker Red CMXRos acquired with (a) compressed and (b) uncompressed pulses. The image in (a) is a merged image from the green compressed pulses in the GFP channel and red compressed pulses in the Red channel. Image (b) is from uncompressed control pulses. By pulse compression, the fluorescence intensity is enhanced by 3.6 and 3.2 fold for the green and red signals, respectively[154]. (Copyright © 2012, IEEE).

Label-free multimodal nonlinear optical images of porcine skin cross-sections illuminated by compressed and uncompressed pulses are compared in Fig. 4.7. All of the nonlinear optical signals from compressed pulses were greatly improved compared to those from uncompressed pulses. The improvement of 2PF, SHG, and THG signals were calculated to be 1.9, 2.4, and 8.5 fold, respectively. 2PF emission was observed from the stratum corneum (left) and from collagen in the papillary dermis and reticular dermis (right)[169]. SHG revealed collagen structure in the papillary dermis and reticular dermis. THG showed optical heterogeneities in the stratum granulosum cells in the epidermis, and the stratum spinosum and stratum basale cells in epidermis-dermis junction[170].

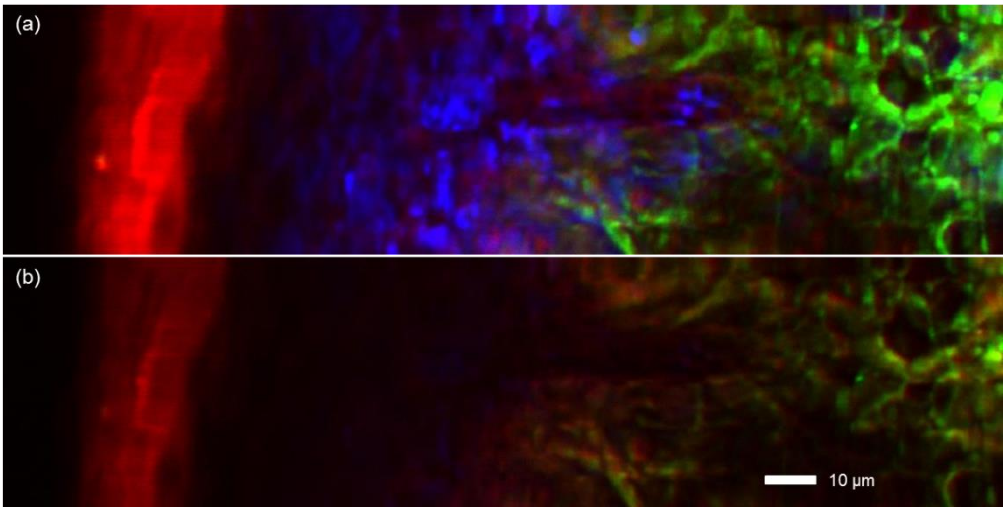

Fig. 4.7. Label-free multimodal nonlinear optical imaging of porcine skin acquired with (a) compressed and (b) uncompressed pulses. 2PF, SHG, and THG are represented in red, green, and blue pseudo-color[154]. (Copyright © 2012, IEEE).

While phase shaping alone can tailor 2P excitation and SHG and THG spectra from ultrafast laser pulses, amplitude shaping to first spectrally filter desired wavelengths is practically robust and easy to implement as long as the laser power is sufficient. Phase shaping techniques can be sensitive to spectral phase acquired in biological samples, thus deteriorating the excitation selectivity and efficiency. Amplitude shaping does not need a complex spectral phase, which requires expertise in coherent control theory and frequently employs an adaptive algorithm that can be time-consuming when adapting to different biological systems[105]. The total power of our SC before entering the microscope was 100 mW, which is more than sufficient for nonlinear optical imaging of biological samples.

In addition to spectral selection, phase shaping to compress pulses to the TL can effectively improve the efficiency of nonlinear optical processes. The enhancement of 2PF signal was more than three-fold in the cell imaging experiment. This approach provides higher order dispersion compensation besides group delay dispersion and rapid switching between different excitation without modifying any optical setup, as compared to using bandpass filters[165] or to changing the wavelength of a narrow-band pulsed laser source[171,172]. Higher order dispersion compensation can significantly improve 2PF efficiency for broadband pulses (> 30 nm), reduce necessary imaging power, and thus lower photodamage to biological samples[106,157]. Fast switching with a programmable shaper can ease alignment tasks and assist image co-registration of fluorophores. The switching speed is of tens of milliseconds and is limited by the pulse shaper in the setup. This method can easily be applied to SHG and THG imaging as demonstrated in the tissue imaging experiment. The 2PF and SHG signal improvement in the skin tissue experiment is lower than that in the cell experiment, likely due to loss of scattered photons in biological tissue. The THG signal had a greater improvement as compared to the SHG signal, as THG is a higher order nonlinear process and is more sensitive to the pulse peak power before and after pulse compression.

The Yb:KYW laser based SC spans a spectral range of 900-1160 nm, which is centered in the optical window of biological tissue and thus suffers little scattering and absorption in tissue imaging. The spectral range provides a longer wavelength 2P excitation from 450 to 580 nm, filling the gap between Ti:sapphire and Cr:forsterite broadband lasers. This spectral range can also be used for SHG and THG imaging with sufficient quantum efficiency for most silicon-based photo-detectors. Ongoing work will extend the SC bandwidth by increasing the PCF length and/or the pump power. Several SC sources of similar spectral ranges have been demonstrated in microscopy and spectroscopy applications. The Ti:sapphire laser based SC has spectra within 600-1000 nm[109,173,174], and the Er:fiber SC has a spectrum from 900-1500 nm[175].

To conclude this section, multimodal nonlinear optical microscopy in biological samples was performed by locally compressing a fiber SC from 900 - 1160 nm. The coherent SC pulses generated by pumping an

ANDi PCF with an Yb:KYW laser was spectrally filtered and compressed under a microscope objective by a pulse shaper. SHG signal of green (930-990 nm) and red (1100-1160 nm) pulses was enhanced by 4.4 and 2.8 fold, respectively, by local pulse compression. In a cell imaging experiment, selective 2PF imaging of fluorophores and improved fluorescence signals by factors over 3 were demonstrated. In a skin tissue imaging experiment, multimodal nonlinear optical imaging, including 2PF, SHG and THG, and improved signal level were shown. Shaping the SC provides selective and efficient 2PF imaging over a long-wavelength broadband (450-580 nm) with a single beam and an easily tunable setup. The approach can potentially be applied to efficient 3PF imaging of fluorophores with their excitation spectra in the UV range. As 3PF typically has lower efficiency, a broader bandwidth may be necessary in local compression to achieve higher peak power. The realization of 3PF will be addressed in the next section, and combined with 2PF, SHG, and THG imaging.

4.1.3. Nonlinear optical microscopy by shaping supercontinuum pulses of 780-1300 nm

With the development of the WB-extended SC spanning from 780 to 1300 nm, the multiphoton excitation spectral range can be further extended to a 2P excitation of 390 to 650 nm, and a 3P excitation of 260 to 433 nm. In this section, local pulse compression of the ultrabroadband SC in a highly dispersive imaging system is presented. A large amount of dispersion in the system was arbitrarily introduced by placing high-index glass in the beam path for spectral focusing CARS imaging, which will be discussed in Section 4.2. Even in this highly dispersive system, local compression successfully compresses the pulses of selected bands from the coherent SC, as evidenced by comparison of the SHG spectra of the compressed pulses to the theoretically modeled results, as well as by the measured MIIPS traces. Label-free, efficient 2PF, SHG, 3PF, and THG imaging of rat mammary tissue is demonstrated, visualizing intrinsic weak nonlinear optical signals. The approach will be combined with spectral focusing CARS to establish a multimodal multiphoton imaging platform in Chapter 5.

The experimental setup is illustrated in Fig. 4.8, and several modifications were incorporated in the setup from the previous section: (1) a polarization-maintaining ANDi PCF (NL-1050-NEG-1-PM, NKT Photonics) was employed for highly-polarized WB-extended SC generation. (2) A pair of dichroic mirrors (DMLP900, Thorlabs) were inserted in the beam path before and after the shaper to separate and recombine the WB band (pump) below 900 nm. (3) A 4" and 3" of SF57 glass blocks were placed in the main SC (Stokes, 900-1300 nm) and the WB band beam paths to pre-chirp the pulses for spectral focusing CARS, contributing to the high dispersion in the system. (4) A super-apochromat objective (UPLSAPO 60xW/IR, N.A. = 1.20, Olympus) with broadband chromatic aberration correction in the near-infrared region was employed. Note that only the main SC transmitted through the long-pass dichroics was used in this section. The WB band was not used and blocked during the experiment.

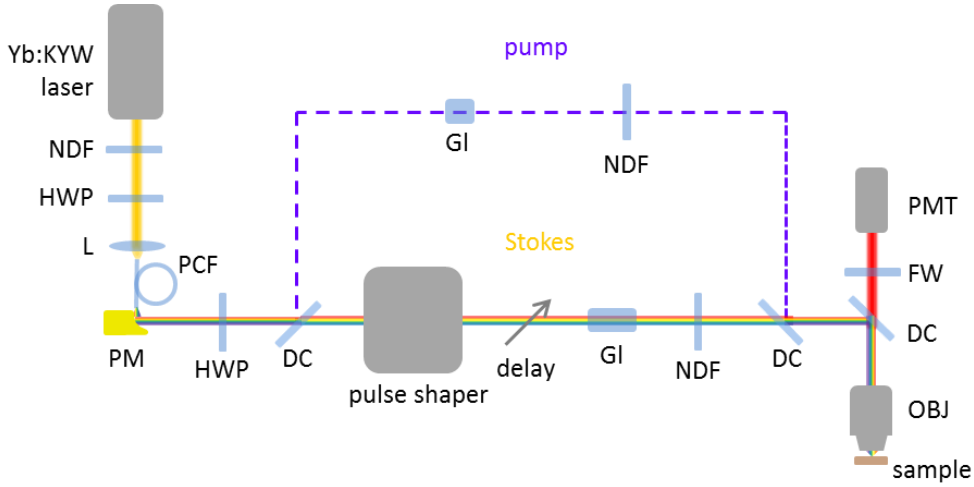

Fig. 4.8. The experimental setup for nonlinear optical microscopy by shaping supercontinuum pulses of 780-1300 nm. DC: dichroic mirror; FW: filter wheel; Gl: glass; HWP: half-wave plate; KYW: potassium yttrium tungstate; L: lens; NDF: neutral density filter; OBJ: objective; PCF: photonic crystal fiber; PM: parabolic mirror; PMT: photomultiplier tube; Yb: ytterbium.

Local pulse compression in the highly dispersive system was performed by conducting a MIIPS scan at the objective focus to compress the spectrally filtered pulses. Here, the selected spectral bands are 910-970, 1080-1200, and 1140-1200 nm, and the unfiltered SC was also examined for global pulse compression. The SHG spectra of the compressed and uncompressed pulses are shown in Fig. 4.9. The significantly enhanced SHG signal and the smooth SHG spectra covering the designated spectral ranges indicate successful local pulse compression of the pulses to the TL. The limited SHG enhancement

outside a narrower bandwidth for the globally compressed pulses suggests unsuccessful pulse compression. The recorded MIIPS traces of these spectral windows validate the pulse compression results [Fig. 4.9(c)]. For locally compressed pulses, the clean MIIPS traces as parallel lines separated by π confirm TL compression of the pulses[142,143]. For globally compressed pulses, the fine periodic structures in the MIIPS traces show unsuccessful compression because the pulse width of the full SC exceeds the temporal extent achievable by the pulse shaper.

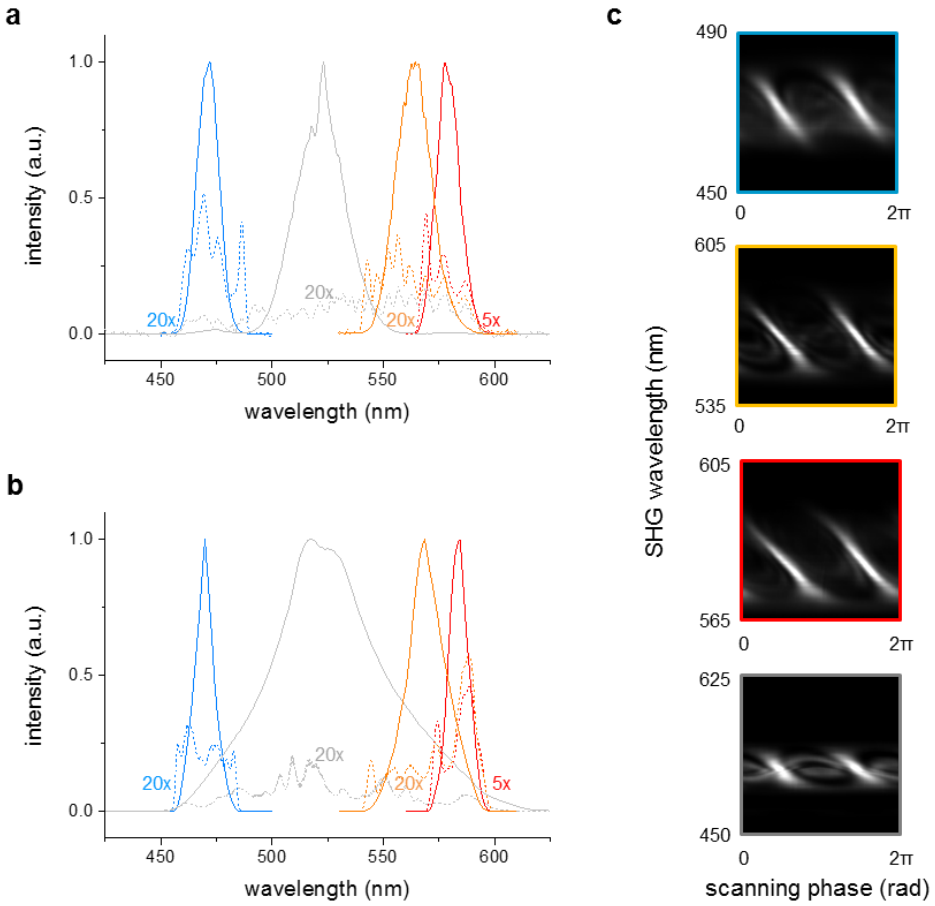

Fig. 4.9. Local pulse compression in a highly dispersive optical imaging system. (a) Experimental and (b) theoretical SHG spectra of the compressed (uncompressed) pulses [cyan: 910-970 nm, orange: 1080-1200 nm, red: 1140-1200 nm, Gray: unfiltered 900-1300 nm. Solid (dot) lines: compressed (uncompressed)]. The SHG spectra of the uncompressed pulses are multiplied by the specified numbers for comparison. (c) Measured MIIPS traces of the selected spectral ranges, with the colors of the grids corresponding to the SHG spectra in (a) and (b).

The theoretical SHG spectra of the compressed and uncompressed pulses are calculated using the measured spectral phase and the SC spectrum [Fig. 4.9(b)]. The comparison reinforces successful local pulse compression. The simulated SHG spectra of the locally compressed pulses agree well with the

experimental results. On the other hand, the simulated SHG spectrum of the globally compressed pulses shows a much broader bandwidth and a higher enhancement factor, indicating unsuccessful global compression in the experiment. Quantitatively, pulse compression enhances the SHG signal of the 910-970-nm, 1080-1200-nm, 1140-1200-nm bands by factors of 31.81, 40.67, 11.12, which agrees well with the theoretical values of 32.92, 36.11, 7.92. The SHG signal of the full main SC is only enhanced by 41.55, which is far from the theoretical value of 132.79 due to the unsuccessful global pulse compression[142].

In the highly dispersive system, local compression greatly enhance the efficiency of nonlinear optical imaging. Fig. 4.10(a) shows 2PF, SHG, 3PF, and THG imaging of rat mammary tissue acquired by using the locally compressed and uncompressed pulses. 2PF imaging was performed using the 910-970-nm band, SHG and THG were performed using the 1140-1200-nm band, and 3PF was performed using the 1080-1200-nm band. The signal enhancement not only increases the contrast in 2PF and SHG imaging but, more importantly, also raises the signal level above the background noise in 3PF and THG imaging. The result indicates that compression of broadband pulses can be beneficial to imaging intrinsically weak nonlinear optical signals in biological samples.

To calculate the signal enhancement factors, a filter that selects the pixels with photon counts greater than the mean value within the image and less than the detection upper limit of the photomultiplier is applied to the compressed pulse images. The filter excludes the pixels with lower signal intensities that might vanish in the uncompressed pulse images as well as those with saturated photon counts in the compressed pulse images. The ratio of the compressed pulse signal to the uncompressed pulse signal in each modality is shown in Fig. 4.10(b). For 2PF and SHG, the enhancement factors are 22 and 9, which are close to the SHG enhancement in the MIIPS pulse compression result. The deviation is likely due to the heterogeneous molecular distribution, as well as the multiple scattering and phase distortion in the biological sample. For 3PF and THG, the enhancement factors are 13.5 and 127.5, which are much lower (3PF) or higher (THG) than those expected from the MIIPS pulse compression results. This is due to the

weak 3PF (THG) signal that is below the noise background (almost undetectable) using the uncompressed pulses. Nevertheless, the estimation shows the potential of local pulse compression to image intrinsic biomolecules and structures of weak nonlinear optical response.

a

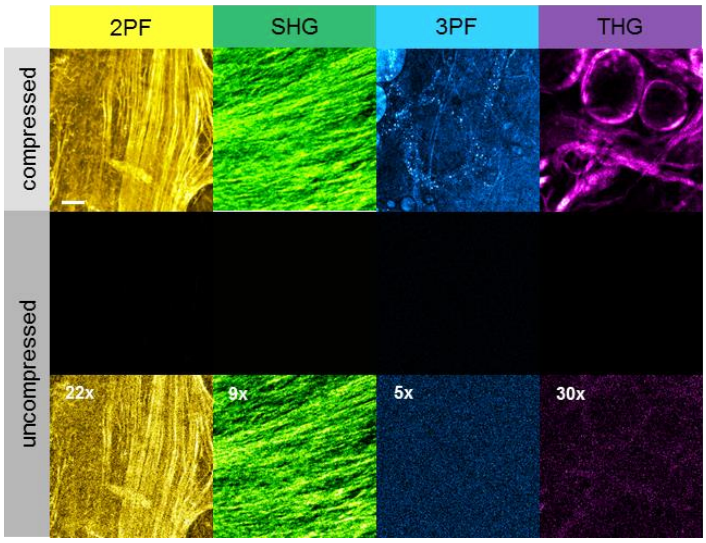

b

modality	signal enhancement
2PF	22.0 x
SHG	9.0 x
3PF	13.5 x
THG	127.5 x

Fig. 4.10. Efficient multiphoton imaging by local pulse compression in a highly dispersive system. (a) Images are shown for four different multiphoton imaging modalities. The displayed dynamic range of the images in one specific modality is set equal. In the bottom image for each modality, the signal of the uncompressed pulse images is multiplied by the specified number for comparison. For 3PF and THG, the multiplication is to show the noise background and the almost undetectable signal, respectively. (b) The enhancement factors calculated from the nonlinear optical signal in the images.

It is worth noting that multiple locally compressed pulses of different spectral ranges can be customized, with the selected bands separated in time. The method will enable single-beam, multi-color multiphoton imaging[176], and the temporal displacement between pulses can avoid the generation of other multiphoton signals, such as CARS or four-wave mixing (FWM), simultaneously.

To conclude this section, local pulse compression of the coherent SC is demonstrated in a highly dispersive optical system. The SHG signals from a BBO crystal generated by compressed and uncompressed pulses of selected spectral ranges show successful local compression. The main SC cannot be fully compressed however, due to the extended pulse width that exceeds the temporal extent attainable by the pulse shaper. Local pulse compression of the coherent SC enables efficient 2PF, SHG, 3PF, THG imaging of rat mammary tissue in a highly dispersive optical system. The improved efficiency enables label-free imaging molecules and structures that have an intrinsically weak nonlinear optical response.

This method will be combined with spectral focusing described in next section, and applied to multimodal nonlinear optical imaging in Chapters 5 and 6.

4.2. Adaptive spectral focusing for hyperspectral CARS imaging

4.2.1. Optimal spectral focusing for CARS imaging in the CH stretching region

To generate strong and high spectral resolution CARS signals, the spectrally dispersive power of the ultrabroadband SC can be concentrated into a single vibrational frequency by spectral focusing[53,127,177,178] in which both pump and Stokes pulses are chirped so that their instantaneous frequency difference remains the same during their interaction time to coherently drive a molecular vibration. Spectroscopic acquisition is achieved by scanning the delay between two pulses, which effectively tunes the frequency difference. The experimental setup was briefly addressed in the previous section, but here the pump beam was unblocked, recombined with the Stokes (main SC) beam by a dichroic, and sent into the microscope for hyperspectral CARS imaging, as illustrated in Fig. 4.11.

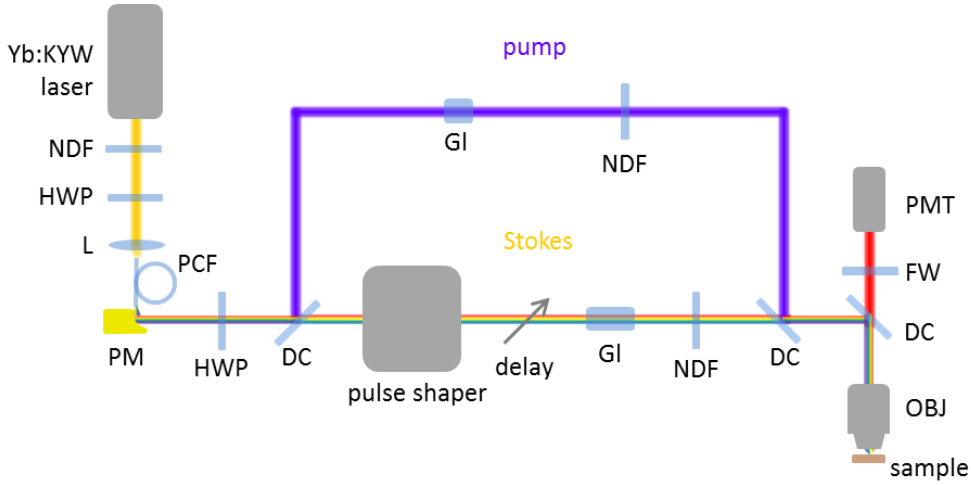

Fig. 4.11. Experimental setup for adaptively spectral focusing the SC for CARS imaging in the CH stretching and silent regions. DC: dichroic mirror; FW: filter wheel; Gl: glass; HWP: half-wave plate; KYW: potassium yttrium tungstate; L: lens; NDF: neutral density filter; OBJ: objective; PCF: photonic crystal fiber; PM: parabolic mirror; PMT: photomultiplier tube; Yb: ytterbium.

Blocks of 3” and 4” SF57 glass were placed in the pump and the Stokes beam paths, respectively, to pre-chirp the pulses. The 3” and 4” amount of glass corresponds to a chirp of about 16000 and 13800 fs^2 at

833 and 1115 nm, respectively, which was calculated using the Sellmeier equation and the relationship with second-order spectral phase[100],

$$n^2(\lambda) = 1 + \sum_k \frac{A_k \lambda^2}{\lambda^2 - \lambda_k^2} \tag{4.5}$$

$$\psi_2 = \frac{-\lambda^3 L}{2\pi c^2} \frac{d^2 n}{d\lambda^2} \ . \tag{4.6}$$

An additional spectral phase of 4500 fs^2 was introduced onto the Stokes beam by the shaper to minimize the dispersion mismatch of the two beams for optimal performance of spectral focusing in the CH stretching region. This optimal phase was determined by the acquired polystyrene spectrum that had the highest spectral resolution, highest signal strength, and the best correspondence to the spontaneous Raman data after a chirp scan with step intervals of 100 fs^2 [Fig. 4.12(a-b)]. Considering the dispersion contribution from the SC itself, the shaper, and the objective, the cumulative dispersion at the objective focus is estimated to be larger than 20000 fs^2. The spectral resolution of the system was calculated to be 14 cm^{-1} based on the measured FWHM (19 cm^{-1}) of the 2913 cm^{-1} peak in the CARS spectrum of DMSO [Fig. 4.12(c)].

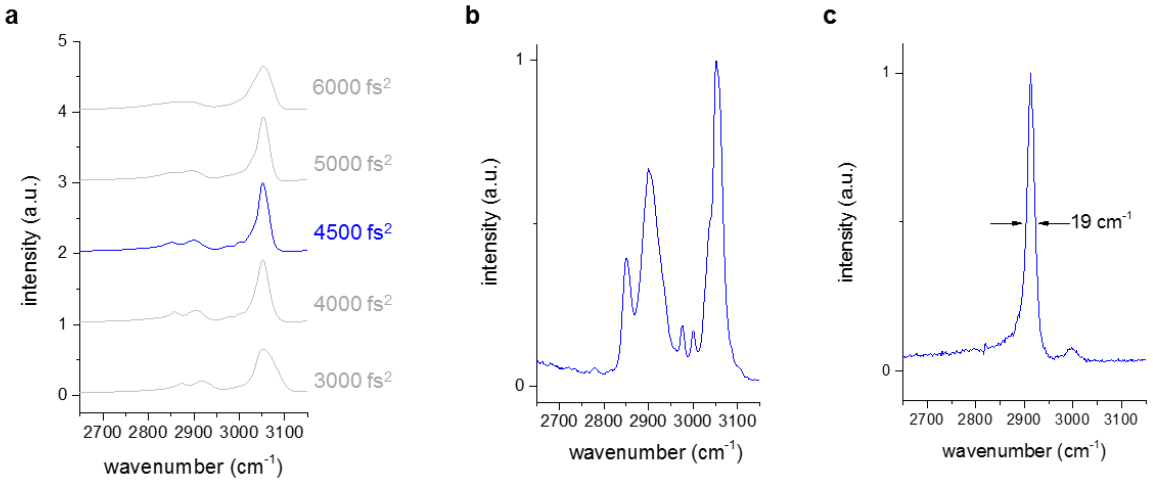

Fig. 4.12. Optimal spectral focusing in the CH stretching region. (a) CARS spectra of polystyrene in CH stretching region. Spectra around the optimal spectral phase introduced by the shaper are shown (blue lines: optimized phase, gray lines: surrounding phases). (b) Raman spectrum of polystyrene. (c) CARS spectrum of DMSO acquired with optimal spectral focusing, the FWHM of the peak at 2913 cm^{-1} is 19 cm^{-1}.

Hyperspectral CARS imaging of biological samples was demonstrated using a murine developing mammary tumor sample. Fig. 4.13 shows selected images from a hyperspectral image dataset from 2700 to 3250 cm^{-1}. Various biomolecules and structures can be visualized in images of different vibrational frequencies. CH_2 stretching at 2850 cm^{-1} can be used to target adipocytes and nerve, both of which are rich in lipid contents. CH_3 stretching at 2950 cm^{-1} can visualize not only lipids but also the protein distribution in the stroma. CH aromatic stretching at 3050 cm^{-1} generates signals only from proteins. The OH stretching at 3250 cm^{-1} visualizes the water distribution within the tissue, showing similar contrast as 3050 cm^{-1}. Throughout the hyperspectral images, the erythrocytes can be identified in the blood vessel, either visualized by the resonant CARS signal or by the non-resonant FWM signal.

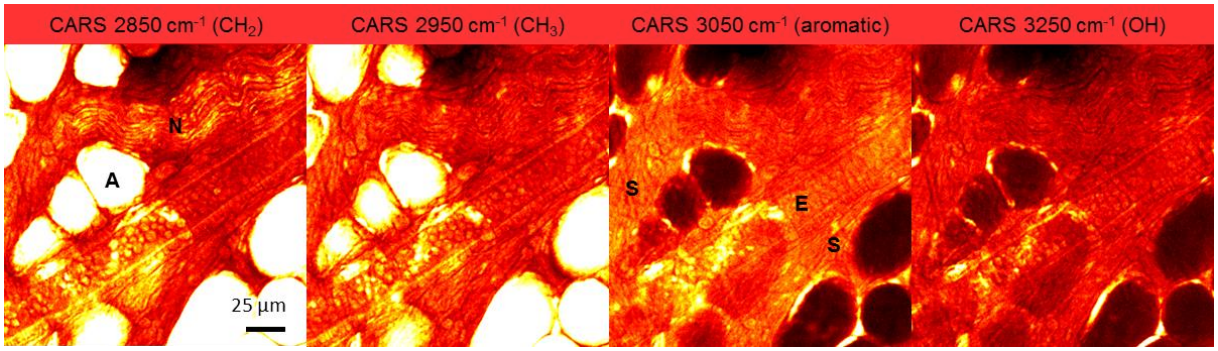

Fig. 4.13. Hyperspectral CARS imaging of an area in a murine developing mammary tumor. **A** adipocyte; **N** nerve; **S** stroma; **E** erythrocyte. Scale bar: 25 µm.

4.2.2. Adaptive spectral focusing for CARS imaging and capability of SRS imaging

With the ultrabroad bandwidth of the SC, the attainable vibrational frequency is not limited to only the CH stretching region, but can have a broader spectral range defined by the SC spectrum. By amplitude and phase shaping of the main SC pulses, the excitation pulses can be customized to different vibrational regions without any optical realignment. This concept of adaptive spectral focusing, as well as the potential for using the coherent SC for SRS, is demonstrated here. In the same setup, 2" and 4" blocks of SF57 glass were used, instead of the previous 3" and 4" blocks, in the pump and Stokes beam paths, respectively. An acousto-optic modulator (3200-124, Gooch and Housego) was inserted into the pump beam path for high-frequency modulation at 2 MHz for SRS. The CARS and SRS spectroscopy was

conducted in transmission mode with a focusing objective (LUMPlanFl/IR, 60xW, N.A. = 0.9, Olympus) and a collecting objective (LUMPlanFl, 40xW, N.A. = 0.8, Olympus). The CARS signal was detected by another photomultiplier tube (H7421-50, Hamamatsu) which was sensitive to near-infrared signals up to 890 nm. The SRS signal was detected by a photodiode (DET10C, Thorlabs) and demodulated by a lock-in amplifier (SR844, Stanford Research Systems) before computer readout.

The top row of Fig. 4.14 shows representative CARS and SRS spectra of methanol in the CH stretching region around the optimally introduced spectral phase of 1500 fs^2, as well as the spontaneous Raman spectrum for comparison. The change of optimal phase reflects the reduced amount of dispersion in this setup, but can be easily re-optimized by arbitrary phase shaping. Switching the Stokes bandwidth to 935-1130 nm enabled spectroscopic acquisition down to the vibrationally silent region (2100-2400 cm^{-1}). The bottom row of Fig. 4.14 shows the CARS spectra of acetonitrile around the optimal dispersion of 0 fs^2 in the vibrational frequency range of 2000-2500 cm^{-1}, as well as the spontaneous Raman spectrum. The additional phase needed for imaging in the vibrational silent region was less in comparison to imaging in the CH stretching region. This is due to more intrinsic and material dispersion at the shorter wavelength range of the main SC, which was used as the Stokes pulse, resulting in reduced dispersion mismatch between the pump and the Stokes pulses.

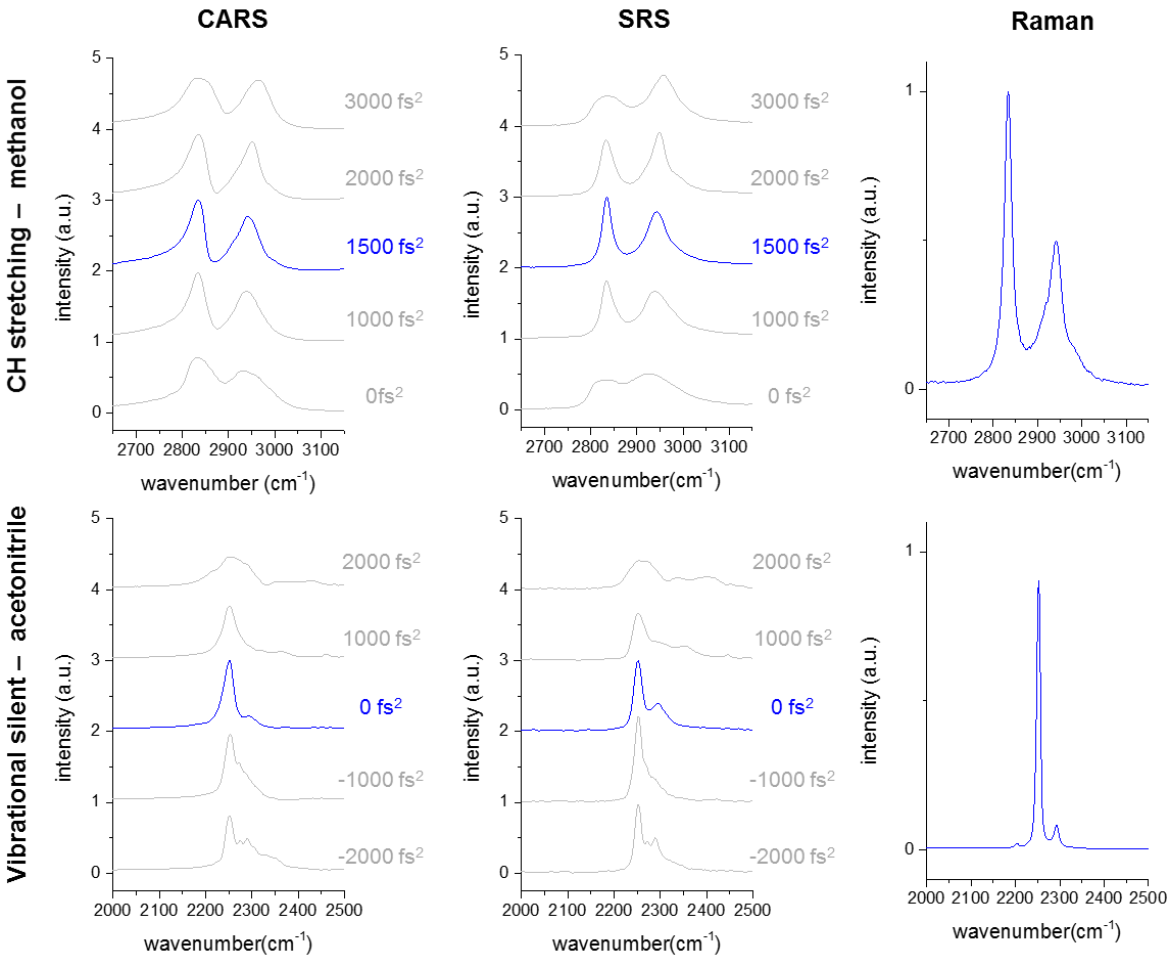

Fig. 4.14. Adaptive spectral focusing in different vibrational spectral ranges: CARS and SRS spectra of methanol in CH stretching region (top row) and acetonitrile in the silent region (bottom row). Spectra around the optimal spectral phase introduced by the shaper are shown (blue lines: optimized phase; gray lines: surrounding phases). Their Raman spectra are also shown for comparison.

To demonstrate the feasibility of vibrational imaging in the silent region, Fig. 4.15 shows CARS imaging of a deuterated compound that was taken up by human dermal fibroblasts in culture. The Raman spectrum and the structural formula of the compound are also shown. The drug, at a concentration of 100 μM, was added to the cell culture and incubated for 24 hours. The culture media was replaced with fresh media before the imaging session. The deuterated compound could be clearly visualized within the cells when the instantaneous frequency difference was tuned to 2100 cm^{-1}, at which the CD bonds possess a strong vibrational response. On the other hand, the non-resonant signal outlined only the morphology of the cells when the vibrational frequency was tuned off-resonant to 2250 cm^{-1}. We note that the spectrum of the SC can support hyperspectral CARS imaging in the vibrational fingerprint region, but the low-wavenumber

spectral focusing CARS acquisition is limited by the current system setup. In next section, a single-beam interferometric strategy enabling broadband CARS spectroscopy in the fingerprint region is presented.

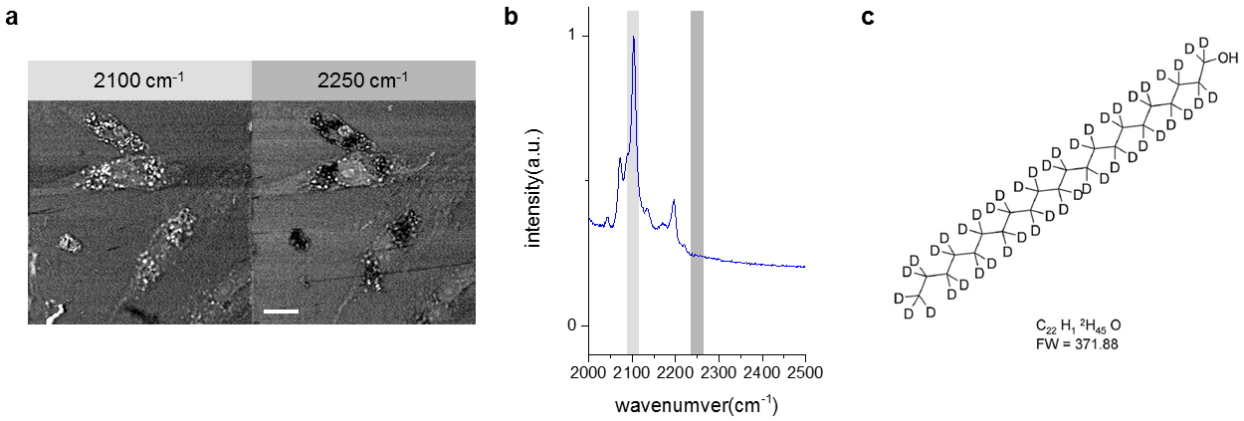

Fig. 4.15. Monitoring drug delivery using CARS imaging in the vibrationally silent region. (a) CARS imaging of a deuterated drug taken up by human dermal fibroblasts in culture (scale bar: 20 µm). (b) The Raman spectrum and (c) the structural formula of the drug.

4.3. Single-beam CARS spectroscopy in the fingerprint region

4.3.1. Single-beam interferometric CARS spectroscopy

Vibrational spectroscopy is a label-free technique for investigating the chemical content of samples. Compared to spontaneous Raman scattering, CARS provides coherent signal enhancement, realizing real-time vibrational spectroscopic imaging[5,7]. Experimental and computational methods have been developed to retrieve the informative resonant CARS signal and to reject the non-resonant background, especially for spectroscopic applications[33,36,39,40,178-181]. Among them, pulse shaping enables coherent control of the driving fields and the extraction of spectral information in a single-beam alignment-insensitive configuration[11,12]. Several pulse shaping strategies have been proposed to detect molecular vibrational signatures using a single-beam setup, including sinusoidal-phase[101,182,183], time-resolved pump-probe[109], spectral focusing[110], and narrow-band probe methods[41-43,111,184-186]. Currently, two of the major challenges in single-beam CARS spectroscopy include a limiting vibrational bandwidth that can be attained by the laser sources, and the non-trivial extraction and representation of the Raman spectrum.

Fiber SC light sources with extended vibrational bandwidth present an alternative to solid-state lasers. The use of fiber SC for CARS spectroscopy has been demonstrated in a multi-beam configuration, as demonstrated in the previous section[124,127,187,188]. For single-beam methods, however, few known fiber SC sources have sufficient coherence, bandwidth, and power for coherent control[189]. Previous works have demonstrated the use of a fiber SC for sinusoidal-phase or time-resolved CARS measurements[109,183]. However, the applicability of a narrow-band probe[41-43,111,184-186] by use of a fiber SC has not been demonstrated, possibly due to more demanding spectral phase stability and coherence requirements. The fiber SC generated in ANDi fiber, with excellent phase stability and coherence, can be advantageous for this high-precision phase shaping application[118,120,138]. In this section, single-beam interferometric CARS spectroscopy in fingerprint region is demonstrated by narrow-band phase shaping of a coherent fiber SC generated in an ANDi fiber. The pulse shaping strategy and direct vibrational spectrum retrieval are presented. The retrieved spectra of several chemical species agree with their spontaneous Raman data across the fingerprint region.

The experimental setup is illustrated in Fig. 4.16. Pulses of 1041 nm, 180 fs (FWHM), and 80 MHz from a compact Yb:KYW laser (FemtoTRAIN IC model-Z, High Q Laser) were coupled into the ANDi fiber (NL-1050-NEG-1, NKT Photonics). The fiber was pumped along the slow axis with an output (input) power of 345 (600) mW. Due to weak birefringence of the fiber, a portion of the SC was depolarized and removed by a polarizer. The remaining SC, with a power of 205 mW (~2.5 nJ of pulse energy), was modulated by a pulse shaper (MIIPSBox 640, Biophotonics Solutions Inc.) and then focused by a near-infrared objective (LUMPlanFl/IR 60xW, N.A. = 0.9, Olympus). The spectral phase of the SC at the objective focus was characterized and compensated by the pulse shaper prior to arbitrary pulse shaping[150,190].

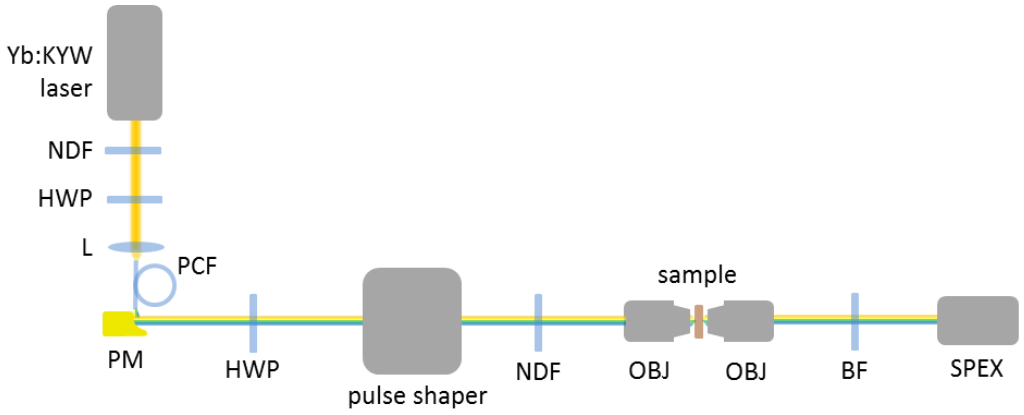

Fig. 4.16. Experimental setup for single-beam CARS spectroscopy in the fingerprint region. BF: bandpass filter; HWP: half-wave plate; KYW: potassium yttrium tungstate; L: lens; NDF: neutral density filter; OBJ: objective; PCF: photonic crystal fiber; PM: parabolic mirror; SPEX: spectrometer; Yb: ytterbium.

The pulse shaping strategy was simplified from the narrow-band probe approach with impulsive vibrational excitation, as illustrated in Fig. 4.17[42,111,186]. The SC spectral tail below 900 nm was blocked using a knife-edge at the Fourier plane of the pulse shaper in order to detect CARS signal below 900 nm. A narrow bandwidth centered at the lowest-wavelength peak of the SC spectrum was phase-shifted by $\pm\pi/2$ radian to serve as the probe pulse. One pixel on the spatial light modulator was modulated, corresponding to a 10 cm^{-1} spectral resolution in the setup. The CARS data of $\pm\pi/2$ pulses were subsequently acquired for retrieving the Raman spectra.

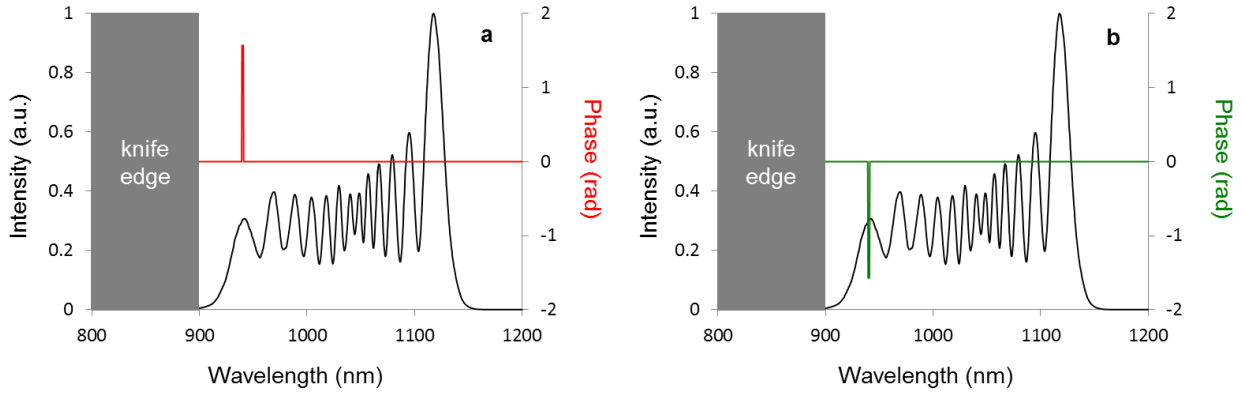

Fig. 4.17. Pulse shaping strategy for retrieving Raman spectra. The SC below 900 nm was blocked using a knife-edge at the Fourier plane of the pulse shaper (gray area). The narrow-band probe pulses centered at the shortest-wavelength peak of the SC spectrum were phase shifted by (a) $\pi/2$ (red) or (b) $-\pi/2$ (green) radian[44].

For CARS measurements, the SC power was attenuated by a neutral density filter to 10 mW for solvent samples and to 4 mW for the KGW crystal ($KGd(WO_4)_2$, potassium gadolinium tungstate) at the objective

focus. The forward CARS signal from samples between two coverslips was collected by another objective (LUMPlanFl 40xW, N.A. = 0.8, Olympus) and delivered into a spectrometer equipped with an EMCCD camera (ProEM 1600, Princeton Instruments). The exposure time was 1 ms, and 50 acquisitions were averaged. To validate these spectroscopic measurements, corresponding spontaneous Raman spectra were measured on a commercial confocal Raman microscope (LabRAM HR, Horiba) at the power of 8 mW. The integration time using this Raman microscope was 1 s to achieve the equivalent signal-to-noise ratio. Theoretically, the CARS process can be described in two steps, as mentioned earlier in Section 2.1.5:

$$A(\Omega) = \chi^{(3)}(\Omega)\int_0^\infty E_p(\omega')E_s^*(\omega'-\Omega)d\omega' \tag{4.7}$$

$$P(\omega) = \int_0^\infty A(\Omega)E_{pr}(\omega-\Omega)d\Omega \tag{4.8}$$

where E_p, E_s, and E_{pr} are the pump, Stokes, and probe fields, respectively. The $\chi^{(3)}(\Omega)$ term is the third-order nonlinear susceptibility, including the resonant, $\chi_R^{(3)}(\Omega)$, and the non-resonant, $\chi_{NR}^{(3)}$, contributions. For the single-beam approach, the shaped pulses act as E_p, E_s, and E_{pr} simultaneously. The CARS spectra generated by the $\pm\pi/2$ pulses described earlier are

$$S^{\pm}(\omega) = |P_{NR}(\omega)|^2 + |P_R(\omega)|^2 \mp 2|P_{NR}(\omega)||P_R(\omega)|\,\mathrm{Im}\{e^{i\phi(\omega)}\} \tag{4.9}$$

where $\phi(\omega)$ is the phase induced by the vibrational resonance. The imaginary part of the resonant CARS signal can be obtained by calculating

$$\mathrm{Im}\{P_R(\omega)\} = |P_R(\omega)|\,\mathrm{Im}\{e^{i\phi(\omega)}\} \sim \frac{S^-(\omega)-S^+(\omega)}{[S^-(\omega)+S^+(\omega)]^{1/2}}\ . \tag{4.10}$$

The purely resonant term, $|P_R(\omega)|^2$, is relatively small and neglected. A constant pre-factor is dropped since it does not affect the spectrum. The Raman spectrum, which is the imaginary part of $\chi_R^{(3)}(\Omega)$, can be retrieved by correcting the impulsive vibrational excitation,

$$\mathrm{Im}\{\chi_R^{(3)}(\Omega)\} = \frac{\mathrm{Im}\{P_R(\Omega)\}}{\int_0^{\infty} E_p(\omega')E_s^*(\omega'-\Omega)d\omega'} . \tag{4.11}$$

A simulation of this modeling and processing is shown in Fig. 4.18. The experimental parameters, including the SC spectrum and the pulse shapes, were implemented in the simulation. A hypothetical molecule was assumed to possess vibrations modeled by complex Lorentzians evenly distributed from 600 to 1800 cm^{-1} [Fig. 4.18(a), blue line]. The vibrational excitation spectrum of the compressed SC pulses was calculated to be smooth over the spectral range of interest [Fig. 4.18(a), gray line]. The CARS signal generated by the shaped pulses shows spectral features of $\mathrm{Im}\{\chi_R^{(3)}(\Omega)\}$ on top of the non-resonant CARS spectra, which results from the interference of co-propagating resonant and non-resonant contributions [Fig. 4.18(b)]. The extracted spectrum recovered the Raman spectrum with only minor distortion [Fig. 4.18(c)], which originated from the purely resonant contribution neglected in Equation (4.9).

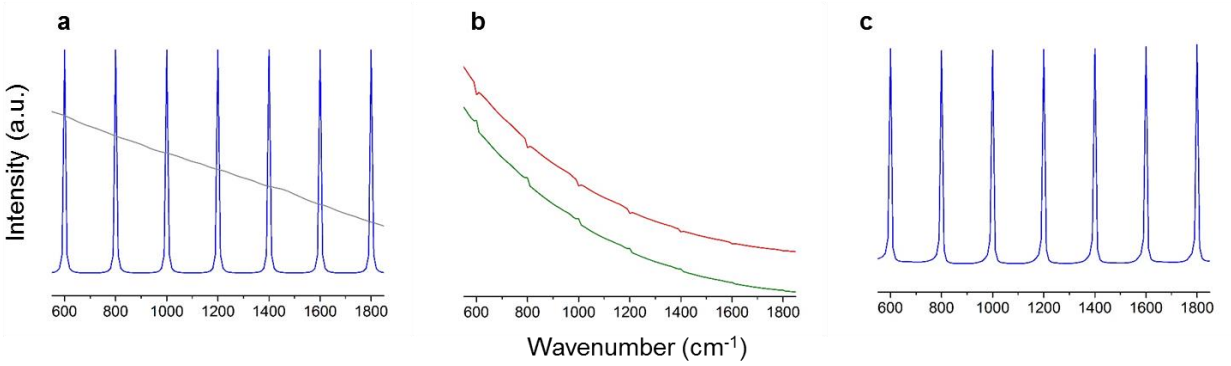

Fig. 4.18. Theoretical modeling of the retrieval of Raman spectrum in single-beam interferometric CARS. (a) Raman spectrum of a hypothetical molecule (blue) and vibrational excitation spectrum of the compressed supercontinuum (gray). (b) The CARS spectra generated by π/2 (red) and -π/2 (green) pulses. Two spectra are offset vertically. (c) The retrieved spectrum which closely resembles the original Raman spectrum[44].

The retrieved CARS spectra and the spontaneous Raman spectra of acetone, isopropanol, and toluene are shown in Fig. 4.19. The CARS spectra agree well with their corresponding Raman data within the fingerprint region. For acetone, the highest detected shift at 1702 cm^{-1} (C=O stretching) is close to the frequency difference between the two furthest peaks in the SC spectrum (1709 cm^{-1}), which dictates the accessible vibrational bandwidth by the SC. The strong C-C stretching vibration of isopropanol at

819 cm^{-1} is used to estimate the spectral resolution of the system, which is measured to be 13 cm^{-1} (FWHM). At this spectral resolution, the two close peaks of toluene at 1000 cm^{-1} and 1027 cm^{-1} are easily resolved.

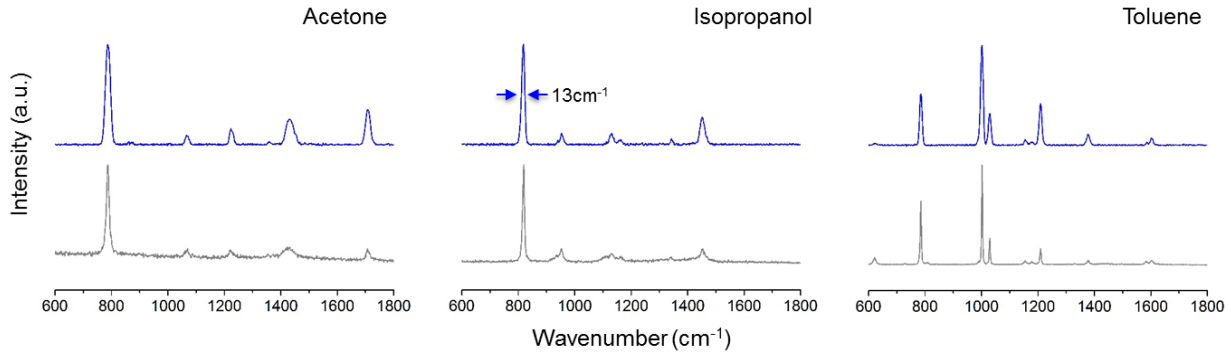

Fig. 4.19. Retrieved Raman spectra (blue) of acetone, isopropanol, and toluene, and their corresponding spontaneous Raman spectra (gray). The retrieved spectra are vertically offset for comparison. The CARS measurement shows good agreement with the spontaneous data. The peak of isopropanol at 819 cm^{-1} is used to quantify the spectral resolution (13 cm^{-1}, FWHM)[44].

The retrieved and spontaneous Raman spectra of a KGW crystal at two orientations ($E||N_g$, $E||N_m$: input electric fields parallel to the N_g and N_m refractive index axes, respectively) are shown in Fig. 4.20. The CARS measurement is sensitive to the orientation of the crystal. In the $E||N_g$ orientation, the CARS data reproduce two major shifts at 767 cm^{-1} and 900 cm^{-1} as in the Raman spectrum[191]. In the $E||N_m$ orientation, the peak at 767 cm^{-1} is observed to be much weaker in both the retrieved and Raman spectra.

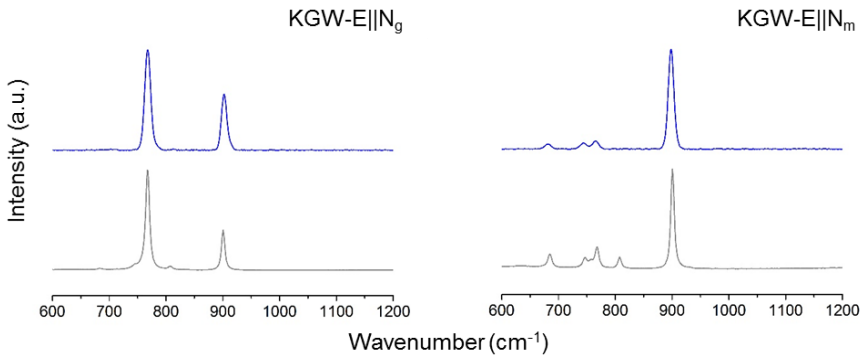

Fig. 4.20. Retrieved Raman spectra (blue) of a KGW crystal at two orientations ($E||N_g$, $E||N_m$) and their corresponding spontaneous Raman spectra (gray). The retrieved spectra are vertically offset for comparison. The CARS measurement reproduces the orientation-sensitive spontaneous Raman spectra[44].

The spectral broadening of the SC generated in the ANDi fiber is mainly governed by self-phase modulation, as is evident from its fringe-shaped spectrum. The reduced and definite spectral phase can be

easily compensated to higher orders by a pulse shaper at the focus of a high-NA objective, and therefore suitable for coherent control applications. The fiber was pumped at the slow axis to reduce the coupling between the slow and the fast axes, which can degrade the SC generation. An input power of 600 mW was used to induce sufficient spectral broadening for CARS spectroscopy in the fingerprint region. However, a higher input power up to 800 mW has been tested with broader spectrum without damaging the fiber. The depolarization was observed to be higher (41%) than that reported in our previous study (7%) because a different strand of fiber was used[153]. The power, the spectrum, and the spectral phase of the SC were measured to be consistent for more than 100 hours of operation, showing good long-term stability.

The fringe-shaped spectrum might appear to be unsuitable for single-beam CARS spectroscopy because the vibrational excitation may also be structured. Our simulation demonstrates smooth vibrational excitation, and the experiments retrieve Raman spectra across the fingerprint region with good agreement to their corresponding spontaneous Raman data. The detectable spectral range up to about 1750 cm^{-1} is limited by the SC bandwidth, which can be further extended by inducing wave-breaking[128]. The full power of the SC is 205 mW before the pulse shaper and 35 mW at the objective focus. The nJ-order pulse energy is comparable to some lasers used in single-beam CARS. The SC generation setup is simple and low-cost, mainly consisting of a compact Yb:KYW laser and a short piece of fiber (9 cm). The broad bandwidth of the fiber SC provides sufficient vibrational excitation for CARS while the moderate pulse energy and compactness can potentially be beneficial for biophotonics applications.

A narrow-band probe pulse shaping strategy was utilized for retrieving Raman spectra, and for determining the molecular contents of samples. The $\pm\pi/2$ phase shifts, as a complex conjugate pair, introduce a small change to the non-resonant background that is used as the local oscillator for homodyne mixing with the resonant signal. Therefore, a signal normalization step that might normally be needed when using 0 and π phase shifts can be relaxed. In addition, the difference spectrum yields the imaginary part of the CARS signal directly without post-processing using the Fourier transform or Kramers-Kronig

transformation[36,37,42,43]. Despite the simplicity, this pulse shaping approach has low probe pulse energy and relies heavily on homodyne mixing with the non-resonant signal. The spectra retrieved from the differential measurement can suffer from lower signal-to-noise ratio due to limited dynamic range because the non-resonant signal can easily saturate the detector at low excitation power. By optimizing the detection and pulse shaping scheme, a higher signal-to-background ratio could potentially be achieved.

4.3.2. Optimized amplitude shaping for single-beam CARS spectroscopy

As the single-beam CARS method presented in the previous section has a limited signal-to-background ratio, optimization of the pulse shaping strategy and the detection system is needed to improve its applicability. Two limiting factors mentioned above include: (1) low probe pulse power to generate sufficient resonant signal, and (2) overwhelming reference intensity from the non-resonant background. These two issues can be resolved if one can arbitrarily adjust the signal and the reference beam intensity as in an optical coherence tomography (OCT) setup[192]. Interestingly, the experimental condition in single-beam CARS is similar to a spectral-domain OCT (SD-OCT) in which spectral interferometry is utilized for detecting weak scattering signals from samples[193]. However, in single-beam CARS, only one-beam is employed to generate the broadband CARS spectrum, and direct tuning of the optical intensity of the signal and the reference beams, as is the case in SD-OCT, is therefore not feasible.

A careful examination of the single-beam CARS model reveals that the resonant CARS signal is linearly proportional to that of the probe pulse and quadratically proportional to that of the impulsive excitation (pump and Stokes) pulses. On the other hand, the non-resonant reference is solely and cubically proportional to the impulsive excitation. Therefore, the adjustment of the "signal" (CARS) and "reference" (non-resonant background) arms in single-beam CARS can be indirectly achieved by gray-level tuning the relative intensity of the probe pulse and the impulsive excitation pulse in the incident

laser spectrum. Coincidently, this spectral reshaping can be accomplished by amplitude shaping of the incident laser pulses by using the same pulse shaper in the setup.

In this section, an amplitude-and-phase shaping strategy is demonstrated for contrast enhanced single-beam interferometric CARS spectroscopy. Theoretical modeling demonstrates the feasibility of the approach and predicts the optimal amplitude shape. Experimental results agree well with the theory within the amplitude shaping capability of the shaper. In addition, a spectrometer design with a larger dynamic range is implemented to better resolve the homodyne-amplified resonant signal and to tolerate a higher excitation power.

In the experimental setup [

Fig. 4.21(a)], the high-quality coherent fiber SC was generated by pumping a 21-cm polarization-maintaining ANDi fiber (NL-1050-NEG-1-PM, NKT photonics) with an Yb:KYW laser of 80-MHz repetition rate, 220-fs pulse width, and 1041-nm center wavelength (FemtoTRAIN IC model-Z, High Q Laser). The fiber was pumped along the slow axis by adjusting the half-wave plate to control the polarization of the incident laser. The output (input) coupling power was maintained at 430 (700) mW and was observed to be stable for more than 50 hours at this elevated power, as compared to our previous study[44]. The use of a polarization-maintaining fiber with a large intentional birefringence ($>1.7x10^{-4}$) allowed for higher pumping power and a broader spectrum without inducing the polarization dynamics that can degrade the SC generation[153]. Greater than 99.8% of the output SC power remained in the slow axis and resulted in a more usable power (429 mW) for the pulse shaper, which requires a polarized incident light for the desired control[11].

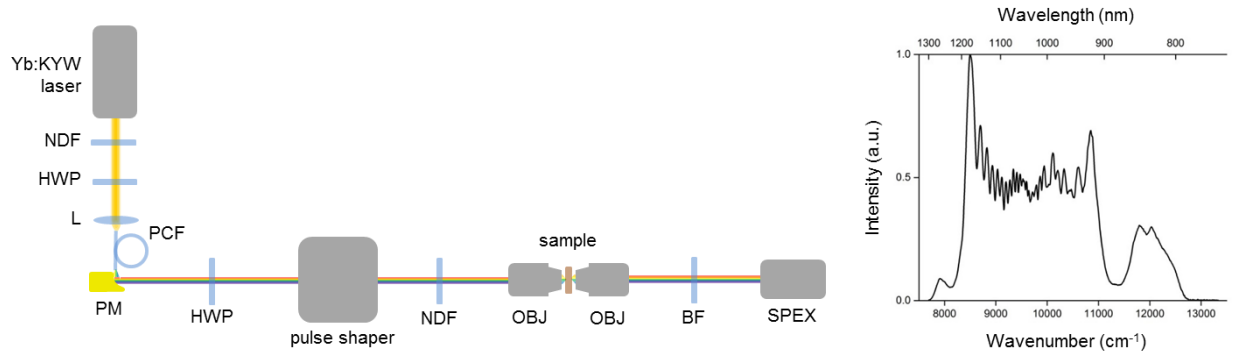

Fig. 4.21. Experimental setup (left) and the SC spectrum (right) for optimized single-beam CARS spectroscopy by amplitude shaping. BF: bandpass filter; HWP: half-wave plate; KYW: potassium yttrium tungstate; L: lens; NDF: neutral density filter; OBJ: objective; PCF: photonic crystal fiber; PM: parabolic mirror; SPEX: spectrometer; Yb: ytterbium.

The output SC spectrum [

Fig. 4.21(b)] spans the optical biological window from 780 to 1300 nm, which is attractive for biomedical applications[139]. The SC was guided into a pulse shaper (MIIPSBox 640, Biophotonics Solutions, Inc.) in which the spectrum below 900 nm was blocked at the Fourier plane of the shaper for detecting blue-shifted CARS signals below 900 nm [Fig. 4.22(a)]. The output from the pulse shaper was then guided into a near-infrared objective (LUMPlanFl/IR, 60xW, N.A. = 0.9, Olympus). The forward signal generated from the toluene sample was collected by another objective (LUMPlanFl, 40xW, N.A. = 0.8, Olympus) and sent into a home-built spectrometer equipped with an EMCCD (ProEM 1600, Princeton Instruments). Inside the spectrometer, a cylindrical lens was placed in front of the EMCCD to vertically distribute the CARS signal across 200 pixels on the camera so that the spectrometer can permit a higher input signal with an accumulated dynamic range.

For single-beam interferometric CARS spectroscopy, the shaper was used to introduce a $\pm\pi/2$ narrow-band phase shift close to the short-wavelength end of the main SC spectrum for retrieving the vibrational signature of samples from the modulation of the CARS spectra [Fig. 4.22(a-b)]. By subtracting the $-\pi/2$ spectrum from the $+\pi/2$ spectrum, the imaginary part of the third-order nonlinear susceptibility $\chi^{(3)}$, which corresponds to the spontaneous Raman spectrum, can be easily retrieved without any non-resonant background removal algorithm. Following our earlier modeling[44], the CARS spectra generated by the $\pm\pi/2$-phase pulses can be described as

$$S^{\pm}(\omega) = |P_{NR}(\omega)|^2 + |P_R(\omega)|^2 \mp 2|P_{NR}(\omega)||P_R(\omega)|\mathrm{Im}\{e^{i\phi(\omega)}\}. \tag{4.12}$$

The Raman-like spectrum can be retrieved by the difference spectrum between two measurements [Fig. 4.22(c)] given by

$$\mathrm{Im}\{\chi^{(3)}\} \propto \mathrm{Im}\{P_R(\omega)\} = |P_R(\omega)|\mathrm{Im}\{e^{i\phi(\omega)}\} \propto S^{-}(\omega) - S^{+}(\omega). \tag{4.13}$$

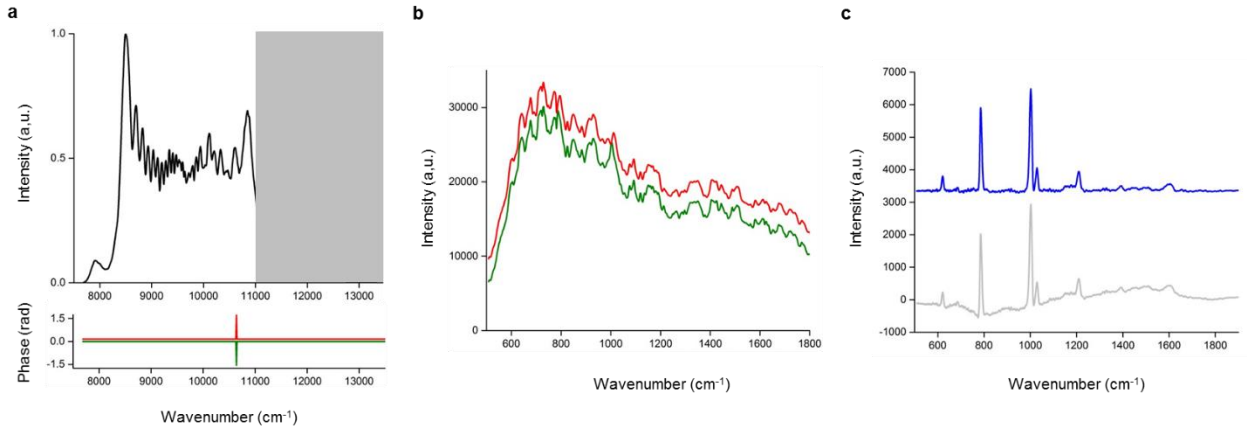

Fig. 4.22. Single-beam CARS spectroscopy using ±π/2 phase-shifted probe pulses. (a) The SC spectrum (top) and the ±π/2 phases applied (bottom). (b) The CARS spectra of ±π/2-phase pulses. (c) The difference spectra after (blue) and before (gray) baseline subtraction. The two phases in (a) and the spectra in (b) and (c) are offset for visualization.

Next, the feasibility of amplitude shaping to enhance the signal-to-background ratio was examined theoretically. The pulse shaper was utilized to adjust the relative power of the narrow-band probe pulse to that of the impulsive excitation pulse. As oftentimes there is an upper threshold of laser power to prevent sample damage, the aim here is to maximize the homodyne-amplified interference that contains resonant information, at a fixed amount of total optical power. Assuming the total incident SC power is *x*, the probe power is *y*, and the pump-and-Stokes power is *x* - *y*. The amplitudes of the pulses are proportional to the square roots of their optical powers,

$$\mathrm{E}_{p+s}(\omega) \propto \sqrt{x-y} \tag{4.14}$$

$$\mathrm{E}_{pr}(\omega) \propto \sqrt{y}\ . \tag{4.15}$$

The interference and non-resonant terms are then proportional to

$$2|P_{NR}(\omega)||P_R(\omega)|\mathrm{Im}\{e^{i\phi(\omega)}\} \propto (E_{p+s}^3)(E_{p+s}^2 E_{pr}) \propto [(x-y)^5 y]^{1/2} \tag{4.16}$$

$$|P_{NR}(\omega)|^2 \propto (E_{p+s}^6) \propto (x-y)^3 . \tag{4.17}$$

Taking the derivative with respect to *x*, one can find the maxima at $y = x/6$ for the interference term, or a probe power of 1/6th of the total power. Considering a broadband laser of 300 nm bandwidth and a narrow-band probe pulse with 1/300th of the total power, the optimally amplitude-shaped pulses will enhance the interference term by 4.52 fold and suppress the non-resonant background by 1.71 fold, with a 7.73-fold improvement of signal-to-background ratio from this analytical examination.

The numerical modeling is carried out with probe pulses with 1/300th, 1/60th, 1/6th of the total laser power, and with an incident laser spectrum as shown in Fig. 4.22(a). The simulated results of amplitude-shaped input spectra, the ±π/2-phase CARS spectra, and the difference spectra are shown in Fig. 4.23(a). Signal improvement and background suppression are observed when higher relative probe power is used. From 1/300th to 1/6th relative probe power, the interference signal is improved by 4.29 times while the non-resonant background is reduced by 1.70 times, with a 7.29-fold improvement of signal-to-background ratio, agreeing well with the analytical result.

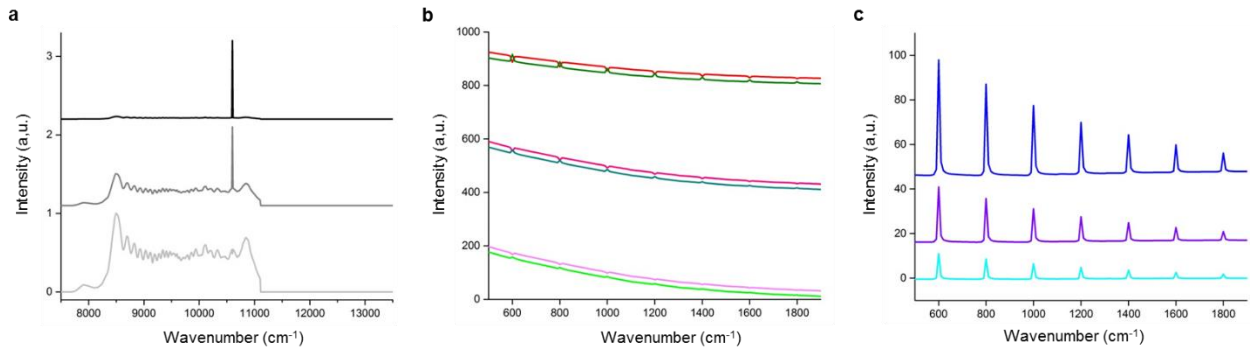

Fig. 4.23. Numerical modeling for amplitude-shaping enhanced single-beam CARS spectroscopy. (a) The SC spectra. (b) The CARS spectra of ±π/2-phase pulses. (c) The difference spectra. In all (a-c), the spectra from top-to-bottom are of probe pulses with 1/6th, 1/60th, and 1/300th of the total power. Spectra are offset for visualization.

Experimentally, the total power sent into the sample was maintained at 4 mW. This is the maximum power when using amplitude shaping to block the SC spectrum, except to fully transmit the narrow-band probe pulses. The amplitude shaping utilized the imperfection of the pulse shaper calibration, which resulted in ~1-5% leakage across the amplitude-shaped spectral range, to create a spectral shape that

resembles that in Fig. 4.24(a). This form of the spectrum possesses the highest relative probe pulse power of 1/60th of the total power. The integration time was 10 ms and 50 spectral acquisitions were averaged in each measurement. For two relative probe powers (unshaped: ~1/300th and shaped: 1/60th), the SC spectra, ±π/2-phase CARS spectra, and the difference spectra are shown. Using the high relative probe power of 1/60, the homodyne-amplified signals experienced an improvement of 2.4 fold, as compared to the unshaped spectrum. The ratio of homodyne-amplified signal to non-resonant background was negligible (1.05 fold). Currently, higher relative probe power is not possible due the 1-5% leakage in amplitude shaping mentioned earlier, and the SC power is limited to generate sufficient CARS signal at a high relative probe power. Despite these limitations, this experiment serves as a proof-of-concept demonstration of amplitude shaping to modify different contributions in single-beam interferometric CARS spectroscopy and to enhance the homodyne-amplified Raman-like spectrum.

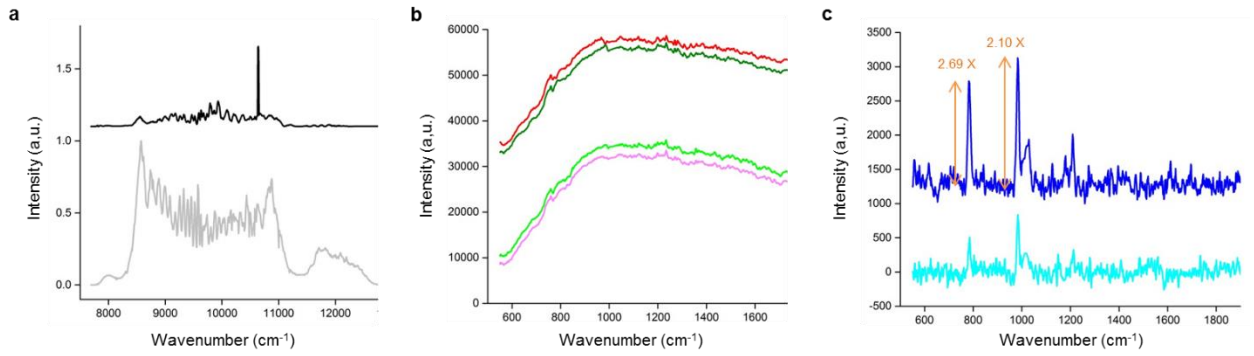

Fig. 4.24. Experimental results for amplitude-shaping enhanced single-beam CARS spectroscopy. (a) The SC spectra. (b) The CARS spectra of ±π/2-phase pulses. (c) The difference spectra. In all (a-c), the spectra on top are amplitude-shaped spectra while those at the bottom are original spectra. All the spectra are offset for visualization.

In conclusion, relative adjustments of the CARS signal and the non-resonant background is demonstrated in single-beam CARS spectroscopy by employing amplitude shaping to re-shape the incident laser spectrum. Analytical, numerical, and experimental results show enhancement of the homodyne-amplified signal by optimally distributing the probe and the impulsive excitation powers. The proposed method can provide higher signal-to-background and improve the applicability of single-beam CARS spectroscopy. If the vibrational resonance is strong enough or higher laser power is available, the CARS spectrum of -π/2 pulses can potentially reveal the Raman spectrum, $\mathrm{Im}\{\chi_R^{(3)}(\Omega)\}$, on top of the non-resonant background

directly, and one measurement will be sufficient for determining the vibrational signatures. The concept of amplitude shaping enhancement is not limited to single-beam CARS but can be applied to single-beam SRS as well[194].

5. LABEL-FREE MULTIMODAL MULTIPHOTON MOLECULAR IMAGING

In this chapter, the coherent fiber SC and the pulse shaping strategies are synergistically combined to establish a multimodal multiphoton imaging platform. 2PF, SHG, 3PF, THG, and hyperspectral CARS imaging were enabled by local compression and spectral focusing of the coherent SC pulses. Various biomolecules and structures are visualized and identified in cancerous and normal breast tissue from a human subject. The complimentary biochemical information of multiple modalities forms a multiphoton molecular profile *in situ*, facilitating investigation of biological samples in their native states.

5.1. Evolution of multimodal multiphoton imaging

Multimodal multiphoton imaging incorporates multiple nonlinear optical processes as contrast mechanisms to "see things in different light". The complimentary molecular visualization using different modalities offers a wealth of biochemical information and forms a more complete picture of the complex biological systems. Research efforts have been devoted to the development of multimodal imaging platforms to fulfill this aim. As each imaging modality demands specific laser pulse characteristics for optimal performance, accommodating all the desired techniques without compromise on each one is not trivial. Efficient and selective 2PF, SHG, 3PF, and THG imaging requires compressed femtosecond lasers covering multiple spectral ranges. High spectral resolution CARS (SRS) imaging typically utilizes two synchronized picosecond lasers with their frequency difference matched the molecular vibration. In addition, the complex multimodal signals occurring simultaneously upon ultrafast pulse illumination necessitates careful design of illumination and detection schemes to avoid excitation and emission cross-talk. Table 5.1 summarizes, to the best of our knowledge, some of the most important developments in multimodal multiphoton imaging. The purpose here is not to present an exhaustive list covering all the multimodal multiphoton platforms, but consider only the developments where more than three nonlinear

modalities are included, in addition to the linear imaging technologies. For more details regarding multimodal multiphoton imaging techniques, readers are referred to these reviews and the citations within[195-198].

Table 5.1. Developments of multimodal multiphoton imaging platforms.

Modalities	Laser source	Pulse processing	Applications	Features	Ref
2PF, SHG, 3PF, THG, SF-CARS	Yb:KYW (1040 nm, 220 fs, 80 MHz, 2.4 W) laser pumped PCF (to 780-1300 nm, 480 mW)	2PF/SHG/3PF/THG: compressed by shaper SF-CARS: chirped by glass and shaper	Human and rat mammary tissue and tumor	Fiber based, single source, customized pulse shape	This work
2PF, SHG, M-CARS	Fiber laser (770 nm, 3.4 ps, 40 MHz) + SC fiber laser (900-1350 nm, 16 fs, 40 MHz)	2PF/SHG: compressed by prism pair M-CARS: SC compressed by prism pair	Murine liver, pancreatic duct, brain tumor	Ultrabroadband M-CARS	61
2PF, SHG, SF-CARS	Ti:sapphire (660-970 nm, 5 fs, 80 MHz, 600 mW)	2PF/SHG: compressed by prism pair SF-CARS: chirped by glass	Mouse tail section	Single source	199
2PF, SHG, SFG, fs-CARS	Ti:sapphire (750~870 nm, 110 fs, 76 MHz, 3.5 W) + OPO x 2 (both to 915~1340 nm)	None	Mouse brainstem, skeletal muscle, hypodermis	High complexity	200
2PF, SHG, *OCT, *PV-CT	Ti:sapphire (690~1040 nm, 100 fs, 1.35 W) + *PCF (broadened to 90 nm bandwidth)	None	Bone-marrow-derived cells in mouse skin	None	201
2PF, SHG, THG, *FLIM	Ti:sapphire (690~1040, 100fs, 80 MHz, 1-3.5 W)	2PF/SHG/THG: compressed by built-in compressor in laser	Human mammary tissue, ovary tissue & tumor, onion, potato	None	202
2PF, SHG, ps-CARS	Yb fiber laser (1038 nm, 140 ps, 1 MHz) + CW Ti:sapphire (850~950 nm) + PCF (to 893~913 nm & 1205~1242 nm)	None	Atherosclerotic plaque deposition at a human artery wall	Fiber based, single source, CW seeded FOPA	72
2PF, SHG, THG	Yb fiber laser (1030 nm, 27 fs, 62 MHz, 50 mW)	2PF/SHG/THG: compressed by shaper	*Poecilia reticulata* tail, *Drosophila melanogaster* wings	Fiber based, single source	203
2PF, SHG, THG	Yb:KYW (1040 nm, 80 MHz, 220 fs, 2.4 W) pumped PCF (to 900-1160 nm, 360 mW)	2PF/SHG/THG: compressed by shaper	Porcine skin section	Fiber based, single source	154
SHG, THG, TSFG, M-ARS	Nd:YAG (1064 nm, 33 kHz) + PCF (to 1100-1600 nm)	None	Yeast cells	Broadband M-CARS	204
2PF, SHG, ps-CARS, *1PF	Ti:sapphire (825 nm, 3 ps, 76 MHz) + OPO (to 674 nm) + *multiple CW lasers	None	Basal cells carcinoma	None	205
SHG, THG, FWM	Er:fiber (1550 nm, 130 fs, 40 MHz, 9 nJ)	SHG/THG/FWM: compressed by prism pair	*C. elegans*	Special prism compressor design	206
2PF, SHG, ps-CARS	Ti:sapphire (700~1000 nm, 120 fs, 76 MHz) + OPO (1100~1600 nm)	None	Rat fibrotic liver tissue section	Spectral filtering for ps-CARS	207
2PF, SHG, THG, fs-CARS	Ti:sapphire (790 nm, 80 MHz, 3 W) + OPO (to 1290 & 2036 nm) + PPLN (to 1018 nm)	None	Rat liver tissue	None	208
2PF, SHG, fs-CARS	Ti:sapphire (780 nm, 140 fs, 80 MHz) + PCF	2PF/SHG/fs-CARS: compressed by prism pair	C. elegans	None	209
2PF, SHG, SF-CARS	Ti:sapphire (800 nm, 80 MHz, 550 mW) + PCF	2PF/SHG/SF-CARS: chirped by glass	Rabbit aorta section	None	127
2PF, SHG, SFG ps-CARS	Nd:Vanadate (1064 nm, 6 ps, 76 MHz) + OPO x 2 (both to 700~1000 nm)	None	Human mammary tumor	None	210
2PF, SHG, ps-CARS, *Raman	Nd:Vanadate (1064 nm, 7 ps, 76 MHz) + OPO + DPSS (532 nm)	None	Porcine skin	None	211
2PF, SHG, ps-CARS	Ti:sapphire (700~1000 nm, 2.5 ps, 78 MHz) x 2	None	Arterial walls and atherosclerotic lesions from Ossabaw pig	None	212
2PF, SHG, THG	Yb-doped (1028 nm, 200 fs, 50 MHz, 1 W)	None	*C. elegans*	Single source	213

Table 5.1. Developments of multimodal multiphoton imaging platforms (continued).

2PF, SHG, THG	Ti:sapphire + OPO	None	*D. melanogaster* embryos, A. thaliana seed, rat lung tissue	None	[22]
2PF, SHG, THG	Ti:sapphire (760~840 nm, 25 fs, 200 KHz~4 MHz, 120 mW) + Nd:glass (1064 nm, 150 fs, 94 MHz, 100 mW)	2PF: compressed by prism pair	Rat cardiomyocyte	None	[89]
2PF, SHG, 3PF	Ti:sapphire (750nm, 100 fs)	None	Various murine tissue, cortical and hippocampal tissue from AD patients, mouse mammary tumor and tissue	Single source	[21]
2PF, SHG, THG	Cr:forsterite (1230 nm, 120 fs, 150 mW)	None	Maize stem, rice leaf, *Commelina communis L.*	Single source	[65]

Abbreviations – (CARS) ps-CARS: picosecond CARS, fs-CARS: femtosecond CARS, M-CARS: multiplex CARS, SF-CARS: spectral focusing CARS; DPSS: diode-pump solid-state; FWM: four-wave mixing; PV-OCT: phase variance OCT; TSFG: third-order sum frequency generation. Symbols – "-": full spectral extent; "~": tunable spectral range; "*": (for) non-multiphoton modalities.

The pioneering work toward multimodal multiphoton imaging was initiated when 2PF, SHG, and 3PF were integrated by introducing additional detection channels on a Ti:sapphire laser based system[21,82]. However, 3PF is practically more difficult to apply due to its lower excitation efficiency. Adding THG is not as straight forward because of the demands in UV optics and detectors, and this third-order modality can be implemented more easily when shifting to a longer-wavelength excitation such as Yb-doped and Cr:forsterite lasers[22,65,89,202,213]. CARS and SRS need two different wavelengths of synchronized pulses, and can be achieved by using two Ti:sapphire lasers, by pumping OPO(s), or pumping a PCF with a solid-state laser, or by variations of these methods[127,200,204,205,207-212]. The two-beam setup in CARS and SRS provides two distinct spectral bands and serves as a versatile basis for multimodal imaging. It was then recognized in recent years that sources with broad spectral coverage combined with pulse processing, such as spectral filtering, pulse compression, and chirping, present an appealing solution to multimodal imaging[72,154,203,206]. An ideal ultrabroadband source should be one covering the wavelengths for all the modalities, especially for CARS and SRS, by either an ultrabroadband Ti:sapphire or by SC generation[189,199]. Modern evolution of PCF engineering and SC generation points to the promising use of Yb-pumped high-quality fiber SC spanning the optical biological window[139]. Flexible pulse shaping of such single fiber-based source enables selective and adaptive multimodal multiphoton imaging.

5.2. Multimodal multiphoton molecular imaging by shaping supercontinuum pulses

5.2.1. Flexible excitation and detection for multimodal multiphoton imaging

The coherent broadband SC and ultrafast pulse shaping enable customization of the excitation pulses for multimodal multiphoton imaging. In this section, local pulse compression and adaptive spectral focusing of the ultrabroadband SC pulses are integrated to perform high-quality 2PF, SHG, 3PF, THG, and hyperspectral CARS imaging of biological tissues. The experimental setup of this pulse shaping microscope is illustrated in Fig. 5.1.

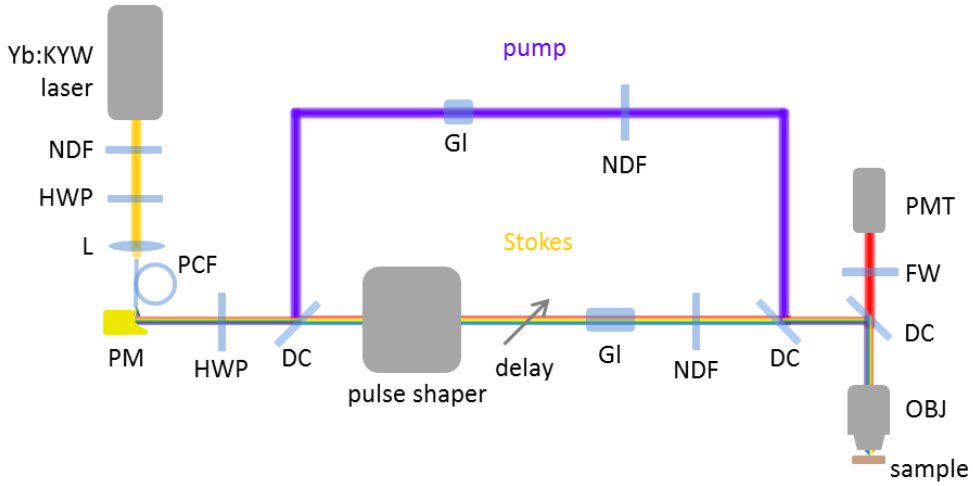

Fig. 5.1 Experimental setup of the pulse shaping microscope. DC: dichroic mirror; FW: filter wheel; Gl: glass; HWP: half-wave plate; KYW: potassium yttrium tungstate; L: lens; NDF: neutral density filter; OBJ: objective; PCF: photonic crystal fiber; PM: parabolic mirror; PMT: photomultiplier tube; Yb: ytterbium.

An Yb:KYW laser delivering pulses of 1041-nm central wavelength, 220-fs pulse width, and 80-MHz repetition rate (FemtoTRAIN IC, High Q Laser) was employed as the pump laser for coherent fiber SC generation. The laser power was adjusted by a neutral density filter, and coupled into a 21 cm polarization-maintaining ANDi fiber (NL-1050-NEG-1-PM, NKT Photonics) by an aspheric lens (C330TME-C, Thorlabs). The laser polarization was aligned by a half-wave plate to the slow axis. The output (input) coupling power was 480 (800) mW during all imaging sessions. The SC spectrum was recorded by an optical spectrum analyzer and observed to be stable for more than 40 hours of operation. The output SC was collimated by an off-axis parabolic mirror (Toptica Photonics) and guided into the

imaging system. The parabolic mirror alignment was optimized by observing the beam shape on a beam profiler (BGS-USB-SP620, Ophir-Spiricon) at a distance longer than the system beam path.

In the imaging system (Fig. 5.1), the wave-breaking (WB) band (780-880 nm) was reflected by a dichroic (DMLP900, Thorlabs) as the pump beam[44], and the main SC (900-1300 nm) was sent into a pulse shaper (MIIPSBox 640, Biophotonics Solutions, Inc.) as the Stokes beam. A tunable delay line was installed in the Stokes beam path for adjusting the temporal displacement between the two beams for spectral focusing CARS. Blocks of 3" and 4" SF57 glass were placed in the pump and Stokes beam paths, respectively, for pre-chirping the pulses. The two beams were recombined by another identical dichroic, guided into the microscope modified from a commercially available frame (BX61WI, Olympus), and focused by a super-apochromat objective (UPLSAPO 60xW/IR, N.A. = 1.20, Olympus). At the objective focus, the pulses were tailored for specific multiphoton modalities. Imaging was performed by raster scanning a piezoelectric stage (P-575.3R7, PI). The pixel dwell time was 200 μs for all imaging modalities, except that some 3PF images were acquired with 1 ms pixel dwell times to accommodate the weaker signal. All the multiphoton signals were collected in the backward (epi-) direction, passed through a filter wheel, and were detected by a photomultiplier tube (H7421-40 Hamamatsu).

Table 5.2 shows the excitation and detection wavelengths for multiphoton imaging in this study, along with the target molecules and the full powers used under the microscope objective. The excitation pulses were amplitude and phase shaped from the SC and paired with corresponding emission filters to target different endogenous molecules of interest. For 2PF, SHG, 3PF, and THG imaging, local pulse compression was employed to compress spectrally selected pulses for efficient multiphoton imaging of endogenous molecules and structures[154]. For 2PF imaging, 910-970 nm was used to target FAD, elastin, and retinol. For SHG and THG imaging, 1140-1200 nm was used to minimize 2PF signals and to also shift the emission to spectral ranges where the photomultiplier tube had higher quantum efficiency. SHG and THG were employed to image non-centrosymmetry (collagen) and optical heterogeneity (lipid, collagen, nerve, and microvesicles). For 3PF imaging, 1140-1200 nm (human) or 1080-1200 nm (rat) was

used to target NAD(P)H. The MIIPS-assisted pulse shaper was utilized to measure and to compress the selected bands to near the transform-limit (TL) at the microscope objective focus[128,143]. The pulse compression phase masks were recorded and applied in the imaging experiments. For CARS imaging, adaptive spectral focusing was employed to optimally chirp the SC pulses for targeting vibrations in the CH stretching region (2800-3200 cm^{-1}). The pump beam was the WB band of the SC from 780-880 nm, and the Stokes beam was spectrally filtered from the main SC to 1030-1215 nm. By monitoring the CARS spectrum of a polystyrene plate, an additional chirp of 4500 fs^2 was introduced onto the Stokes beam by the shaper for optimal performance of the spectral focusing, with a measured spectral resolution of 14 cm^{-1}. The optimal phase introduced was recorded and applied in the imaging sessions. The fiber SC provided more than sufficient power under the microscope objective for each imaging modality. For SHG imaging, the power was attenuated to 4.7 mW, and for CARS imaging in the CH-stretching region, the Stokes beam was attenuated to 8.7 mW.

Table 5.2. The excitation and the detection wavelengths, the target molecules, and the full excitation powers under the microscope objective for multimodal multiphoton imaging.

Modality	Excitation wavelength (nm)	Detection wavelength (nm)	Target molecules	Full power under objective (mW)
2PF	910 – 970	542 – 582	FAD, elastin, retinol	5.5
SHG	1140 – 1200	571 – 600	Collagen	10.0
3PF	1140 – 1200	417 – 477	NAD(P)H	16.6
THG	1140 – 1200 (human) 1080-1200 (rat)	381 – 399	Lipid, collagen, nerve, microvesicles	10.4
CARS CH-stretching	780 – 880 (pump) 1030-1215 (Stokes)	642 – 705	Lipid, protein, water	11.1 (pump) 21.0 (Stokes)
*CARS Vibrational silent	780 – 880 (pump) 935-1130 (Stokes)	593 – 705	Deuterium label	11.1 (pump) 23.6 (Stokes)

5.2.2. Multimodal multiphoton imaging and molecular profiles of human breast cancer

The human tissue used in this research was obtained under a protocol approved by the University of Illinois at Urbana-Champaign and Carle Foundation Hospital Institutional Review Boards. The samples were from a 52 year-old female patient diagnosed with infiltrating lobular carcinoma of 1.3 x 1.2 x 0.7 cm^3 and lobular carcinoma *in situ* on the right breast. After simple complete mastectomy of both breasts, excess cancerous tissue from the right breast and benign tissue from the left breast not used for diagnosis were stored in saline in conical tubes and placed in a cooler to be transported to the imaging

laboratory at the Beckman Institute. Thick sections (1-2 mm) of the tissue were removed from the tissue specimen using a razor blade, placed on a microscope slide, covered with a coverslip, and sealed to form an imaging chamber for multimodal imaging within 12 hours. After imaging, the sample was fixed in formalin for corresponding hematoxylin and eosin (H&E) stained histology.

Label-free multimodal multiphoton images and the H&E histology of the cancerous and normal human breast are shown in Fig. 5.3 and Fig. 5.4, respectively. 2PF, SHG, 3PF and THG images along with two CARS images at 2850 cm^{-1} and 3050 cm^{-1} are demonstrated in each image set. The CARS images at 2850 cm^{-1} and 3050 cm^{-1} are employed to map the lipid and the protein contents, respectively. The full hyperspectral CARS image data will be shown in Section 0. Two composite images (red/green/blue: CARS 3050 cm^{-1}/SHG/CARS 2850 cm^{-1}; cyan/magenta/yellow: 3PF/THG/2PF) are also shown in order to visualize the relative distribution of the biomolecular contents. Furthermore, a pseudo-histology image was generated by color-merging the six images (red/blue/gray/cyan/magenta/yellow: 2PF/ CARS 3050 cm^{-1}/CARS 2850 cm^{-1}/SHG/THG/3PF). The complimentary information from different modalities enables us to infer the molecular composition within the field-of-view *in situ*, that is, within the tissue slice.

In order to gain more insight from the cross-modality comparison, a visualization approach is proposed for correlating the multimodal signals, termed as the multiphoton molecular profile (MPMP), which is displayed on a hexagonal radar plot incorporating the intensities of the 6 images (2PF, SHG, 3PF, THG, CARS 2850 cm^{-1}, and CARS 3050 cm^{-1}) and a hyperspectral CARS spectrum (2700-3200 cm^{-1}). The design of the MPMP analysis is illustrated in Fig. 5.2. The correlation of the highly specific multiphoton signals reveals the lipid-protein transition, the optical structure, the metabolic activity, and the relationship between them. On the other hand, the CARS spectrum in the CH stretching region offers knowledge of the molecular vibrations, including CH_2 (2850 cm^{-1}), CH_3 (2930 cm^{-1}), =CH (3015 cm^{-1}), CH aromatic (3050 cm^{-1}), and OH stretching (>3200 cm^{-1}) signatures. The complimentary information contents enable us to further understand the BCa microenvironments and the relevant biochemical events.

The analysis and the interpretation are first demonstrated in this chapter, and will be utilized to identify multiphoton molecular biomarkers in rat mammary tumor development in Chapter 7.

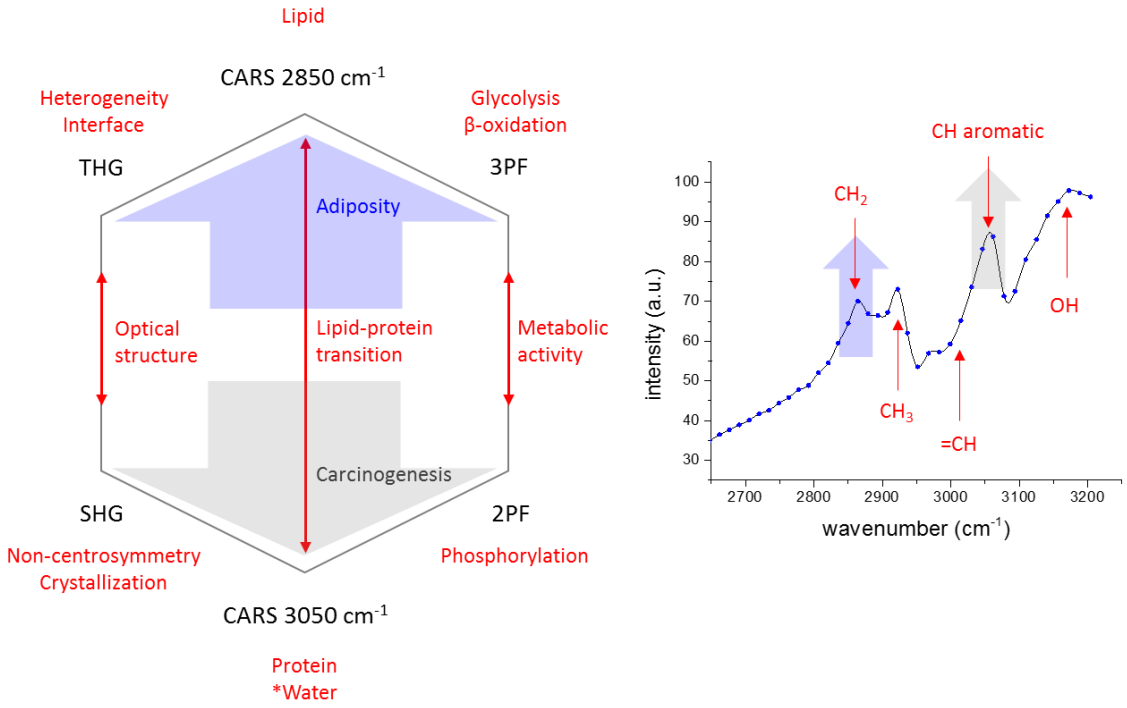

Fig. 5.2. Multiphoton molecular profile analysis. The hexagonal radar plot (left) shows the correlation of the multimodal multiphoton responses, including CARS 2850 cm^{-1}, 3PF, 2PF, CARS 3050 cm^{-1}, SHG, THG. The CARS spectrum (right) in the CH stretching region provides the molecular vibrational information.

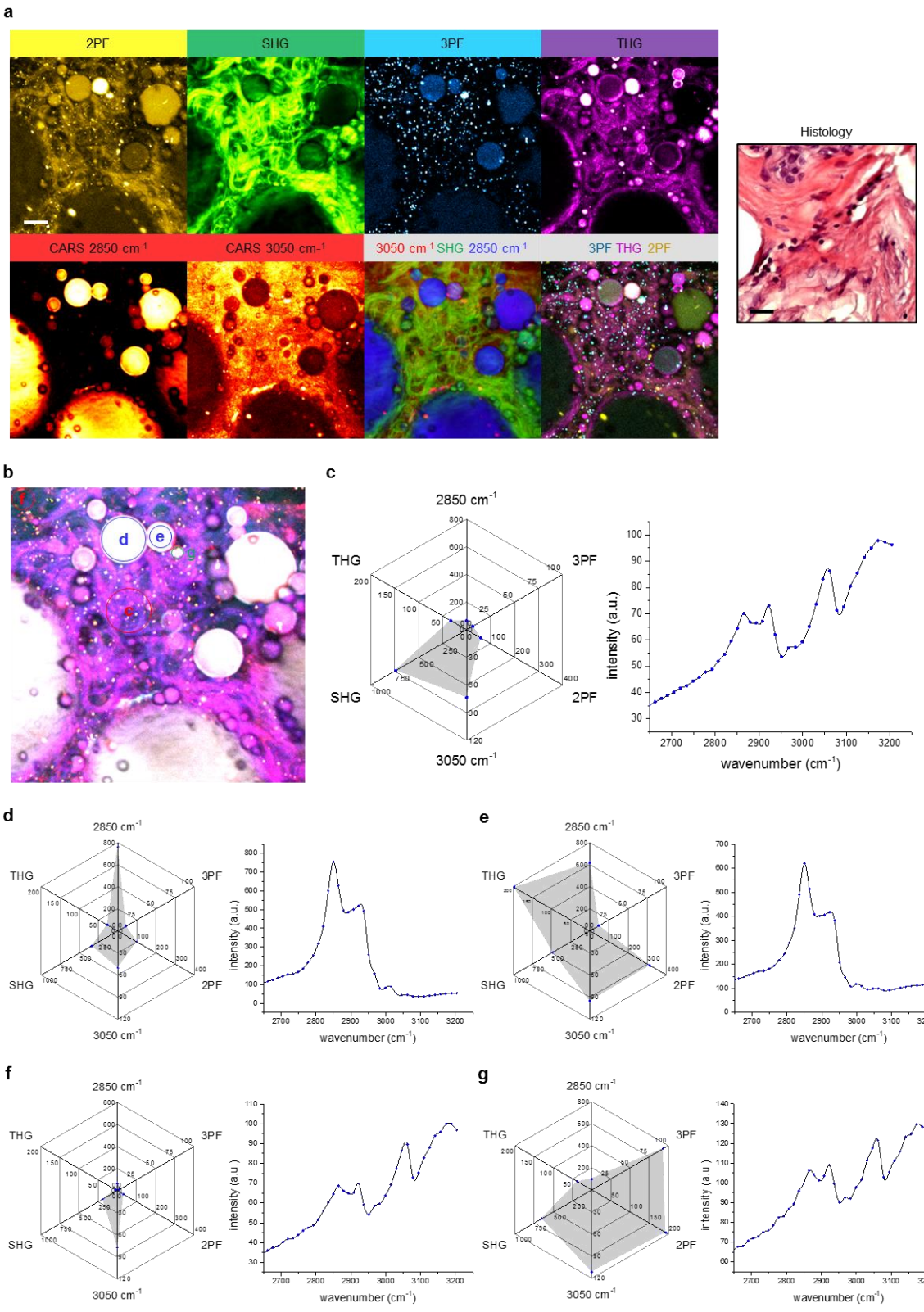

Fig. 5.3. Multimodal multiphoton molecular imaging of cancerous human breast tissue. (a) Multiphoton images and histology. (b) Pseudo-histology generated from the multimodal images. (c-g) Multiphoton molecular profiles of the selected regions in (b). Scale bar in (a): 25 µm.

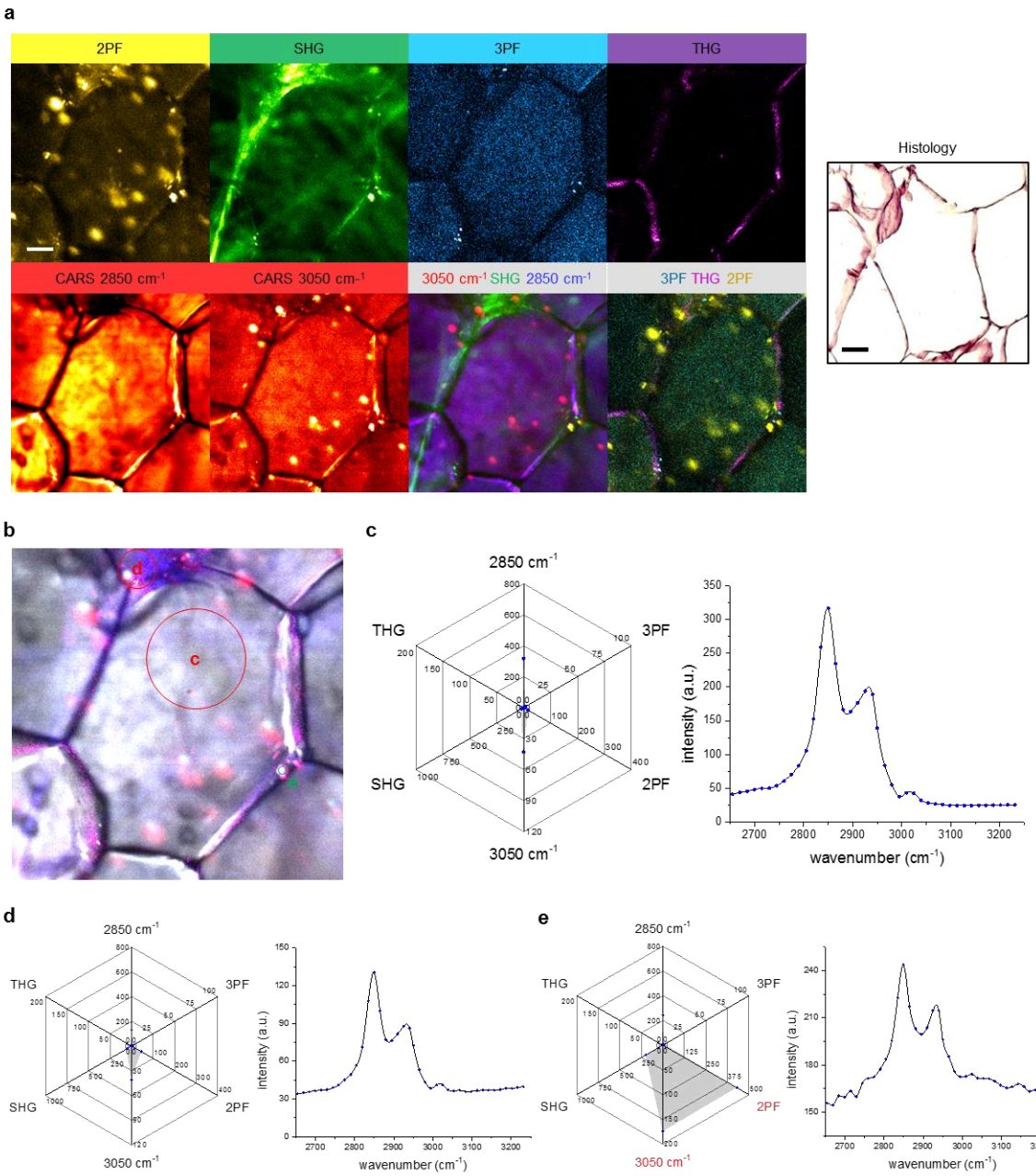

Fig. 5.4. Multimodal multiphoton molecular imaging of normal human breast tissue. (a) Multimodal images and histology. (b) Pseudo-histology generated from the multimodal images**.** (c-e) Multiphoton molecular profile of the selected regions in (b). Scale bar in (a): 25 µm.

In the cancerous tissue (Fig. 5.3), the 2PF image shows several morphological features, including the lipid-like circular objects of different sizes, small punctuate bright spots, and convoluted fiber-like structures. Comparing with the CARS 2850 cm^{-1} image, which is sensitive to the CH_2 stretching vibration, the circular objects can be identified as lipid droplets (LDs)[69,73,74]. The observation can be

further confirmed by the THG image, which is able to delineate the lipid boundaries[22]. However, in the 2PF, 3PF, and THG images, these LDs demonstrate different signal intensities, suggesting different biochemical compositions. The fluorescence of the bright spots at the longer-wavelength 2P excitation (910-970 nm) can originate from FAD or retinol in biological tissues[22,87]. Interestingly, various bright spots are also observable in the 3PF and THG images. Differentiating these microvesicles based on relative intensity of different modalities and their CARS spectra will be discussed in detail later (Fig. 5.5). The fiber-like structures in the 2PF image at this excitation wavelength are typically elastin fibers[22]. However, in comparison to SHG image, which enables mapping of collagen fibers, a large portion of this 2PF signature overlaps with the collagen fibers. The result suggests co-localization of 2P-excited fluorophores, FAD, retinol, or other fluorophores, with the collagen fibers. The SHG image also shows the irregular dense collagen fibers with intense SHG signal, which may be identified and classified as a tumor-associated collagen signature-1 (TACS-1)[214,215].

The 3PF imaging, with a fundamental wavelength of 1140-1200 nm, targeted the intrinsic fluorophore NAD(P)H[21,92,93]. Besides a seemingly different set of bright spots in the 3PF image, as compared to the 2PF and THG images, there is also weak 3PF signal inside some of the LDs[93]. The THG image provides an overall structural outline based on the optical heterogeneity that arises from lipid, protein, and water interfaces[4]. This imaging modality visualizes the LDs of different sizes and collagen organization, as well as another set of bright spots in comparison to the 2PF and 3PF images[22,75]. CARS 2850 cm^{-1} and CARS 3050 cm^{-1} offer two complimentary images of lipid and protein compositions using the CH_2 stretching and the CH aromatic stretching vibrations, respectively[59,69]. CARS 3200 cm^{-1} (data not shown), targeting the OH stretching vibration of water, demonstrated a similar image as CARS 3050 cm^{-1}, indicating co-localization of protein and water molecules[48].

The MPMPs of selected areas in the cancerous tissue and the normal tissue are shown in Fig. 5.3(c-g) and Fig. 5.4(c-e), respectively. Fig. 5.3(c) is the molecular profile of a tumor stromal area specified in Fig. 5.3(b). The strong SHG and CARS 3050 cm^{-1} signals in the radar plot indicate high collagen density

and high protein concentration, respectively. The CARS spectrum shows several protein vibrational features, including vibrations at 2930 cm^{-1} (CH_3 stretching) and 3050 cm^{-1} (CH aromatic stretching) and a plateau above 3200 cm^{-1} (OH stretching) from co-localized water molecules[6,59,69]. Note that the weak signals of CARS 2850 cm^{-1}, THG, and 3PF signal also show low lipid composition at this stromal site.

Fig. 5.3(d,e) show the molecular profiles of two LDs within the tumorous stroma displayed in Fig. 5.3(b). From their CARS spectra, one can observe the typical vibrational signatures of lipid with a major peak at 2850 cm^{-1} (CH_2 stretching) and a minor peak at 2930 cm^{-1} (CH_3 stretching)[6,69]. On the other hand, their radar plot representations differ considerably in that Fig. 5.3(e) has much stronger 2PF, CARS 3050 cm^{-1}, SHG, and THG signals than Fig. 5.3(d) does. Another interesting observation is that the MPMP of the larger LD at the bottom-left corner of the image (data not shown) resembles that of the normal breast tissue in Fig. 5.4(c), which has only one strong signal from CARS 2850 cm^{-1} in the radar plot and a lipid-like CARS spectrum[6,69]. These results can be useful to investigate and identify LDs of different chemical compositions. While the larger lipids still maintain similar biochemical composition as that of the normal tissue, the LDs of Fig. 5.3(d,e) are potentially experiencing some biochemical transformation to different states. The increase of 2PF intensity can result from up-regulation of FAD during tumor progression[214]. As SHG is sensitive to non-centrosymmetric structure, the increase of the SHG signal is likely from crystalline cholesterol (SHG)[77], but can also result from the collagen fibers at the lipid-stroma interface. The intense THG signal in Fig. 5.3(e) suggests that the focal plane is at the lipid boundary, which can be confirmed by the CARS 3050 cm^{-1} image in the same area showing no empty space like that in the other LDs. For the imaging plane in the proximity of the lipid-stroma interface, the backward signals from CARS 3050 cm^{-1}, SHG, and THG in the stroma and the backward-scattered forward-propagating photons combined together increase the signal levels of these coherent nonlinear processes.

Fig. 5.3(f) depicts the molecular profile of an area at the top-left corner in Fig. 5.3(b). The void in the 2PF, SHG, and THG images is similar to the large LDs, but the absence of signal in the CARS 2850 cm^{-1}

and the 3PF images deviates from the expected characteristics of the LDs. In the CARS 3050 cm^{-1} image, a higher signal suggests that the area is rich in protein and water content, which is confirmed by the CARS spectrum showing typical protein and water signatures[48,59]. Fig. 5.3(g) is of a small area demonstrating intense 3PF signal, as specified in Fig. 5.3(b). This area also shows strong 2PF, CARS 3050 cm^{-1}, and SHG signals. Hyperspectral CARS demonstrates a protein-like spectrum, suggesting a highly fluorescent protein in the tumor stromal area. From these observations, the molecular composition of the fluorescent materials is likely a mixture of NAD(P)H, FAD, and other non-lipid molecules with strong 2PF and 3PF signals.

In the multimodal multiphoton images of the normal breast tissue (Fig. 5.4), adipose tissue can be clearly identified in the CARS 2850 cm^{-1} image, and lipid boundaries outlined in the THG image confirms the lipid composition. Fig. 5.4(c) shows the MPMP of a LD area. The CARS spectrum demonstrates typical lipid signatures. On the other hand, the signals in the 2PF, SHG, 3PF, THG and CARS 3050 cm^{-1} images are low. In a more collagenous area [Fig. 5.4(d)], the MPMP shows a weak SHG response, which is due to the little collagen composition as can be confirmed by the histology. Fig. 5.4(e) shows a bright fluorescent spot with extreme 2PF and CARS 3050 cm^{-1} signals. However, the CARS spectrum demonstrates no peak at 3050 cm^{-1} and a lipid-like spectrum, indicating the high signal in CARS 3050 cm^{-1} is due to 2PF cross-talk.

At last, the various microvesicles observed in the 2PF, 3PF, and THG images in Fig. 5.3 are investigated. The three images were first processed through a two-dimensional fast Fourier transform filter with a passband of 2-8 pixels, and thresholded to retrieve the images containing only the bright point-like features. Points smaller than 1 pixel and larger than 30 pixels were further excluded to create the masks for computing MPMPs, as shown in Fig. 5.5(a). Image processing and visualization was performed using Matlab (Mathworks) and ImageJ (National Institutes of Health). The MPMPs calculated using the masks from the three modalities are shown in Fig. 5.5(b). By comparing the radar plots and the CARS spectra, the THG microvesicles can be identified as small LDs showing lipid signatures of high CARS 2850 cm^{-1}

and THG signals, as well as a lipid-like CARS spectrum with a major peak at 2850 cm^{-1} and a minor peak at 2930 cm^{-1} [6,22,69]. The higher SHG and CARS 3050 cm^{-1} signals indicate these small LDs are located within the stromal area rich in collagen and protein. The 2PF microvesicles show a weaker lipid-like spectrum but with an elevated baseline, suggesting reduced lipid composition and higher fluorescence background. The origin of the fluorescence background can be validated by the intense 2PF signal which highlights a strong fluorescence from these microvesicles that can also be excited by the pump and Stokes pulses. The lower lipid concentration is also reflected in the lower THG signal, as compared to the THG microvesicles. The high SHG and CARS 3050 cm^{-1} signals confirm the presence of the 2PF microvesicles in the stromal region. The high 2PF signal and the lipid-like CARS spectrum lead to the conclusion that the molecular composition is retinol, which is a lipid molecule with strong fluorescence upon longer-wavelength 2P excitation (910-970 nm)[22]. The fluorescence of abundant 3PF microvesicles are likely from NAD(P)H[21], based on the excitation (1140-1200 nm, corresponding to 3P excitation at 380-400 nm) and the detection wavelengths (417-477 nm) used[216]. The CARS spectrum of the 3PF microvesicles shows reduced composition of lipid and increased contribution from protein (3050 cm^{-1}) and water (3200 cm^{-1})[48,59]. Additionally, there are microvesicles showing strong signal in all 2PF, 3PF, and THG images. The radar plot of these points demonstrates moderate to high intensity in all six images. The 3PF and 2PF signals are particularly strong, which can originate from high NAD(P)H and FAD related to metabolic activities[93]. The spectrum demonstrates a feature between lipid and protein, as well as a high fluorescence background. The molecular composition of these microvesicles are likely a mixture of FAD, retinol, NADH and some other biomolecules.

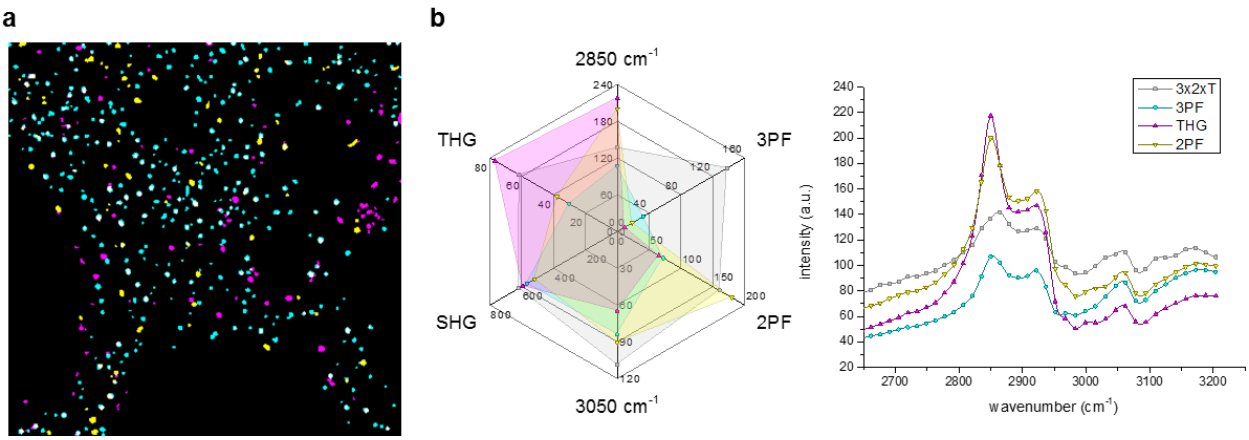

Fig. 5.5. Multimodal analysis of the microvesicles in cancerous human breast tissue images. (a) The identified microvesicles in 3PF (cyan), THG (magenta), 2PF (yellow), and intersection of three modalities (gray, 3x2xT). The multiphoton molecular profiles of the microvesicles.

To conclude this section, label-free multimodal multiphoton imaging visualizes various biomolecules and structures in cancerous and normal human breast tissue. MPMP enables correlation of complimentary molecular information in the nonlinear optical signals and the vibrational spectra to investigate the biochemical composition of the *in situ* tissue microenvironment. The technology can potentially serve as a label-free optical histopathology method for cancer diagnosis, real-time tumor margin detection, and cancer biomarker identification.

5.3. Remarks on multimodal multiphoton molecular imaging

5.3.1. Validation of nonlinear optical imaging modalities

To validate the nonlinear optical imaging modalities, power dependence test of each modality was performed by imaging cancerous and normal murine mammary tissue. Images (380 x 380 pixels, 0.5 x 0.5 μm^2/pixel) were acquired with different power levels, and the average photon counts were measured and plotted against the excitation powers measured before the microscope on double logarithmic scales [Fig. 5.6(a,b)]. The data were linearly fitted, and the calculated slopes are shown in the insets. The results approximate the theoretically predicted quadratic dependence of excitation powers in 2PF and SHG, the cubic dependence of excitation powers in 3PF and THG, and the quadratic and linear dependence in

pump and Stokes power, respectively, in CARS. The slight deviation from the theory can result from the diverse biomolecular composition and the low or saturated signal within the field-of-view.

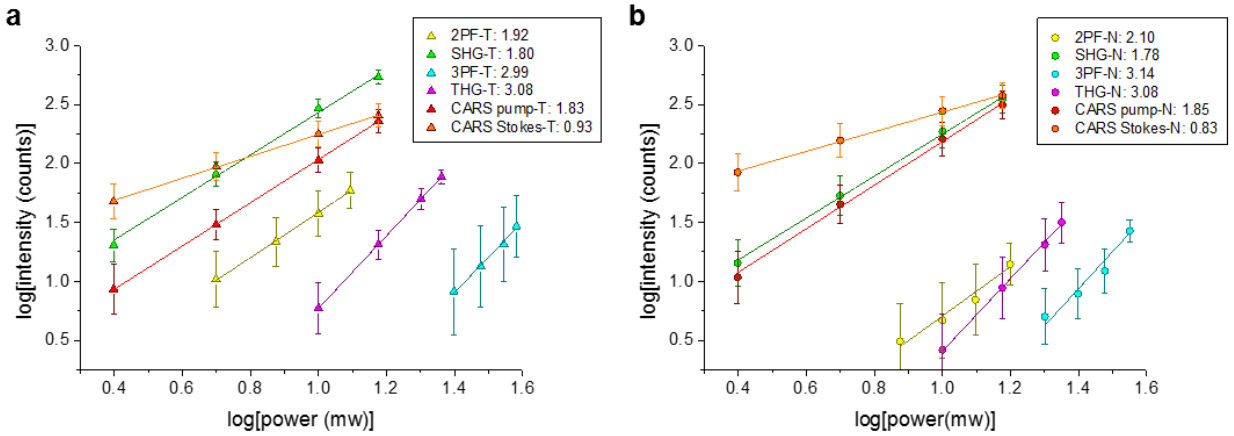

Fig. 5.6. Power dependence tests of the multiphoton modalities. Double logarithmic plots of the photon counts to the excitation powers for (a) tumor and (b) normal samples. Insets show the slopes calculated from linear fitting of the data. T: tumor; N: normal.

5.3.2. Three-dimensional imaging capability

One of the important advantages of multiphoton imaging is its three-dimensional imaging capability afforded by scanning the highly-localized nonlinear excitation[1,2,4,5,217]. Fig. 5.7 demonstrates depth-resolved imaging of rat mammary tissue with the multiphoton modalities used in this study. Representative sites were imaged from right beneath the surface to 120 µm deep into the tissue at a 20 µm step size. The depth resolving power is especially obvious by the striking difference between the 2PF images at depths of 60 µm and 80 µm, as well as the SHG images at depths of 40 µm and 60 µm. The morphological differences between these depths marks the layered structures in the samples, which can be easily interrogated by multiphoton imaging. Even at the depth of 120 µm, the signal is still more than sufficient to construct informative images, as a result of efficient signal generation by the tailored SC pulses. Currently, the imaging depth is limited by our scanning stage, but our results demonstrate that deeper imaging depth is feasible.

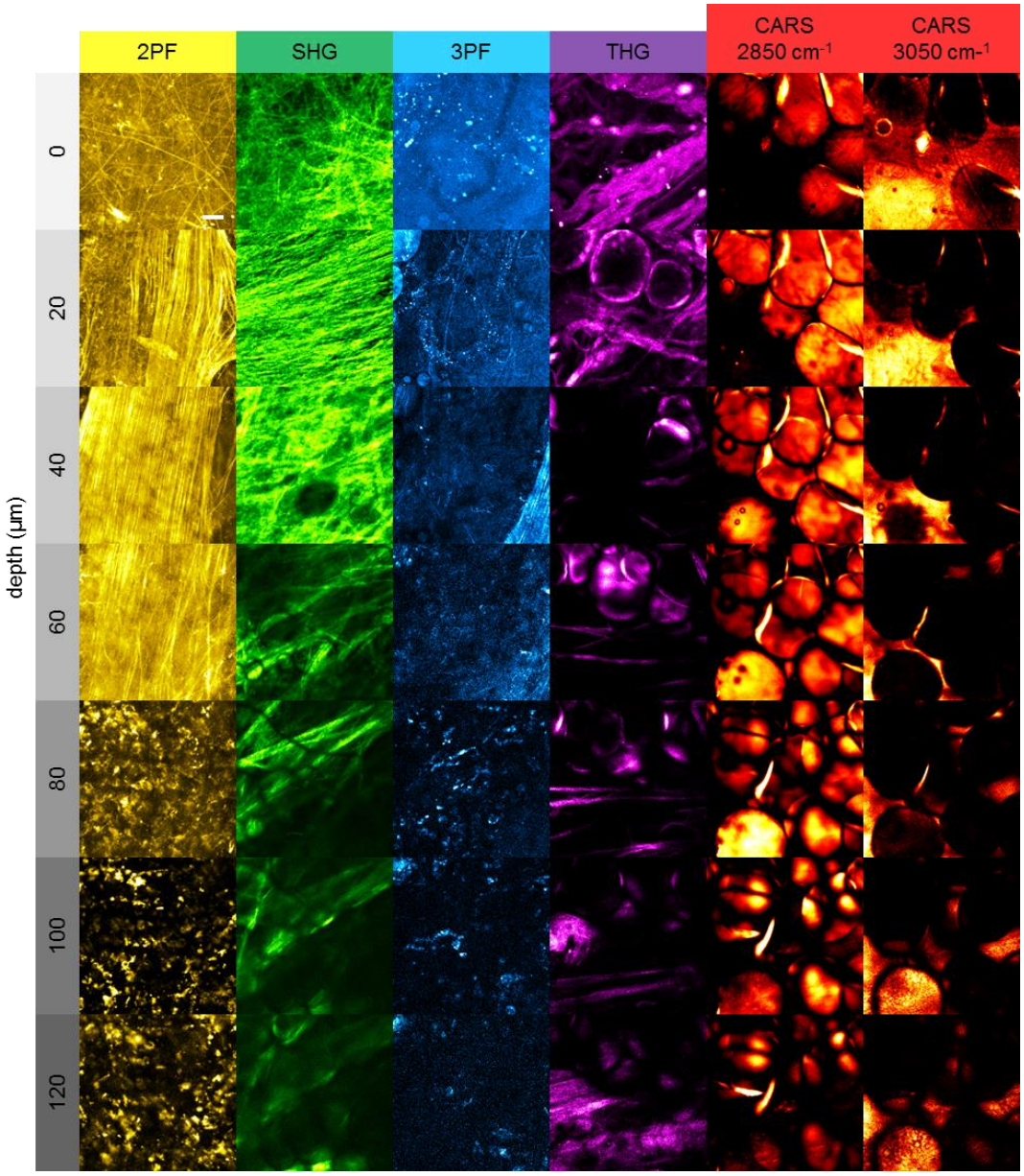

Fig. 5.7. Depth-resolved multimodal multiphoton imaging enhanced by the tailored SC pulses. In each modality, a representative area in rat mammary tissue was imaged from the surface (0 μm) to a depth of 120 μm in the sample. Scale bar: 25 μm.

To assess the effects of local pulse compression, the corresponding 2PF, SHG, 3PF, and THG imaging results using uncompressed pulses are shown in Fig. 5.8. The data demonstrate that local pulse compression effectively enhances the imaging contrast for multiphoton imaging in the highly dispersive system, confirming the results in Section 4.1.3. Particularly for 3PF and THG imaging, this enhancement elevates the signal level above the background noise. However, the improvement of penetration depth is not obvious within the current depth limit. With the uncompressed pulses, 2PF and SHG imaging can still

resolve the same morphological features at the 120 µm depth, but 3PF and THG imaging simply loses the image contrast. While the signal-to-noise ratio will keep decreasing with increased imaging depth, we anticipate that the imaging contrast enhancement by local pulse compression will increase the penetration depth in deeper tissue imaging.

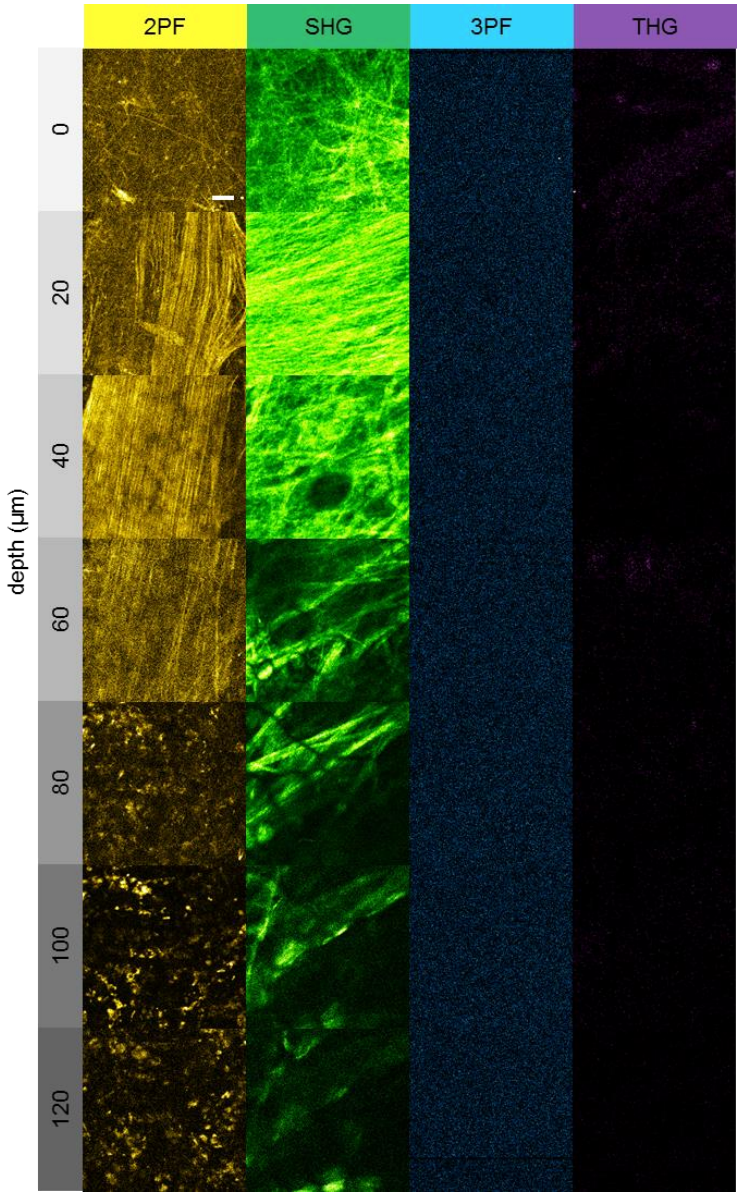

Fig. 5.8. Depth-resolved 2PF, SHG, 3PF, and SHG imaging using uncompressed SC pulses, for comparison to Fig. 5.7. The displayed dynamic ranges are adjusted to show the image contrast (2PF, SHG) or the background noise (3PF, SHG). If using the same dynamic ranges as in Fig. 5.7, all the features will not be visible, like those presented in Section 4.1.3. Note that the CARS imaging utilized chirped pulses in Fig. 5.7 already, so no corresponding comparison is available here. Scale bar: 25 µm.

5.3.3. Hyperspectral CARS imaging in the CH stretching region

In Section 5.2.2, the CARS images at 2850 cm^{-1} (CH_2 stretching) and 3050 cm^{-1} (CH aromatic stretching) are selected from the hyperspectral cube to represent the lipid and the protein contents, respectively. Here, the full spectroscopic imaging results from 2650 to 3200 cm^{-1} are demonstrated in order to provide a picture of the rich information within. Fig. 5.9 and Fig. 5.10 show the hyperspectral data of the cancerous and the normal human breast tissue, respectively. Note that other important vibrations in this frequency range include 2930 cm^{-1} (CH_3 stretching), 3015 cm^{-1} (=CH stretching) and 3200 cm^{-1} (OH stretching).

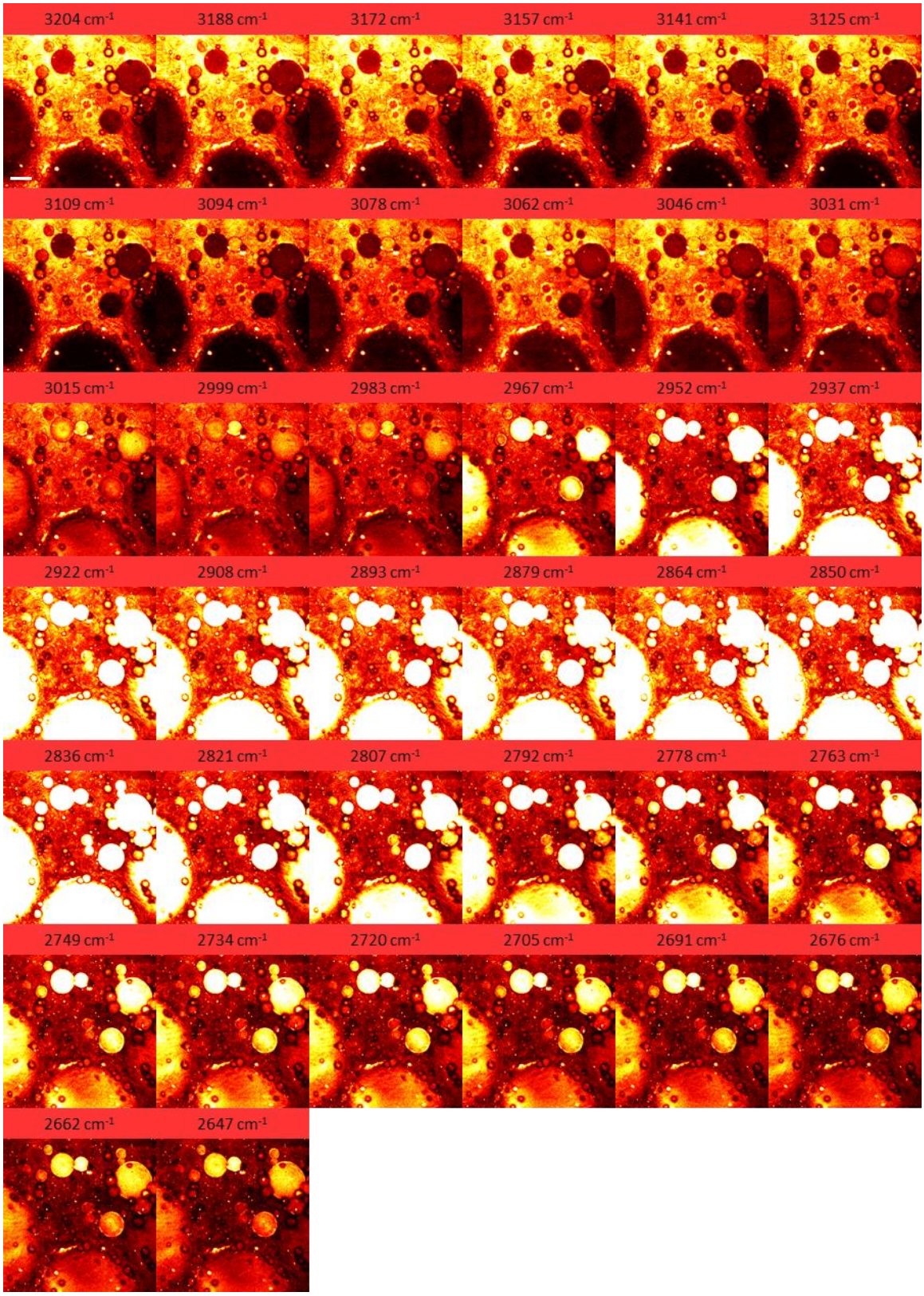

Fig. 5.9. The hyperspectral imaging data in 2650-3200 cm^{-1} of cancerous human breast tissue. Scale bar: 25 µm.

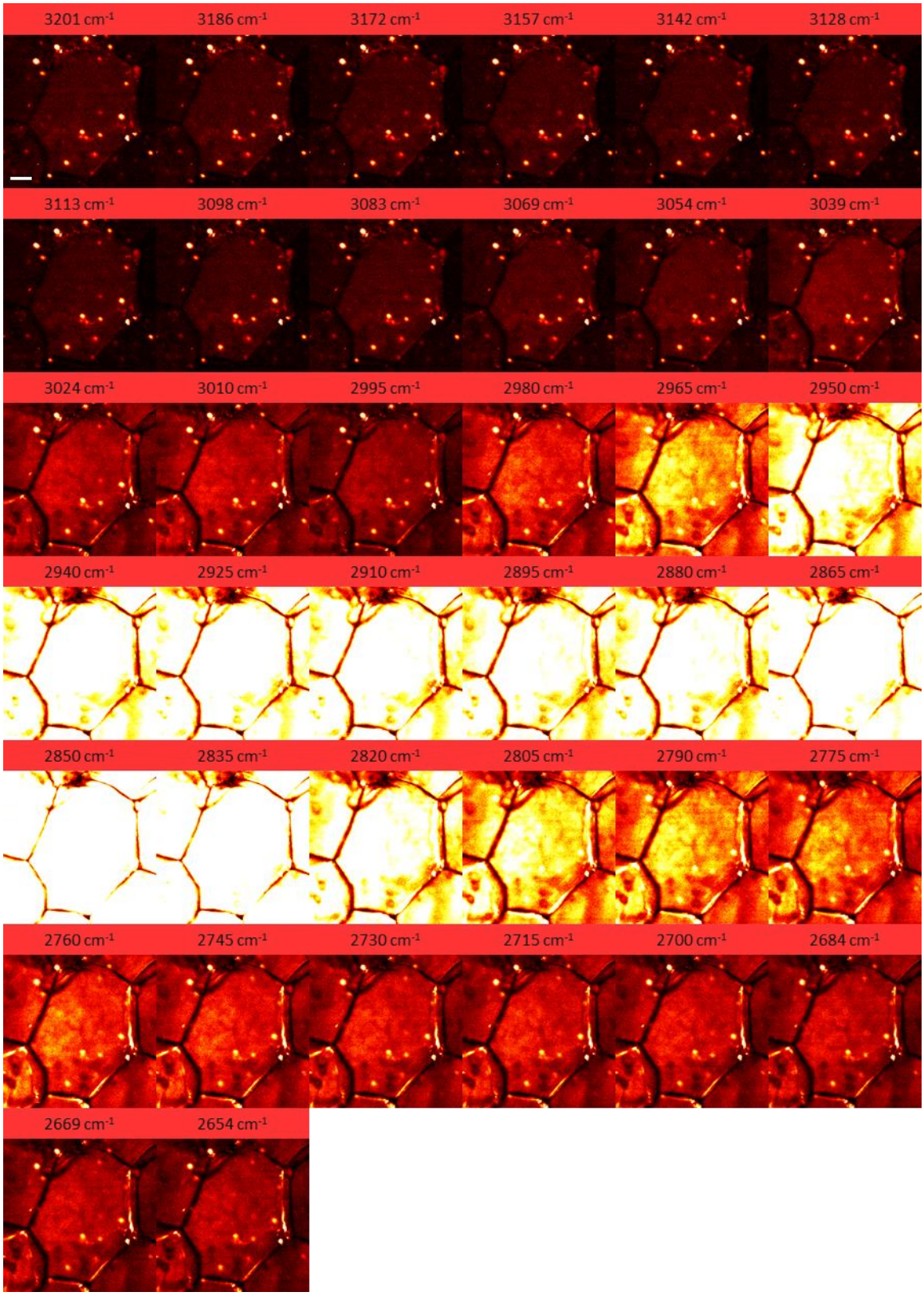

Fig. 5.10. The hyperspectral imaging data in 2650-3200 cm^{-1} of normal human breast tissue. Scale bar: 25 µm.

5.3.4. Extended excitation map by tailored supercontinuum pulses

The excitation-detection combinations used in the study are only a subset of a broader excitation-detection map that is possible with this system (Fig. 5.11). By flexibly pulse shaping the fiber SC of 780-1300 nm, one can explore shorter and longer 2PF and 3PF (2PF: 390-650 nm; 3PF: 260-433 nm), arbitrary SHG and THG (SHG: 390-650 nm; THG: 260-433 nm), and broadband CARS and SRS (<3500 cm^{-1}). Shorter- and longer-wavelength 2PF and 3PF would enable probing of a wider range of intrinsic fluorophores, especially those with the excitation peaks in the UV range[21,28]. Arbitrary SHG and THG spectral selection allows one to explore a broader frequency dependence of SHG and THG as well as sum or difference generation[204]. Broadband CARS and SRS offer vibrational imaging down to the vibrationally silent region and potentially to the fingerprint region[127,218]. The excitation-detection combinations can be customized for targeting diverse molecular species in different biological applications of interest, with push-button simplicity. The work presented here serves as a proof-of-concept and may have a broader impact in biomedical imaging and basic research.

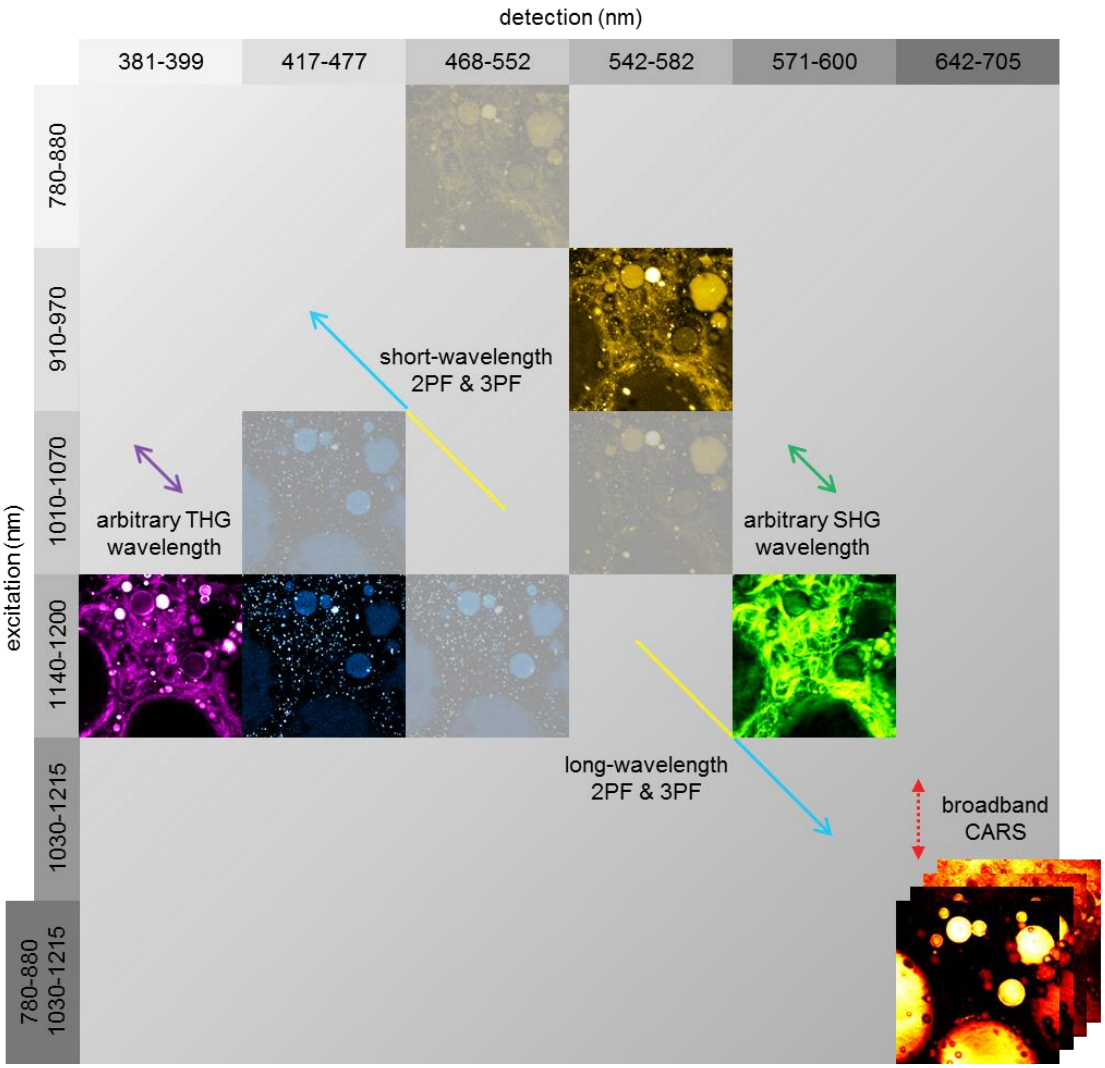

Fig. 5.11. The excitation-detection map of tailored SC pulses for multimodal multiphoton imaging. The bright images show the excitation and detection utilized in this study, while the dimmed images are not used. The arrows and the grey areas indicate the excitation-detection combinations that can be further explored.

6. MULTIPHOTON MOLECULAR IMAGING OF BREAST CANCER DEVELOPMENT

In this chapter, longitudinal breast cancer (BCa) development was investigated by using a carcinogen-induced rat mammary tumor model and the multimodal multiphoton imaging. The molecular and structural signatures revealed by multimodal multiphoton imaging are identified as biomarkers in early and late BCa development. The transformation of the biomarkers and the correlations between phenotypic behaviors offer direct insight into BCa development. Note that this research used a carcinogen-induced rat mammary tumor model as a pre-clinical model for human breast cancer. Throughout this thesis, and particularly in Chapters 6 and 7, the term "breast cancer" (BCa) will refer generally to both the pre-clinical rat mammary tumor model and clinical human breast cancer. Future studies will be required to elucidate the molecular differences that exist between humans and this pre-clinical rat model during carcinogenesis.

6.1. Nonlinear optical imaging in breast cancer research

As discussed in the previous chapters, the most powerful aspect of multiphoton imaging is the diverse molecular contrast that is fulfilled by the various nonlinear optical processes, in additional to the advantages of optical sectioning, deeper imaging penetration, reduced phototoxicity, and fast acquisition. Two-photon fluorescence (2PF) and three-photon fluorescence (3PF) microscopy enable imaging of endogenous fluorophores by using a near-infrared laser[1,2]. Second harmonic generation (SHG) and third harmonic generation (THG) imaging map optical non-centrosymmetry and heterogeneity derived from the second- and the third-order nonlinear susceptibilities of samples, respectively[3,4]. Coherent anti-Stokes Raman scattering (CARS) and stimulated Raman scattering (SRS) microscopy visualize the chemical distribution based on the intrinsic molecular vibrations[5,6].

In light of the molecular imaging capability, multiphoton microscopy has been applied to study the biomolecules in BCa microenvironments. Label-free 2PF and SHG imaging of cellular species and collagen fibers was previously demonstrated in mouse mammary tumor[21]. The regulation of intrinsic fluorophores, such as FAD and NAD(P)H, and the reorganization of collagen fibers in BCa were previously investigated using 2PF and SHG imaging[214,215]. Metabolism in breast epithelial and cancerous cells were probed by multiphoton fluorescence lifetime imaging and characterized by an optical redox ratio[219,220]. Examination of the functional roles of lipids in BCa was enabled by CARS microscopy[221,222], and highly sensitive BCa margin detection was realized by CARS spectroscopic imaging[19]. THG imaging is a technique sensitive to lipid boundary and microvesicles, but has found limited applications in BCa research[22]. New findings in BCa are continuously revealed by multiphoton imaging. Label-free molecular imaging combined with quantitative analysis offers complimentary information for BCa detection and diagnosis in parallel with conventional histopathology and biochemical assays[223-227]. While each multiphoton modality targets a specific subset of molecular species, these studies mainly focused on the biomolecules detectable by the specific optical setups. Understanding the complex relationship between biomolecules is often missing from cancer studies, and requires integration of multimodal data, such as what is demonstrated here, to more comprehensively investigate the BCa microenvironment.

In this study, a penta-modal imaging platform utilizing pulse shaping of a coherent fiber supercontinuum (SC) was employed, enabling 2PF, SHG, 3PF, THG, and hyperspectral CARS imaging. BCa development in a carcinogen-induced rat mammary tumor model was examined through a 9-week longitudinal study. Spatial distributions of various biomolecules and structures were visualized by label-free multimodal imaging, and the multiphoton molecular biomarkers during early and late tumor formation were identified. The multiphoton molecular profile (MPMP) analysis further provides biochemical insight into the molecules and the *in situ* microenvironments without any standard histological sample processing.

6.2. Animal procedures and imaging setup

6.2.1. Animal procedures

The animal experiments were conducted under a protocol approved by the University of Illinois at Urbana-Champaign Institutional Animal Care and Use Committee. A total of 18 female rats (F344, Harlan, 7-weeks old at the start) were included in the study, with 9 carcinogen-induced animals and 9 control animals. For the cancerous animal group, mammary tumors were induced by intraperitoneally injecting N-nitroso-N-methylurea (MNU, Sigma) at a concentration of 55 mg/kg[228,229]. For the control animal group, the same quantity of saline was injected to account of any effect caused by the injection. Two injections were used. The first injection was performed on the left abdominal side, followed by a second injection one week later on the right abdominal side. The MNU-induced rat mammary tumor is a well-established animal model in BCa research, for the pathological features, the hormone dependency, and the immunohistochemical response of the lesions mimic human ductal carcinoma *in situ* (DCIS)[230-234]. The dosage and the timing of MNU administration can be easily modified to control the carcinogenic process with a short latency[229,235]. Therefore, this model is particularly suitable for investigating the development of BCa. Recently, optical imaging technologies, such as optical coherent tomography (OCT) and nonlinear interferometric vibrational imaging (NIVI), have been utilized to identify the structural and molecular signatures in this BCa model, respectively, demonstrating the feasibility of using advanced optical methods as means for surgical guidance and cancer detection[19,236].

One tumor-induced animal and one control animal were sacrificed each week. The mammary glands were excised, transferred into a saline-filled Petri dish with lid, and stored in a refrigerator at 4℃ before the imaging experiments, which were conducted within 12 hours of resection. The tumor developmental status was determined by an experienced biologist (E.J.C.) during the surgery and categorized into 5 stages as (a) normal: white and thin mammary gland; (b) suspicious: slightly darker mammary gland as compared to normal tissue; (c) developing: tumor mass <1 mm in diameter, orange-color and rice-like

granular formation; (d) tumorous: tumor mass 1-3 mm in diameter, multiple granular features, (e) necrotic: tumor 3-10 mm in diameter, with necrosis core.

6.2.2. Imaging sites selection

In the early BCa experiment, no palpable tumor was identified on the abdominal side of the animal. The selection of imaging sites was determined in order to capture the onset of molecular changes in the carcinogen-induced animals. In weeks 1-3, only suspicious areas were found in the mammary glands, and the imaging sites were chosen within these suspicious areas, unless otherwise specified. In weeks 4 and 5, developing tumors were identified, and the imaging sites were selected at the center and at the margin of the tumors. One normal area in week 5 was also imaged for comparison. In the saline-injected animals, the imaging sites were chosen to approximately correspond to the same regions of the mammary glands where the tumors were found in the carcinogen-induced animals. For each animal, 3-5 sites were imaged, and representative data were collected.

In the late BCa experiment, palpable tumors were identified on the abdominal side of the carcinogen-induced animals. Developing tumor and necrotic areas were identified in the mammary glands. The imaging sites were chosen within, at the margin of, nearby (5 mm), and away from (>10 mm) the identified tumors. In the control animals, the imaging sites were selected to be approximately at the same regions of the mammary glands as in the tumor-bearing animals. For each animal, 3-5 sites were imaged, and representative results from each animal were collected. Table 6.1 (Table 6.2) summarizes throughout the early (late) BCa longitudinal study the status of the imaging sites, the distance away from the tumor(s), and the references to the figures in this chapter.

Table 6.1. Summary of the imaging sties in the early breast cancer longitudinal study.

Week	Cancer or control	Figure reference	Imaging site identification	Distance from imaging site	Multiphoton molecular profile	Note
Early breast cancer						
1	Cancer	Fig. 6.2(a)	Suspicious	OS		
		NS	Normal	OS		
		Fig. 6.2(b)	Suspicious	OS	Fig. 7.1	
		Fig. 6.2(c)	Suspicious	OS		
	Control	NS	Normal	OS		
		Fig. 6.2(d)	Normal	OS		
		Fig. 6.2(e)	Normal	OS		
2	Cancer	Fig. 6.3(a)	Normal	OS		
		Fig. 6.3(b)	Normal	OS		
		NS	Normal	OS		
		Fig. 6.3(c)	Normal	OS		
		Fig. 6.3(d)	Normal	OS	Fig. 7.2	
	Control	NS	Normal	OS		
		Fig. 6.3(e)	Normal	OS		
		Fig. 6.3(f)	Normal	OS		
		Fig. 6.3(g)	Normal	OS		
3	Cancer	Fig. 6.4(a)	Suspicious	OS		
		Fig. 6.4(b)	Suspicious	OS	Fig. 7.3	
		NS	Normal	OS		
		NS	Normal	OS		
		Fig. 6.4(c)	Normal	OS		
	Control	Fig. 6.4(d)	Normal	OS		
		Fig. 6.4(e)	Normal	OS		
		NS	Normal	OS		
		Fig. 6.4(f)	Normal	OS		
4	Cancer	Fig. 6.5(a)	Developing	OS		
		Fig. 6.5(b)	Developing	Margin		
		Fig. 6.5(c)	Developing	OS	Fig. 7.4	
		Fig. 6.5(d)	Developing	OS		
	Control	NS	Normal	OS		
		NS	Normal	OS		
		Fig. 6.5(e)	Normal	OS	Fig. 7.5	
5	Cancer	Fig. 6.6(a)	Developing	OS		
		Fig. 6.6(b)	Developing	Margin	Fig. 7.6	
		Fig. 6.6(c)	Normal	OS		
		Fig. 6.6(d)	Developing	OS		
	Control	NS	Normal	OS		
		Fig. 6.6(e)	Normal	OS		
		NS	Normal	OS		

Abbreviations: Cancer: carcinogen-induced animal; Control: saline-injected animal; NS: not selected; OS: on-site.

Table 6.2. Summary of the imaging sties in the late breast cancer longitudinal study.

Week	Cancer or control	Figure reference	Imaging site identification	Distance from imaging site	Multiphoton molecular profile	Note
Late breast cancer						
6	Cancer	Fig. 6.7(a)	Developing	OS		
		Fig. 6.7(b)	Developing	Margin	Fig. 7.7	
		Fig. 6.7(c)	Developing	5 mm away		
		Fig. 6.7(d)	Developing	5 mm away		
		Fig. 6.7(e)	Normal	>10 mm away		
	Control	Fig. 6.7(f)	Normal	OS		
		NS	Normal	OS		
		Fig. 6.7(g)	Developing	OS	Fig. 7.8	
7	Cancer	Fig. 6.8(a)	Developing	OS		
		Fig. 6.8(b)	Developing	OS	Fig. 7.9	
		NS	Normal	OS		
		Fig. 6.8(c)	Developing	Margin		
		Fig. 6.9	Developing	OS		Large area
	Control	Fig. 6.8(d)	Normal	OS		
		Fig. 6.8(e)	Suspicious	OS		
		Fig. 6.8(f)	Suspicious	OS		
		Fig. 6.10	Suspicious	OS		Large area
8	Cancer	Fig. 6.11(a)	Tumorous	5 mm away		
		Fig. 6.11(b)	Developing	Margin		
		Fig. 6.11(c)	Tumorous	OS	Fig. 7.10	
		Fig. 6.12	Developing	OS		Large area
		Fig. 6.13	Tumorous	Margin		Large area
	Control	NS	Normal	OS		
		Fig. 6.11(d)	Normal	OS		
		NS	Normal	OS		
		Fig. 6.14	Normal	OS		Large area
9	Cancer	Fig. 6.15(a)	Normal	OS		
		Fig. 6.15(b)	Necrotic	Margin		
		Fig. 6.15(c)	Necrotic	OS	Fig. 7.11	
		NS	Necrotic	OS		
		Fig. 6.16	Necrotic	Margin		Large area
		Fig. 6.17	Necrotic	OS		Large area
	Control	Fig. 6.15(d)	Normal	OS		
		NS	Normal	OS		
		Fig. 6.18	Normal	OS		Large area
		NS	Normal	OS		

Abbreviations: Cancer: carcinogen-induced animal; Control: saline-injected animal; NS: not selected; OS: on-site.

6.2.3. Imaging setup

The imaging setup for this study resembles that presented in Chapter 5. An Yb:KYW laser delivering pulses of 1041-nm central wavelength, 220-fs pulse width (FWHM), and 80-MHz repetition rate (FemtoTRAIN IC, High Q Laser) was employed as the pump laser for coherent fiber SC generation. The laser power was adjusted by a neutral density filter, and coupled into a 21-cm segment of polarization-maintaining ANDi fiber (NL-1050-NEG-1-PM, NKT Photonics) by an aspheric lens (C330TME-C, Thorlabs). The laser polarization was aligned by a half-wave plate to the slow axis of the fiber. The output (input) coupling power was maintained at 480 (800) mW during all imaging sessions. The output SC was

collimated by an off-axis parabolic mirror (Toptica Photonics) and guided into the imaging system. The alignment of the parabolic mirror was performed by optimizing the beam shape monitored by a beam profiler (BGS-USB-SP620, Ophir-Spiricon) placed at a distance longer than the system beam path.

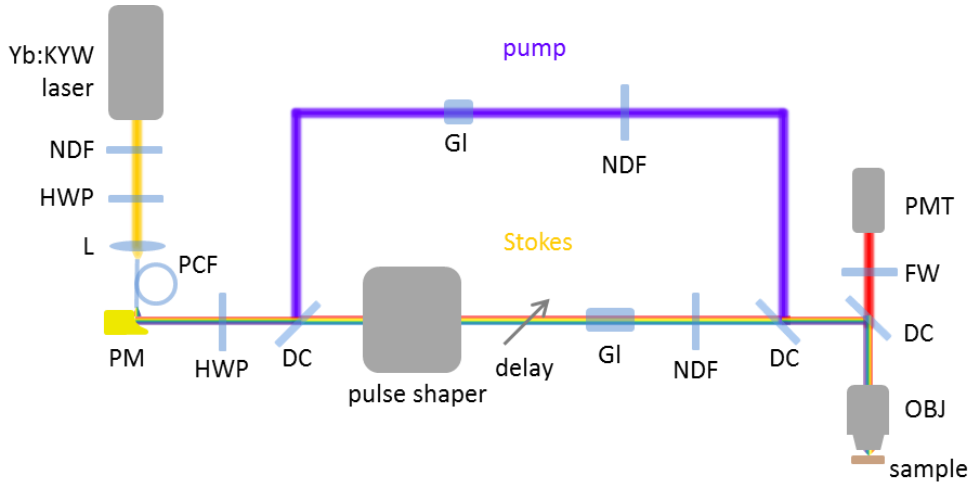

Fig. 6.1. Schematic of the imaging system. DC: dichroic mirror; FW: filter wheel; Gl: glass; HWP: half-wave plate; KYW: potassium yttrium tungstate; L: lens; NDF: neutral density filter; OBJ: objective; PCF: photonic crystal fiber; PM: parabolic mirror; PMT: photomultiplier tube; Yb: ytterbium.

In the imaging system, the wave-breaking band (780-880 nm) of the SC was reflected by a dichroic mirror (DMLP900, Thorlabs) as the pump beam, and the main SC (900-1300 nm) was sent into a pulse shaper (MIIPSBox 640, Biophotonics Solutions, Inc.) and used as the Stokes beam. A tunable delay line was installed in the Stokes beam path for adjusting the temporal displacement between two beams for spectral focusing CARS. Blocks of 3" (4") SF57 glass were placed in the pump (Stokes) beam for pre-chirping the pulses. The two beams were recombined by another identical dichroic, guided into the microscope modified from a commercially available frame (BX61WI, Olympus), and focused by a super-apochromat objective (UPLSAPO 60xW/IR, N.A. = 1.20, Olympus). At the objective focus, the pulses were tailored for specific multiphoton imaging modalities. Imaging was conducted by raster scanning a piezoelectric stage (P-575.3R7, PI). The pixel integration time was 200 µs for all the imaging modalities. Starting at week 6, an additional 3PF image was acquired with each imaging set using a 1 ms pixel integration time to accommodate the weak 3PF signal. All the multiphoton signals were collected in the

backward (epi-) direction, passed through a filter wheel, and detected by a photomultiplier tube (H7421-40, Hamamatsu).

6.2.4. Pulse processing

The excitation pulses were amplitude and phase shaped from the SC to target different endogenous molecules of interest. For 2PF, SHG, 3PF, and THG imaging, local pulse compression was employed to compress spectrally selected pulses for efficient multiphoton imaging. For 2PF imaging, 910-970 nm was used to target FAD and elastin. For SHG and THG imaging, 1140-1200 nm was used to minimize 2PF cross-talk and also to shift the emission to the spectral ranges where the photomultiplier tube offered a higher quantum efficiency. SHG and THG were employed to image non-centrosymmetry (collagen) and optical heterogeneity (lipid, collagen, nerve, and microvesicles), respectively. For 3PF imaging, 1140-1200 nm (week 1-5) or 1080-1200 nm (week 6-9) was used to target NAD(P)H. The MIIPS-assisted pulse shaper was utilized to measure and to compress the selected bands to near the transform-limit at the microscope objective focus[128,143]. The pulse compression phase masks were recorded and later applied in the imaging sessions. For CARS imaging, adaptive spectral focusing was utilized to optimally chirp the pulses for targeting vibrations in the CH stretching region. The Stokes beam was spectrally filtered to 1030-1215 nm. An additional chirp of 4500 fs^2 was introduced onto the Stokes beam by the shaper for optimal performance of spectral focusing, with a measured spectral resolution of 14 cm^{-1}. The full laser powers at the microscope objective focus were 5.5 (2PF), 10.0 (SHG), 16.6 (3PF), 10.4 (THG), 11.1 (pump), and 21.0 (Stokes) mW. For SHG imaging, the power was attenuated to 4.7 mW. For CARS imaging, the Stokes beam was attenuated to 8.7 mW.

6.2.5. Resolution of the imaging modalities

The resolution of the system can be analyzed from the fine features presented in the multimodal multiphoton images[170]. The microvesicles in the 2PF, 3PF, THG, and CARS images and the thin collagen fibers in the SHG image of Fig. 6.9 are analyzed. The five selected features in each modality are fitted by

a Gaussian function and the FWHMs are calculated. The minimal value of the five measurements represents the resolution of the modality. The lateral resolutions of 2PF, SHG, 3PF, THG, and CARS imaging are measured to be 0.83 ± 0.09, 1.05 ± 0.17, 0.70 ± 0.06, 0.82 ± 0.08, and 0.86 ± 0.13 μm, respectively.

6.2.6. Multiphoton molecular profile analysis

The multiphoton molecular profile (MPMP) analysis was described in Section 5.2.2. Briefly, a hexagonal radar plot is employed to display the raw photon counts of the 6 images (2PF, SHG, 3PF, THG, CARS 2850 cm^{-1}, CARS 3050 cm^{-1}) along with a hyperspectral CARS spectrum (2700-3200 cm-1). The radar plot enables visualization of the correlation of the multiphoton signals and provides insight into lipid-protein transformation (CARS 2850 cm^{-1}, CARS 3050 cm^{-1}), metabolic activities (2PF, 3PF), molecular structures (SHG, THG). The CARS spectrum offers molecular vibrational information to interrogate the chemical contents. The highly specific multiphoton signals and the CARS spectrum offer complimentary information for identifying the molecular compositions.

6.3. Multimodal multiphoton imaging of breast cancer development

The experimental results of the longitudinal study are presented in two sections. In Section 0, early BCa development in weeks 1-5 is presented and discussed. During weeks 1-5, the tumor formation was not palpable on the abdominal surface of the animals. In Section 6.3.2, late BCa development in weeks 6-9 is presented and discussed. During weeks 6-9, the tumor was palpable on the abdominal surface of the animals. For simplicity, CARS and the vibrational wavenumbers are abbreviated as Rxxxx, e.g. CARS at 2850 cm^{-1} is represented as R2850. To organize the large amounts of data for easy referencing, the imaging results of each week are presented first and followed by the description of the observations.

6.3.1. Multimodal imaging of early breast cancer development

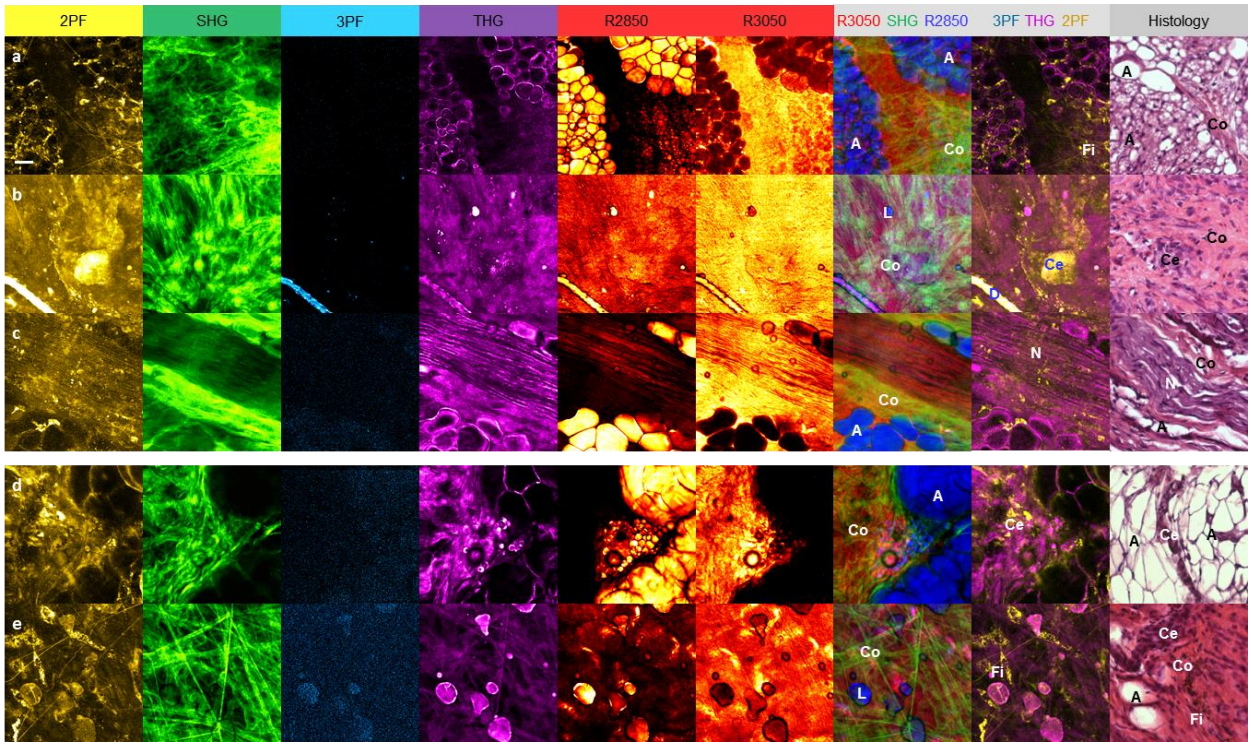

Fig. 6.2. Week 1 multimodal imaging of breast cancer development. (a-c) Carcinogen-induced experimental group. (d,e) Saline-injected control group. Morphological features: **A** adipose tissue, **Ce** hypercellularity, **Co** collagen fiber, **D** mammary duct, **Fi** fibroblasts, **L** altered lipid, **N** nerve. Scale bar: 25 µm.

In week 1, morphological changes can already be observed in the carcinogen-induced animal. Fig. 6.2(a) shows an area with collagenous tissue **Co** (SHG) separating two adipose domains **A** (R2850, THG). The lipid droplets (LDs) within the field of view (FOV) are smaller, especially for those at the bottom-right corner where dense collagen fibers and fibroblasts **Fi** (2PF) are identified. This cross-modality comparison indicates that the lipogenesis may be related to the activated fibroblasts and the deposition of collagen fibers. The histology demonstrates numerous small LDs **A** and nuclei, as well as some collagen fibers **Co** in the FOV. In Fig. 6.2(b), a prominent FAD-fluorescent cell cluster **Ce** (2PF) is surrounded by dense and granular collagen fibers **Co** (SHG) extending outward. Additionally, small LDs **L** (R2850, THG) are found in the proximity of the cell cluster. The increased cellularity and the small LDs are likely relevant to the initiation of BCa development. A mammary duct **D** is also observed at the bottom-left corner of the image[227], displaying high 2PF, 3PF, THG, and R2850 signals. The aggregation of dark-

staining nuclei **Ce** and the abundant fibrous tissue **Co** are validated by the histological comparison. Fig. 6.2(c) exhibits nerve bundles **N** (THG, R2850) surrounded by collagen fibers **Co** (SHG, THG) and an outer layer of adipose tissue **A** (R2850, THG). No abnormal feature is observed in this image set. The axon fibers **N**, the collagen fibers **Co**, and the adipocytes **A** can also be found in the histology.

In the saline-injected group, Fig. 6.2(d) displays a clear boundary between the collagenous tissue **Co** (SHG, THG) and the adipose tissue **A** (R2850, THG). In the movie of hyperspectral CARS imaging (data not shown), small LDs are observed to be moving in between these two tissue types. From these results, one can infer that this area is likely at the boundary of a lobule (left) and the surrounding adipose tissue (right). Note also that in the fibrous tissue, there are a few high-2PF cells **Ce**. However, the identical morphological features are not recognized in the H&E histology, which shows a higher density of cells **Ce** surrounded by the adipose tissue **A**. Fig. 6.2(e) exhibits a stromal region with straight collagen fibers **Co** (SHG) and some isolated LDs **L** (R2850, THG). The fibroblasts **Fi** (2PF) demonstrate typical spindle-shape morphology and highly fluorescent microvesicles in the cytoplasm. The histology shows a large amount of eosinophilic collagenous stroma **Co** and basophilic nuclei **Ce**, as well as several adipocytes **A**. Some of the cells with elongated nuclei are identified as fibroblasts **Fi**.

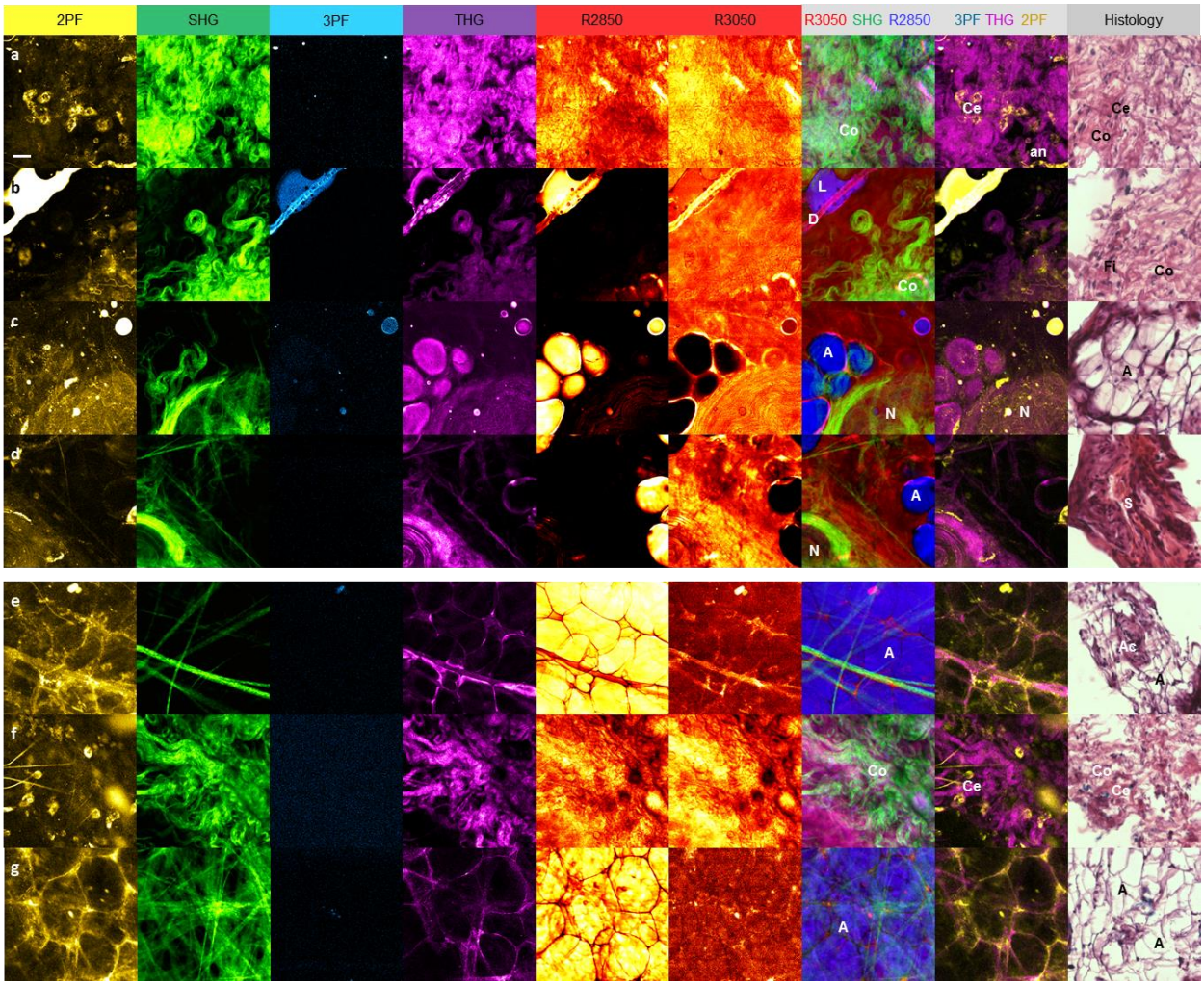

Fig. 6.3. Week 2 multimodal imaging of breast cancer development. (a-d) Carcinogen-induced experimental group. (e-g) Saline-injected control group. Morphological features: **A** adipose tissue, **Ac** acinus, **an** angiogenesis, **Ce** hypercellularity, **Co** collagen fiber, **D** mammary duct, **Fi** fibroblast, **L** altered lipid, **N** nerve, **S** stroma. Scale bar: 25 µm.

In week 2, a stromal area [Fig. 6.3(a)] with abundant collagen fibers **Co** (SHG, THG) shows aggregation of FAD-fluorescent cells (2PF), which exhibit a tumorigenic morphology of epithelial cells or fibroblasts[237]. A small duct-like structure **an** (2PF) is likely associated with angiogenesis, which will be confirmed by the results in later weeks 6-9. The histology also demonstrates curled collagen network **Co** and some nuclei **Ce** scattered in between. In Fig. 6.3(b), a mammary duct **D** (2PF, 3PF, THG, R2850, R3050) is found to be attached to an altered lipid domain **L** (R2850, THG) which demonstrates high 2PF and 3PF signals. The high 2PF and 3PF signals suggest that the change of lipid composition is related to the increase of FAD and NAD(P)H levels and therefore may be relevant to metabolic activities. At the bottom-right corner of the FOV, dense collagen fibers **Co** (SHG), elastin fibers (2PF), and FAD-

fluorescent cells (2PF) are found co-localized. These morphological features provided by 2PF and SHG imaging resemble those of fibrocystic tissue[223]. A higher density of fibroblasts **Fi** are found in the collagenous connective tissue **Co** in the histology. Fig. 6.3(c,d) show two regions with axon fibers **N** (THG, R2850) surrounded by epineurium collagen (SHG) and adipose tissue **A** (R2850, THG). No sign of tumor development is observed in Fig. 6.3(c,d). In the histology micrographs, Fig. 6.3(c) demonstrates mainly adipose tissue **A**, while Fig. 6.3(d) demonstrates mainly fibrous stroma **S** with a higher density of nuclei.

In the control animal, Fig. 6.3(e,g) are of typical adipose tissue filled with large LDs **A** (R2850, THG) and little connective tissue (SHG, R3050). The histology shows mainly adipose tissue **A**, and an acinus **Ac** is identified in Fig. 6.3(e). Fig. 6.3(f) represents a normal stromal region, in which the epithelial cells and fibroblasts **Ce** (2PF) are sparsely distributed as compared to Fig. 6.3(a). The same morphological features can be confirmed in the H&E histology.

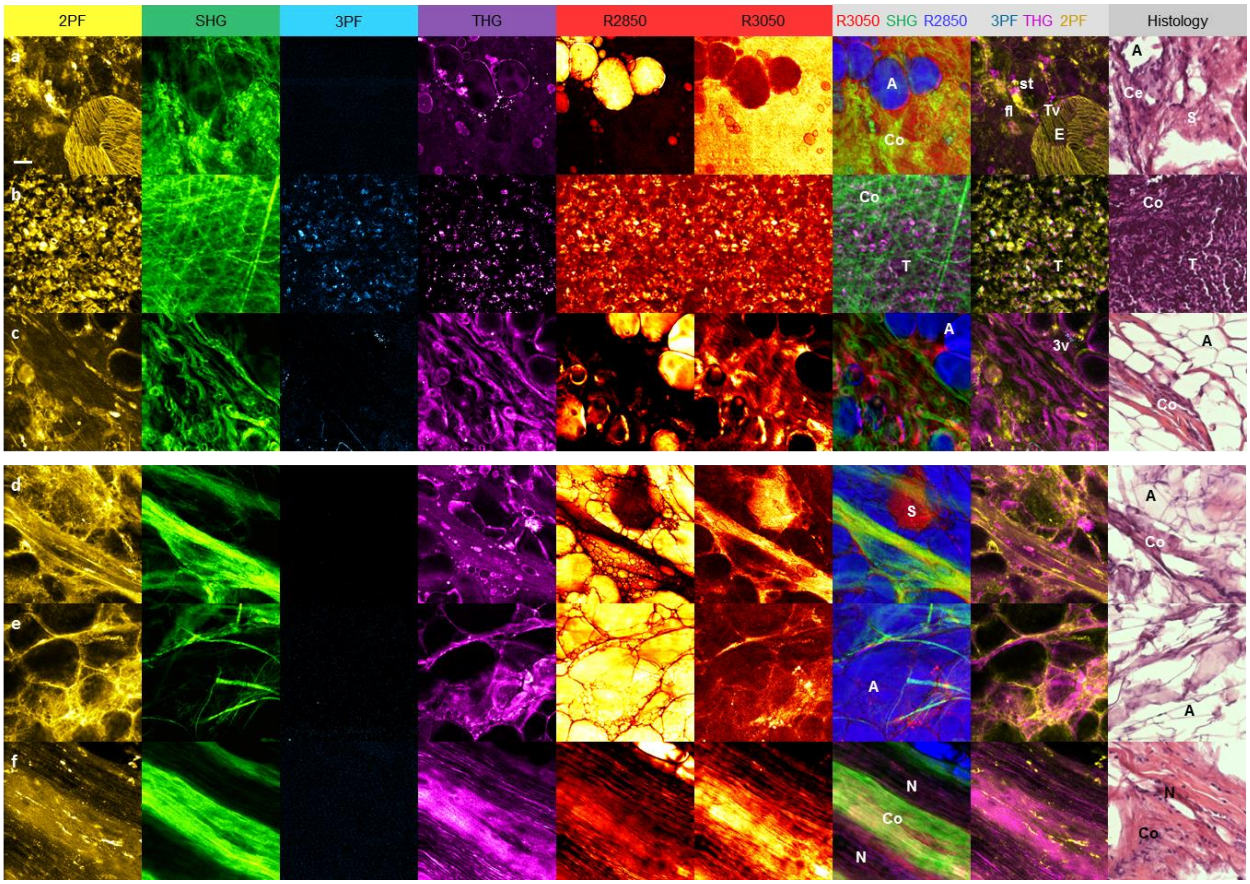

Fig. 6.4. Week 3 multimodal imaging of breast cancer development. (a-c) Carcinogen-induced experimental group. (d-f) Saline-injected control group. Morphological features: **A** adipose tissue, **Co** collagen fiber, **E** elastin fiber, **fl** fluorescent feature, **N** nerve, **S** stroma, **st** stellate structure, **T** tumor, **Tv** THG-sensitive microvesicle, **3v** 3PF-sensitive microvesicle. Scale bar: 25 µm.

In week 3, Fig. 6.4(a) shows a striking net-like structure **E** (2PF), which is attributed to elastin fibers[22]. The collagen **Co** (SHG) nearby demonstrates a granular morphology distinct from that of collagen type I, as well as a void located at the center of the elastin net. This finding suggests that the elastin fibers may be related to collagen remodeling. At the periphery of the adipose tissue **A** (R2850, THG), highly-2PF substances **fl** and high-THG stellate structures **st** are found next to each other. The stellate structures can also be observed in the R2850 and the R3050 images. In addition, there are THG-sensitive microvesicles **Tv** in between the LDs and the elastin net. These THG-sensitive microvesicles are not visible in the R2850 image, indicating their non-lipid nature. This image set reveals the complex co-occurring processes of lipid, collagen, elastin, cells, and microvesicles in the microenvironment. In the histology, the stromal area **S** shows eosinophilic connective tissue with relatively low density of cells. In the

surrounding of the adipose tissue **A**, an increase of cellularity **Ce** is marked with higher density of nuclei, confirming relevance of the lipid degradation to the tumorigenesis.

The imaging site in Fig. 6.4(b) shows a large amount of highly fluorescent cells **T** (2PF, 3PF) in a random and unpolarized arrangement. The collagen fibers are observed to be thinner and to have lower SHG intensity as compared to those in the normal tissue. Based on these results, these highly fluorescent cells are suggestive of tumorous cells forming a tumor nest. The observation is validated by the histological micrograph, in which the dark-staining nuclei are ubiquitous in the tumor **T**, and only little connective tissue is found in this area. In the THG image, the microvesicles resembling those observed in Fig. 6.4(a) are recognized, and these microvesicles are co-localized with or nearby the cellular fluorescence. The imaging data suggest that the THG-sensitive microvesicles are relevant to tumor formation[75]. Fig. 6.4(c) displays a lipid-stroma interface in a normal area. Interestingly, some 3PF-sensitive microvesicles **3v** can be visualized in the surrounding of the adipose tissue **A** (R2850, THG). The histology demonstrates the adipose tissue **A** and some fibrous connective tissue in the FOV.

In the control animal, the R3050 image in Fig. 6.4(d) maps the non-collagenous stromal **S** with weak 2PF signal within adipose tissue. The histology shows similar morphological features as compared to the multiphoton images. Fig. 6.4(e) displays a normal adipose domain with large LDs **A** (R2850, THG) and little fibrous tissue. The histology demonstrates mostly adipose tissue **A** with some thin sheets of connective tissue. Fig. 6.4(f) shows the nerve fibers **N** (THG, R2850) and the surrounding collagen fibers **Co** (SHG) in the normal mammary gland. The wavy axons and the collagen fibers are also found in the H&E micrograph.

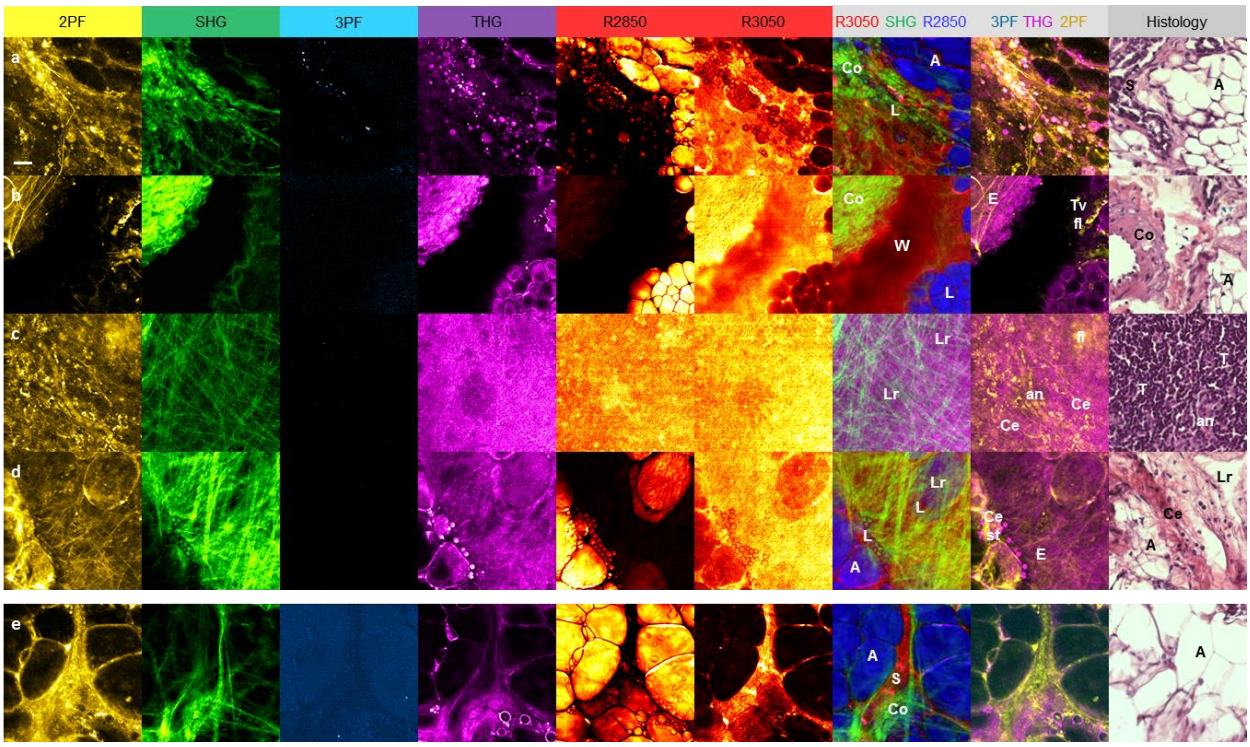

Fig. 6.5. Week 4 multimodal imaging of breast cancer development. (a-d) Carcinogen-induced experimental group. (e) Saline-injected control group. Morphological features: **A** adipose tissue, **Ce** hypercellularity, **Co** collagen fiber, **E** elastin fiber, **fl** fluorescent feature, **L** altered lipid, **Lr** lipid residual, **S** stroma, **st** stellate structure, **T** tumor, **Tv** THG-sensitive microvesicle, **W** water. Scale bar: 25 µm.

In week 4, a lipid-stroma interface [Fig. 6.4(a)] exhibits a large quantity of smaller LDs **L** (R2850, THG), which are likely the lipid vesicles secreted by the adipose tissue **A** (R2850, THG). Interestingly, not all of these "droplets" in the R2850 image can be identified in the THG and the 2PF images and vice versa, indicating different molecular compositions of these droplets. However, their coexistence suggests a close relationship between them. In the surrounding area, the collagen fibers **Co** (SHG) demonstrate a dense and granular morphology. In the histology, the stromal area **S** demonstrates many dark-staining and enlarged nuclei, as well as many empty spaces that are likely small LDs before histological processing. In Fig. 6.5(b), highly dense collagen fibers **Co** (SHG, THG) form a fibrotic cluster along with elastin fibers (2PF). The histology shows a glandular structure with surrounding dense connective tissue. An empty surrounding area **W** (R3050) is filled with water. From these observations, the FOV is identified as a fibrocystic area[223]. The LDs **L** (R2850, THG) at the bottom-right corner are smaller as compared to those in the normal adipose tissue. The LDs are also observed in the H&E histology. Some of the lipid

microvesicles (R2850) and the THG-sensitive microvesicles **Tv** are present at the periphery of the LDs. At the same location, a high-2PF feature **fl** is observed. The co-occurrence of the lipid microvesicles, THG-sensitive microvesicles, and strong 2PF fluorescence is similar to the observations in Fig. 6.5(a) and Fig. 6.4(a).

In Fig. 6.5(c), a prominent developing blood vessel **an** (2PF) is surrounded by elastin fibers (2PF) and high-2PF cells, which are likely tumor cells or endothelial cells responsible for angiogenesis. The weaker SHG signal and the mesh-like morphology of the collagen fibers are indicative of collagen type V composition in the tumor[226]. A high density of tumorous cells **T** are found in the histology, and the angiogenic site **an** can be recognize by red-staining erythrocytes and the connective tissue in the surrounding. The THG image displays high spatial-frequency features, suggesting high optical heterogeneity as a results of molecular heterogeneity. The THG image also reveals two darker areas at the center and the top-right corners. At the corresponding locations in the R2850 and the R3050 images, these regions demonstrate high and low signals, respectively. The cross-modality comparison points out that these two locations are likely to be two LDs. However, only a small amount of lipid composition **Lr** (R2850) remains. The center site is replaced by a growing blood vessel, and the top-right site exhibits moderate 2PF signal. These findings relate lipolysis to the generation of the high-2PF molecules, increased cellularity, and angiogenesis in BCa development. Nevertheless, no obvious feature of lipid can be observed in the H&E histology.

In Fig. 6.5(d), adipose tissue **A**, smaller LDs and altered lipid **L**, and lipid residuals **Lr** (R2850, THG) are recognized in the FOV. Several stellate structures **st** (THG) are identified at the periphery of the larger LDs. A high-2PF cell cluster is found near the stellate structures, and the boundaries of the larger LDs also show strong 2PF signal. In addition, elastin fibers **E** (2PF) radiating outward from these LDs are observed. These features are similar to those in Fig. 6.4(a) and Fig. 6.5(a,b). The histology demonstrates denser connective tissue and nuclei **Ce** at the periphery of the adipose tissue **A**. Within the connective

tissue, there are also some empty areas that correspond to lipid residuals **Lr** observed in the multiphoton images.

In the control group, Fig. 6.5(e) exhibits an area of typical normal mammary gland with a large proportion of adipose tissue **A** (R2850, THG) as well as the collagenous **Co** (SHG, THG) and non-collagenous **S** (R3050, 2PF) stromal tissue in between. The histology shows mainly adipocytes **A** and little connective tissue.

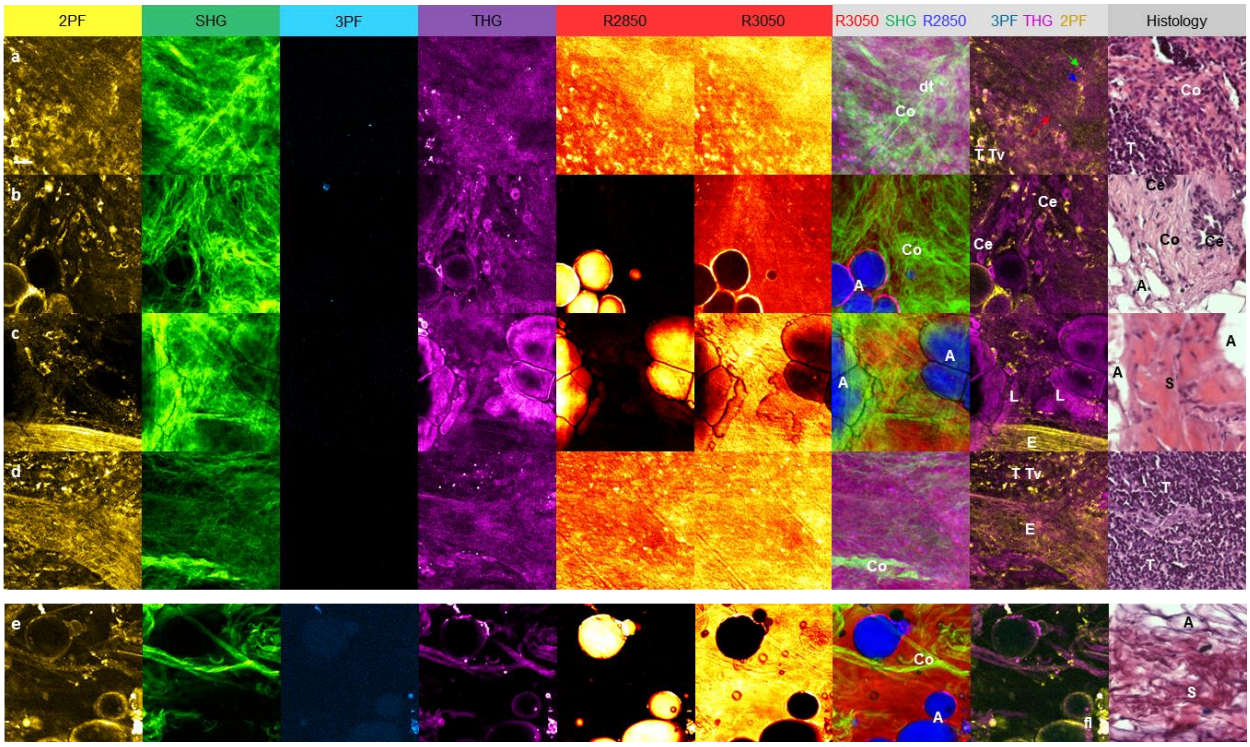

Fig. 6.6. Week 5 multimodal imaging of breast cancer development. (a-d) Carcinogen-induced experimental group. (e) Saline-injected control group. Morphological features: **A** adipose tissue, **Ce** hypercellularity, **Co** collagen fiber, **dt** ductal structure, **E** elastin fiber, **fl** fluorescent feature, **L** altered lipid, **N** nerve, **S** stroma, **T** tumor, **Tv** THG-sensitive microvesicle. Scale bar: 25 μm.

In week 5, Fig. 6.6(a) displays a tumor-stroma boundary, with tumor cells **T** (2PF) infiltrating the extracellular matrix. Interestingly, there are also THG-sensitive microvesicles **Tv** in the tumor area. The co-localization of the THG-sensitive microvesicles and the tumor cells is consistent with the results in Fig. 6.4(b), confirming the association of these microvesicles with carcinogenesis[75]. In the FOV, A gradual decrease of the amount of the FAD-fluorescent cells (2PF) and a gradual increase of the amount of the collagen fibers (SHG) point to the direction of tumor progression (red arrow). The collagen fibers

are found to align both parallel to and perpendicular to the tumor-stroma boundary. While the parallel collagen organization potentially serves as a defense mechanism to tumor growth, the perpendicular ductal structure **dt** (SHG) can facilitate invasion[214,215]. The local invasion is supported by the THG-sensitive microvesicles (green arrow) and the FAD-fluorescent cells (red arrow) located in and around the ductal collagen structure in the stromal area. The histology shows clearly dense nuclei in the tumor nest **T** and increased cellularity in the nearby collagenous connective tissue **Co**. However, the tubular formation and the sign of invasion are not as obvious as in the multiphoton images.

Fig. 6.6(b) displays a boundary between adipose tissue **A** (R2850, THG) and collagenous stromal tissue **Co** (SHG). Increased cellular activities **Ce** can be observed not only in the 2PF image but also in the THG image. This is evident of the presence of two cell types. While their molecular difference is revealed by multiphoton imaging, their functional difference in BCa development is still to be determined. Also found in the THG image are the THG-sensitive microvesicles sparsely distributed in the FOV. The adipose tissue **A**, the fibrous connective tissue **Co**, and the increased cellularity are also recognized in the histology. Fig. 6.6(c) demonstrates similar features as observed in Fig. 6.4(a) and Fig. 6.5(d). The altered lipid **L** (R2850, THG) is found near adipose tissue **A** (R2850) and is likely changing or losing its lipid composition, based on the decrease of the R2850 signal. An elastin sheet **E** (2PF) with parallel fibrils is similar to the elastin net in Fig. 6.4(a). The collagen fibers are expelled from the location of the elastin sheet, indicating the relationship between elastin organization and collagen organization. The histology shows dense stromal tissue **S** and two lipid domains **A** on the sides, similar to the multiphoton images. Fig. 6.6(d) shows a slightly different morphology of elastin fibers **E** (2PF) consisting of a looser arrangement and crosslinks between parallel fibrils, which are likely forming the elastic lamella in the blood vessel wall[238]. The locally dense collagen fibers **Co** (SHG), the high-2PF cells, and the THG-sensitive microvesicles **Tv** in the FOV are recognized as signs of tumorigenesis. The H&E micrograph demonstrates abundant tumorous cells with dark-staining nuclei and only little connective tissue within the FOV.

In the control group, Fig. 6.6(e) demonstrates straight collagen fibers **Co** (SHG) and normal adipose tissue **A** (R2850, THG). An abnormal fluorescent feature **fl** (2PF, 3PF) is found at the bottom-right corner in the FOV. However, no sign of tumorigenesis is observed in this area. The histology displays highly fibrous stroma and the surrounding adipose tissue.

6.3.2. Multimodal imaging of late breast cancer development

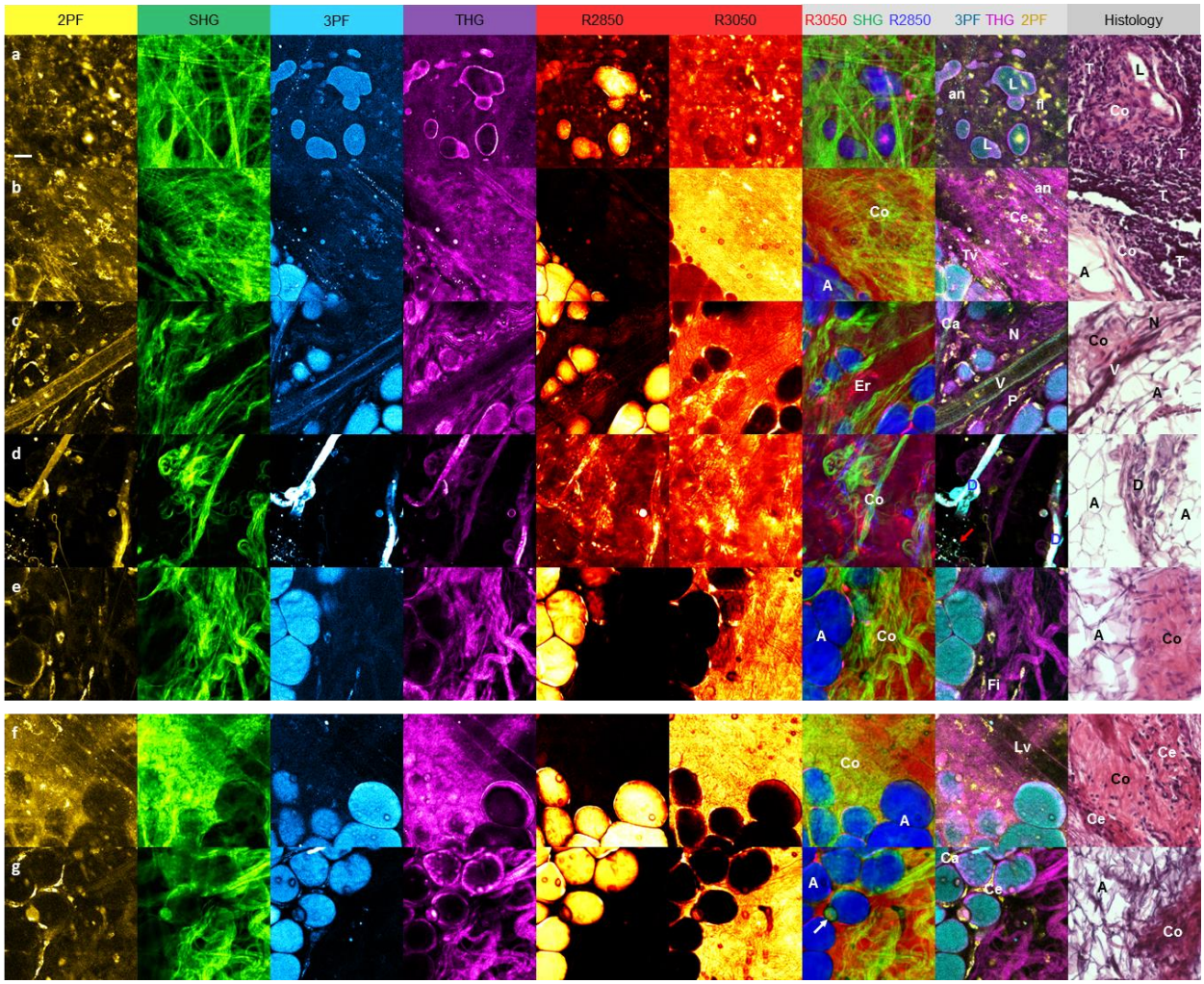

Fig. 6.7. Week 6 multimodal imaging of breast cancer development. (a-e) Carcinogen-induced experimental group. (f-g) Saline-injected control group. Morphological features: **A** adipose tissue, **an** angiogenesis, **Ca** capillary, **Ce** hypercellularity, **Co** collagen fiber, **D** mammary duct, **Er** erythrocyte, **Fi** fibroblast, **L** altered lipid, **Lv** lymphatic vessel, **N** nerve, **T** tumor, **V** blood vessel, **3v** 3PF-sensitive microvesicle. Scale bar: 25 µm.

In week 6, Fig. 6.7(a) demonstrates a stromal region with several lipid domains **L** (R2850, THG, 3PF). Interestingly, 3PF also provides imaging contrast from the LDs, so the molecular composition of the LDs

may contain fluorophores responsive to UV excitation (fundamental at 1080-1200 nm corresponding to 3P excitation at 360-400 nm). Based on the excitation and the detection wavelengths used, the fluorophore is likely to be NAD(P)H[216]. Another unique feature revealed by 3PF imaging is the bright microvesicles **an** aligned in a tubular arrangement, which is identified as an angiogenic feature[239,240]. In comparison to the stroma in the control animal in an earlier week [Fig. 6.2(e)], some amorphous high-2PF substances **fl** are observed here, and the same morphological features also appear in the R3050 image, indicating the protein nature of these tumor-associated substances. The tumorigenic activities can be confirmed in the histology, in which a large number of dark-staining nuclei are found within the FOV. The presence of collagenous connective tissue **Co** and the altered lipid morphology **L** also correspond well with the multiphoton images.

Fig. 6.7(b) displays a lipid-stromal interface marked by adipose tissue **A** (R2850, THG) and collagen fibers **Co** (SHG) in stromal tissue (R3050). In the stromal area, fluorescent cells **Ce (**2PF, 3PF) are observed. The highly fluorescent microvesicles within the cytoplasm and the irregular cell shape are indicative of cancerous cells[214,219,220,223]. Also, THG-sensitive microvesicles **Tv** are found surrounding the LDs and in the stroma. Interestingly, some of these THG-sensitive microvesicles are also observed in the 3PF image and vice versa, suggesting the difference in the molecular composition of THG- and 3PF-sensitive microvesicles. In particular, 3PF imaging shows microvesicles **an** aligned in a tubular arrangement, which is strongly related to angiogenesis[239,240]. In the histology, the stroma is infiltrated by tumorous cells **T** of dark-staining nuclei. Some fibrous connective tissue **Co** is located between the stromal tissue and the adipose tissue **A**. Empty spaces are found in the tumorous stroma as well as between the connective tissue and the adipocytes, agreeing well with the observations in multiphoton images.

In Fig. 6.7(c), a prominent tubular structure is observed in all the multiphoton images. Inside this tubular structure, small round cells of 6-7 μm in diameter are identified as erythrocytes **Er** (R3050, R2850, THG)[75]. In the hyperspectral CARS imaging movie, the erythrocytes are observed to be moving in the

blood vessel **V**. The blood vessel wall can be delineated by 2PF and 3PF signals but can also be visualized in the R2850 and the R3050 images. The outer layer of the blood vessel is enclosed by collagen fibers (SHG). A smaller ductal structure showing similar nonlinear optical responses may be a branching capillary **Ca**. Note that no 3PF-sensitive microvesicle is observed around the developed blood vessels here, suggesting the correlation of the 3PF-sensitive microvesicles to the early angiogenic process[239,240]. Nerve fibers **N** (THG, R2850) are found in the proximity of the LDs and the blood vessels, with a reduced amount of collagen as compared to those in normal mammary tissue in earlier weeks [Fig. 6.2(c), Fig. 6.3(c,d), Fig. 6.4(f)]. The curved feature of the nerve fibers may result from reorganization of the collagen fibers during BCa development. In the FOV, there are two types of high-2PF cells showing morphological differences. One cell type of a rounder shape is likely a cancer-associated epithelial cells, while the other type with an elongated shape are likely pericytes **P** in the proximity of blood vessel and nerve[241]. In the histology, a dark-staining tubular structure is recognized as the blood vessel **V**. The axon fibers **N**, the fibrous connective tissue **Co**, and the adipocytes **A** can be found in the surrounding of the blood vessel.

Fig. 6.7(d) exhibits several tubular structures of similar morphology. By cross comparison between modalities, the central tube with high SHG signal is recognized as a thick collagen fiber **Co**. The other two tube-like structures on the sides with high 2PF, 3PF, THG, R2850 signals are identified as mammary ducts **D**[227], which demonstrate similar multiphoton responses as those in earlier weeks [Fig. 6.2(b), Fig. 6.3(b)]. However, one of the mammary ducts here (left) was either malformed during tumor formation, or structurally damaged during tissue sectioning. The images reveal a distorted end and highly fluorescent microvesicles (3PF, 2PF, red arrow) nearby. Note also that this mammary duct is surrounded by irregular collagen fibers (SHG) and fluorescent cells (2PF). The H&E micrograph shows the mammary ducts **D** within the fibrous connective tissue and the surrounding adipose tissue **A**. Fig. 6.7(e) is a site away from the tumor area (>10 mm), exhibiting no obvious features of tumor formation. The adipose tissue **A** (R2850, THG) demonstrates normal and intact LDs, and the stroma shows regular

collagen organization **Co** (SHG, THG) with a few fibroblasts **Fi** (2PF) in between. The histology also shows the normal adipose tissue **A** and the fibrous stroma **Co** with purple-staining nuclei scattered within.

In the control animal, Fig. 6.7(f) demonstrates an interface of adipose tissue **A** (R2850, THG) and collagenous connective tissue **Co** (SHG). In the connective tissue, a ductal structure **Lv** with thinner walls is recognized. The duct displays different multiphoton responses in comparison to the mammary ducts and the blood vessels. Moderate 2PF, SHG, and THG signals at the boundaries and low 2PF, SHG, and THG signals inside the duct are observed. The comparison suggests that this feature is another type of ductal structure and is likely a lymphatic vessel. In the histology, a relatively denser connective tissue **Co** and a higher number of cells **Ce** are found in this area of the control animal. Fig. 6.7(g) demonstrates a normal lipid-stromal boundary. Interestingly, there are a few fluorescent cells **Ce** (2PF, 3PF) at the edge of the two tissue types. A capillary **Ca** with the characteristics of ductal structure (2PF) and bright 3PF-sensitive microvesicles attached is found in between the LDs **A** (R2850, THG). Another interesting feature is a bubble-like structure (white arrow), demonstrating high 2PF, SHG, and moderate THG, R2850 signals, which may contain different molecular compositions derived from the larger LDs. In the H&E histology, the adipocytes **A** and the dense connective tissue **Co** can be identified.

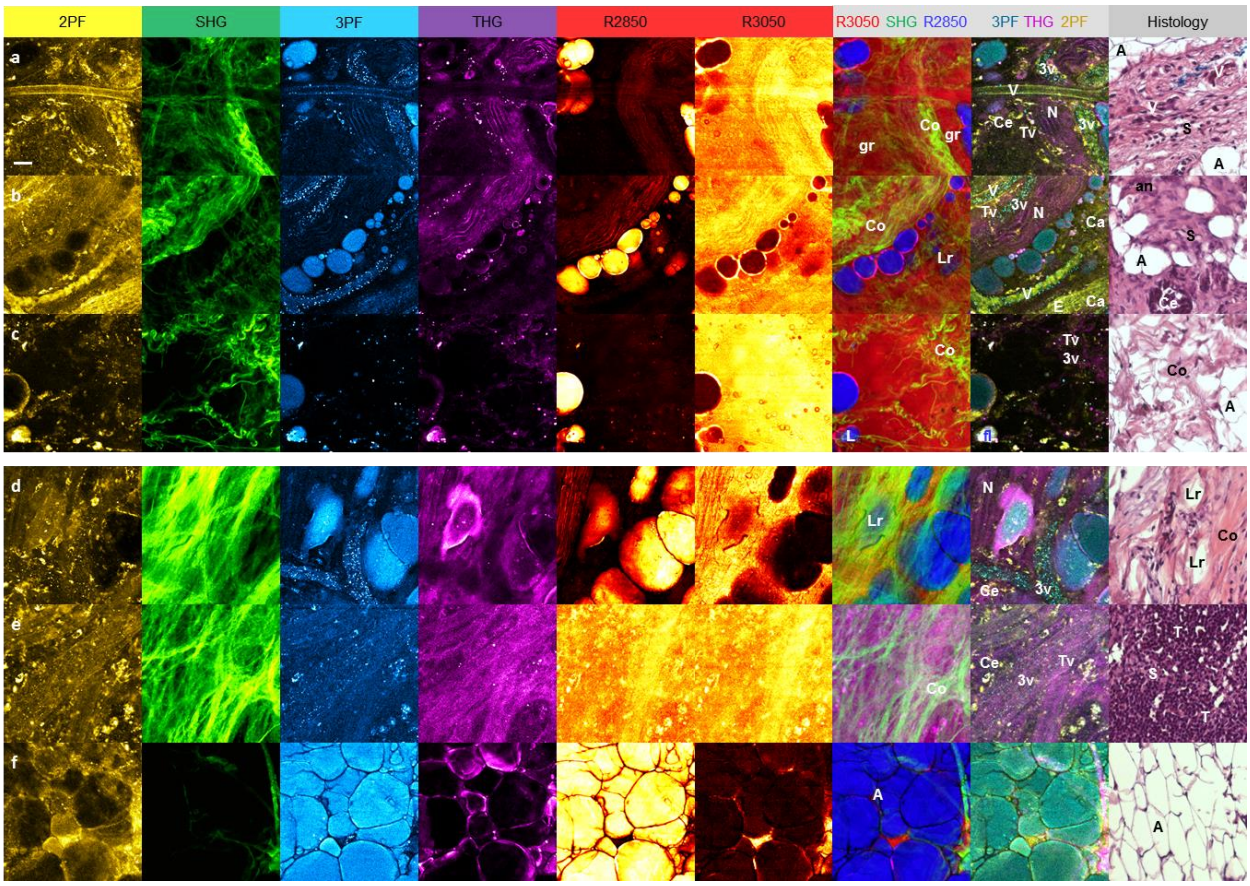

Fig. 6.8. Week 7 multimodal imaging of breast cancer development. (a-c) Carcinogen-induced experimental group. (d-f) Saline-injected control group. Morphological features: **A** adipose tissue, **an** angiogenesis, **Ca** capillary, **Ce** hypercellularity, **Co** collagen fiber, **E** elastin fiber, **fl** fluorescent feature, **gr** granular structure, **L** altered lipid, **Lr** lipid residual, **N** nerve, **S** stroma, **Tv** THG-sensitive microvesicle, **V** blood vessel**, 3v** 3PF-sensitive microvesicle. Scale bar: 25 µm.

In week 7, Fig. 6.8(a) demonstrates high-2PF cells **Ce** (2PF), and the cellular pleomorphism is indicative of tumorigenesis, which is confirmed by the co-localized THG-sensitive microvesicles **Tv**. Surrounded by these cells is a large aggregate of granular cells **gr** (R3050) with high protein contents and sparsely-distributed high-2PF spots. These observations indicate that the area is likely forming a tumor nest. On the other hand, despite similar morphology in the R3050 image, the granular aggregate **gr** on the right side of the FOV demonstrates high 2PF signal and is surrounded by high-3PF microvesicles **3v**. As the 2PF and the 3PF imaging are targeting mainly FAD and NAD(P)H, the observation of high 2PF and 3PF fluorescence suggests high metabolism related to carcinogenesis. The more developed blood vessel **V** is marked by vessel walls (2PF, 3PF), surrounded by attached 3PF-sensitive microvesicles, and supported by collagenous connective tissue (SHG). In comparison to the more developed blood vessel, other aligned

3PF-sensitive microvesicles **3v** along with partially formed vessel walls of elastin fibrils (2PF) and supportive collagen fibers (SHG) lead to the possibility that this unique combination of features is a developing blood vessel. Also shown in the FOV is a curved nerve bundle **N** (THG, R2850) which is likely disrupted as a result of tumor development, similar to the observation in Fig. 6.7(c). Finally, a comparison between the THG and the 2PF images reveals the THG-sensitive cells that are distinct from the high-2PF cells, suggesting the presence of different cell types. The observation confirms the findings in Fig. 6.6(b). In the histology, the broken tubular structures **V** are recognized as blood vessels that are disrupted during the histological preparation. The fibrous stromal tissue **S** is filled with nuclei of different sizes, and some adipocytes **A** are also found in the surrounding.

Fig. 6.8(b) shows a library of the different stages of the neovascularization. The two relatively mature developing blood vessels **V** demonstrate high-2PF vessel walls surrounded by attached 3PF-sensitive microvesicles. Two capillaries **Ca** are identified on the right side of the image, with similar multiphoton responses as compared to those of the developing vessels, but with smaller dimensions. At the bottom-right corner, an elastin net **E** (2PF) demonstrating crosslinks between elastin fibrils is likely forming elastic lamella of the blood vessel wall[238]. Interestingly, at the top-left corner of the image, a strand of 3PF-sensitive microvesicles are well aligned without the presence of any vessel wall. This effect is possibly due to the nearby blood vessel releasing 3PF-sensitive microvesicles into the microenvironment to initiate angiogenesis. It is worth noting that the THG-sensitive microvesicles at the top-left corner are located in between two strands of 3PF microvesicles, suggesting tumorigenic processes in the surrounding microenvironment. The histology demonstrates a tumorous stroma **S** with a higher density of cell nuclei and LDs **A** of different sizes. An aggregate of dark-staining nuclei **Ce** is forming a tumor. A tubular eosinophilic structure **an** is likely related to angiogenesis.

Fig. 6.8(c) shows an altered lipid domain **L** (R2850) co-localized with highly fluorescent substances **fl** (2PF, 3PF) in the tumorous stromal area. Accompanied with the lipid alteration, the THG-sensitive **Tv**

and 3PF-sensitive microvesicles **3v** are found in the FOV. The H&E-stained histology exhibits the fibrous connective tissue **Co** and the adipose tissue **A**.

In the control animal in week 7, an abnormal tumor-like formation was identified during the surgery. Some cancerous features are observed in the multiphoton images as well. The most outstanding feature in Fig. 6.8(d) is the branching 3PF-sensitive microvesicles **3v** indicative of angiogenesis. Irregular-shape high-2PF cells **Ce** are found in the proximity and are likely tumorigenic endothelial cells. Also, a lipid residual **Lr** (R2850, THG, 3PF) is recognized surrounding a nerve bundle **N** (THG, R2850). The histology micrograph demonstrates collagenous connective tissue **Co**, lipid residuals **Lr**, and some aggregates of nuclei. Fig. 6.8(e) shows some tubular structures in the multimodal images (2PF, 3PF, THG). The 3PF-sensitive microvesicles **3v** are aligned with the tubes at the center of the FOV. These observations suggest blood vessel formation or angiogenic substances transported by the tubular structures. In addition, there are THG-sensitive microvesicles and high-2PF cells present in this imaging site. Both of the signatures are related to tumor development. The tumorigenic activity is confirmed in the histology which shows a high density of dark-staining nuclei and little connective tissue in the FOV. Fig. 6.8(f) demonstrates a normal adipose tissue area with abundant adipose tissue (R2850, THG, 3PF) and little connective tissue (R3050, SHG). The same morphological features can be found in the H&E micrograph.

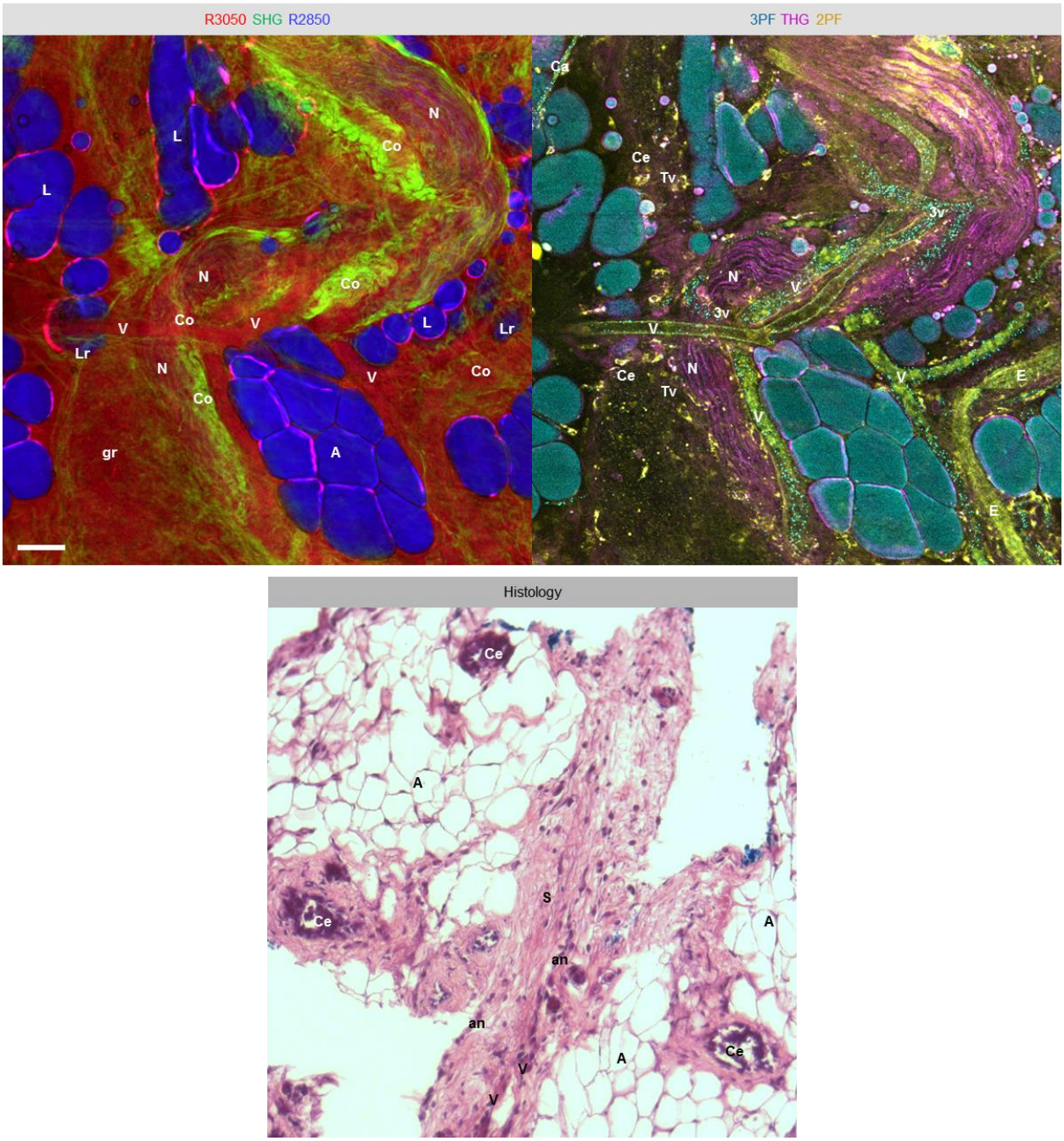

Fig. 6.9. Week 7 large-area multimodal imaging of breast cancer development in a carcinogen-induced rat. Morphological features: **A** adipose tissue, **an** angiogenesis, **Ce** hypercellularity, **Co** collagen fiber, **E** elastin fiber, **gr** granular structure, **L** altered lipid, **Lr** lipid residual, **N** nerve, **S** stroma, **Tv** THG-sensitive microvesicle, **V** blood vessel, **3v** 3PF-sensitive microvesicle. Scale bar: 50 µm.

Fig. 6.9 demonstrates large-area multimodal images in the carcinogen-induced animal in week 7. Two composite images (R3050-SHG-R2850 and 3PF-THG-2PF) are presented to visualize the relative spatial distribution of different multiphoton signatures. A variety of characteristics related to carcinogenesis can

be recognized. The altered lipid domains **L,** lipid residuals **Lr** (R2850, THG, 3PF), and the THG-sensitive microvesicles **Tv** are identified in different areas in the FOV. Tumorigenic high-2PF cells **Ce** are found surrounding a large and more developed tumorous area marked with small protein-rich granules **gr** (R3050). Curved and disrupted nerve fibers **N** (THG, R2850) are observed, and those at the top-right region even demonstrate high 2PF signal, suggesting a change of the chemical composition. Collagen organization **Co** (SHG) of different forms can be visualized, such as locally dense collagen, curved collagen around the nerve bundles, reticular and reduce collagen at the location of the elastin fibrils **E** (2PF), reduced collagen at the tumorous area, and tubular formations enclosing the developed vessels **V** (2PF, 3PF). While collagen remodeling has been related to tumor development[214,215], multimodal imaging demonstrates that each of these arrangements is related to a specific carcinogenic event visualized by the other co-registered modalities.

In this extended FOV, the angiogenic process at different stages can be observed through the spatial distribution of the high-2PF vessel walls, the elastin fibers (2PF), and the 3PF-sensitive microvesicles. More mature blood vessels **V** are marked with clearly visible vessel walls (2PF, 3PF) attached by 3PF-sensitive microvesicles **3v**. The elastin fibers **E** (2PF) appear as a cross-linked net in one end and loosely aligned fibers in the other end, representing a developing blood vessel. The 3PF-sensitive microvesicles are also found outside the blood vessels in several locations, suggesting the onset of angiogenesis or the release of signaling molecules by or from within the blood vessels. Interestingly, a closer examination of the 3PF-THG-2PF image reveals that the highest density of 3PF microvesicles **3v** is at the intersection of three developing blood vessels converging into the nerve bundles **N** (THG). This observation may suggest that these microvesicles are beginning to form new blood vessels that will disrupt the nerve bundle. Nevertheless, an experiment monitoring the dynamics of these biomolecules would be necessary to further elucidate these complex biological processes.

In the histology, several cell aggregates **Ce** forming acinar structures are observed, and most of them are surrounded by dense connective tissue. At the center of the FOV, a large domain of stromal tissue **S** is

located in between two large domains of adipose tissue **A**. Within the stroma, in addition to some cellular aggregates enclosed by fibrous connective tissue, there are some darker-staining tubular features that are likely developing blood vessels **V** or malignant endothelial cells in the angiogenic site **an**.

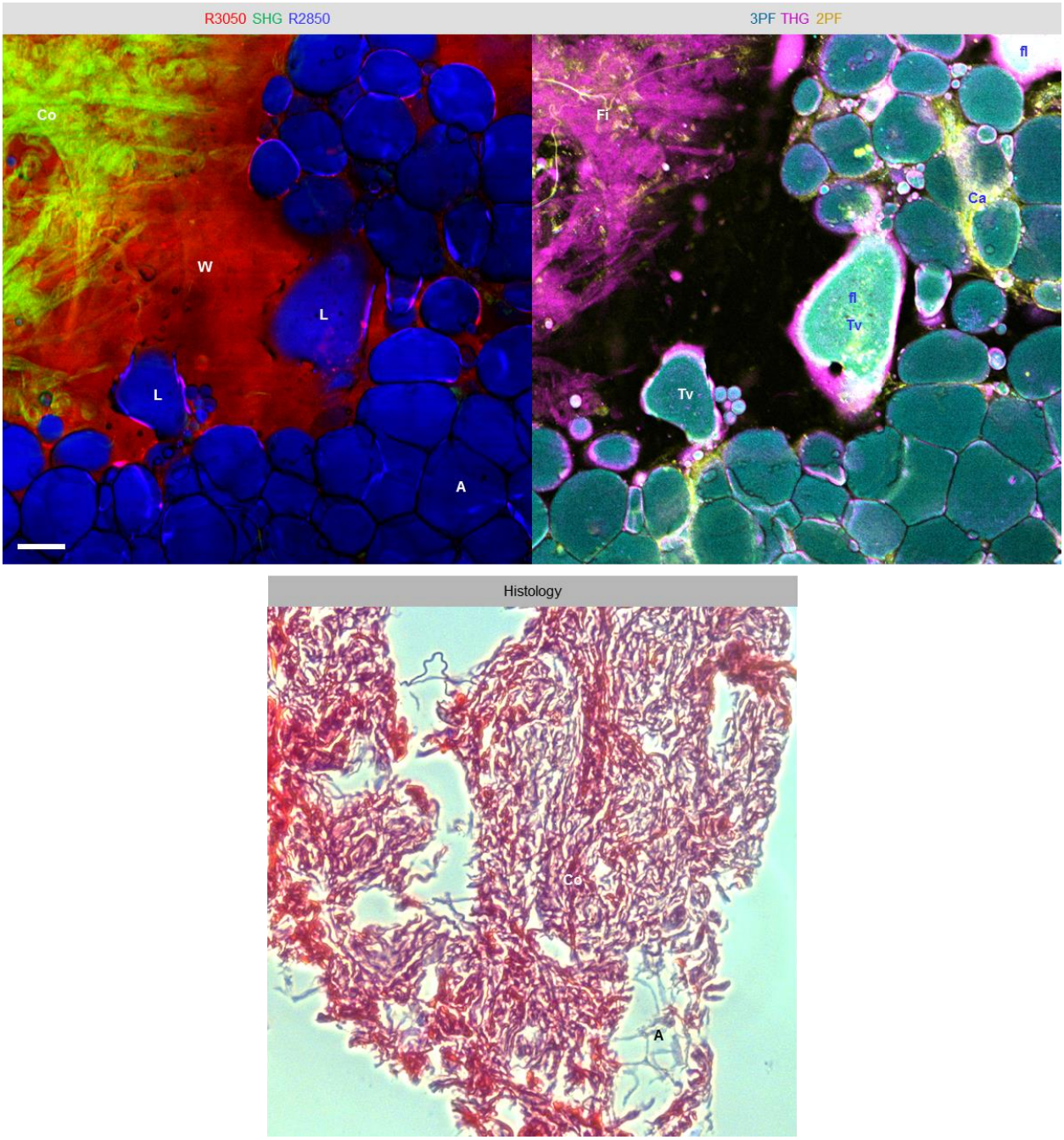

Fig. 6.10. Week 7 large-area multimodal imaging of normal breast tissue in a saline-injected rat. Morphological features: **A** adipose tissue, **Ca** capillary, **Co** collagen fiber, **Fi** fibroblast, **fl** fluorescent feature, **L** altered lipid, **Tv** THG-sensitive microvesicle, **W** water. The histology of this area is disrupted during sample preparation. Scale bar: 50 µm.

Fig. 6.10 shows the large-area images of the mammary tissue of a control animal. While this animal was visually found with mammary areas suspicious for tumor development, in fact there were cancer-like features observed in the multiphoton images. The image displays a large fibrocystic structure with dense collagen aggregation **Co** (SHG, THG) and an elevated quantity of fibroblasts **Fi** (2PF) inside. Two altered LDs **L** (R2850, THG) are found to contain THG-sensitive microvesicles **Tv**, and one of them even demonstrates strong 2PF and 3PF signals **fl**. Another highly fluorescent area is identified at the top-right corner of the image, also containing high-2PF substances and THG-sensitive microvesicles. A capillary **Ca** marked with aligned 3PF-sensitive microvesicles is found in between adipose tissue, showing high 2PF signal itself and in the surrounding area. The histology of this imaging site is disrupted during sample preparation. Nevertheless, within the FOV, abundant fibrous connective tissue **Co** is identified, and only little adipose tissue **A** is found.

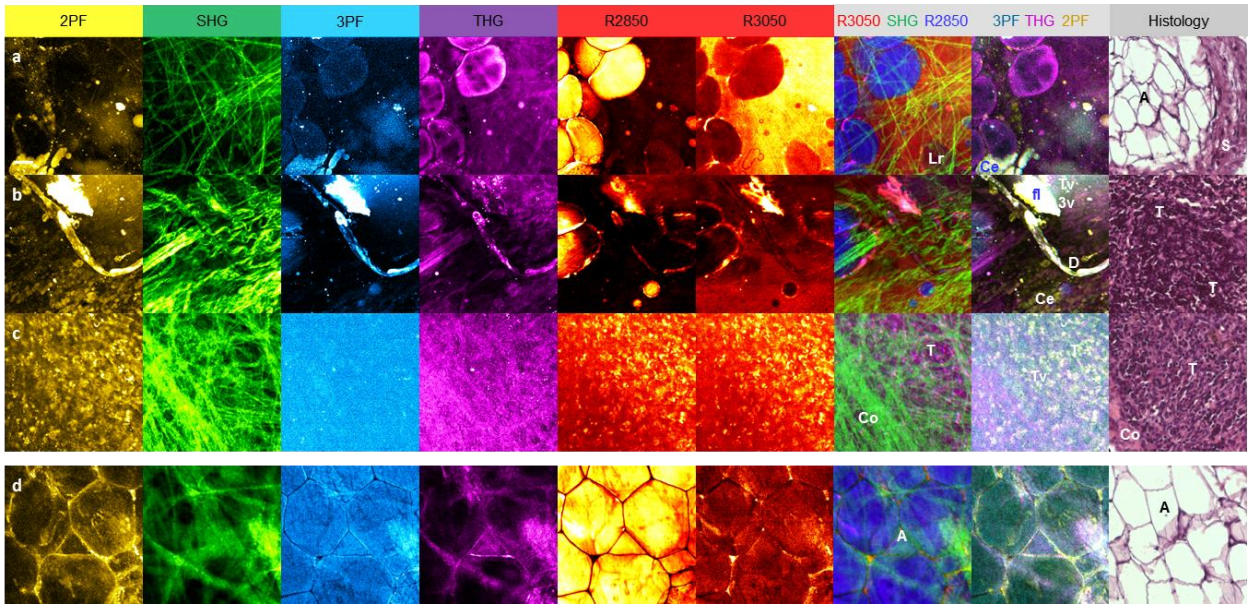

Fig. 6.11. Week 8 multimodal imaging of breast cancer development. (a-c) Carcinogen-induced experimental group. (d) Saline-injected control group. Morphological features: **A** adipose tissue, **Ce** hypercellularity, **Co** collagen fiber, **D** mammary duct, **fl** fluorescent feature, **Lr** lipid residual, **S** stroma, **T** tumor, **Tv** THG-sensitive microvesicle, **3v** 3PF-sensitive microvesicle. Scale bar: 25 µm.

In week 8, the imaging site in Fig. 6.11(a) is at a lipid-stroma boundary 5 mm away from the tumor. A highly fluorescent cell cluster **Ce** (2PF, 3PF) is found in the adipose tissue, indicating its correlation with the lipid contents. Similar results have been observed in early BCa development [Fig. 6.2(b)]. A lipid

residual **Lr** (R2850, R3050) has already lost its lipid composition as is evident by its low R2850 signal. Simultaneously, some cloudy fluorescent areas (2PF, 3PF) and various microvesicles (2PF, 3PF, THG) are observed in the surrounding. The histology shows a clear boundary of adipose tissue **A** and the stromal tissue **S**. The image set in Fig. 6.11(b) is at the margin of the normal and the cancerous tissue. A mammary duct **D** (2PF, 3PF, THG, R2850) is identified at the center of the FOV. An irregular feature **fl** showing strong 2PF and 3PF fluorescence is next to the mammary duct. Meanwhile, some THG- and 3PF-sensitive microvesicles **Tv, 3v** are found near the fluorescent feature. Numerous round high-2PF cells **Ce** are arranged as parallel cords in the same orientation as the collagen fibers **Co**. In the histology, malignant tumor cells **T** with prominent nuclei are ubiquitous in the FOV. Some of the tumor cells (the upper **T**) appear to align in a cord-like arrangement, agreeing well with the observation in the multiphoton data. The imaging site of Fig. 6.11(c) is inside a developing tumor, showing a boundary between tumor cells **T** (2PF, R2850, R3050) and the surrounding collagen fibers **Co** (SHG). The tumor cells show irregular morphology, and some of the cells appear to be permeating into the collagenous stroma. The cellular pleomorphism in the tumorous area **T** and the surrounding collagenous connective tissue **Co** are also identified in the histology. In the control group, the images in Fig. 6.11(d) exhibit normal adipose tissue (R2850, THG, 3PF) with little connective tissue. The H&E histology shows the same morphological features.

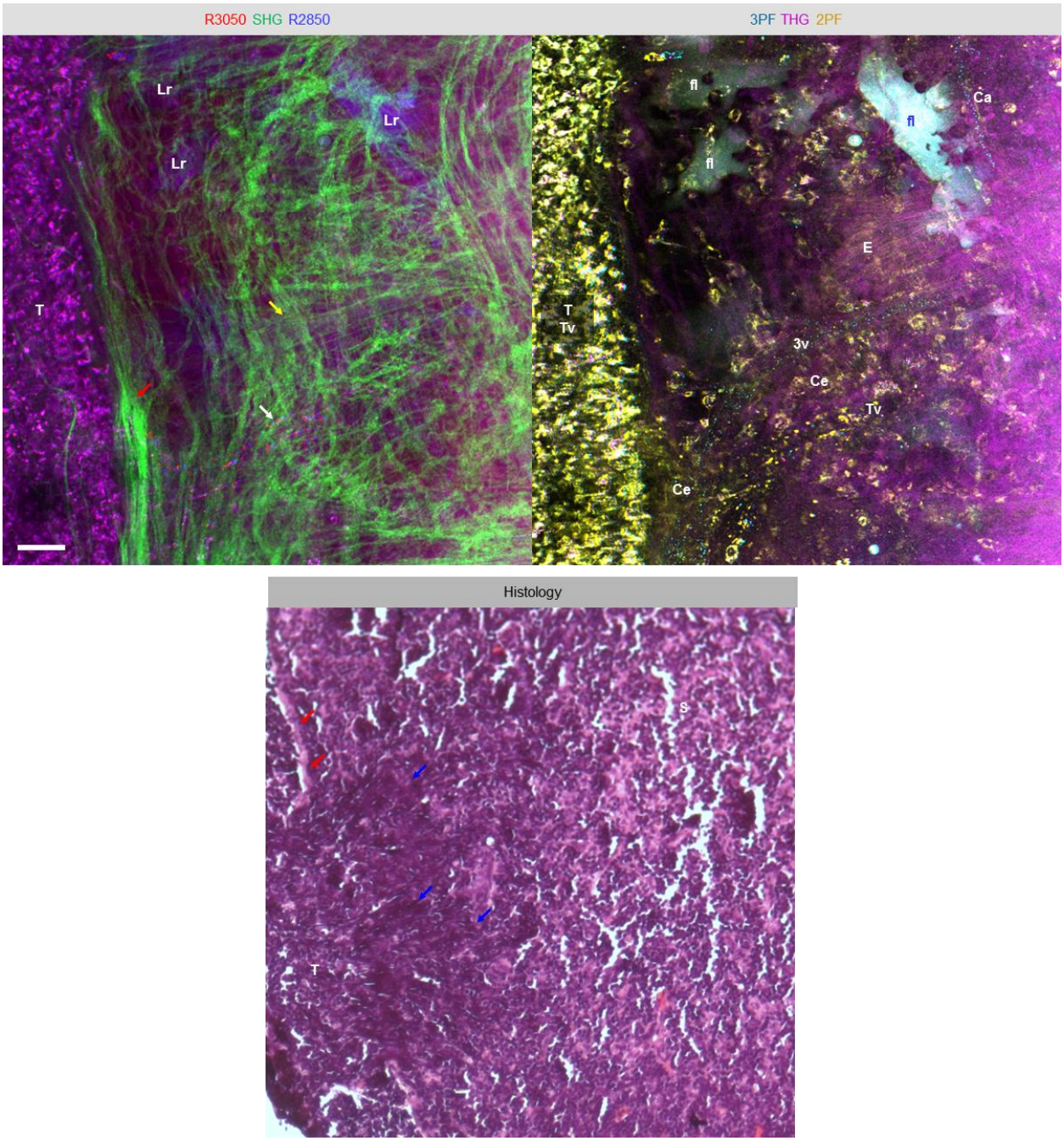

Fig. 6.12. Week 8 large-area multimodal imaging (1 of 2) of breast cancer development in a carcinogen-induced rat. Morphological features: **Ce** hypercellularity, **E** elastin fiber, **fl** fluorescent feature, **Lr** lipid residual, **S** stroma, **T** tumor, **Tv** THG-sensitive microvesicle, **3v** 3PF-sensitive microvesicle. Scale bar: 50 µm.

In a large-area image of the carcinogen-induced animal in week 8 (Fig. 6.12), various BCa signatures can be recognized. A large quantity of tumor cells **T** (2PF, 3PF, THG, R2850, R3050) are enclosed by the straightened collagen boundary (SHG, red arrow), which can be designated as the TACS-2 feature[214,215]. Within the tumor nest, the cells demonstrate irregular sizes and shapes, and appear to be smaller than

those observed in the extracellular matrix that resemble tumorigenic epithelial cells and fibroblasts **Ce**[237, 242]. In the same area, THG-sensitive microvesicles **Tv** are also observed, supporting the association of the THG-sensitive microvesicles with carcinogenesis. To the right of the TACS-2 features, some collagen fibers are aligned perpendicular to the collagen wall (SHG, yellow arrow). This orientation can be classified as a TACS-3 feature[214,215], which can facilitate invasion of tumor and transport of tumorigenic materials. The phenomena are further validated in the 2PF, 3PF and THG images. The 2PF imaging demonstrates tumorigenic cells **Ce** and fluorescent substances in the proximity of the TACS-3 feature. 3PF imaging exhibits evidence for the transport of 3PF-sensitive microvesicles **3v** in between and in parallel to the TACS-3 feature. THG imaging displays the THG-sensitive microvesicles **Tv** in the surrounding area of the TACS-3 feature as well. Another strand of various microvesicles **Vs** is visible in the 2PF, 3PF, THG, R2850, and R3050 images and is also supporting evidence for tumor invasion. At the boundary of the tumor cells and the aligned microvesicles, the tumor cells form a protrusion and infiltrate into the connective tissue.

In this FOV, there are also several lipid residuals **Lr** (R2850) demonstrating high 2PF and 3PF signals **fl**. In the proximity of the lipid residuals, a developing capillary **Ca** (3PF) and an elastin net **E** (2PF) are identified, suggesting the relation of lipolysis to angiogenesis. The orientation of the elastin fibrils is in concert with that of the collagen fibers and the 3PF-sensitive microvesicles, and is therefore likely forming blood vessels in the same orientation. It is worth noting that the collagen reorganization in the FOV might also be related to the transformation of collagen from type I to type V with reduced SHG signal and a reticular arrangement[226]. It has been suggested that collagen V is anti-adhesive to cancer cells and can serve a defense mechanism[226]. However, this anti-adhesive nature might also facilitate free movement of cancer cells, such as those located in the void in between the tumor nest and the stroma shown here. A real-time imaging experiment would be needed to further understand the causes and the effects of these biological events.

The histology agrees well with the multiphoton data. The tumor cells **T** in the tumor nest are marked with highly-dense dark-staining nuclei. The connective tissue enclosing the tumor clearly defines a boundary (red arrows), which is designated as the TACS-2 feature in the multiphoton images[214,215]. Several cords of malignant cells (blue arrows) are found infiltrating into the stromal area **S**, confirming the occurrence of local invasion. Compared to the H&E histology, the multimodal multiphoton images reveal different aspects of the tumor invasion, such as collagen reorganization, transportation of tumorigenic microvesicles, angiogenesis, and lipid metabolism.

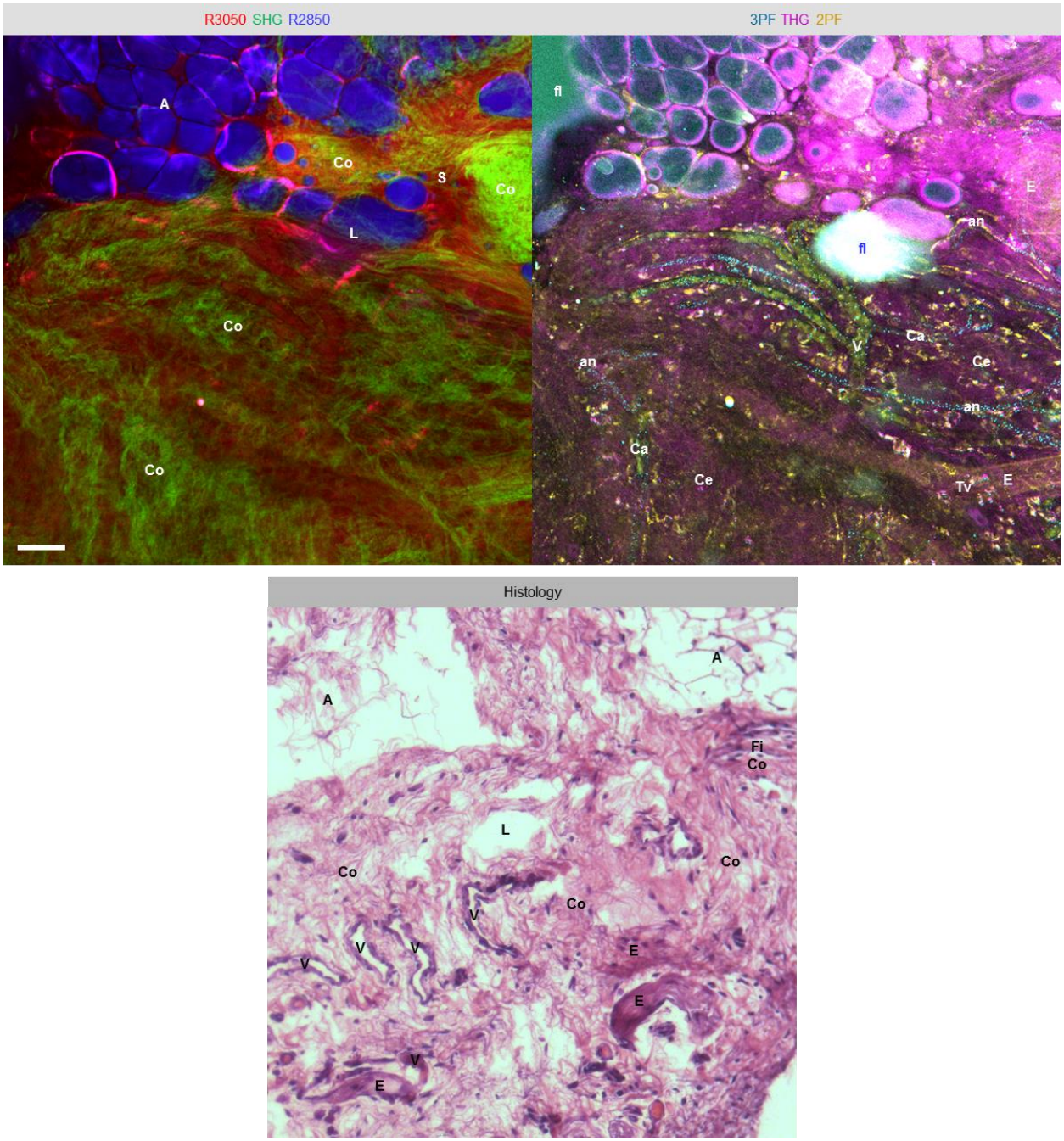

Fig. 6.13. Week 8 large-area multimodal imaging (2 of 2) of breast cancer development in a carcinogen-induced rat. Morphological features: **A** adipose tissue, **an** angiogenesis, **Ca** capillary, **Ce** hypercellularity, **Co** collagen fiber, **E** elastin fiber, **Fi** fibroblast, **fl** fluorescent feature, **L** altered lipid, **Tv** THG-sensitive microvesicle, **V** blood vessel. Scale bar: 50 µm.

Another large-area imaging of the cancerous tissue in week 8 (Fig. 6.13) visualizes the interface of highly vascular tumorous stroma and the nearby adipose tissue. A very distinct set of tumorigenic signatures are found in this area in comparison to Fig. 6.12. Under bright-field microscopy, numerous blood vessels red in color were observed. In the multimodal images, various stages of angiogenesis are identified in the

tumorous stroma, including more developed blood vessels **V** with higher 2PF signal and less 3PF-sensitive microvesicles, capillaries **Ca** with similar features but smaller in size, developing blood vessels **an** with lower 2PF signal and more 3PF-sensitive microvesicles, and elastin fibrils **E** (2PF) without 3PF-sensitive microvesicles. The stromal collagen fibers **Co** (SHG, THG) present an inverse contrast to the high-2PF blood vessels, indicating the relevance of collagen remodeling to angiogenesis[238]. On the other hand, the collagen fibers around the elastin fibrils **E** (2PF) demonstrate similar contrast as the elastin fibrils, suggesting a different underlying process. An examination of the angiogenic site **an** closer to the top-right corner of the FOV reveals that the elongated high-2PF cells line up with the 3PF-sensitive microvesicles, which can be tumor and endothelial cells forming the blood vessel walls. While there are no aligned high-2PF cellular features without the 3PF-sensitive microvesicles, one can infer that these cells are recruited by the 3PF-sensitive microvesicles. These observations suggest two distinct forms of angiogenic mechanisms – one with elastin fibrils (2PF) forming crosslinks in between and co-aligned with collagen fibers (3PF) enclosing the vessel, and the other with 3PF-sensitive microvesicles (3PF) recruiting tumor or endothelial cells to initiate vascularization.

In addition to angiogenesis, the adipose tissue **A** (R2850, THG, 3PF) is found to possess loosely attached LDs **L**. Some of these LDs lose their typical round shape and appear to be migrating into the tumorous stroma. The degradation of the LDs is related to the loss of the connective tissue due to the lack of collagen fibers (SHG) and the presence of empty space in the surrounding area. From results in earlier weeks [Fig. 6.2(b), Fig. 6.5(c) Fig. 6.7(a), Fig. 6.10], in the proximity of the altered LDs there usually exist amorphous fluorescent materials, which are also observed here with a highly-fluorescent feature **fl** (3PF, 2PF). In the single-modal images, the 3PF image demonstrates very high signal from this feature, the THG image also shows moderate signal, and a blood vessel (2PF, THG) is found passing through this feature. The up-regulated 3PF fluorescence is indicative of metabolic changes, and the presence of the blood vessel suggests the correlation of lipolysis and angiogenesis. Closer to the top-right corner of the

image, an abnormally dense collagen aggregate **Co** (SHG) showing elastin fibrils **E** within (2PF) is identified as fibrocystic tissue.

The histology demonstrates good correspondence to the multiphoton images. Numerous elongated and dark-staining lumens in the FOV are designated as developing blood vessels **V**. Meanwhile, there are thicker purple-staining connective tissue **E** of elastin fibers. Other collagenous connective tissue **Co** demonstrates very different arrangements within the stroma. A sphere-like organization of the connective tissue with fibroblasts **Fi** within is identified at the corresponding location of the fibrocystic tissue as in the multiphoton images. The adipose tissue **A** at the top-left and the top-right of the FOV appears to be disrupted during histological processing, but the membranes of the adipocytes are still discernable. The LDs **L** within the connective tissue leave large empty spaces within the stroma, confirming the observation in the multiphoton images.

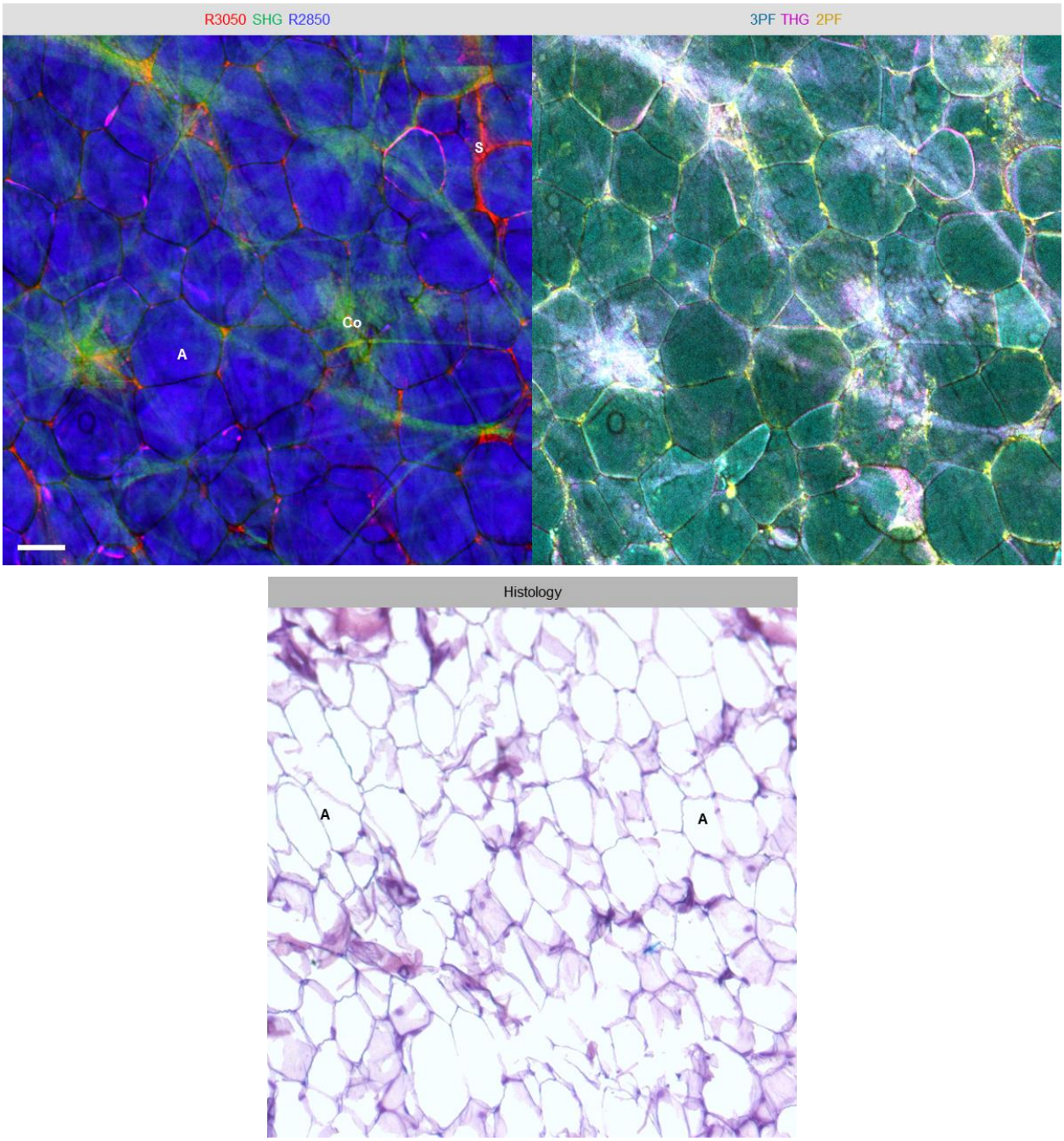

Fig. 6.14. Week 8 large-area multimodal imaging of normal breast tissue in a saline-injected rat. Morphological features: **A** adipose tissue, **Ce** hypercellularity, **S** stroma. Scale bar: 50 µm.

The large-area multimodal imaging of the normal tissue in the control group (Fig. 6.14) displays a normal adipose tissue **A** (R2850, THG, 3PF), with little stromal connective tissue **S** (R3050) and collagen fibers **Co** (SHG) within. The histology demonstrates similar features as in the multiphoton data.

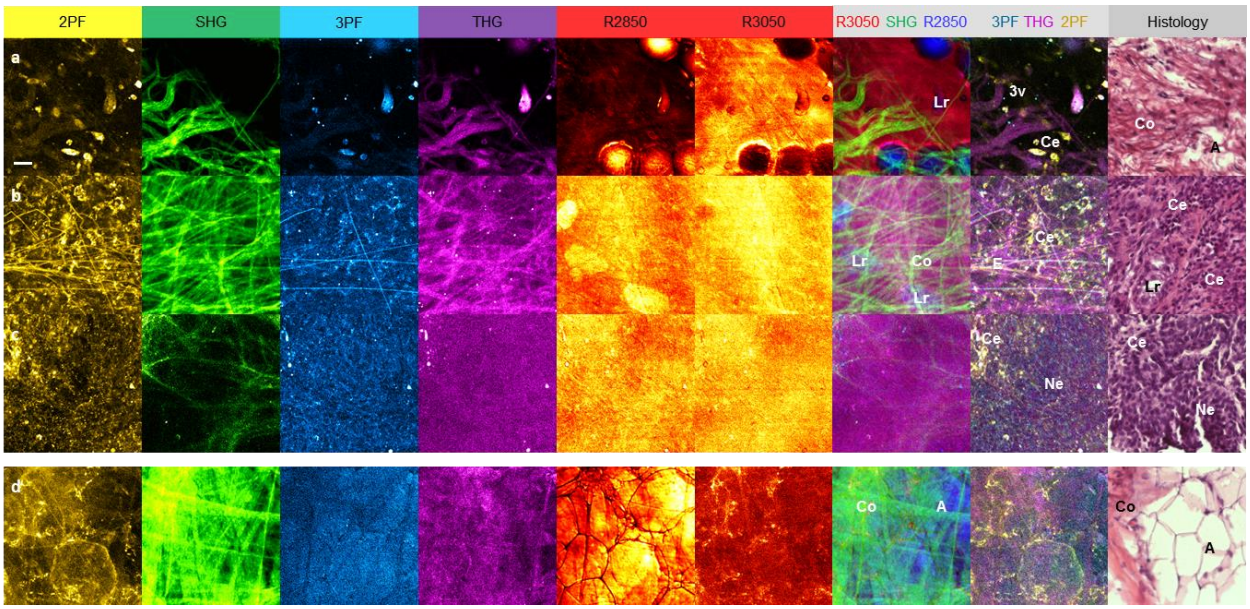

Fig. 6.15. Week 9 multimodal imaging of breast cancer development. (a-c) Carcinogen-induced experimental group. (d) Saline-injected control group. Morphological features: **A** adipose tissue, **Ce** hypercellularity, **Co** collagen fiber, **E** elastin, **Lr** lipid residual, **Ne** necrosis, **3v** 3PF-sensitive microvesicle. Scale bar: 25 µm.

In week 9, Fig. 6.15(a) displays an area away (>10 mm) from a large tumor (>3 mm in diameter). The multiphoton images present a relatively normal lipid-stromal interface. However, a few features are indicative of tumor development. The lipid residual **Lr** (R2850, THG) demonstrates high 3PF and 2PF fluorescence, and some 3PF-sensitive microvesicles **3v** are distributed in the FOV. In addition, increased cellular activity **Ce** (2PF) is observed in the proximity of the adipose tissue. The histology shows mainly fibrous connective tissue **Co** with some empty spaces which are likely adipocytes **A** and smaller LDs. Fig. 6.15(b) was acquired at the margin of the large tumor. Some isolated lipid residuals **Lr** demonstrating weak R2850 signal, and THG-sensitive microvesicles are observed. Tumorigenic cells **Ce** (2PF) are found within the collagen network **Co** (SHG). In the histology, hypercellularity is observed as abundant dark-staining nuclei in the fibrous connective tissue. Some empty areas left by the lipid residuals **Lr** are also seen in the FOV. Fig. 6.15(c) is at the center of the necrotic tumor. The images show a mesh-like cellular arrangement **Ne** (2PF, 3PF) with reduced 2PF and 3PF intensities and very little collagen fibers (SHG). Only a small portion of the cells **Ce** shows stronger 2PF fluorescence. Interestingly, there are still a few small lipid-like microvesicles (R2850) within the FOV, which also demonstrate high 2PF and 3PF signals. The histology shows mainly enlarged and dark-staining nuclei,

especially in the necrotic area **Ne**. Only very few eosinophilic features are observed in the surrounding of increased cellularity **Ce**. In the control group, Fig. 6.15(d) shows normal collagen fibers **Co** (SHG) and adipose tissue **A** (R2850). Similar morphological features are confirmed in the histology.

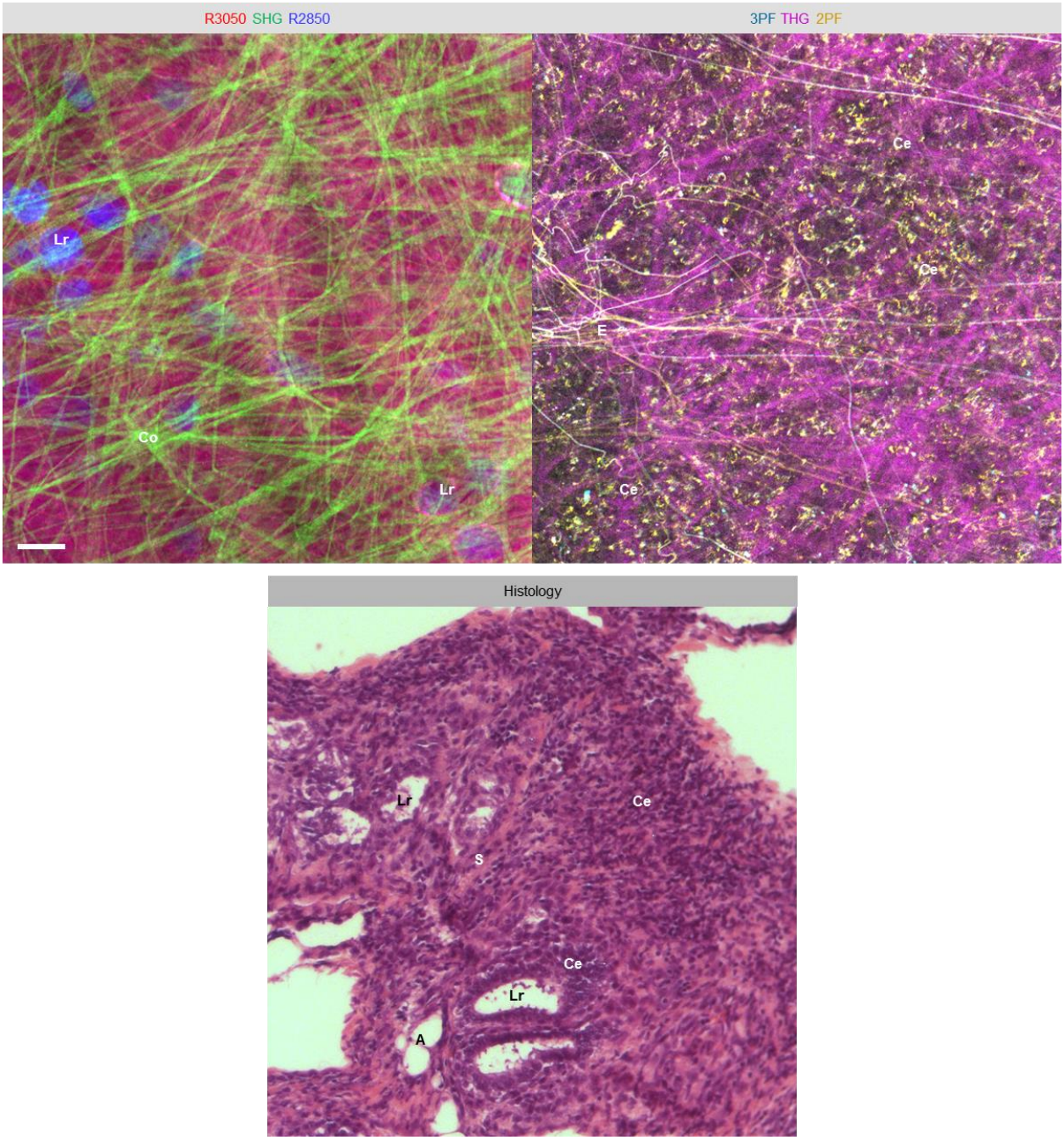

Fig. 6.16. Week 9 large-area multimodal imaging (1 of 2) of breast cancer development in a carcinogen-induced rat. Morphological features: **Ce** hypercellularity, **Co** collagen fiber, **fl** fluorescent feature, **Lr** lipid residual, **T** tumor, **S** stroma. Scale bar: 50 µm.

The large-area imaging of the carcinogen-induced animal in week 9 (Fig. 6.16) covers an extended FOV of Fig. 6.15(b). Nevertheless, the entire area demonstrates similar morphological features and multiphoton responses. A large quantity of high-2PF tumorous cells **Ce** (2PF) are observed to possess various sizes, shapes, and fluorescence intensity. The collagen fibers **Co** (SHG, THG) are relatively intact in this region. Several lipid residuals **Lr** (R2850) and the 3PF-senstivie and THG-sensitive microvesicles across the FOV are recognized. The elastin fibers **E** (2PF) are arranged more randomly, and no sign of angiogenesis is identified in this area. In the histology, the same phenotypic features are identified. Abnormally increased number of tumorous cells **Ce** is found within the FOV. The stroma **S** still contains significant amount of connective tissue, and some lipid residuals **Lr** are recognized in the tumorous stroma.

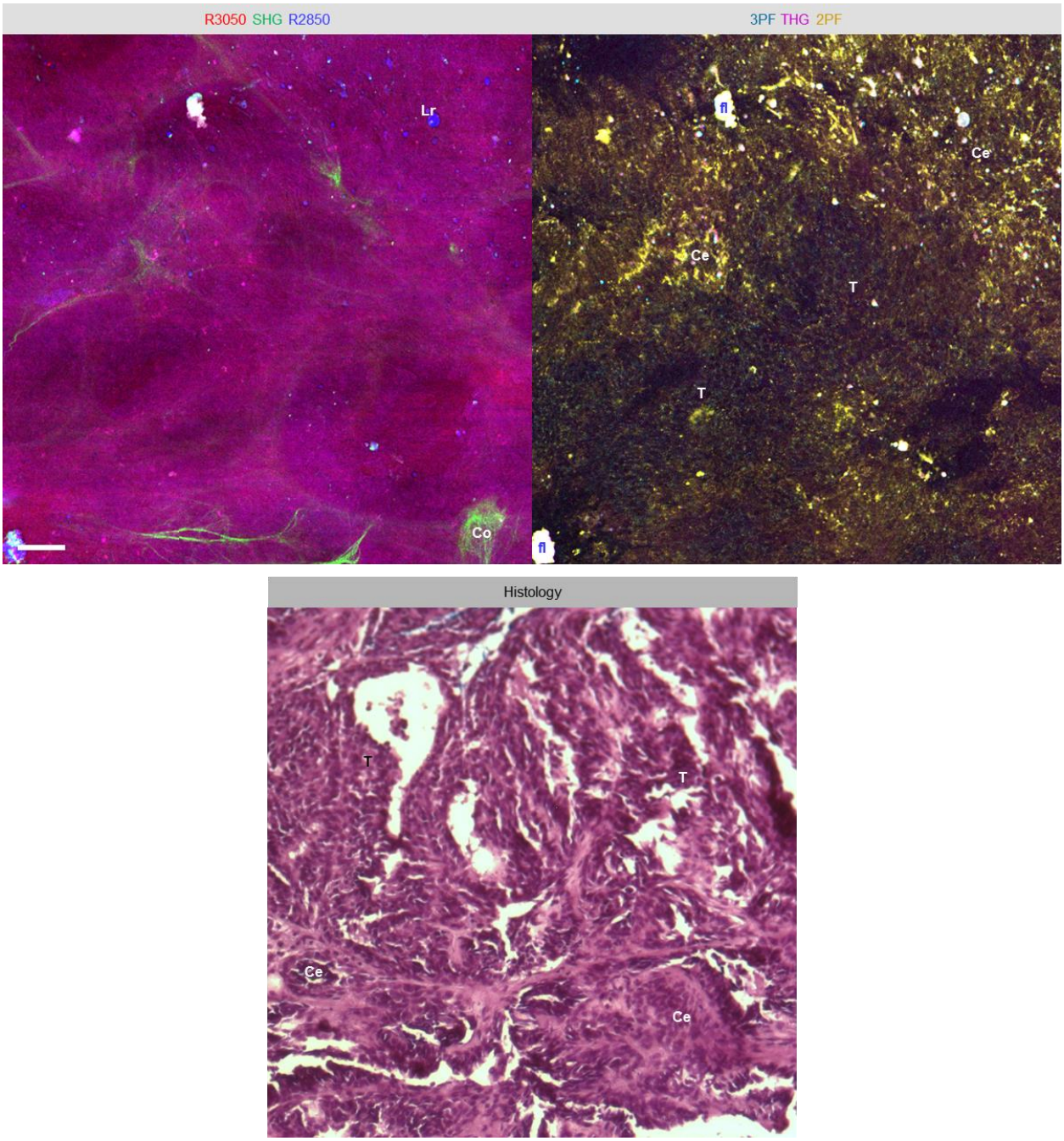

Fig. 6.17. Week 9 large-area multimodal imaging (2 of 2) of breast cancer development in a carcinogen-induced rat. Morphological features: **Ce** hypercellularity, **Co** collagen fiber, **fl** fluorescent feature, **Lr** lipid residual, **T** tumor. Scale bar: 50 µm.

Fig. 6.17 displays another large-area image in week 9, which is the extended FOV of Fig. 6.15(c). This necrotic area is also observed to be relatively homogeneous. The tumor cells **T** (2PF, 3PF) are less fluorescent and present as a mesh-like structure of several larger domains outlined by the remaining collagen fibers (SHG). Only a few areas demonstrate high-2PF cells **Ce** in the proximity of the lipid

residuals **Lr** (R2850) scattered around. Investigation of the single-modal images reveals that these small lipid residuals show very different multiphoton responses and are likely of different biomolecular compositions. Some of them even demonstrate high SHG signal, which is likely originating from the crystallization of cholesterol[77]. In the H&E histology, tumor areas **T** with abundant dark-staining nuclei and the increase cellularity **Ce** within the connective tissue are found. Some of the tumorous areas appear to be empty and are likely the necrotic regions that are lost during the histological processing.

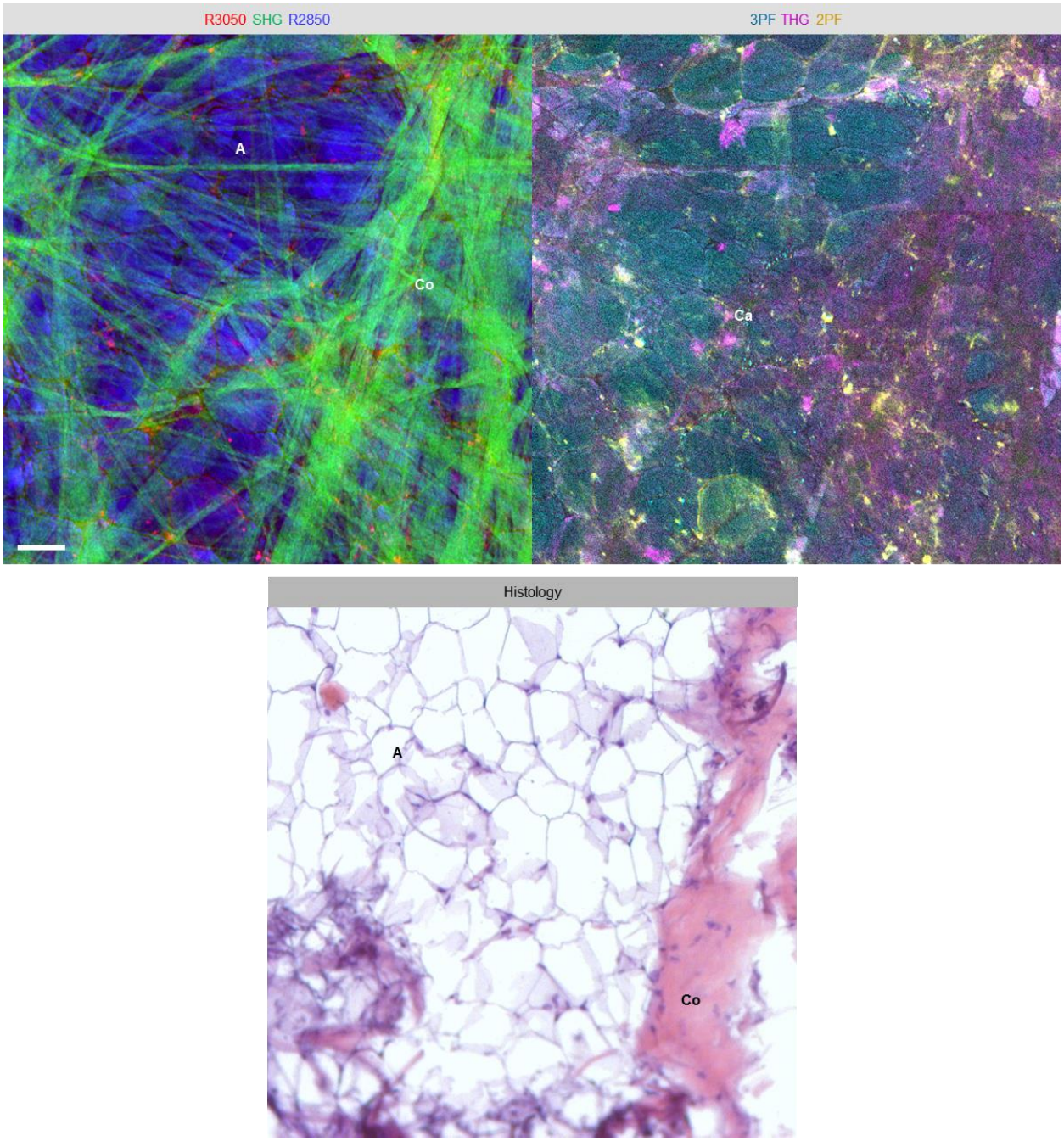

Fig. 6.18. Week 9 large-area multimodal imaging of normal breast tissue in a saline-injected rat. Morphological features: **A** adipose tissue, **Ca** capillary, **Co** collagen fiber. Scale bar: 50 µm.

The large-area imaging in week 9 (Fig. 6.18) demonstrates normal adipose tissue **A** (R2850, THG, 3PF) as well as a relatively larger amount of collagen fibers **Co** (SHG) and high-2PF biomolecules. Note also that there are a few capillaries **Ca** (3PF) with aligned 3PF-sensitive microvesicles in between the LDs. The adipose tissue **A** and the fibrous connective tissue **Co** are also observed in the histology.

6.4. Remarks on the angiogenic states based on the 3PF-sensitive microvesicles

In this section, the states of the angiogenesis are investigated based on the density of the 3PF-sensitive microvesicles in addition to the 2PF and the SHG features in the surrounding. The various angiogenic structures present in the large-area image in week 7 of the BCa development (Fig. 6.9) are examined. Fig. 6.19 demonstrates the merged SHG-3PF-2PF (green-cyan-yellow) image, and the identified angiogenic features within the FOV. Features labeled (a-d) are the more developed blood vessels with detectable elastin walls, and (a) even has a well-defined SHG outer layer. These developed blood vessels have less 3PF-sensitive microvesicles. Features labeled (e-g) are the developing blood vessels with solid 2PF-sensitive walls that likely consist of tumorigenic endothelial cells. These developing blood vessels present more 3PF-sensitive microvesicles. Features labeled (h,i) are the forming elastic lamella with few 3PF-sensitive microvesicles. Features labeled (j-n) are the initiating angiogenic structures with abundant 3PF-sensitive microvesicles but no clear elastin wall or 2PF-sensitive cell wall. Features labeled (o,p) are the capillaries with solid 2PF-sensitive walls which are attached by the 3PF-sensitive microvesicles.

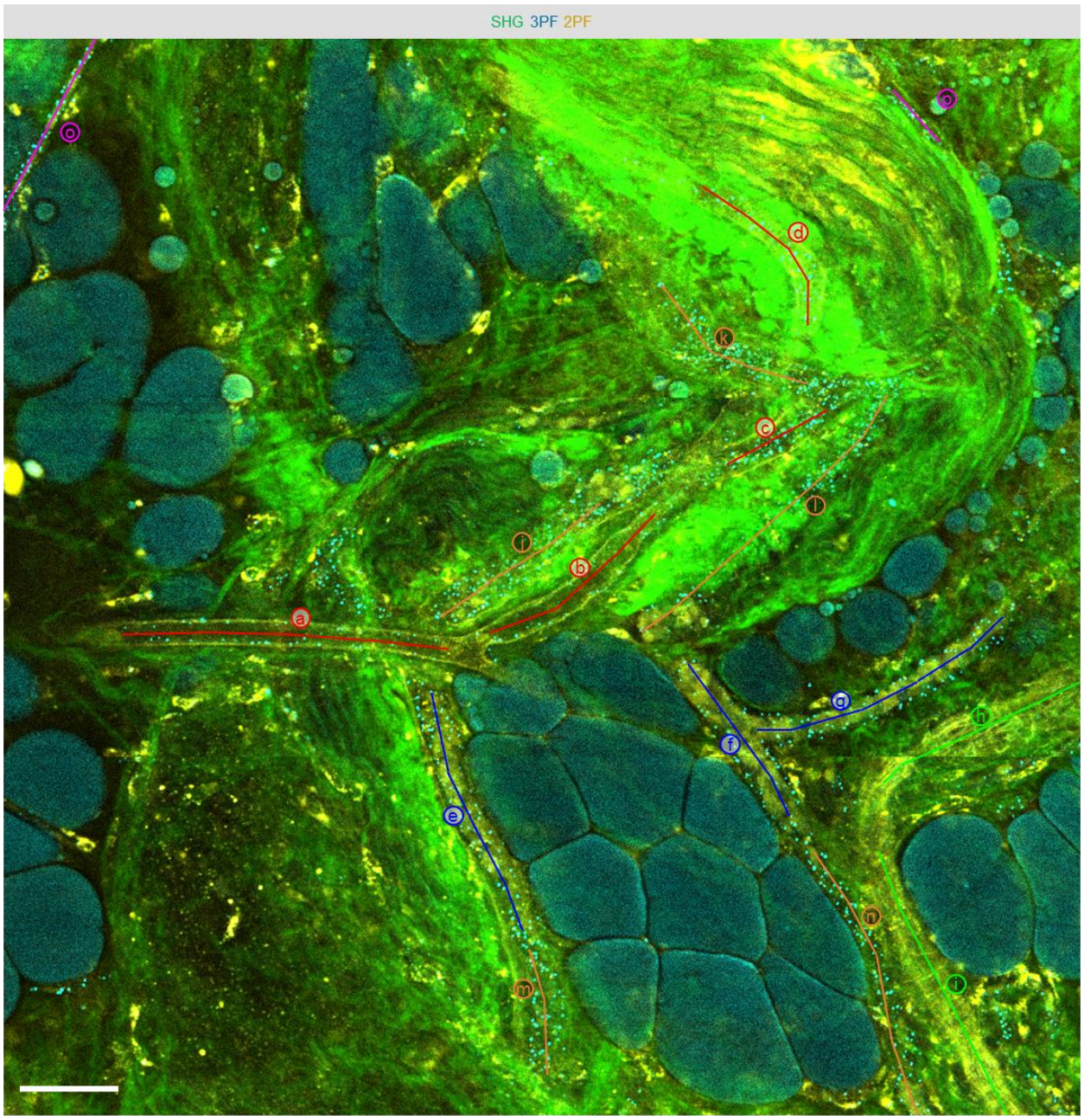

Fig. 6.19. Various angiogenic structures in week 7 of breast cancer development in a carcinogen-induced rat. (a-d) Structures with well-defined elastin wall; (e-g) structures with solid 2PF-sensitive wall; (h,i) structures with forming elastic lamella; (j-n) structures with 3PF-sensitive vesicles but no well-defined wall; (o,p) capillaries with well-defined 2PF-sensitive wall and 3PF-sensitive vesicles but smaller in dimension. Scale bar: 50 µm.

Table 6.3 summarizes the area coverage of the 3PF-sensitive microvesicles, the length and the width of the angiogenic structures, and the line (area) density of the 3PF-sensitive microvesicles of the identified features. The line (area) density is defined as the 3PF-sensitive microvesicle area divided by the angiogenic structure length (area). Fig. 6.20 displays the line density and the area density of the 3PF-sensitive microvesicles with respect to the width of the identified angiogenic structures. The difference between each feature is more obvious in the line density plot as compared to the area density plot. The developed blood vessel with well-defined elastin wall has a lower line density (a,b) but can also serve as the pathways to deliver the microvesicles to the angiogenic sites (c,d) where a higher line density is observed. On the contrary, the initiating angiogenic sites labeled (j-n) present higher line density. The developing blood vessels labeled (e-g) have an intermediate line density of 3PF-sensitive microvesicles. The forming elastic lamellas labeled (h,i) have a larger width and a lower 3PF-sensitive microvesicle line density. The capillaries labeled (o,p) have comparable line density as those with the solid 2PF-sensitive vessel wall but much narrower width. The analysis demonstrates that the density of the 3PF-sensitive microvesicles as well as the dimensions and the vascular structures observed in the 2PF and the SHG images can serve as guiding factors to differentiate angiogenic features in the BCa development.

Table 6.3. The area coverage of the 3PF-sensitive microvesicles, the length and the width of the tubular structures, and the line and the area density of the 3PF-sensitive microvesicle of the identified angiogenic features in Fig. 6.19.

Label	3PF-sensitive microvesicle area (μm^2)	Angiogenic structure length (μm)	Angiogenic structure width (μm)	3PF-sensitive microvesicle line density (μm^2/ μm)	3PF-sensitive microvesicles area density (%)	2PF elastin wall	2PF solid wall	2PF elastin net	SHG collagen wall
a	78.25	167.25	11.75	0.47	3.98	v			v
b	56.75	111.50	14.50	0.51	3.51	v			p
c	147.50	74.00	16.75	1.99	11.90	v			p
d	116.00	102.75	14.25	1.13	7.92	v		v	p
e	191.00	140.50	14.25	1.36	9.54	v	v		P
f	135.25	126.00	14.50	1.07	7.40		v		
g	170.75	143.75	10.25	1.19	11.59		v		
h	40.00	116.20	22.00	0.34	1.56			v	
i	29.00	148.00	16.25	0.20	1.21	v		v	
j	227.75	98.75	14.75	2.31	15.64	p	p	p	p
k	270.00	105.25	15.25	2.57	16.82	p		p	p
l	203.25	176.25	14.50	1.15	7.95		p		p
m	106.00	69.50	23.00	1.53	6.63	p		p	P
n	163.50	139.00	12.50	1.18	9.41	p			
o	128.00	100.75	5.00	1.27	25.41		v		
p	48.25	41.00	3.25	1.18	36.21		v		P

Abbreviations: “v”: with the identified morphology; “p”: with the partially formed morphology. The labels are colored according to the features identified in Fig. 6.19.

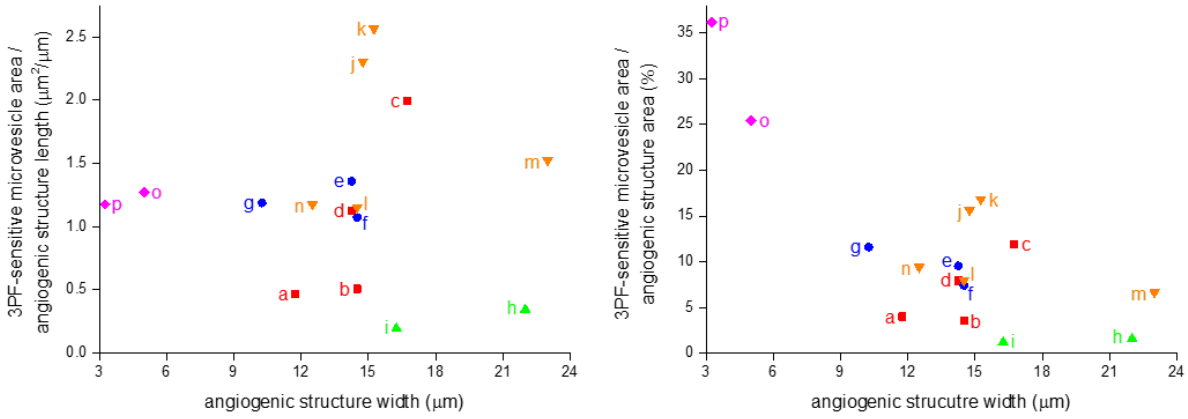

Fig. 6.20. The line density (left) and the area density (right) of the 3PF-sensitive microvesicles with respect to the width of the angiogenic structures. Note that the data points are colored according to the features identified in Fig. 6.19.

It is worth noting that the different angiogenic features are initially categorized based on their morphology in the SHG-3PF-2PF image. Nevertheless, these features can be related to and be affecting

each other in the complex neovascularization process. The features labeled (c,e,j,m) are connected, the features labeled (c,j,k) are merged together, and the feature labeled (h) presents a small segment of the 2PF-sensitive solid wall like those in features (e-g). These observations confirm the same functionality of these seemingly different tubular structures in the multiphoton images.

To summarize this chapter, label-free multimodal multiphoton molecular imaging is employed to investigate BCa development in a pre-clinical rat mammary tumor model through a 9-week longitudinal study. Diverse morphological features and changes are identified in the mammary tumor microenvironments during early- and late-state of BCa development. The observations not only agree well the H&E-stained histology but also provide rich and complimentary information from different modalities. In the next chapter, the multiphoton molecular profile analysis will be performed to analyze the molecular contents of the phenotypic features in the multiphoton images, facilitating identification of the multiphoton molecular biomarkers during the mammary tumor development.

7. MULTIPHOTON MOLECULAR PROFILES AND BIOMARKERS IN BREAST CANCER DEVELOPMENT

In this chapter, the multiphoton molecular profile (MPMP) analysis is employed to investigate the molecular contents of the morphological features in multiphoton images in the previous chapter. The 2PF, SHG, 3PF, THG, R2850, R3050 signals, and the hyperspectral CARS spectrum provide an *in situ* and label-free multiphoton profile for identifying biomolecules and their transformations in the mammary tumor microenvironments. The multiphoton molecular biomarkers during early and late mammary tumor development are discussed in the context of the phenotypic features revealed by multiphoton imaging.

7.1. Multiphoton molecular profiles of biomolecules in breast cancer development

Due to the availability of the improved 3PF imaging starting at week 6, the MPMP analysis from weeks 0 to 5 and that from weeks 6 to 9 adapts different scales when displaying the 3PF signal. Also, the pseudo-histology contains a contribution from the 3PF images starting at week 6, which is colored yellow and shows mostly the 3PF-sensitive microvesicles. Throughout the MPMP analysis, there are occasionally extremely strong signals. In this case, the scale of the radar plot is adjusted to show the special behavior, and the corresponding modality in the radar plot is highlighted in red color.

7.1.1. Molecular profiles in early breast cancer development

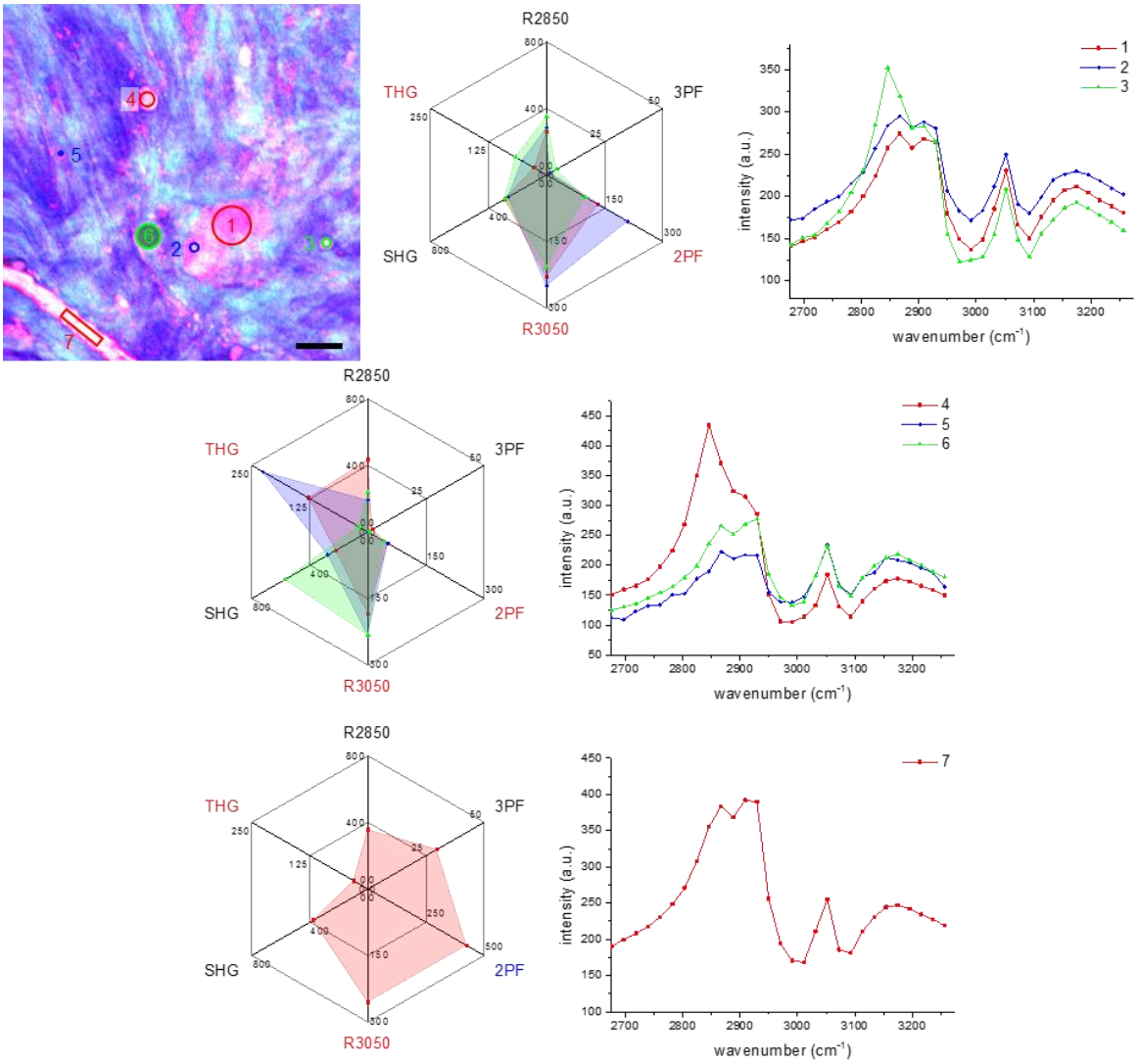

Fig. 7.1. Multiphoton molecular profiles of cancerous rat mammary tissue in week 1 of breast cancer development. Scale bar: 25 µm.

In the selected image in week 1 (Fig. 7.1), area 1 is within the high-2PF cell cluster, which shows strong 2PF and R3050 signals in the radar plot and a protein-like CARS spectrum marked with CH_2 stretching at 2930 cm^{-1}, CH aromatic stretching at 3050 cm^{-1}, and the co-existing water OH stretching at >3200 cm^{-1}. Also within the cell cluster, area 2 contains the THG-sensitive microvesicles which demonstrates higher THG signal and higher 2PF signal. Area 3 displays a similar profile as compared to area 2, but with slightly higher THG signal and slightly lower 2PF signal. However, the CARS spectrum demonstrates a

lipid-like feature with a peak at 2850 cm^{-1}, but still possesses the protein peak at 3050 cm^{-1}. As compared to area 3, area 4 exhibits higher THG signal, lower 2PF signal, and a higher 2850 cm^{-1} peak in the CARS spectrum. The small difference in areas 3 and 4 suggests the co-occurrence of a decrease in lipid composition (R2850, THG) and an increase of 2PF fluorescence and protein composition (R3050). The observation is indicative of lipid degradation and protein synthesis. From the non-lipid nature of this fluorescent material and the excitation and detection wavelengths used, one can infer that the 2PF is likely from FAD[22,92]. Area 5, targeting the THG-sensitive microvesicles, presents an intense THG signal and a protein-like CARS spectrum. Thus, even though they are oftentimes found in the proximity of the altered lipid, they possess a non-lipid molecular composition. While THG has been known to generate imaging contrast form lipid[22], collagen[75], nerve fibers[99], myofibrils[88], hemoglobin[83], and other biomolecules (see Table 2.1), it is possible that the THG-sensitive microvesicles here are hemoglobin, but can also be new biomolecules that are detectable by THG imaging. Area 6 is dense collagen fibers in the stroma, demonstrating high SHG and high R3050 signals. Area 7 is the mammary duct, showing high 2PF, 3PF, R3050 signals, and a protein-like CARS spectrum.

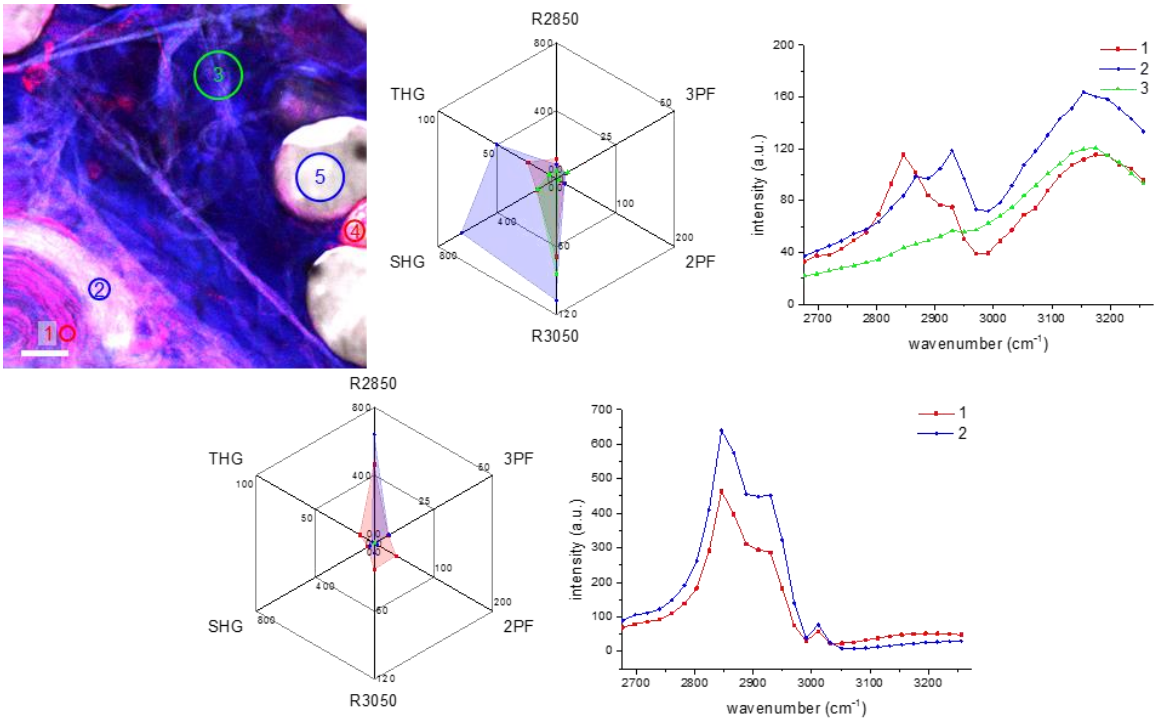

Fig. 7.2 Multiphoton molecular profiles of cancerous tissue in week 2 of breast cancer development. Scale bar: 25 µm.

In week 2, a representative image showing neural tissue, adipose tissue, and connective tissue is analyzed (Fig. 7.2). Area 1 is an axon fiber, consisting of both lipid and protein compositions which show moderate signal at 2850 cm^{-1} in the CARS spectrum. The lipid composition demonstrates a moderate THG response. Area 2 is located at collagenous connective tissue, showing high SHG and THG signals, and can be identified as epineurium tissue surrounding the nerve fibers. Area 3 is of a stromal area with little collagen fibers within. The CARS spectrum shows mostly the water contribution with a gradually increasing intensity toward higher wavenumbers. The slight fall-off beyond 3200 cm^{-1} is due to reduced overlap of the pump and Stokes beams in spectral focusing CARS in our setup. Area 4 is targeting a smaller LD demonstrating weak 2PF signal. In comparison, area 5 is a normal LD with stronger R2850 signal and higher intensity in the CARS spectrum, but no significant contribution from other modalities is observed. The results again relate the generation of FAD to the loss of lipid composition. An interesting feature in this area is that the CARS spectrum presents no peak at 3050 cm^{-1}. While this area demonstrates no obvious sign of tumor formation, the CH aromatic vibration at 3050 cm^{-1} can serve as a marker of carcinogenesis.

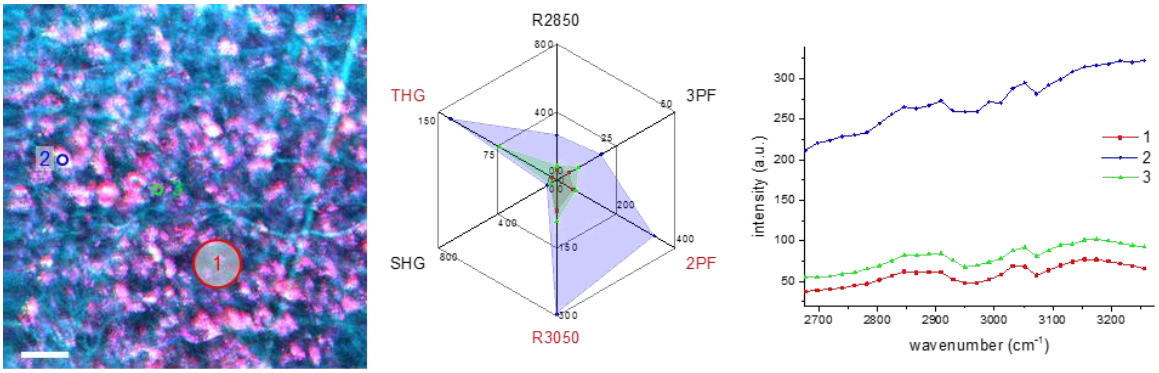

Fig. 7.3. Multiphoton molecular profiles of a cancerous tissue in week 3 of breast cancer development. Scale bar: 25 µm.

In an image set showing proliferation of tumor cells in week 3 (Fig. 7.3), high-2PF and high-3PF cells, reduced collagen fibers, and THG-sensitive microvesicles are recognized in the FOV. In a void-like circular area 1, low multiphoton signals from all the modalities are observed. Area 2 is targeting a cluster of microvesicles showing intense THG and strong 3PF signals within a high-2PF cell. The high R3050 signal observed is due to fluorescence background, as is evident by the CARS spectrum showing a vertical shift as compared to those of areas 1 and 3. The higher 2PF and 3PF signals indicate increased amount of FAD and NAD(P)H, which is likely due to the interaction of the THG-sensitive microvesicles and the cancerous cells. To validate the hypothesis, THG-sensitive microvesicles outside the cytoplasm in area 3 are investigated. The radar plot shows prominent THG but lower 2PF and 3PF signals. The result clearly distinguishes the free THG-sensitive microvesicles from those interacting with the tumor cells. The associated abnormal up-regulation of FAD and NAD(P)H in the tumor cells indicates higher metabolism in the tumor cell[214,219,220,223].

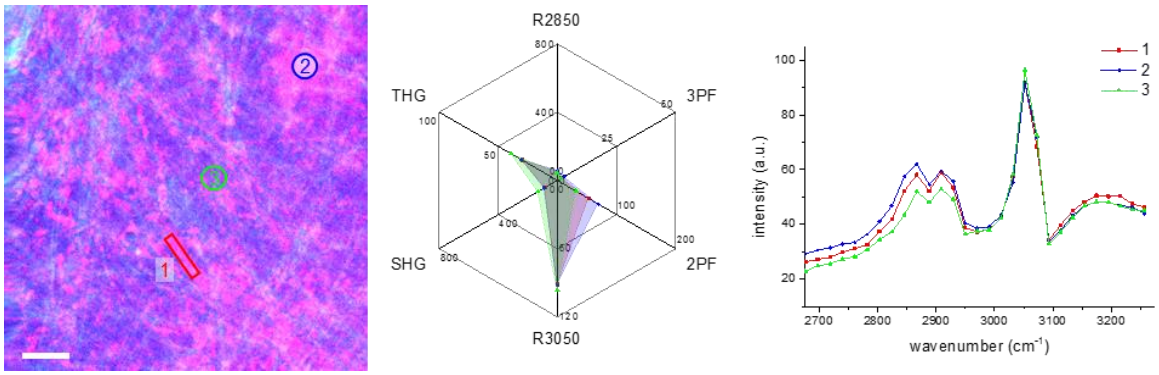

Fig. 7.4. Multiphoton molecular profiles of a cancerous tissue in week 4 of breast cancer development. Scale bar: 25 µm.

In the representative image in week 4 (Fig. 7.4), angiogenesis is recognized in the tumorous stroma, which demonstrates the characteristics of hypercellularity, reduced collagen, and lipid degradation. The selected areas within the FOV all show very similar MPMPs. The radar plots demonstrate high R3050, moderate 2PF and THG, and low R2850 and SHG signals, while the CARS spectra show a protein-like signature with a strong response at 3050 cm^{-1}. Area 1 is at the angiogenic site, showing high 2PF signal from the blood vessel wall. Area 2 is at the lipid residual site, which is reflected by the slightly higher signal at 2850 cm^{-1} in the spectrum. The lipid residual also demonstrates 2PF signal stronger than that of the angiogenic site. Area 3 is at the cancerous stroma. Lower 2PF, higher SHG, lower CARS signal around 2850 to 2930 cm^{-1}, and higher CARS signal at 3050 cm^{-1} are identified as compared to the other two areas.

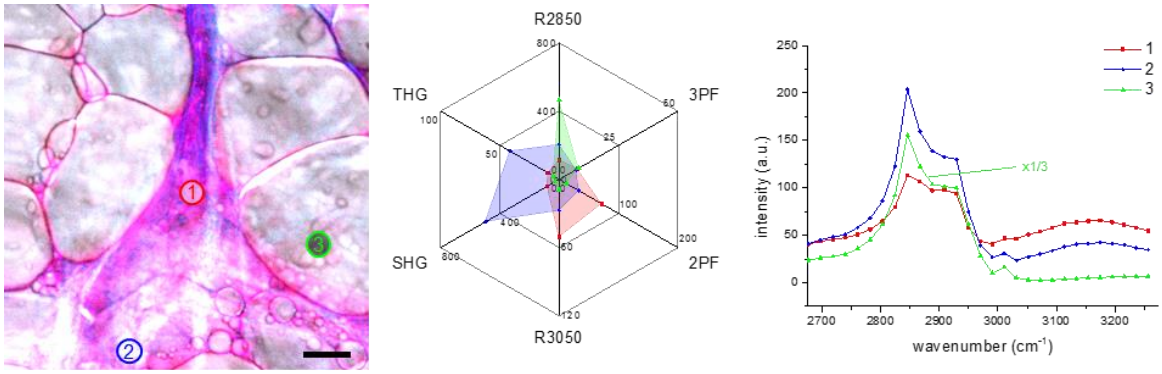

Fig. 7.5. Multiphoton molecular profiles of a normal mammary gland in the saline-injected animal in week 4. Scale bar: 25 µm.

Fig. 7.5 demonstrates a representative image of normal mammary gland from the control animal in week 4. Areas 1 and 2 are selected in the connective tissue, and their difference can be easily distinguished by the multiphoton responses. While area 1 has higher 2PF and R3050 signals, area 2 has higher SHG and THG signals. In area 1, the higher 2PF is derived from higher FAD fluorescence, elastin fibrils and other high-2PF substances, and the higher R3050 points us to higher protein composition. Nevertheless, the peak at 3050 cm^{-1} is not observable in the CARS spectrum, indicating that the R3050 contribution is from water molecules. In area 2, the higher SHG and THG signals designate higher collagen density. Interestingly, the peak at 3050 cm^{-1} is also not discernable in the CARS spectrum. The lack of 3050 cm^{-1} peak in the stroma in the control animal strongly suggests this CH aromatic vibration

can serve as a carcinogenic protein biomarker. For comparison, area 3 displays a normal adipose tissue with a strong R2850 signal and a typical lipid CARS spectrum.

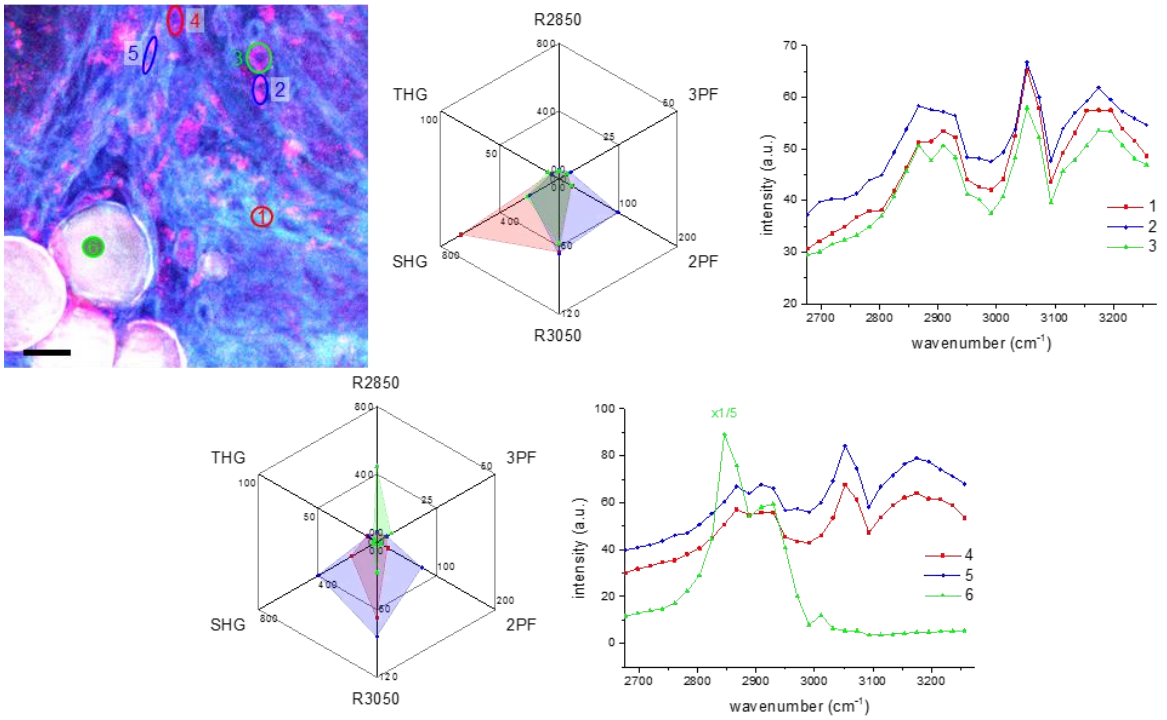

Fig. 7.6. Multiphoton molecular profiles of a cancerous tissue in week 5 of breast cancer development. Scale bar: 25 μm.

In week 5 (Fig. 7.6), a lipid-stroma interface demonstrating collagen reorganization and high cellular activities is investigated. In area 1 of locally dense collagen, intense SHG signal is confirmed in the radar plot, and higher 2930 cm^{-1} signal relative to 2850 cm^{-1} signal are observed in the CARS spectrum. Area 2 and 3 are targeting two cells with different multiphoton responses. Cell 2 shows higher 2PF signal (4.7-fold) as compared to cell 3, while cell 3 shows higher THG signal (1.6-fold) as compared to cell 2. However, their CARS spectra show no obvious difference. These results demonstrate the capability of multimodal imaging to distinguish two cell types based on their intrinsic multiphoton response. The results can be further confirmed by cells in areas 4 and 5 showing similar MPMPs as cells 3 and 2, respectively. Finally, area 6 is located within a large LD, demonstrating strong R2850 signal in the radar plot and the typical lipid spectrum with a major peak at 2850 cm^{-1} and a minor peak at 2930 cm^{-1}.

7.1.2. Molecular profiles in late breast cancer development

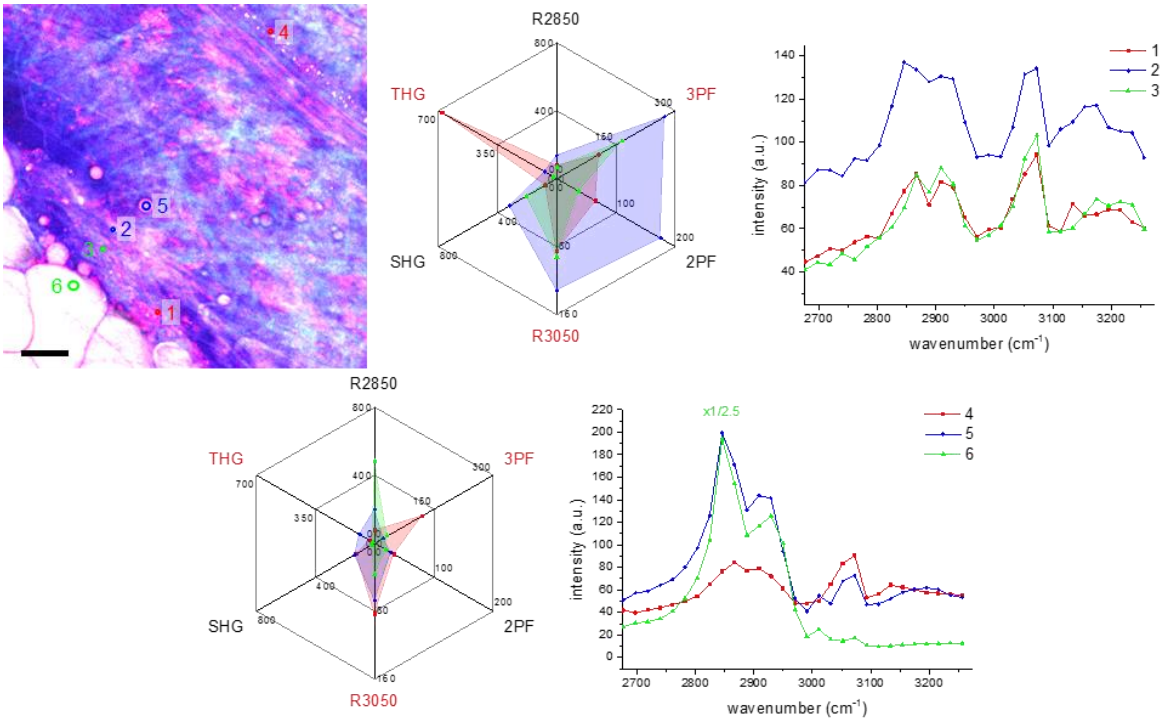

Fig. 7.7. Multiphoton molecular profiles of a cancerous tissue in week 6 of breast cancer development. Scale bar: 25 µm.

In week 6, Fig. 7.7 shows MPMPs of several selected areas targeting different microvesicles observed in the multiphoton images. Position 1 demonstrates very intense THG, moderate 3PF, and moderate 2PF signals. The CARS spectrum illustrates a protein-like signature. This microvesicle presents similar molecular profiles as compared to the area 5 in Fig. 7.1 and is likely hemoglobin[83]. With one more dimension of information provided by 3PF, this type of microvesicle also shows high 3PF signal. Position 2 is a microvesicle demonstrating extreme 3PF and R3050 signals, and intense 2PF signal. The CARS spectrum shows a peak at 2850 cm^{-1} higher than that of 2930 cm^{-1}, indicating the lipid-derived nature of the microvesicle. The high 2PF and 3PF fluorescence suggests up-regulated FAD, NAD(P)H, and therefore the metabolic activity associated with the lipid contents. Position 3 is a 3PF-sensitive microvesicle found in the proximity of adipose tissue. However, the CARS spectrum shows the protein nature of the microvesicle. Interestingly, the radar plot and the CARS spectrum are very similar to that of the 3PF-sensitive microvesicles in an angiogenic site at position 4. Therefore, the microvesicle at position

3 is also angiogenesis-associated. A detailed examination of the 2PF and 3PF images [Fig. 6.7(b)] reveals a small amount of elastin fibers (2PF) and aligned 3PF-microvesicles (3PF) from position 1 extending to position 3, which are likely initiating the angiogenic process. Position 5 is an isolated LD. A significant decrease in CARS signal in the CH stretching region in comparison to the larger LD at position 6 demonstrates the loss of lipid contents, while an increase of the signal at 3050 cm^{-1} shows an increase in the protein contents. The lipid-protein transformation is reflected on the radar plot as increase of 2PF and R3050 signals and decrease of R2830 and 3PF signals.

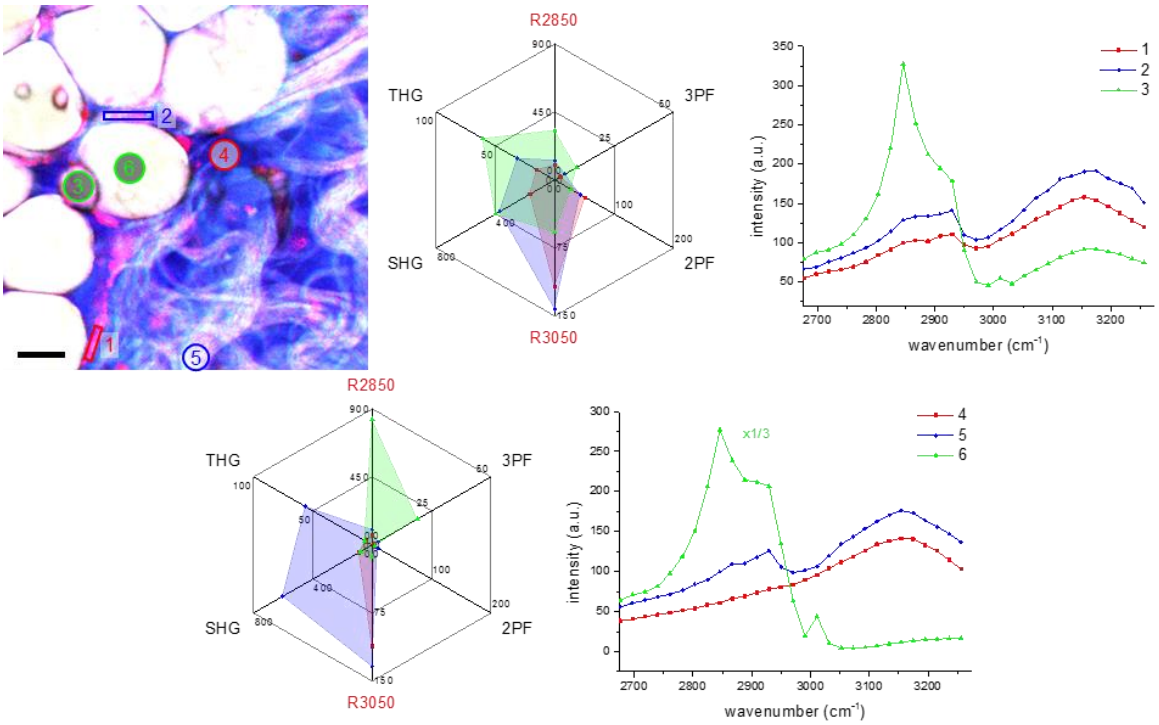

Fig. 7.8. Multiphoton molecular profiles of a normal mammary gland in the saline-injected animal in week 6. Scale bar: 25 µm.

Fig. 7.8 demonstrates a representative site of a normal mammary gland from a control animal in week 6. Areas 1 and 2 are targeting FAD-fluorescent cells surrounding the LDs. Area 2 shows higher SHG and THG responses due to higher collagen content in the area. Area 3 presents a feature resembling a smaller LD. While the area displays the characteristics of a lipid-like CARS spectrum, the higher SHG, THG, and R3050 signals suggest a difference in the molecular composition as compared to most of the LDs, which are represented by area 6. Based on its close proximity to the LDs, the lipid-like spectrum, and the higher

SHG signal, this feature is likely a small LD containing a higher level of cholesterol. Area 4 and 5 are chosen within the stroma. Area 4 demonstrates high R3050 signal in the radar plot, which is thought to originate from water based on its CARS spectrum. Area 5 shows higher SHG and THG signals due to the higher collagen contents. Interestingly, for all the non-lipid areas (1, 2, 4, 5) within the FOV, no 3050 cm^{-1} peak is observed, confirming that the CH aromatic stretching vibration at 3050 cm^{-1} is strongly indicative of tumorigenesis.

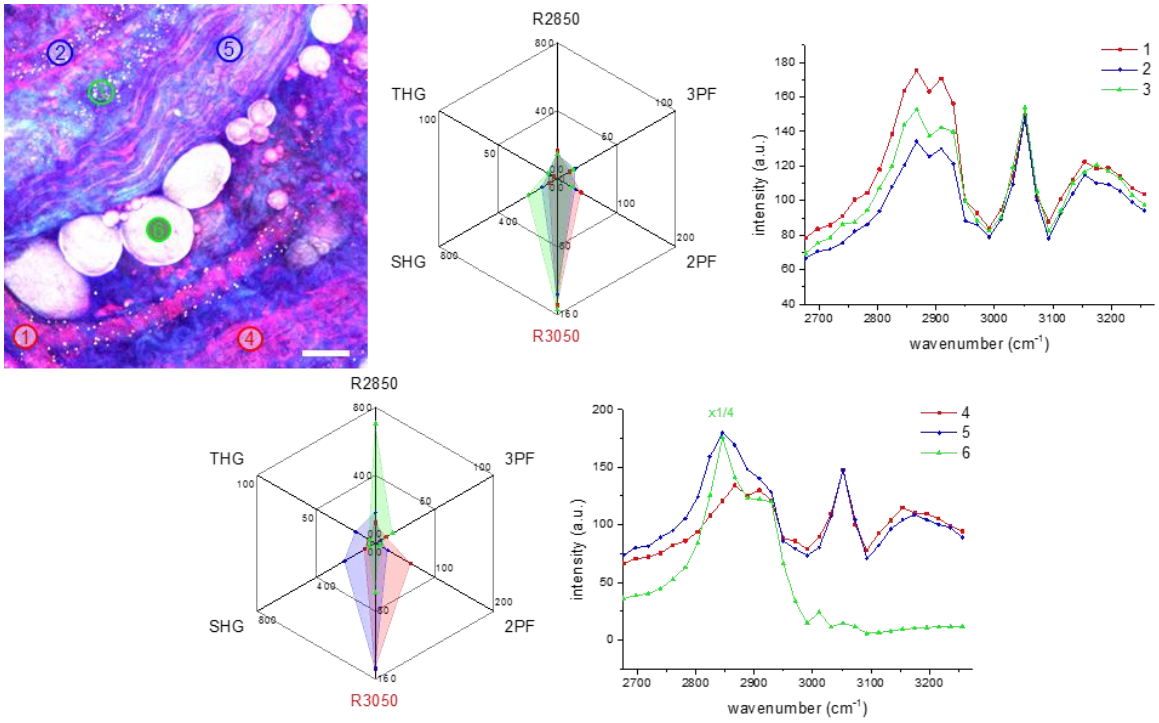

Fig. 7.9. Multiphoton molecular profiles of a cancerous tissue in week 7 of breast cancer development. Scale bar: 25 µm.

Fig. 7.9 displays a representative image from week 7 of the BCa development. Various angiogenic stages are identified within the FOV. Areas 1, 2, and 3 show a similar molecular profile with only intense R3050 signal in the radar plot and a protein-like CARS spectrum. A detailed comparison of the multiphoton signals in the radar plots show the subtle differences between them. In area 1, the blood vessel shows higher 2PF signal from the blood vessel wall and lower 3PF signal due to fewer 3PF-sensitive microvesicles. In area 2, the blood vessel shows lower 2PF signal from the developing vessel wall and higher 3PF signal due to more 3PF-sensitive microvesicles. In area 3, only 3PF microvesicles are found

without an observable vessel wall. However, higher SHG signal in this region suggests that the microvesicles are being transported through the space in between the aligned collagen fibers.

Area 4 is of the elastin fibrils forming crosslinks between each other. The hyperspectral CARS imaging (data not shown) visualizes moving substances with the elastin fibrils, which are the same as those in area 1, indicating that the elastin fibrils are likely a growing blood vessel and forming elastic lamella. The MPMP also resembles that of area 1. Within area 5 are the nerve fibers, which are known to possess a mixture of lipid and protein contents and can also be visualized by THG imaging. The lipid and protein composition can be recognized in the CARS spectrum showing the protein signatures of the aromatic CH stretching at 3050 cm^{-1} and the broadband water response at >3200 cm^{-1}, as well as the lipid signature of CH_2 vibration at 2850cm^{-1}. Area 6 is located within a LD, demonstrating a typical lipid profile of strong R2850 and prominent CH_2 stretching vibration at 2850 cm^{-1}.

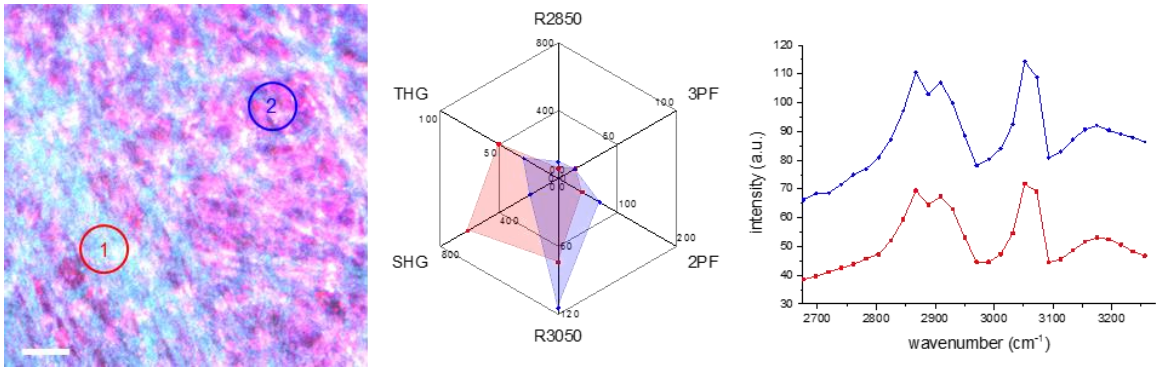

Fig. 7.10. Multiphoton molecular profiles of a cancerous tissue in week 8 of breast cancer development. Scale bar: 25 µm.

Fig. 7.10 shows the MPMPs of selected areas in a cancerous site in week 8. While the FOV is within a large tumor, their CARS spectra show similar vibrational signatures, except that the spectrum of area 2 demonstrates a horizontal shift due to the fluorescence background. Nevertheless, their radar plots illustrate very different trends. In area 1, with more connective tissue, higher SHG and THG signals generated from the collagen fibers are observed. In area 2, with more tumor cells, higher 2PF signal from FAD is identified.

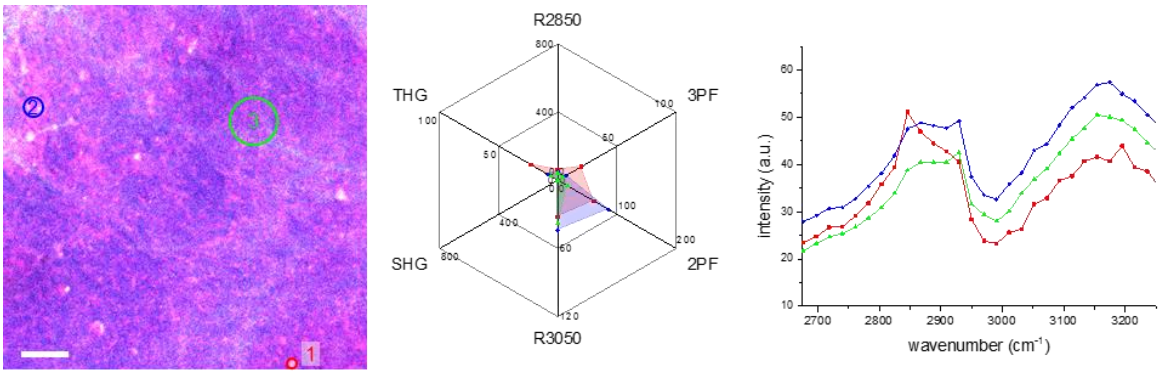

Fig. 7.11. Multiphoton molecular profiles of a cancerous tissue in week 9 of breast cancer development. Scale bar: 25 µm.

In a necrotic site in week 9, the most obvious feature is the loss of the collagen contents, as can be noted by the vanishing SHG signals in all three different characteristic areas. At location 1, a small spot resembling a lipid residual demonstrates moderate 2PF and 3PF signals. The higher THG signal suggests its lipid composition, which is confirmed by its CARS spectrum showing a moderate peak at 2850 cm^{-1}. From these correlations, one can infer that the molecular composition of this spot possesses a small amount of lipid and intrinsic fluorophores that are likely to be FAD, retinol, and NAD(P)H. In area 2, a slightly higher FAD fluorescence and protein-water signal in the CARS spectrum indicates the tumor cell activity, which is not observable in area 3, a site of necrosis.

7.2. Multiphoton molecular biomarkers in breast cancer development

7.2.1. Molecular biomarkers in early breast cancer development

FAD-fluorescent cells (2PF)

As a principal electron donor in the mitochondrial electron-transport chain, FAD is an important endogenous fluorophore indicative of cellular metabolism. A decrease of FAD fluorescence in BCa cell lines has been recognized, as compared to normal mammary cell lines[219]. An increase of FAD fluorescence and an increase of its lifetime have been identified in invading tumor cells as compared to the primary tumor mass[214]. In the results of early BCa development presented here, FAD-rich cells can already be visualized by 2PF imaging, with increased cell number [Fig. 6.4(b), Fig. 6.5(c), Fig. 6.6(a)]

and in the form of cell aggregates [Fig. 6.2(b), Fig. 6.3(a)]. These cellular components demonstrate morphological difference and contain tumor cells, epithelial cells, fibroblasts, endothelial cells, and other cell types. While various FAD-rich cells can be detected by 2PF, each cell type may play a different role in carcinogenesis. For example, the presence of activated fibroblasts is relevant to collagen reorganization and elastin synthesis to facilitate tumor formation[242].

NAD(P)H-fluorescent cells (3PF)

NAD(P)H is a principal electron donor in the mitochondrial electron-transport chain indicative of cellular metabolism. An increase of NAD(P)H fluorescence and a decrease of its lifetime have been related to down-regulated cellular metabolism[220]. An increase of NAD(P)H fluorescence has been found in BCa cells as compared to normal mammary epithelial cells[219]. Among the FAD-fluorescent cells, the tumor cells in Fig. 6.4(b) can also be visualized by 3PF imaging, suggesting a high NAD(P)H level. The higher cellular NAD(P)H fluorescence observed is in concert with tumorigenesis. However, these tumor cells also demonstrate high 2PF signal from FAD, which differs from the result of low cellular FAD fluorescence in the tumor mass[214]. Results presented here suggest that in the imaging site, the cellular metabolism is transforming from oxidative phosphorylation to aerobic glycolysis. Therefore, in this intermediate stage, both high FAD and NAD(P)H levels are contributing to high 2PF and 3PF signals, respectively.

Elastin organization (2PF)

The presence and the arrangement of elastin fibers are identified as important biomarkers in early BCa development. In the cancerous stroma, elastin is found as fibers co-localized with dense collagen fibers [Fig. 6.2(a,b), Fig. 6.5(a,d)], fibers in fibrocystic breast [Fig. 6.3(b), Fig. 6.5(b)], and net- or sheet-like features interplaying with collagen organization [Fig. 6.4(a), Fig. 6.5(c), Fig. 6.6(c,d)]. Functionally, elastin fibers maintain the tissue shape upon stretching or contracting. In these data, most of the elastin fibers co-localized with the collagen fibers are likely to provide tissue elasticity. More importantly, because the elastic lamella and elastin fibers in a blood vessel wall can be visualized by 2PF imaging as

well[238], the presence of aligned elastin fibers can be indicative of angiogenesis. The aligned elastin fibers of net- or sheet-like features are likely undergoing neoangiogensis. Interestingly, their thickness and interactions with collagen organization vary at different imaging sites, suggesting different stages or even different forms of angiogenesis in the BCa microenvironments.

Angiogenesis (2PF)

Angiogenesis is a key factor in cancer development to supply oxygen and nutrients to the tumor and to promote metastasis[243]. In the experiments presented here, the onset of angiogenesis is already observed in week 4 of the BCa development [Fig. 6.5(c)]. The sprouting tubular structure is visualized only by 2PF imaging. The fluorescence signal may originate from elastin fibers, FAD in activated endothelial cells, and tumor cells. In the region surrounding the angiogenic site, FAD-fluorescent cells and randomly aligned elastin fibrils are displayed by 2PF imaging as well. Thinner collagen fibers with weaker SHG signal are exhibited by SHG imaging. The altered lipid contents are revealed by CARS and THG imaging. The co-occurrence of these events suggests the correlation between them during the angiogenic process.

Collagen organization (SHG, THG)

Collagen fibers revealed by SHG imaging have been related to BCa development. Tumor-associated collagen signatures (TACS) designate three matrix arrangements as biomarkers of tumor formation, including locally dense collagen, straightened collagen around a tumor, and radially aligned collagen normal to the tumor boundary[214,215]. The composition of collagen type V in desmoplasia has also been recognized as a BCa biomarker[244], and has been demonstrated to have shorter fibers, lower SHG signal, and lower forward-to-backward SHG signal ratio in a gel model[226]. In the early BCa experiment presented here, a TACS-1 signature of locally dense collagen is already found in the stroma [Fig. 6.2(b), Fig. 6.3(a)], the lipid-stromal boundary [Fig. 6.2(a), Fig. 6.4(a), Fig. 6.5(a), Fig. 6.6(b)], fibrocystic tissue [Fig. 6.3 (b), Fig. 6.5(b)], and in the proximity of the tumor site [Fig. 6.6(a,d)]. While these features are all associated to carcinogenesis, their discernable morphological differences imply the functional discrepancy, which can be revealed by multimodal imaging. For example, Fig. 6.2(b) shows a comet-like

feature of locally dense collagen with elongated fibers, which are found to be surrounding a FAD-fluorescent tumorigenic cell cluster in the 2PF image. Additionally, Fig. 6.4(a) demonstrates a granular collagen structure alongside an elastin net feature in the 2PF image, which is related to angiogenesis.

In the early stages of tumor formation, no obvious TACS-2 and TACS-3 feature was observed in these results. However, in week 5 [Fig. 6.6(a)], the collagen arrangement resembles both TACS-2 and TACS-3 features, demonstrating collagen layers parallel to the tumor boundary, and a ductal structure positioned perpendicular to the boundary, respectively. These observations provide evidence of collagen remodeling toward TACS-2 and TACS-3. From the reported SHG response of collagen type V, locally "reduced" collagen, possessing weaker SHG signal and shorter fibers, can potentially serve as a biomarker in SHG and THG imaging. Fig. 6.4(b), Fig. 6.5(c), and Fig. 6.6(d) present thinner collagen fibers crossing and cross-linking with each other. The tumorigenic events involved are identified by multimodal imaging as FAD-fluorescent tumor cells, angiogenesis, and the formation of ductal structures, respectively. These results support incorporating the locally reduced collagen as another tumor-associated collagen signature named TACS-4.

Local invasion (SHG, 2PF, THG, R2850, R3050)

The occurrence of local invasion can be cross-validated by multimodal imaging. As described by the collagen organization, the initiation of TACS-3 features is observed in the SHG image in Fig. 6.6(a). The ductal structure projecting from the tumorous area into the collagenous area is also visible in the 2PF and the CARS images with lower imaging contrast. Interestingly, the FAD-fluorescent cells and the tumor-associated THG-sensitive microvesicles are found nearby and inside this ductal structure in the collagenous area. These observations are evidence of local invasion supported by the TACS-3 feature.

Fibrocystic breast (SHG, 2PF, THG)

The fibrocystic breast is characterized by fibrous tissue and cysts containing amorphous materials. SHG imaging of highly-dense collagen fibers in the fibrocystic breast has been demonstrated[223]. In Fig. 6.3(b)

and Fig. 6.5(b), highly-dense and round collagen structures are visualized by SHG and THG imaging. Inside these dense collagen features, elastin fibers and FAD-fluorescent cells are revealed in the 2PF image. Even though the fibrocystic breast is considered benign, these results lead to the speculation that the fibrocystic tissue observed in early BCa development may transform into a more malignant-appearing microenvironment later in this BCa animal model.

Tumor-associated THG-sensitive microvesicles (THG)

THG-sensitive microvesicles have been reported to be associated with tumor in melanoma[75]. In our imaging results, the THG-sensitive microvesicles are found in various pre-cancerous and cancerous microenvironments, including tumorous stroma [Fig. 6.2(b)], the lipid-stromal interface [Fig. 6.4(a), Fig. 6.5(a)], tumor nest [Fig. 6.4(b)], fibrocystic breast [Fig. 6.5(b)], and the tumor-stroma boundary [Fig. 6.6(a)]. From the MPMP analysis (Fig. 7.1, Fig. 7.3), one type of the THG-sensitive microvesicles with moderate THG signal and a lipid-like CARS spectrum are identified as small LDs. As these microvesicles are found in the proximity of lipid contents and demonstrate up-regulated FAD fluorescence, they are likely micro-LDs secreted by the adipocytes, or lipolytic products undergoing metabolic activities to support tumor growth, which will be discussed later in lipogenesis and lipolysis. Interestingly, there exists another type of THG-sensitive microvesicles with the characteristics of an extreme THG signal and a protein-like CARS spectrum. Because these microvesicles are found in tumor regions, they can serve as a biomarker in early BCa and be designated as tumor-associated THG-sensitive microvesicles (TATVs) here. From the discussion in MPMP profile analysis, the molecular composition of these TATVs is likely to be hemoglobin[83], but they can also be new biomolecules that can be visualized by THG imaging. Investigating the molecular contents of these microvesicles is one of the future directions for this research.

Stellate structure (THG, R2850)

A unique stellate structure can be identified in the THG image at the boundary of LDs [Fig. 6.4(a), Fig. 6.5(d)] during early BCa development. This feature is also visible in the R2850 image, demonstrating

a wrinkle-like morphology on the LD surface. Accompanying the stellate structure, high-2PF lipid boundaries, elastin fibers (2PF), smaller LDs, and lipid residuals (R2850, THG) are also found within the images. Based on these observations, the stellate structure is likely relevant to lipid degradation and elastin synthesis. The molecular or cellular origin of the stellate structure is still to be determined.

Lipogenesis and lipolysis (R2850, THG, 2PF)

Coherent Raman imaging and THG imaging have been established as powerful tools to interrogate the lipid contents in biological tissue *in situ*[22,245]. In BCa research, CARS imaging has been applied to study the effects of excess lipid in mammary tumor progression[221,222]. Recently, SRS imaging has been utilized to investigate the accumulation of esterified cholesterol in prostate cancer[246]. In our multimodal imaging data, the lipid contents in the BCa microenvironment are not only visualized by CARS and THG imaging, but are further related to its metabolism by 2PF imaging and to the collagenous tissue by SHG and THG imaging. Lipogenesis and lipolysis are both observed during early BCa development. Lipogenesis is characterized by the orderly accumulation of small LDs (~3-20 μm in diameter) in the stromal areas with FAD-fluorescent cells and collagen fibers [Fig. 6.2(a), Fig. 6.5(b)]. On the other hand, lipolysis is recognized as irregularly sized and shaped LDs distributed in the cancerous microenvironments, such as within stromal areas near mammary ducts [Fig. 6.2(b), Fig. 6.3(b)] and near the lipid-stroma boundary [Fig. 6.4(a,c), Fig. 6.5(a,d), Fig. 6.6(b,c)].

Of particular interest is the lipid-stroma interface. The lipid alterations and breakdown revealed by CARS and THG imaging are accompanied by microvesicles and irregularly-shaped LDs being released into the stromal area [Fig. 6.4(a,c), Fig. 6.5(a,d), Fig. 6.6(b,c)]. In the areas surrounding these altered LDs, highly FAD-fluorescent cells, elastin fibers, and amorphous substances were revealed by 2PF imaging, and the collagen remodeling that is co-occurring was observed by SHG imaging. While lipid has been found to facilitate BCa growth and metastasis[221,222], the increased FAD-fluorescent cells and substances demonstrate up-regulated metabolism during lipolysis[214,223], which provides energy to promote tumor formation, likely through β-oxidation[247]. Also, the presence of elastin fibers suggests the onset of

angiogenesis[238], which can be fueled by the nearby lipid metabolism as well. In another stromal area [Fig. 6.2], the lipid microvesicles scattered around the connective tissue appear to be in concert with tumor growth, which is evident by the FAD-fluorescent cluster, the locally dense collagen, and the TATVs. Due to the morphological differences as compared to the LDs at the lipid-stroma boundary, these results suggest that these lipid microvesicles are the lipolytic products of the smaller LDs from lipogenesis [Fig. 6.2(a)] or the lipid secreted by the mammary duct [Fig. 6.3(b)].

CH aromatic stretching vibration (R3050, 3050 cm^{-1})

With an excellent response from the CH stretching vibration (2800-3200 cm^{-1}), CARS imaging has been utilized to study the biochemical compositions in BCa microenvironments. Label-free imaging of the CH_2 stretching vibration at 2840 cm^{-1} has enabled interrogation of lipid contents in cells and in tissue, and has found increased collagen fibers and cancer metastasis with increased adiposity[221,222]. Interferometric CARS allowed for the spectroscopic imaging of endogenous lipid and protein composition and has successfully defined molecular tumor margins with >99% accuracy[19]. While much research has been focused on detecting lipid and protein with CH_2 stretching at ~2840 cm^{-1} and CH_3 stretching at ~2930 cm^{-1}, respectively, mapping protein composition with the CH aromatic stretching at 3050-3060 cm^{-1} can not only avoid the interference of the lipid signal, as in the case of 2930 cm^{-1}, but also provide a direct visualization of protein as a biomarker of carcinogenesis[248]. Throughout the spectroscopy data presented here and in the molecular profile analysis, a prominent peak at 3050 cm^{-1} can be easily identified in the pre-cancerous and cancerous regions, except for a normal area in week 2 (Fig. 7.2). Additionally, in the results from a control animal (Fig. 7.5), the lack of a vibrational response at 3050 cm^{-1} in stroma further validates this vibrational BCa biomarker at 3050 cm^{-1}. Understanding the tumorigenic protein biomolecules corresponding to this Raman shift is of particular interest and is one of the future directions of this research.

OH stretching vibration (3200-3400 cm^{-1})

Water molecules possess a broadband OH stretching response at 3200-3400 cm^{-1}, which has also been identified as a biomarker in BCa tissue using spontaneous Raman imaging[248]. In the hyperspectral CARS imaging in this thesis research, covering 2700-3250 cm^{-1}, the image contrast in the OH band (3200 cm^{-1}) highly resembles that of a protein band (3050 cm^{-1}) and is distinguished from that of a lipid band (2850 cm^{-1}). Because normal breast tissue has more adipose tissue, the lipophobic nature of water and the co-localization of water and protein make the OH vibration a somewhat straight-forward cancer biomarker. Meanwhile, the tail of the water band extends down to ~3000 cm^{-1}, and is oftentimes treated as an undesirable background in CARS imaging in the CH stretching region. However, the homodyne amplification of the OH vibration and the CH aromatic vibration coherently enhances the signal at 3050 cm^{-1} and makes the CH aromatic vibration an even stronger indicator. It is noted that the relative intensity of the 3050 cm^{-1} to 3200 cm^{-1} peaks can potentially reveal more insight regarding the protein-water ratio and interaction, and is also one of the future directions of this research.

7.2.2. Molecular biomarkers in late breast cancer development

FAD-fluorescent cells (2PF)

In the late BCa development, the FAD-fluorescent cells continuously serve as a reliable biomarker. The FAD-fluorescent cells are found to be rather ubiquitous at the lipid-stroma interface [Fig. 6.7(b,e), Fig. 6.11(a), Fig. 6.15(a), Fig. 6.9, Fig. 6.13], surrounding the (forming) blood vessels [Fig. 6.7(c), Fig. 6.8(a,b), Fig. 6.9, Fig. 6.13], in the tumorous stroma [Fig. 6.7(a), Fig. 6.11(b), Fig. 6.15(b), Fig. 6.9, Fig. 6.12, Fig. 6.13, Fig. 6.16], tumor nest [Fig. 6.11(c), Fig. 6.12], and at necrotic sites [Fig. 6.15(c), Fig. 6.17]. Their morphological diversity not only represents different cell types, but also reflects the heterogeneity in the developed cancerous areas. The elongated cells near blood vessels can be identified as endothelial cells or pericytes [Fig. 6.7(c)], while the spiky-appearing cells in fibrous tumor stroma can

be recognized as activated fibroblasts [Fig. 6.15(b)]. Finally, the irregularly-shaped cells enclosed by the TACS-2 or TACS-3 features are identified as tumor cells [Fig. 6.11(c), Fig. 6.12][214,215].

NAD(P)H-fluorescent cells (3PF)

In the experiment involving the late BCa development, the improved 3PF imaging enabled one to better visualize cellular NAD(P)H fluorescence. Up-regulation of NAD(P)H fluorescence has been recognized as a BCa biomarker indicative of metabolic changes from oxidative phosphorylation to aerobic glycolysis[219,220]. Results here demonstrate high cellular NAD(P)H fluorescence in different cancerous microenvironments, including the lipid-stroma boundary [Fig. 6.7(b), Fig. 6.13], angiogenic sites [Fig. 6.8(a), Fig. 6.9], the tumor-stroma boundary (Fig. 6.12), tumorous stroma (Fig. 6.15, Fig. 6.16), and necrotic sites (Fig. 6.15, Fig. 6.17). The vesicular morphology within the cells is evidence of the mitochondrial origin of the NADH fluorescence. In a tumor mass (Fig. 6.12), the tumor cells present intense 3PF signal. In necrotic sites (Fig. 6.15, Fig. 6.17), the 3PF appears to be lower and more uniform in the cytoplasm. These observations reflect a lower rate of aerobic phosphorylation or potentially suggest a change in the cellular metabolism in late BCa development.

Tumor cells (2PF, 3PF, THG, R2850, R3050)

While tumor cells can be visualized by 2PF imaging, their different multiphoton responses and their morphological differences indicate different developmental stages. In a non-invading tumor site [Fig. 6.11(c)], the tumor cells are enclosed by TACS-2 features, and the TATVs are found co-localized with the tumor cells. These FAD-fluorescent cells show no NADH fluorescence in the 3PF images, suggesting the metabolic activity is mainly oxidative phosphorylation. In sharp contrast to the non-invading cells, the tumor cells near an invading tumor-stroma interface [Fig. 6.12] demonstrate high 3PF and 2PF signals, indicating high metabolic activities of both oxidative phosphorylation and aerobic glycolysis[214,219]. In the same image, the invading cells localized in the collagenous stroma present negligible 3PF and lower 2PF signals, showing the drastic shift in metabolism to oxidative phosphorylation as compared to the tumor cells near the boundary. In a necrotic area found at a later stage

of BCa development [Fig. 6.15(c), Fig. 6.17], the cellular NAD(P)H fluorescence is observed to be relatively uniform within the FOV in comparison to the FAD fluorescence, which exhibits an overall lower signal except for some highly fluorescent clusters. Based on these results, the metabolism in the necrotic area is likely aerobic glycolysis of a lower rate, but a small portion inside the necrotic area potentially possesses mixed metabolic activities of phosphorylation, glycolysis, and β-oxidation.

Elastin organization (2PF)

The elastin fibers in late stage BCa are found to be less co-localized with collagen fibers, and either demonstrate a random alignment or participate in neo-angiogenesis. The reduced amount of elastin fibers co-localized with collagen fibers suggests reduced elasticity of the connective tissue, which echoes the observation of physically firmer tumor formation during the animal surgery in the late BCa development. The elastin fibers in angiogenesis exhibit diverse morphological features, interacting with 3PF-sensitive microvesicles and collagen fibers, as will be discussed in the following paragraphs.

Angiogenesis (3PF, 2PF, SHG, THG, R2850, R3050)

In contrast to early BCa development, angiogenesis is found to be ubiquitous and in different forms in late BCa development. The most prominent feature revealed by multimodal imaging is the punctuate angiogenesis-associated 3PF-sensitive microvesicles (AA3Vs) aligned parallel to the growing vasculatures [Fig. 6.7 (a,b), Fig. 6.8(a,b), Fig. 6.9, Fig. 6.12, Fig. 6.13]. These AA3Vs are found co-localized with the elastin fibers in vessel walls visualized by 2PF imaging, but are also observed to align in a tubular arrangement without the presence of elastin fibers in some cases. Based on the excitation and emission wavelengths used in this study, it is hypothesized that the 3PF signal of these microvesicles originates from NAD(P)H. The hypothesis is supported by the NAD(P)H oxidase activities and the elevated NADH concentration during angiogenesis[239,240]. Interestingly, not all of the blood vessels demonstrate AA3Vs. In more mature blood vessels with developed elastic lamella and collagen fibers surrounding them [Fig. 6.7(c)], no AA3Vs are observed around the vasculature. These results indicate that

the presence of AA3Vs at the angiogenic sites, but not at the mature blood vessels, confirming the angiogenic nature of these NAD(P)H-fluorescent microvesicles.

From the discussion above, 3PF, 2PF, and SHG imaging combined together enables visualization of different elements in blood vessels, and can further be employed to investigate different forms of angiogenesis. While the mature vessels demonstrate no AA3Vs, the less mature blood vessels can be identified as those with less AA3Vs, but already with visible elastic lamella and an outer layer of collagen fibers [Fig. 6.8(a)]. The developing vasculature is marked with a larger amount of AA3Vs, as well as growing vessel walls of elastin fibrils, FAD-fluorescent cells, or a combination of both (Fig. 6.10, Fig. 6.13). The heterogeneous compositions of vessel walls reflect the neovascularization of different co-occurring mechanisms, which can be confirmed by two types of initiating angiogenic events observed in our results. One type begins with aligned AA3Vs released into the stroma to recruit endothelial cells and other cell types to initiate vascularization, and less elastin fibers are observed. The other type begins with elastin fibrils cross-linking with each other to form the elastic lamella, and less AA3Vs are observed. While our discussion has been focused on high-3PF and high-2PF biomolecules and cells, it is worth mentioning that collagen fibers also experience remodeling during angiogenesis. Specifically for the elastin-initiated type, the collagen fibers co-align in the periphery of the elastin fibers, likely to form the outer layer of the blood vessel wall simultaneously. For the AA3Vs-initiated type, these phenomena are not obvious, and the AA3Vs migrate along the existing collagen fibers and likely disrupt the collagen arrangement in the later stages of angiogenesis.

Collagen organization (SHG, THG)

In late BCa development, locally dense collagen TACS-1 signature is not as obvious as in early BCa development, and appears only near other tissue types disrupted by tumor progression, such as mammary ducts [Fig. 6.7(d), Fig. 6.11(b)] and nerve fibers [Fig. 6.8(b), Fig. 6.10]. The exception is for fibrocystic tissue, as will be discussed below for the fibrocystic breast. The locally-reduced collagen revealed by SHG imaging is identified as a TACS-4 feature in early BCa development. Originating from the shift of

collagen composition from type I to type V[226,244], the TACS-4 feature displays shorter fibers and a reticular morphology in many of the experimental data presented here [Fig. 6.8(a), Fig. 6.9, Fig. 6.11(b), Fig. 6.12, Fig. 6.13, Fig. 6.15(c), Fig. 6.17]. Therefore, the proposed TACS-4 feature can serve as an effective biomarker, particularly in later BCa development.

Besides TACS-1 and TACS-4, TACS-2 [Fig. 6.11(c), Fig. 6.12] and TACS-3 [Fig. 6.12] features of a straightened collagen boundary and a tubular arrangement perpendicular to the tumor boundary, respectively, are also recognized in late BCa development. While the presence of TACS-3 features suggest the onset of local invasion, the multimodal imaging results confirm the occurrence of tumor invasion, which is discussed in the following paragraph.

Local invasion (SHG, 2PF, THG, R2850, R3050)

Tumor invasion is a specific event that can be uniquely visualized and cross-validated by multimodal imaging. As demonstrated in Fig. 6.12, the TACS-2 and TACS-3 features revealed by SHG imaging are indicative of the presence of a primary tumor and local invasion, respectively[214,215]. Starting from the collagen fiber framework, tumor invasion can be identified with other imaging modalities. 2PF imaging shows the invading cells in the primary tumor enclosed by the TACS-2 feature, FAD-fluorescent cells in the stromal area along the TACS-3 feature, as well as the angiogenic elastin fibers near the TACS-3 feature. 3PF imaging displays the AA3Vs, and THG imaging exhibits the TATVs along the TACS-3 features. CARS imaging maps other types of tumorigenic substances transported in parallel to the TACS-3 features, likely through a lymphatic vessel. These observations from different modalities collectively convey different information and provide a more complete picture of tumor invasion.

Fibrocystic breast (SHG, 2PF, THG)

The fibrocystic tissue is identified by dense collagen fibers and cysts of amorphous substances [Fig. 6.10, Fig. 6.13][223]. While the collagen contents are visualized by SHG and THG imaging, the cellular components, such as fibroblasts and myoepithelial cells, as well as the elastin fibers, can be detected by

2PF imaging. In addition, the amorphous materials of lipid, protein, and water can be probed by CARS imaging. At a cancerous lipid-stroma interface (Fig. 6.13), an extremely dense collagen sphere was found to have a high 2PF signal and to contain elastin fibrils. The fibrocystic tissue observed in an abnormal control animal [Fig. 6.10] demonstrates less dense collagen fibers resembling a glandular structure and a larger amount of cells within.

Tumor-associated THG-sensitive microvesicles (THG)

In late BCa development, the unique TATVs are found in various cancerous microenvironments, including at the lipid-stroma boundary [Fig. 6.7(b), Fig. 6.8(c)], angiogenic sites [Fig. 6.8(a,b), Fig. 6.9, Fig. 6.13], tumorous stroma [Fig. 6.15(b), Fig. 6.16], a tumor nest [Fig. 6.11(c), Fig. 6.12], and regions of tumor invasion (Fig. 6.12). The MPMP analysis (Fig. 7.7) demonstrates extreme THG signal and moderate 2PF and R3050 signals, agreeing with the results in early BCa development. With improved 3PF imaging in the later BCa experiments, these TATVs were also found to demonstrate high 3PF signal. Based on the molecular imaging capability of THG imaging as discussed in Section 7.1, it is hypothesized that these microvesicles are hemoglobin[83]. The higher 3PF signal suggests their relevance to the metabolism in the BCa microenvironments. By flexibly tailoring the SC pulses, multiphoton fluorescence imaging with different excitation wavelengths or CARS imaging with a broader vibrational bandwidth may help to provide a better understanding of the biochemical content of these TATVs.

Lipolysis and crystalline cholesterol (R2850, THG, 2PF, 3PF, SHG)

In early BCa development, lipogenesis and lipolysis have been related to tumorigenic events, such as up-regulated FAD-fluorescence, collagen remodeling, and angiogenesis. In late BCa development, no obvious sign of lipogenesis was observed. However, lipid degradation is continuously impacting tumor progressing. Altered LDs are identified at the lipid-stroma boundary [Fig. 6.7(e), Fig. 6.8(c), Fig. 6.9, Fig. 6.11(a,b), Fig. 6.13, Fig. 6.15(a)], tumorous stroma [Fig. 6.7(a), Fig. 6.8(a,b)], and angiogenic sites[Fig. 6.7(c), Fig. 6.9, Fig. 6.13]. More isolated LDs and lipid residuals are found within tumorous stroma [Fig. 6.9, Fig. 6.12, Fig. 6.13, Fig. 6.15(b), Fig. 6.17]. The alteration of the LDs is more severe as

compared to that in early BCa development. The membrane of the LDs is less obvious, and the LDs are broken into smaller ones, or merged to form larger ones. In addition, the LDs are less attached to each other, which may result from the reduced collagen contents and the disrupted connective tissue.

The effect of lipolysis on tumor progression can be further understood by the metabolic mapping enabled by 2PF and 3PF imaging. In the earlier stages of late BCa development, highly FAD-fluorescent cells and elastin synthesis are revealed by 2PF imaging in the proximity of the lipolytic sites, and AA3Vs are found in the surrounding area as well. The increased FAD fluorescence is related to up-regulated cellular metabolism, while the elastin synthesis and AA3Vs are related to angiogenesis. From these observations, the lipid metabolism can provide energy to promote tumor growth and neo-angiogenesis at this stage. In a later stage (Fig. 6.12, Fig. 6.13), significantly higher 3PF and reduced 2PF signals are identified in the irregular lipid residuals in the tumor stroma. The increase of NAD(P)H fluorescence and the decrease of FAD fluorescence agree with the shift of cellular metabolism to aerobic glycolysis in cancer development, but can also be due to β-oxidation of the lipid contents[247]. In a necrotic area in the latest stage (Fig. 6.17), the lipid contents demonstrate high 2PF and 3PF signals, potentially fueling the surrounding metabolic activities, as is evident by the presence of FAD-fluorescent cells nearby. Interestingly, some of these lipid contents even exhibit high SHG signal. Because SHG is sensitive to crystalline non-centrosymmetric materials, these high-SHG substances are likely crystalline forms of cholesterol, which can be identified as a biomarker in late-stage BCa[77].

CH aromatic vibration (R3050, 3050 cm^{-1})

In the early BCa experiment, the CH aromatic vibration at 3050 cm^{-1} was recognized as a BCa biomarker. The frequencies away from this intense lipid vibration, below 3000 cm^{-1}, and the homodyne amplification from co-existing water molecules, make this Raman shift a direct and sensitive measure to probe the carcinogenic protein contents in the microenvironment. In the MPMP analysis, the peak can be easily discerned in the CARS spectra of the tumorous stoma (Fig. 7.7, Fig. 7.9, Fig. 7.10), but not in that of the normal lipid-stroma interface in a control animal (Fig. 7.8). In the radar plot, the intense R3050 signal

oftentimes accompanies a weak R2850 signal, and the area spanned by the multiphoton signal appears as a polygon pointing downward (note R2850, 3PF, and THG are "lipophilic"). As R3050 and R2850 represent protein and lipid compositions, respectively, their ratio can potentially serve as a metric to evaluate the stages of BCa development. Surprisingly, this protein vibrational biomarker vanishes at the latest stage cancer development. In a carcinogen-induced animal in week 9 (Fig. 7.11), no 3050-cm^{-1} vibration was observed in the necrotic area. The data suggests that the vibration at 3050 cm^{-1} can serve not only as a BCa biomarker, but further as a carcinogenic activity indicator. The hypothesis of low carcinogenic activity related to low R3050 signal is evident by the low 2PF and 3PF signals in the same area, which reflect lower cellular metabolism. The protein origin of this R3050 signal is of particular interest. From preliminary data using spontaneous Raman spectroscopy (data not shown), the associated biomolecule is likely to be estrogen or actin.

OH stretching vibration (3200-3400 cm^{-1})

As described in the early BCa development, the lipophobic nature and the co-localization with protein molecules make the water OH stretching vibration at 3200-3400 cm^{-1} a relatively straightforward biomarker. The OH vibration provides additional information to assess BCa development in addition to comparing lipid and protein compositions in a more traditional manner. Evaluating the ratios between OH stretching, CH_2 stretching, and CH aromatic stretching vibrations may provide more insight into the BCa microenvironment and is one of the future directions for this research.

To conclude this chapter, label-free multimodal multiphoton imaging was employed to study BCa development in a carcinogen-induced rat mammary tumor model. 2PF, SHG, 3PF, THG, and hyperspectral CARS imaging was used to visualize cellular components, stromal tissue, and adipose tissue based on their intrinsic molecular properties. The correlation of multiphoton signals and the CARS spectra offer a molecular profile to directly visualize and analyze the *in situ* biochemical composition, allowing for the identification of biomarkers and their transformation in early and late BCa development. FAD-fluorescent cells and elastin organization are observed by 2PF imaging. Collagen reorganization is

displayed by SHG. NAD(P)H-fluorescent cells and angiogenesis-associated microvesicles are revealed by 3PF imaging. Tumor-associated microvesicles and stellate structures are shown by THG imaging. Lipogenesis and lipolysis are recognized by CARS imaging. The CH aromatic vibration at 3050 cm^{-1} is identified as a carcinogenic protein indicator, and the OH vibration at 3200 cm^{-1} is employed as a water probe. These biomolecular characteristics are not only visualized individually, but their interaction and correlation provide further insight into tumor invasion, metabolic changes, neo-angiogenesis, lipid metabolism, and cholesterol crystallization. The flexible penta-modal imaging platform, the label-free *in situ* molecular profiling, and the multiphoton BCa biomarkers identified in this study are likely to have a broader impact in both fundamental research and in the translation of these technologies and techniques to clinical applications.

8. CONCLUSIONS AND FUTURE DIRECTIONS

8.1. Conclusions

The development of novel light sources has always been an underlying driving force for new imaging technologies. The aim of the fiber SC described in this thesis is to achieve a highly coherent, ultrabroadband, fiber-based light source spanning the optical biological window (700-1300 nm) that can be used for various multiphoton imaging modalities. By recognizing the coherent SC generation in all-normal dispersion (ANDi) fibers, a nonlinear ANDi fiber was pumped in the proximity of its minimal dispersion wavelength by a pulsed laser centered at 1040 nm. In the earlier experiments, the SC was generated in a non-birefringent ANDi fiber, achieving a spectral range of 900-1160 nm. The coherence and the compressibility of the SC were demonstrated by compressing the pulses using a MIIPS-assisted pulse shaper. Despite the high coherence, the imaging applications were limited by the attainable power (360 mW output for 600 mW input) and bandwidth. A higher pump power can induce optical wave-breaking (WB) and further extend the bandwidth, but the onset of polarization dynamics disrupted the coherence in an uncontrollable manner. Fabricating a polarization-maintaining ANDi fiber has overcome this limitation and allowed for the generation of high power (480 mW output for 800 mW input), highly-polarized (<0.02% PER), broadband (780-1300 nm) coherent SC.

Considering the spectral-temporal characteristics of the SC, the pulse shaping strategies were customized for several nonlinear optical microscopy and spectroscopy methods. For the SC of 900-1160 nm, local pulse compression was first demonstrated to compress different spectral ranges of the pulses to the transform-limit for selective and efficient two-photon fluorescence (2PF), second harmonic generation (SHG), and third harmonic generation (THG) imaging of biological samples. Coherent anti-Stokes Raman scattering (CARS) spectroscopy in the fingerprint region was realized by introducing $\pm\pi/2$ phase shifts at the higher frequency end of the SC spectrum, creating a unique pulse shape featuring an impulsive vibrational excitation and a narrow-band probe pulse. The non-resonant background from the impulsive

excitation further interfered with the resonant CARS signal, enabling homodyne amplification in a single-beam geometry. The method simultaneously achieved retrieval of the resonant signal and rejection of the non-resonant background. Optimized amplitude shaping was then investigated to improve the signal-to-background ratio by indirectly tuning the relative intensity of the probe pulse to that of the impulsive excitation pulse.

With the improved polarization stability and the higher power of the SC generated in the polarization-maintaining fiber, the pulse shaping strategies could be further advanced for multiphoton imaging applications. A broader spectral range (900-1300 nm) for local pulse compression was allowed for efficient 2PF, SHG, THG, and three-photon fluorescence (3PF) imaging of biological samples. The potential of local pulse compression was demonstrated in a highly dispersive imaging system, which resembled the anticipated situation of a clinical setting with excessive dispersion resulting from beam-guiding optics. On the other hand, this high dispersion was intentionally introduced to spectrally focus the SC pulses for CARS imaging. The extended WB band (780-880 nm) of the SC was employed as the pump beam while the main SC (900-1300 nm) was used as the Stokes beam. Adaptive spectral focusing optimally chirped the pump and the Stokes pulses for CARS imaging in the CH stretching and vibrationally silent regions.

Combining local pulse compression and adaptive spectral focusing, flexible pulse shaping of the coherent fiber SC realized a high-performance multimodal multiphoton imaging platform which enabled 2PF, SHG, 3PF, THG, and hyperspectral CARS imaging without compromise on each modality. Label-free multimodal multiphoton molecular imaging was demonstrated by imaging cancerous and normal human breast tissue. The fundamentally different physical mechanisms of the different modalities provides complimentary visualization of diverse biomolecules and structures, such as FAD, collagen, NAD(P)H, lipid, protein, and the molecular contents of various microvesicles. The well-controlled SC excitation pulses offered quantitative correlation of multimodal multiphoton signals in addition to the CARS spectrum, establishing a multiphoton molecular profile (MPMP) for interrogating the biochemical

composition of *in situ* microenvironments. The MPMPs in the cancerous and normal tissue reveled differences in lipid droplets, stromal tissue, and microvesicles that would otherwise be undetectable using any single modality, or by any currently available immunohistochemical or histological staining technique. These results demonstrate the powerful potential of the technology for molecular breast cancer (BCa) detection and diagnosis.

The label-free multiphoton molecular imaging and MPMP analysis were employed to study BCa development in a carcinogen-induced rat mammary tumor model. BCa biomarkers and their transformation in early and late tumor development were identified. FAD-fluorescent cells and elastin organization were observed by 2PF imaging. Collagen remodeling was demonstrated by SHG. NAD(P)H-fluorescent cells and angiogenesis-associated microvesicles were revealed by 3PF imaging. Tumor-associated microvesicles and stellate structures were shown by THG imaging. Lipogenesis and lipolysis were recognized by CARS imaging. The CH aromatic vibration at 3050 cm^{-1} was identified as a protein indicator in carcinogenesis, and the OH vibration at >3200 cm^{-1} was employed as a water marker. These molecular characteristics are not only visualized individually, but their interaction and correlation also provide further insight into tumor invasion, cellular metabolism, neo-vascularization, lipid metabolism, and cholesterol crystallization in BCa microenvironments.

8.2. Future directions

While the SC demonstrates a broadband fiber-based coherent light source, the translational capability is still limited by the fiber coupling and the associated fiber damage, which may require expertise in fiber processing and coupling to maintain routine operation. Preliminary tests have demonstrated the possibility to process the fiber end tips to resolve these issues. Nevertheless, to attain a clinically friendly fiber SC, an all-fiber system connecting the pump laser to the ANDi fiber and an automated solution to collimate the ultrabroadband SC output are necessary. These advancements will not only alleviate the challenges in

the fiber coupling procedures, but also improve the SC generation stability and reduce the fiber damage for long-term operation.

The pulse shaping strategies described in the thesis, the local pulse compression, adaptive spectral focusing, and the optimal interferometric CARS, were intended to function as individual methods optimized for a specific imaging or spectroscopy purpose. However, these methods can be applied interchangeably. Local pulse compression and adaptive spectral focusing were applied sequentially for multimodal multiphoton imaging. The next step would be to integrate these techniques for simultaneous acquisition, which can potentially be achieved by uniquely designing the SC pulse shapes and improving the detection system. As an example, by locally compressing multiple spectral bands of the SC pulses, the temporally-separated pulse trains can allow for multicolor multiphoton imaging without interfering with each other[176].

In the thesis, multiphoton imaging of the rat mammary tumor microenvironments was performed on *ex vivo* tissue specimens due to the limited imaging speed of the system. The transformation of the multiphoton molecular biomarkers was observed at discrete time points, and the interval changes were lost. The progressive molecular and morphological changes can be further elucidated if an *in vivo* experiment was initiated to continuously monitor mammary tumor development using the same animal over time. Improvements in the SC, the pulse shaping methods, and the speed of the scanning system will enable such an experiment. In addition, the *in vivo* imaging study can potentially benefit from the use of a surgically placed imaging window chamber along with a multimodal image co-registration algorithm[201,249].

Finally, the nonlinear optical microscopy and spectroscopy platform developed in this research for pulse shaping of the coherent SC provides unprecedented flexibility to customize the excitation pulses for targeting biomolecules in various biological systems. The presented technology will also undoubtedly have a broader impact in basic scientific research, biophotonic imaging, and eventually, in clinical translation.

REFERENCES

1. Denk, W., Strickler, J.H. & Webb, W.W. Two-photon laser scanning fluorescence microscopy. Science 248, 73-76 (1990).
2. Hell, S.W. et al. Three-photon excitation in fluorescence microscopy. J Biomed Opt 1, 71-74 (1996).
3. Gannaway, J.N. & Sheppard, C.J.R. Second-harmonic imaging in the scanning optical microscope. Opt & Quant Electr 10, 435-439 (1978).
4. Barad, Y., Eisenberg, H., Horowitz, M. & Silberberg, Y. Nonlinear scanning laser microscopy by third harmonic generation. Appl Phys Lett 70, 922-924 (1997).
5. Zumbusch, A., Holtom, G.R. & Xie, X.S. Three-dimensional vibrational imaging by coherent anti-Stokes Raman scattering. Phys Rev Lett 82, 4142-4145 (1999).
6. Freudiger, C.W. et al. Label-free biomedical imaging with high sensitivity by stimulated Raman scattering microscopy. Science 322, 1857-1861 (2008).
7. Evans, C.L. & Xie, X.S. Coherent anti-Stokes Raman scattering microscopy: chemical imaging for biology and medicine. Annu Rev Anal Chem 1, 883-909 (2008).
8. Zipfel, W.R., Williams, R.M. & Webb, W.W. Nonlinear magic: multiphoton microscopy in the biosciences. Nat Biotech 21, 1369-1377 (2003).
9. Campagnola, P.J. & Loew, L.M. Second-harmonic imaging microscopy for visualizing biomolecular arrays in cells, tissues and organisms. Nat Biotech 21, 1356-1360 (2003).
10. Friedl, P., Wolf, K., von Andrian, U.H. & Harms, G. Biological second and third harmonic generation microscopy. Curr Protoc Cell Biol Chapter 4 (2007).
11. Weiner, A.M. Femtosecond pulse shaping using spatial light modulators. Rev Sci Instr 71, 1929-1960 (2000).
12. Silberberg, Y. Quantum coherent control for nonlinear spectroscopy and microscopy. Ann Rev Phys Chem 60, 277-292 (2009).
13. Meshulach, D. & Silberberg, Y. Coherent quantum control of two-photon transitions by a femtosecond laser pulse. Nature 396, 239-242 (1998).
14. Ranka, J.K., Windeler, R.S. & Stentz, A.J. 1999 Conference on Lasers & Electro-Optics (1999).
15. Dudley, J.M., Genty, G. & Coen, S. Supercontinuum generation in photonic crystal fiber. Rev Mod Phys 78, 1135-1184 (2006).
16. Dudley, J.M. & Taylor, J.R. Ten years of nonlinear optics in photonic crystal fibre. Nat Photonics 3, 85-90 (2009).
17. American Cancer Society: www.cancer.org/cancer/breastcancer/detailedguide/breast-cancer-key-statistics (2014).
18. National Cancer Institute: www.cancer.gov/cancertopics/factsheet/detection/mammograms (2014).
19. Chowdary, P.D. et al. Molecular histopathology by spectrally reconstructed nonlinear interferometric vibrational imaging. Cancer Res 70, 9562-9569 (2010).
20. Millard, A.C. et al. Third-harmonic generation microscopy by use of a compact, femtosecond fiber laser source. Appl Opt 38, 7393-7397 (1999).

21. Zipfel, W.R. et al. Live tissue intrinsic emission microscopy using multiphoton-excited native fluorescence and second harmonic generation. PNAS 100, 7075-7080 (2003).

22. Debarre, D. et al. Imaging lipid bodies in cells and tissues using third-harmonic generation microscopy. Nat Methods 3, 47-53 (2006).

23. Boyd, R.W. Nonlinear Optics 3rd Ed., Academic Press (2008).

24. Campagnola, P.J. et al. Three-dimensional high-resolution second-harmonic generation imaging of endogenous structural proteins in biological tissues. Biophys J 82, 493-508 (2002).

25. Cox, G., Moreno, N. & Feijo, J. Second-harmonic imaging of plant polysaccharides. J Biomed Opt 10 (2005).

26. Wokosin, D.L., Centonze, V.E., Crittenden, S. & White, J. Three-photon excitation fluorescence imaging of biological specimens using an all-solid-state laser. Bioimaging 4, 208-214 (1996).

27. Gu, M. Resolution in three-photon fluorescence scanning microscopy. Opt Lett 21, 988-990 (1996).

28. Maiti, S., Shear, J.B., Williams, R.M., Zipfel, W.R. & Webb, W.W. Measuring serotonin distribution in live cells with three-photon excitation. Science 275, 530-532 (1997).

29. Olivier, N. et al. Cell Lineage reconstruction of early zebrafish embryos using label-free nonlinear microscopy. Science 329, 967-971 (2010).

30. Witte, S. et al. Label-free live brain imaging and targeted patching with third-harmonic generation microscopy. PNAS 108, 5970-5975 (2011).

31. Min, W., Freudiger, C.W., Lu, S. & Xie, X.S. Coherent nonlinear optical imaging: beyond fluorescence microscopy. Annu Rev Physical Chem 62, 507-530 (2011).

32. Maker, P.D. & Terhune, R.W. Study of optical effects due to an induced polarization third order in electric field strength. Phys Rev 137, A801-A818 (1965).

33. Rinia, H.A., Bonn, M., Muller, M. & Vartiainen, E.M. Quantitative CARS spectroscopy using the maximum entropy method: the main lipid phase transition. Chemphyschem 8, 279-287 (2007).

34. Day, J.P.R. et al. Quantitative coherent anti-stokes Raman scattering (CARS) microscopy. J Phys Chem B 115, 7713-7725 (2011).

35. Langbein, W., Rocha-Mendoza, I. & Borri, P. Single source coherent anti-Stokes Raman microspectroscopy using spectral focusing. Appl Phys Lett 95 (2009).

36. Liu, Y., Lee, Y.J. & Cicerone, M.T. Broadband CARS spectral phase retrieval using a time-domain Kramers-Kronig transform. Opt Lett 34, 1363-1365 (2009).

37. Liu, Y., Lee, Y.J. & Cicerone, M.T. Fast extraction of resonant vibrational response from CARS spectra with arbitrary nonresonant background. J Raman Spec 40, 726-731 (2009).

38. Masia, F., Glen, A., Stephens, P., Borri, P. & Langbein, W. Quantitative chemical imaging and unsupervised analysis using hyperspectral coherent anti-stokes Raman scattering microscopy. Anal Chem 85, 10820-10828 (2013).

39. Evans, C.L., Potma, E.O. & Xie, X.S. Coherent anti-stokes Raman scattering spectral interferometry: determination of the real and imaginary components of nonlinear susceptibility $\chi^{(3)}$ for vibrational microscopy. Opt Lett 29, 2923-2925 (2004).

40. Marks, D.L. & Boppart, S.A. Nonlinear interferometric vibrational imaging. Phys Rev Lett 92 (2004).

41. Oron, D., Dudovich, N. & Silberberg, Y. Femtosecond phase-and-polarization control for background-free coherent anti-Stokes Raman spectroscopy. Phys Rev Lett 90 (2003).

42. Lim, S.H., Caster, A.G. & Leone, S.R. Single-pulse phase-control interferometric coherent anti-Stokes Raman scattering spectroscopy. Phys Rev A 72 (2005).

43. Lim, S.H., Caster, A.G. & Leone, S.R. Fourier transform spectral interferometric coherent anti-Stokes Raman scattering (FTSI-CARS) spectroscopy. Opt Lett 32, 1332-1334 (2007).

44. Liu, Y., King, M.D., Tu, H.H., Zhao, Y.B. & Boppart, S.A. Broadband nonlinear vibrational spectroscopy by shaping a coherent fiber supercontinuum. Opt Express 21, 8269-8275 (2013).

45. Freudiger, C.W. et al. Multicolored stain-free histopathology with coherent Raman imaging. Lab Invest 92, 1492-1502 (2012).

46. Ploetz, E., Laimgruber, S., Berner, S., Zinth, W. & Gilch, P. Femtosecond stimulated Raman microscopy. Appl Phys B-Lasers & Optics 87, 389-393 (2007).

47. Nandakumar, P., Kovalev, A. & Volkmer, A. Vibrational imaging based on stimulated Raman scattering microscopy. New J Phys 11, 033026 (2009).

48. Saar, B.G. et al. Video-rate molecular imaging *in vivo* with stimulated Raman scattering. Science 330, 1368-1370 (2010).

49. Freudiger, C.W. et al. Highly specific label-free molecular imaging with spectrally tailored excitation stimulated Raman scattering (STE-SRS) microscopy. Nat Photonics 5, 103-109 (2011).

50. Ozeki, Y. et al. High-speed molecular spectral imaging of tissue with stimulated Raman scattering. Nat Photonics 6, 844-850 (2012).

51. Fu, D. et al. Quantitative chemical imaging with multiplex stimulated Raman scattering microscopy. J Am Chem Soc 134, 3623-3626 (2012).

52. Zhang, D. et al. Quantitative vibrational imaging by hyperspectral stimulated Raman scattering microscopy and multivariate curve resolution analysis. Anal Chem 85, 98-106 (2013).

53. Fu, D., Holtom, G., Freudiger, C., Zhang, X. & Xie, X.S. Hyperspectral imaging with stimulated Raman scattering by chirped femtosecond lasers. J Phys Chem B 117, 4634-4640 (2013).

54. Zhang, D., Sipchenko, M.N. & Cheng, J.X. Highly sensitive vibrational imaging by femtosecond pulse stimulated Raman loss. J Phys Chem Lett 2, 1248-1253 (2011).

55. Cheng, J.X. & Xie, X.S. Coherent Raman scattering microscopy 1st Ed., CRC Press (2012).

56. Movasaghi, Z., Rehman, S. & Rehman, I.U. Raman spectroscopy of biological tissues. Appl Spec Rev 42, 493-541 (2007).

57. De Gelder, J., De Gussem, K., Vandenabeele, P. & Moens, L. Reference database of Raman spectra of biological molecules. J Raman Spec 38, 1133-1147 (2007).

58. Carriles, R. et al. Invited review article: imaging techniques for harmonic and multiphoton absorption fluorescence microscopy. The Rev Sci Instr 80, 081101 (2009).

59. Roeffaers, M.B.J. et al. Label-free imaging of biomolecules in food products using stimulated Raman microscopy. J Biomed Opt 16 (2011).

60. Zhang, X. et al. Label-free live-cell imaging of nucleic acids using stimulated Raman scattering microscopy. Chemphyschem 13, 1054-1059 (2012).

61. Camp Jr, C.H. et al. High-speed coherent Raman fingerprint imaging of biological tissues. Nat Photonics 8, 627-634 (2014).

62. Okuno, M. et al. Quantitative CARS molecular fingerprinting of single living cells with the use of the maximum entropy method. Angewandte Chem Int Ed 49, 6773-6777 (2010).

63. Saar, B.G. et al. Label-free, real-time monitoring of biomass processing with stimulated Raman scattering microscopy. Angewandte Chem Int Ed 49, 5476-5479 (2010).

64. Nadiarnykh, O., Lacomb, R.B., Campagnola, P.J. & Mohler, W.A. Coherent and incoherent SHG in fibrillar cellulose matrices. Opt Express 15, 3348-3360 (2007).

65. Chu, S.W. et al. Multimodal nonlinear spectral microscopy based on a femtosecond Cr:forsterite laser. Opt Lett 26, 1909-1911 (2001).

66. Mizutani, G. et al. Detection of starch granules in a living plant by optical second harmonic microscopy. J Lumin 87-9, 824-826 (2000).

67. Chen, J.X., Volkmer, A., Book, L.D. & Xie, X.S. Multiplex coherent anti-stokes Raman scattering microspectroscopy and study of lipid vesicles. J Phys Chem B 106, 8493-8498 (2002).

68. Nan, X.L., Cheng, J.X. & Xie, X.S. Vibrational imaging of lipid droplets in live fibroblast cells with coherent anti-Stokes Raman scattering microscopy. J Lipid Res 44, 2202-2208 (2003).

69. Slipchenko, M.N., Le, T.T., Chen, H.T. & Cheng, J.X. High-Speed vibrational imaging and spectral analysis of lipid bodies by compound Raman microscopy. J Phys Chem B 113, 7681-7686 (2009).

70. Wang, H.F., Fu, Y., Zickmund, P., Shi, R.Y. & Cheng, J.X. Coherent anti-stokes Raman scattering imaging of axonal myelin in live spinal tissues. Biophys J 89, 581-591 (2005).

71. Wei, L. et al. Live-cell imaging of alkyne-tagged small biomolecules by stimulated Raman scattering. Nat Methods 11, 410-412 (2014).

72. Chemnitz, M. et al. Widely tuneable fiber optical parametric amplifier for coherent anti-Stokes Raman scattering microscopy. Opt Express 20, 26583-26595 (2012).

73. Meyer, T. et al. Expanding multimodal microscopy by high spectral resolution coherent anti-Stokes Raman scattering imaging for clinical disease diagnostics. Anal Chem 85, 6703-6715 (2013).

74. Xie, X.S., Yu, J. & Yang, W.Y. Perspective - living cells as test tubes. Science 312, 228-230 (2006).

75. Weigelin, B., Bakker, G.-J. & Friedl, P. Intravital third harmonic generation microscopy of collective melanoma cell invasion: principles of interface guidance and microvesicle dynamics. Intravital 1, 32-43 (2012).

76. Cheng, J.X., Jia, Y.K., Zheng, G.F. & Xie, X.S. Laser-scanning coherent anti-stokes Raman scattering microscopy and applications to cell biology. Biophys J 83, 502-509 (2002).

77. Suhalim, Jeffrey L. et al. Characterization of cholesterol crystals in atherosclerotic plaques using stimulated Raman scattering and second-harmonic generation microscopy. Biophys J 102, 1988-1995 (2012).

78. Wang, P. et al. Label-free quantitative imaging of cholesterol in intact tissues by hyperspectral stimulated Raman scattering microscopy. Angewandte Chem Int Ed 52, 13042-13046 (2013).

79. Gauderon, R., Lukins, P.B. & Sheppard, C.J.R. Simultaneous multichannel nonlinear imaging: combined two-photon excited fluorescence and second-harmonic generation microscopy. Micron 32, 685-689 (2001).

80. Chu, S.W. et al. Nonlinear bio-photonic crystal effects revealed with multimodal nonlinear microscopy. J Micr 208, 190-200 (2002).

81. Tripathy, U. et al. Optimization of malaria detection based on third harmonic generation imaging of hemozoin. Anal & Bioanal Chem 405, 5431-5440 (2013).

82. Zoumi, A., Yeh, A. & Tromberg, B.J. Imaging cells and extracellular matrix *in vivo* by using second-harmonic generation and two-photon excited fluorescence. PNAS 99, 11014-11019 (2002).

83. Schaller, R.D., Johnson, J.C. & Saykally, R.J. Nonlinear chemical imaging microscopy: near-field third harmonic generation imaging of human red blood cells. Anal Chem 72, 5361-5364 (2000).

84. Bito, K. et al. Protein secondary structure imaging with ultrabroadband multiplex coherent anti-Stokes Raman scattering (CARS) microspectroscopy. J Phys Chem B 116, 1452-1457 (2012).

85. Plotnikov, S.V., Millard, A.C., Campagnola, P.J. & Mohler, W.A. Characterization of the myosin-based source for second-harmonic generation from muscle sarcomeres. Biophys J 90, 693-703 (2006).

86. Prent, N. et al. Intermyofilament dynamics of myocytes revealed by second harmonic generation microscopy. J Biomed Opt 13 (2008).

87. Llewellyn, M.E., Barretto, R.P., Delp, S.L. & Schnitzer, M.J. Minimally invasive high-speed imaging of sarcomere contractile dynamics in mice and humans. Nature 454, 784-788 (2008).

88. Chu, S.W. et al. Studies of $\chi^{(2)}/\chi^{(3)}$ tensors in submicron-scaled bio-tissues by polarization harmonics optical microscopy. Biophys J 86, 3914-3922 (2004).

89. Barzda, V. Visualization of mitochondria in cardiomyocytes by simultaneous harmonic generation and fluorescence microscopy. Opt Express 13, 8263-8276 (2005).

90. Both, M. et al. Second harmonic imaging of intrinsic signals in muscle fibers *in situ*. J Biomed Opt 9, 882-892 (2004).

91. Dombeck, D.A. et al. Uniform polarity microtubule assemblies imaged in native brain tissue by second-harmonic generation microscopy. PNAS 100, 7081-7086 (2003).

92. Huang, S.H., Heikal, A.A. & Webb, W.W. Two-photon fluorescence spectroscopy and microscopy of NAD(P)H and flavoprotein. Biophys J 82, 2811-2825 (2002).

93. Skala, M.C. et al. *In vivo* multiphoton microscopy of NADH and FAD redox states, fluorescence lifetimes, and cellular morphology in precancerous epithelia. PNAS 104, 19494-19499 (2007).

94. Zeng, Y.N. et al. Imaging lignin-downregulated alfalfa using coherent anti-Stokes Raman scattering microscopy. Bioenergy Res 3, 272-277 (2010).

95. Rothstein, E.C., Carroll, S., Combs, C.A., Jobsis, P.D. & Balaban, R.S. Skeletal muscle NAD(P)H two-photon fluorescence microscopy *in vivo*: topology and optical inner filters. Biophys J 88, 2165-2176 (2005).

96. Kao, F.J. The use of optical parametric oscillator for harmonic generation and two-photon UV fluorescence microscopy. Micr Res & Tech 63, 175-181 (2004).

97. Chen, S.Y., Hsu, C.Y. & Sun, C.K. Epi-third and second harmonic generation microscopic imaging of abnormal enamel. Opt Express 16, 11670-11679 (2008).

98. Supatto, W. et al. *In vivo* modulation of morphogenetic movements in *Drosophila* embryos with femtosecond laser pulses. PNAS 102, 1047-1052 (2005).

99. Yelin, D. & Silberberg, Y. Laser scanning third-harmonic-generation microscopy in biology. Opt Express 5, 169-175 (1999).

100. Weiner, A.M. Ultrafast Optics 1st Ed., Wiley Publication (2009).

101. Dudovich, N., Oron, D. & Silberberg, Y. Single-pulse coherently controlled nonlinear Raman spectroscopy and microscopy. Nature 418, 512-514 (2002).

102. Ogilvie, J.P. et al. Use of coherent control for selective two-photon fluorescence microscopy in live organisms. Opt Express 14, 759-766 (2006).

103. Dela Cruz, J.M., Pastirk, I., Comstock, M., Lozovoy, V.V. & Dantus, M. Use of coherent control methods through scattering biological tissue to achieve functional imaging. PNAS 101, 16996-17001 (2004).

104. Pillai, R.S. et al. Multiplexed two-photon microscopy of dynamic biological samples with shaped broadband pulses. Opt Express 17, 12741-12752 (2009).

105. Isobe, K. et al. Multifarious control of two-photon excitation of multiple fluorophores achieved by phase modulation of ultra-broadband laser pulses. Opt Express 17, 13737-13746 (2009).

106. Xi, P., Andegeko, Y., Weisel, L.R., Lozovoy, V.V. & Dantus, M. Greater signal, increased depth, and less photobleaching in two-photon microscopy with 10 fs pulses. Opt Comm 281, 1841-1849 (2008).

107. Dela Cruz, J.M., Pastirk, I., Lozovoy, V.V., Walowicz, K.A. & Dantus, M. Multiphoton intrapulse interference 3: probing microscopic chemical environments. J Phys Chem A 108, 53-58 (2004).

108. Walowicz, K.A., Pastirk, I., Lozovoy, V.V. & Dantus, M. Multiphoton intrapulse interference. 1. control of multiphoton processes in condensed phases. J Phys Chem A 106, 9369-9373 (2002).

109. von Vacano, B. & Motzkus, M. Time-resolving molecular vibration for microanalytics: single laser beam nonlinear Raman spectroscopy in simulation and experiment. Phys Chem Chem Phys 10, 681-691 (2008).

110. Isobe, K. et al. Single-pulse coherent anti-Stokes Raman scattering microscopy employing an octave spanning pulse. Opt Express 17, 11259-11266 (2009).

111. Oron, D., Dudovich, N. & Silberberg, Y. Single-pulse phase-contrast nonlinear Raman spectroscopy. Phys Rev Lett 89 (2002).

112. Brumer, P. & Shapiro, M. One photon mode selective control of reactions by rapid or shaped laser-pulses - an emperor without clothes. Chem Phys 139, 221-228 (1989).

113. Agrawal, G.P. Nonlinear Fiber Optics 4th Ed., Academic Press (2004).

114. Dudly, J. M. & Taylor J. R. Supercontinuum Generation in Optical Fibers 1st Ed., Cambridge University Press (2010).

115. Heidt, A.M. Pulse preserving flat-top supercontinuum generation in all-normal dispersion photonic crystal fibers. J Opt Soc Am B 27, 550-559 (2010).

116. Tomlinson, W.J., Stolen, R.H. & Johnson, A.M. Optical wave breaking of pulses in nonlinear optical fibers. Opt Lett 10, 457-459 (1985).

117. Rothenberg, J.E. & Grischkowsky, D. Observation of the formation of an optical intensity shock and wave breaking in the nonlinear propagation of pulses in optical fibers. Phys Rev Lett 62, 531-534 (1989).

118. Nishizawa, N. & Takayanagi, J. Octave spanning high-quality supercontinuum generation in all-fiber system. J Opt Soc Am B 24, 1786-1792 (2007).

119. Tu, H. et al. Scalar generalized nonlinear Schrödinger equation-quantified continuum generation in an all-normal dispersion photonic crystal fiber for broadband coherent optical sources. Opt Express 18, 27872-27884 (2010).

120. Tu, H., Liu, Y., Turchinovich, D. & Boppart, S.A. Compression of fiber supercontinuum pulses to the Fourier-limit in a high-numerical-aperture focus. Opt Lett 36, 2315-2317 (2011).

121. Jureller, J.E., Scherer, N.F., Birks, T.A., Wadsworth, W.J. & Russell, P.S.J. Widely tunable femtosecond pulses from a tapered fiber for ultrafast microscopy and multiphoton applications. Ultrafast Phen XIII 71, 684-686 (2003).

122. McConnell, G. & Riis, E. Two-photon laser scanning fluorescence microscopy using photonic crystal fiber. J Biomed Opt 9, 922-927 (2004).

123. Paulsen, H.N., Hilligsoe, K.M., Thogersen, J., Keiding, S.R. & Larsen, J.J. Coherent anti-Stokes Raman scattering microscopy with a photonic crystal fiber based light source. Opt Lett 28, 1123-1125 (2003).

124. Kano, H. & Hamaguchi, H. Ultrabroadband (>2500 cm^{-1}) multiplex coherent anti-Stokes Raman scattering microspectroscopy using a supercontinuum generated from a photonic crystal fiber. Appl Phys Lett 86 (2005).

125. Kee, T.W. & Cicerone, M.T. Simple approach to one-laser, broadband coherent anti-Stokes Raman scattering microscopy. Opt Lett 29, 2701-2703 (2004).

126. Vartiainen, E.M., Rinia, H.A., Muller, M. & Bonn, M. Direct extraction of Raman line-shapes from congested CARS spectra. Opt Express 14, 3622-3630 (2006).

127. Pegoraro, A.F. et al. Optimally chirped multimodal CARS microscopy based on a single Ti:sapphire oscillator. Opt Express 17, 2984-2996 (2009).

128. Liu, Y., Tu, H. & Boppart, S.A. Wave-breaking-extended fiber supercontinuum generation for high compression ratio transform-limited pulse compression. Opt Lett 37, 2172-2174 (2012).

129. Druon, F. & Georges, P. Pulse-compression down to 20 fs using a photonic crystal fiber seeded by a diode-pumped Yb:SYS laser at 1070 nm. Opt Express 12, 3383-3396 (2004).

130. Schenkel, B., Paschotta, R. & Keller, U. Pulse compression with supercontinuum generation in microstructure fibers. J Opt Soc Am B 22, 687-693 (2005).

131. von Vacano, B., Buckup, T. & Motzkus, M. Shaper-assisted collinear SPIDER: fast and simple broadband pulse compression in nonlinear microscopy. J Opt Soc Am B 24, 1091-1100 (2007).

132. Amorim, A.A. et al. Sub-two-cycle pulses by soliton self-compression in highly nonlinear photonic crystal fibers. Opt Lett 34, 3851-3853 (2009).

133. Sell, A., Krauss, G., Scheu, R., Huber, R. & Leitenstorfer, A. 8-fs pulses from a compact Er:fiber system: quantitative modeling and experimental implementation. Opt Express 17, 1070-1077 (2009).

134. Südmeyer, T. et al. Nonlinear femtosecond pulse compression at high average power levels by use of a large-mode-area holey fiber. Opt Lett 28, 1951-1953 (2003).

135. McConnell, G. & Riis, E. Ultra-short pulse compression using photonic crystal fibre. Appl Phys B-Lasers & Optics 78, 557-563 (2004).

136. Heidt, A.M. et al. Coherent octave spanning near-infrared and visible supercontinuum generation in all-normal dispersion photonic crystal fibers. Opt Express 19, 3775-3787 (2011).

137. Heidt, A.M. et al. High quality sub-two cycle pulses from compression of supercontinuum generated in all-normal dispersion photonic crystal fiber. Opt Express 19, 13873-13879 (2011).

138. Hooper, L.E., Mosley, P.J., Muir, A.C., Wadsworth, W.J. & Knight, J.C. Coherent supercontinuum generation in photonic crystal fiber with all-normal group velocity dispersion. Opt Express 19, 4902-4907 (2011).

139. Smith, A.M., Mancini, M.C. & Nie, S.M. Bioimaging second window for *in vivo* imaging. Nature Nanotech 4, 710-711 (2009).

140. NKT Photonics: www.nktphotonics.com (2014).

141. von Vacano, B., Buckup, T. & Motzkus, M. *In situ* broadband pulse compression for multiphoton microscopy using a shaper-assisted collinear SPIDER. Opt Lett 31, 1154-1156 (2006).

142. Xu, B., Gunn, J.M., Cruz, J.M.D., Lozovoy, V.V. & Dantus, M. Quantitative investigation of the multiphoton intrapulse interference phase scan method for simultaneous phase measurement and compensation of femtosecond laser pulses. J Opt Soc Am B 23, 750-759 (2006).

143. Lozovoy, V.V., Pastirk, I. & Dantus, M. Multiphoton intrapulse interference. IV. Ultrashort laser pulse spectral phase characterization and compensation. Opt Lett 29, 775-777 (2004).

144. Kempe, M. & Rudolph, W. Impact of chromatic and spherical aberration on the focusing of ultrashort light pulses by lenses. Opt Lett 18, 137-139 (1993).

145. Anderson, D., Desaix, M., Lisak, M. & Quiroga-Teixeiro, M.L. Wave breaking in nonlinear-optical fibers. J Opt Soc Am B 9, 1358-1361 (1992).

146. Tomlinson, W.J., Stolen, R.H. & Shank, C.V. Compression of optical pulses chirped by self-phase modulation in fibers. J Opt Soc Am B 1, 139-149 (1984).

147. Anderson, D., Desaix, M., Karlsson, M., Lisak, M. & Quiroga-Teixeiro, M.L. Wave-breaking-free pulses in nonlinear-optical fibers. J Opt Soc Am B 10, 1185-1190 (1993).

148. Südmeyer, T. et al. Nonlinear femtosecond pulse compression at high average power levels by use of a large-mode-area holey fiber. Opt Lett 28, 1951-1953 (2003).

149. Metzger, B., Steinmann, A. & Giessen, H. High-power widely tunable sub-20 fs Gaussian laser pulses for ultrafast nonlinear spectroscopy. Opt Express 19, 24354-24360 (2011).

150. Tu, H. et al. Cross-validation of theoretically quantified fiber continuum generation and absolute pulse measurement by MIIPS for a broadband coherently controlled optical source. Appl Phys B-Lasers & Optics 106, 379-384 (2012).

151. Finot, C., Kibler, B., Provost, L. & Wabnitz, S. Beneficial impact of wave-breaking for coherent continuum formation in normally dispersive nonlinear fibers. J Opt Soc Am B 25, 1938-1948 (2008).

152. Demmler, S. et al. Generation of high quality, 1.3 cycle pulses by active phase control of an octave spanning supercontinuum. Opt Express 19, 20151-20158 (2011).

153. Tu, H. et al. Nonlinear polarization dynamics in a weakly birefringent all-normal dispersion photonic crystal fiber: toward a practical coherent fiber supercontinuum laser. Opt Express 20, 1113-1128 (2012).

154. Liu, Y., Tu, H., Benalcazar, W.A., Chaney, E.J. & Boppart, S.A. Multimodal nonlinear imaging by pulse shaping of a fiber supercontinuum from 900 to 1160 nm. IEEE JSTQE 18, 1209-1214 (2012).

155. Brakenhoff, G.J., Muller, M. & Squier, J. Femtosecond pulse width control in microscopy by two-photon absorption autocorrelation. J Micr 179, 253-260 (1995).

156. Tang, S., Krasieva, T.B., Chen, Z., Tempea, G. & Tromberg, B.J. Effect of pulse duration on two-photon excited fluorescence and second harmonic generation in nonlinear optical microscopy. J Biomed Opt 11, 020501 (2006).

157. Xi, P., Andegeko, Y., Pestov, D., Lovozoy, V.V. & Dantus, M. Two-photon imaging using adaptive phase compensated ultrashort laser pulses. J Biomed Opt 14, 014002 (2009).

158. Dantus, M., Pestov, D. & Andegeko, Y. Biochemical applications of nonlinear optical spectroscopy 1st Ed., CRC Press (2009).

159. Isobe, K. et al. Nonlinear optical microscopy and spectroscopy employing octave spanning pulses. IEEE JSTQE 16, 767-780 (2010).

160. Meshulach, D. & Silberberg, Y. Coherent quantum control of multiphoton transitions by shaped ultrashort optical pulses. Phys Rev A 60, 1287-1292 (1999).

161. Pastirk, I., Dela Cruz, J., Walowicz, K., Lozovoy, V. & Dantus, M. Selective two-photon microscopy with shaped femtosecond pulses. Opt Express 11, 1695-1701 (2003).

162. Schon, P., Behrndt, M., Ait-Belkacem, D., Rigneault, H. & Brasselet, S. Polarization and phase pulse shaping applied to structural contrast in nonlinear microscopy imaging. Phys Rev A 81 (2010).

163. Palero, J., Boer, V., Vijverberg, J., Gerritsen, H. & Sterenborg, H.J. Short-wavelength two-photon excitation fluorescence microscopy of tryptophan with a photonic crystal fiber based light source. Opt Express 13, 5363-5368 (2005).

164. Keisuke, I. et al. Multi-spectral two-photon excited fluorescence microscopy using supercontinuum light source. Japan J App Phys 44, L167 (2005).

165. Li, D., Zheng, W. & Qu, J.A.Y. Two-photon autofluorescence microscopy of multicolor excitation. Opt Lett 34, 202-204 (2009).

166. Tada, J. et al. Adaptively controlled supercontinuum pulse from a microstructure fiber for two-photon excited fluorescence microscopy. Appl Opt 46, 3023-3030 (2007).

167. Hashimoto, H. et al. Measurement of two-photon excitation spectra of fluorescent proteins with nonlinear Fourier-transform spectroscopy. Appl Opt 49, 3323-3329 (2010).

168. Bestvater, F. et al. Two-photon fluorescence absorption and emission spectra of dyes relevant for cell imaging. J Micr 208, 108-115 (2002).

169. Laiho, L.H., Pelet, S., Hancewicz, T.M., Kaplan, P.D. & So, P.T.C. Two-photon 3-D mapping of *ex vivo* human skin endogenous fluorescence species based on fluorescence emission spectra. J Biomed Opt 10, 024016 (2005).

170. Chen, S.Y., Wu, H.Y. & Sun, C.K. *In vivo* harmonic generation biopsy of human skin. J Biomed Opt 14, 060505 (2009).

171. Makarov, N.S., Drobizhev, M. & Rebane, A. Two-photon absorption standards in the 550-1600 nm excitation wavelength range. Opt Express 16, 4029-4047 (2008).

172. Unruh, J.R. et al. Two-photon microscopy with wavelength switchable fiber laser excitation. Opt Express 14, 9825-9831 (2006).

173. Rehbinder, J., Pohling, C., Buckup, T. & Motzkus, M. Multiplex coherent anti-Stokes Raman microspectroscopy with tailored Stokes spectrum. Opt Lett 35, 3721-3723 (2010).

174. Kano, H. & Hamaguchi, H. In-vivo multi-nonlinear optical imaging of a living cell using a supercontinuum light source generated from a photonic crystal fiber. Opt Express 14, 2798-2804 (2006).

175. Selm, R. et al. Ultrabroadband background-free coherent anti-Stokes Raman scattering microscopy based on a compact Er:fiber laser system. Opt Lett 35, 3282-3284 (2010).

176. Mahou, P. et al. Multicolor two-photon tissue imaging by wavelength mixing. Nat Methods 9, 815-818 (2012).

177. Rocha-Mendoza, I., Langbein, W. & Borri, P. Coherent anti-Stokes Raman microspectroscopy using spectral focusing with glass dispersion. Appl Phys Lett 93 (2008).

178. Hellerer, T., Enejder, A.M.K. & Zumbusch, A. Spectral focusing: High spectral resolution spectroscopy with broad-bandwidth laser pulses. Appl Phys Lett 85, 25-27 (2004).

179. Ogilvie, J.P., Beaurepaire, E., Alexandrou, A. & Joffre, M. Fourier-transform coherent anti-Stokes Raman scattering microscopy. Opt Lett 31, 480-482 (2006).

180. Postma, S. et al. Application of spectral phase shaping to high resolution CARS spectroscopy. Opt Express 16, 7985-7996 (2008).

181. Rocha-Mendoza, I., Langbein, W., Watson, P. & Borri, P. Differential coherent anti-Stokes Raman scattering microscopy with linearly chirped femtosecond laser pulses. Opt Lett 34, 2258-2260 (2009).

182. von Vacano, B., Buckup, T. & Motzkus, M. Highly sensitive single-beam heterodyne coherent anti-Stokes Raman scattering. Opt Letters 31, 2495-2497 (2006).

183. von Vacano, B., Wohlleben, W. & Motzkus, M. Actively shaped supercontinuum from a photonic crystal fiber for nonlinear coherent microspectroscopy. Opt Lett 31, 413-415 (2006).

184. Li, H.W. et al. Coherent mode-selective Raman excitation towards standoff detection. Opt Express 16, 5499-5504 (2008).

185. Katz, O., Levitt, J.M., Grinvald, E. & Silberberg, Y. Single-beam coherent Raman spectroscopy and microscopy via spectral notch shaping. Opt Express 18, 22693-22701 (2010).

186. Wipfler, A., Rehbinder, J., Buckup, T. & Motzkus, M. Full characterization of the third-order nonlinear susceptibility using a single-beam coherent anti-Stokes Raman scattering setup. Opt Lett 37, 4239-4241 (2012).

187. Andresen, E.R., Paulsen, H.N., Birkedal, V., Thogersen, J. & Keiding, S.R. Broadband multiplex coherent anti-Stokes Raman scattering microscopy employing photonic-crystal fibers. J Opt Soc Am B 22, 1934-1938 (2005).

188. Murugkar, S. et al. Coherent anti-Stokes Raman scattering microscopy using photonic crystal fiber with two closely lying zero dispersion wavelengths. Opt Express 15, 14028-14037 (2007).

189. Tu, H. & Boppart, S.A. Coherent fiber supercontinuum for biophotonics. Laser & Photon Rev, 1-18 (2012).

190. Tu, H., Liu, Y., Turchinovich, D. & Boppart, S.A. Compression of fiber supercontinuum pulses to the Fourier-limit in a high-numerical-aperture focus. Opt Lett 36, 2315-2317 (2011).

191. Jakutis-Neto, J., Lin, J.P., Wetter, N.U. & Pask, H. Continuous-wave watt-level Nd:YLF/KGW Raman laser operating at near-IR, yellow and lime-green wavelengths. Opt Express 20 (2012).

192. Huang, D. et al. Optical coherence tomography. Science 254, 1178-1181 (1991).

193. Wojtkowski, M. et al. Ultrahigh-resolution, high-speed, Fourier domain optical coherence tomography and methods for dispersion compensation. Opt Express 12, 2404-2422 (2004).

194. Frostig, H., Katz, O., Natan, A. & Silberberg, Y. Single-pulse stimulated Raman scattering spectroscopy. Opt Lett 36, 1248-1250 (2011).

195. Yue, S.H., Slipchenko, M.N. & Cheng, J.X. Multimodal nonlinear optical microscopy. Laser & Photon Rev 5, 496-512 (2011).

196. Pavillon, N. & Smith, N.I. Multimodal label-free microscopy. 2013 Conference on Lasers and Electro-Optics Pacific Rim (2013).

197. Meyer, T., Schmitt, M., Dietzek, B. & Popp, J. Accumulating advantages, reducing limitations: multimodal nonlinear imaging in biomedical sciences - the synergy of multiple contrast mechanisms. J Biophotonics 6, 887-904 (2013).

198. Hoover, E.E. & Squier, J.A. Advances in multiphoton microscopy technology. Nat Photonics 7, 93-101 (2013).

199. Pope, I., Langbein, W., Watson, P. & Borri, P. Simultaneous hyperspectral differential-CARS, TPF and SHG microscopy with a single 5 fs Ti: Sa laser. Opt Express 21, 7096-7106 (2013).

200. Yang, S. et al. Multi-color ultrafast laser platform for nonlinear optical imaging based on independently tunable optical parametric oscillators. Appl Phys B-Lasers & Optics 111, 617-625 (2013).

201. Graf, B.W. et al. Long-term time-lapse multimodal intravital imaging of regeneration and bone-marrow-derived cell dynamics in skin. Technology 1, 8-19 (2013).

202. Pelegati, V.B. et al. Harmonic optical microscopy and fluorescence lifetime imaging platform for multimodal imaging. Micro Res & Tech 75, 1383-1394 (2012).

203. Nie, B. et al. Multimodal microscopy with sub-30 fs Yb fiber laser oscillator. Biomed Opt Express 3, 1750-1756 (2012).

204. Segawa, H. et al. Label-free tetra-modal molecular imaging of living cells with CARS, SHG, THG and TSFG (coherent anti-Stokes Raman scattering, second harmonic generation, third harmonic generation and third-order sum frequency generation). Opt Express 20 (2012).

205. Vogler, N. et al. Multimodal imaging to study the morphochemistry of basal cell carcinoma. J Biophotonics 3, 728-736 (2010).

206. Selm, R., Krauss, G., Leitenstorfer, A. & Zumbusch, A. Simultaneous second-harmonic generation, third-harmonic generation, and four-wave mixing microscopy with single sub-8 fs laser pulses. Appl Phys Lett 99 (2011).

207. Lu, F.K., Zheng, W., Lin, J. & Huang, Z.W. Integrated coherent anti-Stokes Raman scattering and multiphoton microscopy for biomolecular imaging using spectral filtering of a femtosecond laser. Appl Phys Lett 96, 133701 (2010).

208. Chen, H. et al. A multimodal platform for nonlinear optical microscopy and microspectroscopy. Opt Express 17, 1282-1290 (2009).

209. Li, D., Zheng, W., Zeng, Y. & Qu, J.A.Y. *In vivo* and simultaneous multimodal imaging: integrated multiplex coherent anti-Stokes Raman scattering and two-photon microscopy. Appl Phys Lett 97, 223702 (2010).

210. Downes, A., Mouras, R. & Elfick, A. A versatile CARS microscope for biological imaging. J Raman Spec 40, 757-762 (2009).

211. Jhan, J.W. et al. Integrated multiple multi-photon imaging and Raman spectroscopy for characterizing structure-constituent correlation of tissues. Opt Express 16, 16431-16441 (2008).

212. Le, T.T., Langohr, I.M., Locker, M.J., Sturek, M. & Cheng, J.X. Label-free molecular imaging of atherosclerotic lesions using multimodal nonlinear optical microscopy. J Biomed Opt 12, 054007 (2007).

213. Gualda, E.J. et al. *In vivo* imaging of cellular structures in *Caenorhabditis elegans* by combined TPEF, SHG and THG microscopy. J Microsc 229, 141-150 (2008).

214. Provenzano, P.P. et al. Collagen density promotes mammary tumor initiation and progression. BMC Med 6, 11 (2008).

215. Provenzano, P.P. et al. Collagen reorganization at the tumor-stromal interface facilitates local invasion. BMC Med 4, 36 (2006).

216. Prasad, P.N. Introduction to Biophotonics 1st Ed., Wiley Publication (2003).

217. Gauderon, R., Lukins, P.B. & Sheppard, C.J.R. Three-dimensional second-harmonic generation imaging with femtosecond laser pulses. Opt Lett 23, 1209-1211 (1998).

218. Pegoraro, A.F., Slepkov, A.D., Ridsdale, A., Moffatt, D.J. & Stolow, A. Hyperspectral multimodal CARS microscopy in the fingerprint region. J Biophotonics 7, 49-58 (2014).

219. Ostrander, J.H. et al. Optical redox ratio differentiates breast cancer cell lines based on estrogen receptor status. Cancer Res 70, 4759-4766 (2010).

220. Bird, D.K. et al. Metabolic mapping of MCF10A human breast cells via multiphoton fluorescence lifetime imaging of the coenzyme NADH. Cancer Res 65, 8766-8773 (2005).

221. Le, T.T. et al. Nonlinear optical imaging to evaluate the impact of obesity on mammary gland and tumor stroma. Mol Imaging 6, 205-211 (2007).

222. Le, T.T., Huff, T.B. & Cheng, J.X. Coherent anti-Stokes Raman scattering imaging of lipids in cancer metastasis. BMC Cancer 9, 42 (2009).

223. Wu, X. et al. Label-free detection of breast masses using multiphoton microscopy. PLoS ONE 8, e65933 (2013).

224. Potcoava, M.C., Futia, G.L., Aughenbaugh, J., Schlaepfer, I.R. & Gibson, E.A. Raman and coherent anti-Stokes Raman scattering microscopy studies of changes in lipid content and composition in hormone-treated breast and prostate cancer cells. J Biomed Opt 19, 111605 (2014).

225. Walsh, A., Cook, R.S., Rexer, B., Arteaga, C.L. & Skala, M.C. Optical imaging of metabolism in HER2 overexpressing breast cancer cells. Biomed Opt Express 3, 75-85 (2012).

226. Ajeti, V. et al. Structural changes in mixed Col I/Col V collagen gels probed by SHG microscopy: implications for probing stromal alterations in human breast cancer. Biomed Opt Express 2, 2307-2316 (2011).

227. Yang, Y.L. et al. Differential diagnosis of breast cancer using quantitative, label-free and molecular vibrational imaging. Biomed Opt Express 2, 2160-2174 (2011).

228. Gullino, P.M., Pettigrew, H.M. & Grantham, F.H. N-nitrosomethylurea as mammary-gland carcinogen in rats. J Natl Cancer Inst 54, 401-414 (1975).

229. Thompson, H.J. & Adlakha, H. Dose-responsive induction of mammary gland carcinomas by the intraperitoneal injection of 1-methyl-1-nitrosourea. Cancer Res 51, 3411-3415 (1991).

230. Singh, M., McGinley, J.N. & Thompson, H.J. A comparison of the histopathology of premalignant and malignant mammary gland lesions induced in sexually immature rats with those occurring in the human. Lab Invest 80, 221-231 (2000).

231. Arafah, B.M., Finegan, H.M., Roe, J., Manni, A. & Pearson, O.H. Hormone dependency in N-nitrosomethylurea-induced rat mammary tumors. Endocrinology 111, 584-588 (1982).

232. Crist, K.A., Chaudhuri, B., Shivaram, S. & Chaudhuri, P.K. Ductal carcinoma *in situ* in rat mammary gland. The J Surg Res 52, 205-208 (1992).

233. Chan, M.M., Lu, X., Merchant, F.M., Iglehart, J.D. & Miron, P.L. Gene expression profiling of NMU-induced rat mammary tumors: cross species comparison with human breast cancer. Carcinogenesis 26, 1343-1353 (2005).

234. Thompson, H.J., McGinley, J., Rothhammer, K. & Singh, M. Ovarian hormone dependence of pre-malignant and malignant mammary gland lesions induced in pre-pubertal rats by 1-methyl-1-nitrosourea. Carcinogenesis 19, 383-386 (1998).

235. Mccormick, D.L., Adamowski, C.B., Fiks, A. & Moon, R.C. Lifetime Dose-response relationships for mammary-tumor induction by a single administration of N-methyl-N-nitrosourea. Cancer Res 41, 1690-1694 (1981).

236. Boppart, S.A., Luo, W., Marks, D.L. & Singletary, K.W. Optical coherence tomography: feasibility for basic research and image-guided surgery of breast cancer. Breast Cancer Res Treat 84, 85-97 (2004).

237. Olumi, A.F. et al. Carcinoma-associated fibroblasts direct tumor progression of initiated human prostatic epithelium. Cancer Res 59, 5002-5011 (1999).

238. Wang, H.W., Le, T.T. & Cheng, J.X. Label-free imaging of arterial cells and extracellular matrix using a multimodal CARS microscope. Opt Comm 281, 1813-1822 (2008).

239. Venkateswaran, A. et al. The novel antiangiogenic VJ115 inhibits the NADH oxidase ENOX1 and cytoskeleton-remodeling proteins. Invest New Drug 31, 535-544 (2013).

240. Ushio-Fukai, M. Redox signaling in angiogenesis: Role of NADPH oxidase. Cardiovasc Res 71, 226-235 (2006).

241. Young, B., Lowe, J.S., Stevens, A. & Heath, J.W. Wheater's Functional Histology 5th Ed., Elsevier (2006).

242. Kalluri, R. & Zeisberg, M. Fibroblasts in cancer. Nat Rev Cancer 6, 392-401 (2006).

243. Weis, S.M. & Cheresh, D.A. Tumor angiogenesis: molecular pathways and therapeutic targets. Nat Medicine 17, 1359-1370 (2011).

244. Barsky, S.H., Rao, C.N., Grotendorst, G.R. & Liotta, L.A. Increased content of type-V collagen in desmoplasia of human-breast carcinoma. Am J Pathol 108, 276-283 (1982).

245. Le, T.T., Yue, S.H. & Cheng, J.X. Shedding new light on lipid biology with coherent anti-Stokes Raman scattering microscopy. J Lipid Res 51, 3091-3102 (2010).

246. Yue, S.H. et al. Cholesteryl ester accumulation induced by PTEN loss and PI3K/AKT activation underlies human prostate cancer aggressiveness. Cell Metab 19, 393-406 (2014).

247. Baenke, F., Peck, B., Miess, H. & Schulze, A. Hooked on fat: the role of lipid synthesis in cancer metabolism and tumour development. Dis Mod & Mech 6, 1353-1363 (2013).

248. Surmacki, J., Musial, J., Kordek, R. & Abramczyk, H. Raman imaging at biological interfaces: applications in breast cancer diagnosis. Mol Cancer 12 (2013).

249. Liu, Y. et al. Visualization of hepatobiliary excretory function by intravital multiphoton microscopy. J Biomed Opt 12, 014014 (2007).